Nanobubbles for Ultrasound Mediated Drug Delivery

Damien Vincent Brandon Batchelor

University of Leeds

School of Physics & Astronomy

March 2022

Submitted in accordance with the requirements for the degree of Doctor of Philosophy.

Intellectual Property and Publication Statements

The candidate confirms that the work submitted is his own, except where work which has formed part of jointly authored publications has been included. The contribution of the candidate and the other authors to this work has been explicitly indicated below. The candidate confirms that appropriate credit has been given within the thesis where reference has been made to the work of others.

The work discussed in Chapter 1 and 2 has appeared in the following publication as a review article:

Batchelor, D. V. B. et al. Nanobubbles for therapeutic delivery: Production, stability and current prospects. Curr. Opin. Colloid Interface Sci. 54, 101456 (2021).

All research and writing were performed by D. V. B. B, with co-authors contributing to proof-reading and feedback.

Research and corresponding methodology described in Chapter 5 and 6 has appeared in the following publication:

Batchelor, D. V. B. et al. Nested Nanobubbles for Ultrasound-Triggered Drug Release. ACS Appl. Mater. Interfaces 12, 29085–29093 (2020).

All research and writing were performed by D. V. B. B. with assistance from Dr. James R. McLaughlan (J. R. M.) in the experimental set up for HIFU and PCD experiments. All co-authors provided critical feedback throughout the experimental and writing process.

Research and corresponding methodology described in Chapter 7 and 8 form a publication that is currently under review, in which a first round of comments have been received.

Batchelor, D. V. B. et al. The Influence of Nanobubble Size and Stability on In Vitro Ultrasound Mediated Sonoporation. Under Review (ACS Langmuir) Submitted 11th January 2022, Revision Requests 28th February 2022.

All research and writing were performed by D. V. B. B. with assistance from Dr. Fern Armistead (F.J.A.) for cell culture and HIFU NB destruction experiments. All co-authors provided critical feedback throughout the experimental and writing process.

Other publications co-authored during the course of this studentship include:

Abou-Saleh, R. H., Armistead, F. J., Batchelor, D.V. B. B. et al. Horizon: Microfluidic platform for the production of therapeutic microbubbles and nanobubbles. Rev. Sci. Instrum. 92, 074

Dr. Radwa H. Abou-Saleh (R. H. A.), F.J.A., and D.V.B.B. contributed equally to experimental planning, data acquisition and analysis, and manuscript preparation. D. V. B. B. performed microfluidic experiments assessing the effect of geometry on nanobubble and microbubble concentration. All authors contributed to the initial conceptualization and manuscript preparation. Dr Benjamin R. Johnson (B.R.J.) designed and constructed the Horizon instrument.

*Bourn, M. D. et al. High-throughput microfluidics for evaluating microbubble enhanced delivery of cancer therapeutics in spheroid cultures. J. Control. Release **326**, 13–24 (2020).*

Mr. Matthew D. Bourn (M. D. B.) developed the microfluidic system and performed all cell culture studies, assays and analysis. D. V. B. B. developed and used the acoustic platform and produced microbubbles. All co-authors provided critical feedback throughout the experimental and writing process.

Roach, L. et al. Evaluating Phospholipid-Functionalized Gold Nanorods for In Vivo Applications. Small 2006797, (2021).

D. V. B. B. designed, performed, and analysed the Raman spectroscopy experiments, in collaboration with Dr. L. Roach.

Abou-Saleh, R. H. et al. Freeze-Dried Therapeutic Microbubbles: Stability and Gas Exchange. ACS Appl. Bio Mater. (2020) doi:10.1021/acsabm.0c00982.

D.V. B. B. assisted with the acoustic experimental set up and performed modelling of the predicted vaporisation temperature of microbubbles with different gas cores.

Ingram, N. et al. A Single Short 'Tone Burst' Results in Optimal Drug Delivery to Tumours Using Ultrasound-Triggered Therapeutic Microbubbles. Pharmaceutics 2022, 14, 622. https://doi.org/10.3390/pharmaceutics14030622

D. V. B. B. assisted in discussions, and review and writing of the manuscript.

Acknowledgements

I start by thanking my primary supervisor Prof. Stephen Evans, for almost single-handedly converting me from a 'theoretician' who had never held a pipette, to a fully-fledged experimental biophysicist. His (mostly) unwavering support and guidance, and willingness to offer a (less than) average undergraduate a PhD position is a debt that I can never repay and was truly life changing to someone that had never considered pursuing a career in academia. I would also like to thank my co-supervisors: Dr. Sally Peyman, Dr. James McLaughlan and Dr. Louise Coletta. Sal, for always having an open door and at times being more like a friend than a supervisor. James, for teaching me the correct way to do experiments and explore a parameter space (i.e. go big or go home). Louise, for providing additional insight to my project from a more clinical and pre-clinical perspective, and not to always act like such a physicist. Additional thanks also need to go to both Dr. Radwa Abou-Saleh and Dr. Nicola Ingram for providing support and help throughout the first and second halves of my PhD respectively, despite not being an *official* supervisor, and always giving me the time of day for any questions or feedback. Thanks to Dr. Matthew Bourn for letting me help out with his early morning experiments and get a nice second author paper.

Aside from my supervisory team, there is no doubt in my mind that without the support and friendship from within the MNP group I wouldn't have made it this far. In being a member of MNP, I've been so fortunate to do my PhD within a group of such diverse, talented and fun people. Although almost impossible to acknowledge everyone by name (in alphabetical order): Ash (for the beers) , Abiral (for the beers), Aileen (for the beers) Matt B(for the beers and being an excellent rhythm guitarist and also some science we did), Christa (loves nuts), George (chalk), Holly (wordle and a hatred of seafood), Jack (housemate), Lucien (boring), Sam (small eyes), Harry (chunder tornado), Dela (Sam Moorcroft), Jordan (bubble buddy), Grace (awful memes), Joel (babybels), Liam (rapid prototyping god). A real thanks also needs to extend to the non-MNP members of Moon Flannel/Panic Slap/Midnight Stand-up Barbers, in Joe and Callam for being excellent band members and even better friends.

Aside from co-workers (friends) there are two people most important to me that I have to thank. Firstly, Yannis Philippakis from Foals for being my musical and style icon. Secondly, I also need to thank Dr. Fern (postdoc office/covid housemate). She was perhaps the most integral piece of my PhD journey, providing constant support and laughter throughout the 5 years. Somehow, we didn't go insane after spending next to no time apart during the lockdowns of 2020, and even ended up on a few papers together #powercouple. She is alright, and I hope we can continue to be 'alright' for a long time.

My final thanks go to my family, of which every single member will have supported me in some way in getting my PhD. Most importantly I would like to thank my mum, Adele, for bringing me up as a single parent, and always providing and wanting the best for me. Considering both her children have ended up with a PhD, I don't think she did a bad job.

Abstract

Systemic delivery of therapeutic agents for treating a wide range of diseases can be challenging, where treatment effectiveness is determined by the total dose of drug delivered to the disease site. Thus, new platforms for the non-invasive delivery and triggered release of therapeutics are of significant interest, especially in an aging population where the rate of disease is likely to increase.

Lipid-shelled microbubbles (1-10 μm, MBs) are already in widespread clinical use as contrast agents for echocardiography. In combination with ultrasound (US), MBs can locally increase intra-cellular drug uptake via a process called sonoporation. MBs can be functionalised to act as biomarkers for molecular imaging of disease vasculature and provide localised triggered release of a therapeutic payload. However, they are confined to the vasculature, which can result in poor uptake in the targeted region. Nanobubbles (NBs, < 1 μm) have emerged as promising candidates for US-triggered drug delivery because of their small size, which allows them to passively extravasate and accumulate within tumour tissue.

A new type of therapeutic NB was developed, Nested-NBs, by encapsulation of NBs within drug-loaded liposomes, combining the efficient and well-established drug-loading capabilities of liposomes and utilizing NBs as an acoustic trigger for drug release. Although the encapsulated NBs were destroyed by pulsed HIFU, determined by cavitation detection, no model drug release was observed. Changing modality to continuous wave (CW) HIFU produced release across a range of pressures, likely due to a synergistic effect of mechanical and thermal stimuli. In combination with theoretical models of droplet vaporisation, we predict that NBs contain a mixed population of both gaseous and liquid core particles, which upon CW HIFU undergo rapid phase conversion, triggering liposomal drug release.

Accurate characterisation of NB size and concentration is challenging, due to their sub-micron nature and mixed populations, containing both bubbles and liposomes. A novel method of using a commercially available Nanoparticle Tracking Analysis system was developed, able to distinguish between NBs and liposomes owing to their differing optical properties. This technique was then used to assess the in vitro sonoporation performance on-chip of different sized NBs. However, sonoporation efficiency did not depend exclusively on NB size and concentration. It is hypothesized that both the total lipid and liposome concentration, as well as inter-bubble distance plays an important role in NB stability, consistent with previously proposed theories and simulations. Future work could consist of further optimisation of the development of Nested-NBs, whilst also investigating more fundamental questions such as the mechanisms behind NB stability.

Table of Contents

List of Figures

List of Abbreviations

7-AAD	7-Aminoactinomycin D
ATR-IR	Attenuated Total Reflectance Infrared Spectroscopy
AuNPs	Gold Nanoparticles
C_3F_8	Perfluoropropane
C_4F_{10}	Perfluorobutane
C_5F_{12}	Perfluoropentane
CAIX	Carbonic anhydrase IX
CCD	Charge-coupled device
CEUS	Contrast Enhanced Ultrasound
CF	Centrifugation
CPP	Cell Penetrating Peptide
CPT	Camptothecin
DC-Chol	(3ß-[N-(N',N'-dimethylaminoethane)-carbamoyl]cholesterol
DLS	Dynamic Light Scattering
Dox	Doxorubicin
DPPA	1,2- dipalmitoyl-sn-glycero-3-phosphate
DPPC	1,2-dipalmitoyl-sn-glycero-3-phosphocholine
DPPG	1,2-dipalmitoyl-sn-glycero-3-phospho-(1'- rac-glycerol)
DSPC	1,2- distearoyl-sn-glycero-3-phosphocholine
EDC/NHS	(N-ethyl-N′-(3-(dimethylamino)propyl)carbodiimide/N-hydroxysuccinimide
EPR	Enhanced Permeability and Retention

EtOH	Ethanol
FITC	Fluorescein isothiocyanate
GC/MS	Gas Chromatography/Mass Spectroscopy
GFC	Gel Filtration Chromatography
HFS	Hand Foot Syndrome
HIFU	High Intensity Focused Ultrasound
HPLC	High Performance Liquid Chromatography
MB	Microbubble
MDR-1	Multi-Drug-Resistant-1
MI	Mechanical Index
mRNA	Messenger Ribonucleic Acid
MS-NBS	Microspray NBs
NA	Numerical Aperture
NaOH	Sodium Hydroxide
NB	Nanobubble
Nested-NB	Nested Nanobubble
NNDEA	N,N-diethyl acrylamide
NP	Nanoparticles
NTA	Nanoparticle Tracking Analysis
O2	Oxygen
PBS	Phosphate Buffered Saline
PCD	Passive Cavitation Detection
PDP	Pyridyldithiol propionate

PEG	Polyethylene Glycol
PEO	polyethylene oxide
PI	Propidium Iodide
PLGA	Poly(lactic-co-glycolic acid)
PNP	Peak Negative Pressure
PPO	polypropylene oxide
PRF	Pulse Repetition Frequency
PSMA	Prostate-Specific Membrane Antigen
PTFE	Polytetrafluoroethylene
PTX	Paclitaxel
PVA	Polyvinyl alcohol
PZT	Lead zirconate titanate
RCF	Relative Centrifugal Force
RMM	Resonant Mass Measurement
siRNA	Small Interfering Ribonucleic Acid
TCEP	Tris(2-carboxyethyl)phosphine
TEM	Transmission Electron Microscopy
TFI	Total Fluorescence Intensity
TTL	Transistor-Transistor Logic
UCA	Ultrasound Contrast Agent
US	Ultrasound
UV	Ultraviolet
VEGFR	Vascular Endothelial Growth Factor

1 Introduction

1.1 Overview

Chemotherapy is one of the primary treatment options for non-resectable malignant tumours, or as an adjuvant post-resection. However, its efficacy is hindered due to the side-effects associated with off-site toxicity, whereby the treatment targets healthy tissue in addition to cancerous tissue. This can lead to unwanted side effects, such as immunosuppression and cardiomyopathy [1,2]. High interstitial pressures, poorly formed vasculature and the presence of an extracellular matrix result in central regions of tumours being less responsive to treatment [3–5]. Additionally, many drugs do not make it past pre-clinical testing due to low water solubility and poor stability, despite promise shown during *in vitro* studies [6,7]. Delivery systems such as liposomes and polymersomes have been explored extensively, to reduce toxicity and increase drug stability, with liposomes such as Onivyde® and Genexol PM® currently in clinical use [8–10]. Liposomal formations can also increase circulation lifetime through the use of PEGylated lipids that provide "stealth" properties by preventing opsonization [11,12]. However, liposomal delivery can suffer from increased renal and hepatic clearance thereby reducing the total dose of drug delivered to the tumour [13,14], and risk additional side effects such as hand and foot syndrome and stomatitis [10,15].

To combat the side effects associated with systemic treatments, research into approaches for targeted, triggered drug release has gathered significant interest. To provide the stimuli for triggered release mechanisms, a multitude of micro- and nanoparticles (NPs) have been developed to utilize various release triggers such as: gold NPs (infra-red radiation)[16–18], mesoporous silica NPs (pH) [19,20], superparamagnetic iron oxide NPs (magneto-thermal) [21,22], and microbubbles [23–25], nanodroplets [26,27] and echogenic liposomes[28,29] (ultrasound). Of these, the use of ultrasound (US) is of interest due to its good tissue penetration, diagnostic capabilities, low cost and wide availability. US utilizes high-frequency sound waves (> 20 kHz) to construct images of internal bodily structures, based on their acoustic properties [30]. However, due to the closely matched acoustic impedances of soft tissues, US imaging can suffer from reduced contrast. Further, its use in conjunction with microbubbles (MBs) is already used clinically for diagnostic applications [31], increasing their appeal for triggered, localized, drug delivery.

Microbubbles (MBs), comprising a gas core and stabilizing shell, are used clinically as US contrast agents (UCAs) due to their high impedance mismatch and large scattering cross-section to surrounding tissue. When exposed to an ultrasonic field, bubbles experience volumetric oscillations, scattering US at the same frequency as the driving US, enhancing contrast. Increasing the acoustic pressure can drive bubbles to non-linear harmonic

oscillations. As tissue has a primarily linear acoustic response, this offers potential for further contrast enhancement through the use of non-linear imaging techniques such as amplitude and phase modulation. Due to their size (1 – 10 μm), MBs can flow freely through the vasculature, whilst their resonant frequency lies within the clinically approved range for diagnostic imaging (1 – 15 MHz) [32,33]. This allows the visualization of blood flow and the diagnosis of diseases such as cardiomyopathy [34] and congenital heart disease[35]. Over the past 20 years, many researchers have investigated their potential use as theranostic agents [36–39]. US induced MB oscillations have been shown to increase cell membrane permeability, known as sonoporation, increasing drug uptake and efficacy [40–42]. However, co-delivery of MBs and therapeutics still presents the challenges of toxicity posed by systemic delivery. By directly incorporating drugs into MBs [36,43–47] and increasing US intensity, triggered-release of the drug payload can be achieved at the target site. This approach allows for direct delivery and release of the therapeutic at the tumour site, whilst also reducing systemic toxicity and increasing treatment effectiveness [48–50].

Gaps in the endothelial lining of tumour vasculature can vary between several hundred nanometres to a few microns [51]. As such, due to their size MBs may often suffer from vascular confinement. Coupled with the high interstitial fluid pressure associated with tumours, this may limit their effectiveness for drug delivery, resulting in reduced penetration and inefficient uptake of the therapeutic payload [52]. Nanobubbles (NBs) are of growing interest as due to their smaller size (< 1 μm), they have the potential to extravasate and enter interstitial space in the tumour [53], with studies showing increased retention and accumulation compared to their larger MB counterparts [54,55]**.** This could enable the delivery of a drug directly to the targeted area instead of the surrounding vasculature, increasing treatment effectiveness. NBs can also provide contrast enhancement for diagnostic US, at magnitudes similar to MBs, despite their predicted resonant frequency exceeding clinical limits [55,56].

However, the existence and stability of NBs have met scepticism in the research community. Classical bubble theories predict NB lifetimes on the order of microseconds due to the considerable Laplace pressure associated with sub-micron particles[57]. Notwithstanding this, numerous studies have demonstrated their remarkable stability [56,58], whilst techniques such as resonant mass measurements have confirmed their existence [59,60]. Their interesting physical properties and potential biomedical applications have led to a rapid increase in research in this area, demonstrated by search results of the term “Nanobubble” into the Web of Science online database. Figure 1.1 shows an exponential rise in the number of papers published. For the purpose of clarity the term “Nanobubbles” is colloquially used to refer to ultra-fine bubbles (UFBs) which are defined as bubbles with dimension of less than 1 μm [61]. Current studies range from previously described use as theranostic agents [62–64]**,** fundamental studies on

stability and behaviour [65,66] to non-pharmaceutical applications such as cleaning and agriculture [67,68].

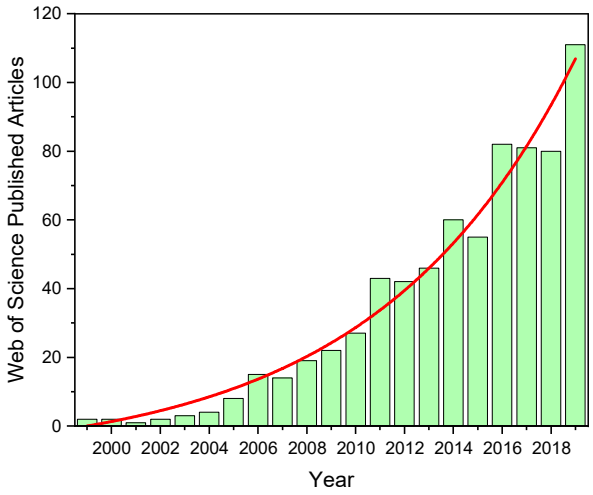

Figure 1.1 - Number of articles published per year with the search term "Nanobubble" from the Web of Science online database.

1.2 Thesis Aims and Project Outline

The main aim of this research project was to develop dual diagnostic and therapeutic (theranostic) NBs, which in combination with US can be used to locally trigger and delivery drugs to a target site. This thesis mainly focused on the application for cancer therapy, although the systems described could be applied to other diseases (i.e. Alzheimer's, in which the blood brain barrier presents a hurdle to drug delivery[69]) by tailoring of the therapeutic payload. Hence, in this thesis a liposome-NB based drug delivery vehicle was developed, and capability for triggered release assessed. Following this, the influence of NB size on their ability to locally promote drug uptake in combination with US was assessed.

The structure of this thesis is as follows:

- **Chapter 2** reviews relevant literature to diagnostic and therapeutic NBs discussing their production, composition, characterisation, stability and potential as theranostic agents.
- **Chapter 3** discusses fundamental theory governing the physical behaviour of bubbles and US, colloidal systems, disease progression and photonics.
- **Chapter 4** describes the underlying theory behind experimental techniques used throughout this thesis.
- **Chapter 5 & 6** describes experimental procedures and development of "Nested-Nanobubbles", in which a NB is encapsulated withing a drug-loaded liposomes, as an internal acoustic nuclei for triggered release.

- **Chapter 7 & 8** describes experimental procedures and results in which the effect of NB size on their sonoporation capabilities is investigated, highlighting potential mechanisms behind NB stability.
- **Chapter 9** provides a summary and conclusion to the work in this thesis and provides outlook for future studies for continuing research in the field.

2 Literature Review

This chapter will focus on current and future developments of shell-stabilized NBs as devices for aiding therapeutic delivery for cancer therapies, which to date has generated the most widespread (pre-)clinical interest. Aspects of NB production and characterization, stability and their potential for therapeutic and diagnostic use are considered.

2.1 Nanobubble Composition

2.1.1 What are Nanobubbles?

The term Nanobubble is used colloquially to refer to ultra-fine bubbles which is the ISO recognized name for bubbles less that a micron in diameter [61]. NBs have a wide range of potential applications depending on their composition. For example, NBs may find application in agriculture and cleaning, but may also be focused on biomedical applications. Studies show that NBs may exist with or without a stabilizing shell, although a recent comment published by Rak and Sedlák discusses the validity of non-shelled NBs [70]. As such, in this thesis, primarily shell-stabilized NBs for clinical applications are considered.

NBs can be produced with various gas-core and shell components, thereby affecting NB stability, bio-compatibility and acoustic response [71]. Low solubility, high molecular weight gases, such as perfluorocarbons (C_nF_{2n+2}) and sulphur hexafluoride (SF_6), are typically chosen, which aid stability by reducing the gas dissolution rate. NBs can also be prepared with an oxygen (O_2) core to treat hypoxia, and will be discussed in more detail later [72,73]. Increasing the gas's molecular weight further increases bubble stability (e.g.C_4F_{10} vs C_3F_8) [56,74], but may also lead to the gas core condensing into a liquid, due to the associated Laplace pressure.

As a rapidly developing field, several studies describe particles as NBs, despite no evidence to suggest so. An example of this is in work by Zhang et al. [75] who produced PLGA (poly(lactic-co-glycolic acid)) nanoparticles, but it is not clear at which stage the NP become gas-filled bubbles - studies such as this are not discussed in this thesis. Similarly, another topic that has generated much interest of late, is that of acoustically-triggered phase transition, or phase-change, droplets. Acoustic droplet vaporisation is a large field in itself and is covered in depth in other reviews and studies [27,76]. In numerous early works by Cavalli et al. [77–79]

stabilized perfluoropentane (C_5F_{12}) emulsions are commonly referred to as NBs. At room temperature, C_5F_{12} is a liquid, with a boiling point of 28 °C and as such at physiological temperature would convert to the gas phase. However, the effect of confinement to a droplet/particle and associated Laplace pressure has on the phase-transition temperature means that thermal stimulation to phase change requires higher temperatures than their bulk transition temperature or additional stimulus, such as can be provided acoustically. It is also unlikely that post-phase transition, these particles would remain sub-micron.

2.1.2 Shell Composition

Phospholipids are commonly chosen as NB shell components [80–82] due to their amphiphilic nature, promoting rapid self-assembly of a monolayer at the bubble liquid-gas interface, subsequently increasing stability and providing increased biocompatibility. The shell improves stability by providing a physical barrier to diffusion, limiting the rate of gas exchange across the gas-liquid interface [57,83]. Phosphatidylcholine (PC) head group are common choices for NB shells, as they are an integral part of biological membranes whilst also possessing chemical inertness and biocompatibility. Those with saturated hydrocarbon tails, such as DPPC (1,2-dipalmitoyl-sn-glycero-3-phosphocholine) [84] and DSPC (1,2-distearoyl-sn-glycero-3-phosphocholine) [85], allow for increased lipid packing density, whilst their longer acyl chain lengths provide increased shell resistance and hence improved stability whilst retaining acoustic response [71,86].

Shells commonly incorporate small amounts (~5 %) of polyethylene glycol (PEG), by conjugation of PEG to lipids with a phosphoethanolamine (PE) head group [87]. These PEG chains extend outwards into the surrounding solution (Figure 2.1a) and due to steric hindrance reduce bubble coalescence whilst also integrating so-called “stealth” properties (reduced immuno-response) [13]. Biotinylated PEG lipids can also act as a conjugating agent allowing for additional functionalization such as the attachment of therapeutics or molecular targeting groups [8889]. The inclusion of small proportions of anionic lipids, such as DPPA (1,2-dipalmitoyl-sn-glycero-3-phosphate) and DPPG (1,2-dipalmitoyl-sn-glycero-3-phospho-(1'-rac-glycerol)), can further reduce coalescence due to the associated electrostatic repulsion between bubbles, whilst also enabling functionalization via electrostatic adsorption [84,90] (Figure 2.1b). Whilst aiding NB stability, the net charge of the NBs should also be considered. Liposomes containing large proportions of anionic phospholipids, and hence increased net charge, can lead to side effects such as thrombogenesis and the onset of epileptic fits in *in vivo* animal models [91].

Cavalli et al. incorporated polysaccharides, such as Chitosan and Dextran as additional shell component[77,79]. These molecules form complexes with lipid membranes (Figure 2.1c), and their ionic properties allow for functionalization by electrostatic attraction, and attachment of Gd-DOTP particles for MRI guided therapy [92,93].

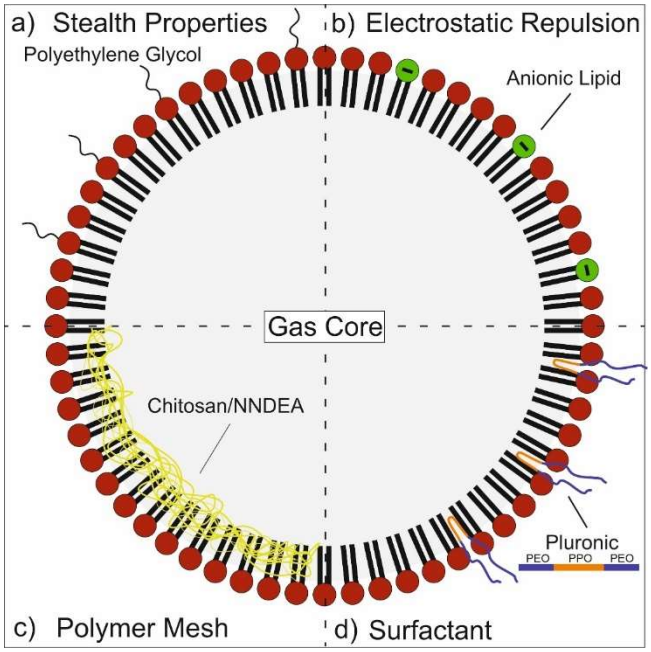

Figure 2.1 - Schematic demonstrating the four most common methods of lipid nanobubble stabilization. a) Incorporation of polyethylene glycol (PEG) by PEGylation of phospholipids. b) Cationic lipids to introduce electrostatic repulsion between bubbles and reduce coalescence. c) Polymer mesh incorporated into phospholipids to reduce the dissolution rate. d) Incorporation of the block copolymer, poloxamer, to reduce surface tension and bubble size.

Poloxamers, such as Pluronics, are tri-block co-polymers that have amphiphilic properties and have been used by Exner et al. to increased NB stability and control size [81,84]. Poloxamers consist of repeating sub-units of polypropylene oxide (PPO) and polyethylene oxide (PEO), organized as $(PEO)_x$-$(PPO)_y$-$(PEO)_x$. The hydrophobic PPO chains are believed to anchor within the lipid monolayer whilst the two hydrophilic PEO side chains extend out into the surrounding medium (Figure 2.1d). Various formulations of poloxamer exist with differing molecular weights and PEO/PPO ratios. Krupka et al. [84] investigated the effect of different poloxamer on bubble size and stability, showing that Pluronic L61 and L81 produced the smallest, most stable bubbles with sizes of 200 – 400 nm. This was attributed to their high relative hydrophobicity which allows for deeper integration into the lipid monolayer. The addition of a cross-linked NNDEA polymer network into the bubble shell resulted in a further reduction in bubble size to ~ 95 nm whilst also increasing acoustic stability [54].

2.2 Nanobubble Production

NBs are produced using a wide range of techniques such as water-solvent mixing, electrolysis, periodic pressure change and acoustic and hydrodynamic cavitation [94–96]. However, the most commonly used methods to prepare NBs for biomedical applications are mechanical agitation, sonication, microfluidics and emulsion techniques. For these techniques, stabilizing shell components are solubilized in an appropriate aqueous buffer, e.g., PBS. Additional materials may also be incorporated during the rehydration process, such as Pluronic's, polymers and drug payloads [54,75]. Mechanical agitation is likely the most widely used NB production technique, owing to its ease of use, short production time and cost-effectiveness. The precursor lipid solution is added to a vial, the air headspace replaced with the prospective gas for the NB core and the mixture mechanically agitated. Disruption to the liquid-gas interface forms bubbles which are subsequently stabilized by the self-assembling shell components. This mechanical agitation is commonly provided using a commercial Vial Mix system that is used for activation of 'Definity' UCAs (Bristol Myers Squibb, United States). NBs can also be made via high power (> 100 W), low frequency (~ 20 kHz) sonication of the shell component suspension [97–99]. Gas is introduced into the sample either by headspace replacement or gas-flow over the sample during sonication. Like mechanical agitation, perturbations to the liquid-gas interface causes the spontaneous formation of bubbles, which are self-stabilized by shell components. Additionally, the pressure drop provided by the incident ultrasonic wave decreases the solubility of the gas in the aqueous phase, as described by Henry's Law [100]. As the solubility drops, the gas phase comes out of solution, forming bubbles which are subsequently stabilized.

An alternative method for NB production was described by Peyman et al. [46,56], utilizing a microfluidic flow focusing geometry. On-chip, a phospholipid solution is combined with gas. The subsequent pressure drop after the nozzle leads to the production of a fine 'spray' of bubbles, consisting of bubbles between 100 – 2000 nm in diameter concentrations similar to those by other methods (~10^{11} /mL). Measurement of the NB concentration is not trivial (as discussed in detail in Section 2.4) due to the propensity of lipids to naturally assemble into liposomes and micelles, which also have dimensions on the nanoscale; however, the production method does not appear to have a large effect, with concentrations typically of ~10^{11} particles/mL, when measured via Resonant Mass Measurement [55,59,101] and Nanoparticle Tracking Analysis [72,99,102]. Other formation techniques utilize either single or double emulsions to produce NBs. Cavalli et al. [77,79] used tip sonication to emulsify liquid C_5F_{12}, producing sub-micron droplets which are hypothesized to phase convert under physiological conditions. However, it is unclear from these studies what the resultant size of the bubble would be, and if it remains sub-micron. Yang et al. [103] used a double emulsion technique followed by solvent

evaporation to produce “NBs” with a PLGA stabilizing shell and an air-core, using PVA as a hydrophilic stabilizer [104]. Post-production, the particles were lyophilized and reconstituted prior to use. However, no evidence was presented in the studies to show the presence of a gas core.

2.3 Nanobubble Isolation

Most of the techniques used for NB production yield populations with a wide range of sizes, containing both micro- and nano-bubbles. The NBs can be isolated as their small size makes them effectively ‘neutrally’ buoyant (Section 3.6). For example, a 1 μm diameter bubble would rise 0.3 cm in 60 minutes. However, a 100 nm bubble would only rise 30 μm in the same amount of time. As such, NBs can be isolated by allowing MBs to rise and removing unwanted supernatant. Centrifugation has also been widely used to separate sub-populations of NBs, whilst also reducing processing time [105,106]. Table 1 shows different isolation techniques and resultant sizes across the literature, in which samples are typically allowed to separate passively, or centrifugation used to provide some control over the resultant NB size. Xing et al. [98] investigated the effect of centrifugation time on NB size. A mixed population of bubbles were produced via tip sonication and then centrifuged at 20 g for between 1 – 5 minutes. The mean bubble size was shown, using Dynamic Light Scattering (DLS), to decrease with increasing centrifugation time, from their initial size of 1.3 μm to 480 nm after 5 minutes centrifugation. Unfortunately, in many papers, centrifugation and separation steps are stated, but often lack clarity and consistency. For example, where centrifugation speed is stated as RPM [90,107] without knowledge of the centrifuge rotor length, the relative centrifugal force (RCF) cannot be calculated, removing the ability to predict bubble rise distance. Other important factors such as vessel height and height of NB extraction (e.g., removal of supernatant) are neglected. Hence, it is difficult to distinguish any correlation between production method, isolation technique and resultant size throughout the literature. Furthermore, variation in lipid and polymer shell components likely affect the initial bubble size.

Whilst centrifugation can actively separate and control the size of NBs; post-production sample manipulation can harm bubble stability and concentration. Because of this, methods to control the bubble size by varying shell components have also been investigated. Krupka et al. [84] showed that incorporating Pluronic into the NB shell led to a decrease in modal bubble size. NBs containing Pluronic L61 (M_w = 2000 Da) had a modal diameter of 208 ± 75 nm compared to non-Pluronic NBs of 881 ± 128 nm. Finer control over bubble size was achieved by varying Pluronic molecular weight. For example, bubbles containing Pluronic L81 (M_w = 2750 Da) were 407 ± 21 nm in size. NB size was furthered reduced to 92 ± 25 nm by Perrera et al. [54] by adding Pluronic L10 (M_w = 3200 Da) and UV cross-linked NNDEA

polymer to the lipid shell. However, a small sub-population of MBs was still observed but could be easily removed via passive flotation.

Table 1 – Isolation techniques for separation of nanobubbles from micro-bubbles and resultant sizes.

Production Method	**Isolation Technique**	**Size (nm)**	**Reference**
Mechanical Agitation	3 Min @ 1300 RPM 3 Mins @ 300 RPM	478 - 494	[106,108]
	3 Mins @ 300 g 3 Mins @ 300 RPM	369 - 486	[55,98,109,110]
	5 Mins @ 50 g	144 - 299	[59,101,105,111]
	3 Mins @ 300 RPM	488	[112]
	2 Hours, Passive	138	[55]
	3 Mins @ 600 RPM	610	[90]
	3 Mins @ 800 RPM x 2	812	[107]
	1 Hour, Passive	172	[62]
Sonication	5 Mins @ 50 g 30 mins @ 805 g	437	[113]
	1 - 5 Mins @ 20 g	400 - 600	[98]
	“Centrifugal Flotation”	480	[80]

2.4 Population Characterisation

Accurate and reproducible characterization of both NB size and concentration is key for assessing their therapeutic potential. NBs are expected to display higher uptake and retention in tumours than their MB counterparts, due to their smaller size. The ability to determine NB size accurately will allow for comparison of tumour uptake across different formulations. Similarly, reliable NB concentration determination is critical for accurate dose delivery, and comparison of efficacy with MBs. As NBs are typically smaller than the optical resolution limit, alternative techniques which indirectly measure size are generally required. Furthermore, at these length scales and in a mixed population sample, many techniques are incapable of distinguishing between bubbles and non-bubbles. In this section, we will consider the most common NB measurement techniques. For further technical detail, we refer to Eklund et al. [114] a review article specifically focused on NB characterisation.

2.4.1 Light Scattering

DLS is a light scattering technique in which the Brownian motion of particles in suspension is observed. DLS calculates particle size of the bulk sample, and uses auto-correlation of scattered light to determine the particle diffusion constant, and hence size (Section 4.3). [115]. The measurable size range of DLS is typically 5 – 10,000 nm, making it suitable for both nano and micro-bubble measurements, however as a bulk measurement technique cannot distinguish between bubbles and non-bubbles, nor determine concentration. Typically, DLS measurements are intensity-weighted, and hence biased towards larger particles. Whilst number and volume-based distributions are possible, solvent and solute optical properties are required, adding an additional layer of complexity for mixed population.

Following a similar principle, Nanoparticle Tracking Analysis (NTA) utilises light scattering in which the Brownian motion of individual particle is tracked, to determine size and concentration (Section 4.2). The measurement range of NTA is 10 – 1000 nm, and does not require optical properties, however, will not detect the presence of any larger bubbles in the sample. At present, commercial NTA cannot distinguish between bubbles and non-bubbles, in which NB solutions will contain both. Nirmalkar et al. (2018a) [116] compared DLS and NTA for NB size measurements. DLS recorded a slightly larger mean size of 173 nm compared to 137 nm for NTA, which may be due to the intensity-based distribution. DLS also measured an increased proportion of larger bubbles. This suggests that the optimal size range for NTA is likely smaller than the previously stated 10 – 1000 nm. Recently Midtvedt et al. [117] have developed “holographic” NTA in which the particle refractive index can be measured in addition to size and concentration. This technique is not yet widely available but holds promise

for widespread use for determination between bubbles, droplets, liposomes or other non-bubble particles.

2.4.2 Resonant Mass Measurement (RMM)

RMM is a more recently implemented technique for NB measurements and works on the principle of buoyant mass, which observes a frequency shift of a self-resonating cantilever as particles with a density of that different to the medium flow through. The direction of this frequency shift determines whether the particles are positively or negatively buoyant (e.g., bubbles or non-bubbles), whilst the magnitude is a marker of particle size. This technique is discussed in more detail in Section 4.4.

Abenojar et al. [118] investigated the accuracy of both NTA and RMM for determining NB size and concentration. Theoretical values for total gas volume determined by NTA and RMM were compared to values measured using Gas Chromatography/Mass Spectroscopy (GC/MS). RMM accurately predicted total gas volume within 10 % of the value measured using GC-MS, whilst NTA predicted a gas volume 72 % lower, highlighting the importance of the measurement technique used. Closer observation of the data shows that, although RMM and NTA total concentration measurements agreed, NTA failed to detect particles > 400 nm compared to RMM, which detected bubbles up to 1 μm in size. This potentially explains the disparity between techniques due to the relationship between bubble size and volume. Similar observations were made in our studies [74], in which both NTA and RMM were used to characterize C_4F_{10} NBs, with NTA once again failing to detect larger NBs.

Although these studies demonstrate the ability of RMM to measure NB populations, as well as the ability to predict total gas volume currently this measurement technique does not consider interactions between an acoustically active bubble and a resonating cantilever. However, the typical resonant frequency of the cantilever is ~ 1 kHz and as such at least 2 orders of magnitude (potentially 3) below predicted resonance of a NB (> 10 MHz) and would be expected to have little effect on NB measurement.

2.4.3 Electron and Optical Microscopy

Transmission Electron Microscopy (TEM) has also been used to observe NB morphology. TEM follows a similar working principle to brightfield microscopy but utilizes a high energy beam of electrons instead of visible light, which due to their smaller wavelength allows for resolutions of up to 10^{-10} m (Section 4.1.3). Hernandez et al. [105] utilized Cryo-EM to characterize NBs, observing a dark core hypothesized to be the encapsulated C_3F_8 gas. NBs exposed to a high intensity US pulse prior to imaging did not have this characteristic. Additionally, the density of this core decreased with prolonged exposure to the electron beam, attributed to breaking of covalent bonds in the lipid shell and subsequent gas loss.

In addition to these techniques, optical microscopy has also been used to determine both NB size and concentration [97,119]. This technique may be suited as a simple, quick method to determine the concentration, simply by counting the number of particles. Any size analysis from this would be restricted by the minimum resolvable distance achievable using optical microscopy, typically 200 - 400 nm depending on the quality of objective. For NBs it is likely a large population of the sample would be below this limit plus there will be increased error of the size measurements as the optical limit is approached.

2.4.4 Acoustic Methods

Although still in a preliminary phase, another method that holds promise for NB size characterisation was described by Moore et al. [120] utilising high frequency (200 MHz) M-Mode imaging. NBs and MBs were entrapped within agarose gels with varying pore size and acoustic backscatter observed. Bubbles smaller in diameter than the gel pore size can undergo stochastic motion, whereas for bubbles larger than the pore size, their motion is restricted. In the experiments, this was reflected by the presence or absence of M-Mode intensity fluctuations respectively. Similar to DLS, autocorrelation of the intensity signal can be used then to roughly approximate NB size.

2.5 Nanobubble Lifetime and Stability

Theoretically predicted NB lifetimes are on the order of seconds; thus, the very existence of stable NBs is a controversial topic and is met with scepticism by many in the microbubble the research community. Despite this NBs, with or without a stabilizing shell, have displayed remarkable stability on the order of weeks, days and months [56,82,121]. In the following sections the theoretical mechanisms behind predicted NB instability, evidence for their stability and the possible reasoning behind this are discussed.

2.5.1 Causes of Instability

For traditional bubbles, (i.e. MBs), there are three main causes of instability: thermodynamic instability, destruction due to buoyant effects and coalescence. The first is due to the associated energy cost of the air-liquid interface, known as the surface tension σ. For a spherical bubble, this leads to a pressure difference between the internal gas and external liquid phases defined as the Laplace pressure (Equation 2.1).

$$\Delta P = -\frac{2\sigma}{R} \qquad \text{Equation 2.1}$$

Due to the inverse relationship between bubble radius and surface tension, predicted pressures exerted on nanoscale bubbles could reach upwards of 3 MPa. The existence of the Laplace pressure also leads to the so-called “Laplace Bubble Catastrophe” in which small perturbations

to bubble size causes bubbles to either rapidly grow or shrink (Figure 2.2a) [116,122]. The Epstein-Plesset mode is described in more detail in Section 3.4. As a result, a 100 nm bubble is predicted to have a life-time approximately three orders of magnitude less than 1 µm bubble. Another mechanism is that due to bubble buoyancy, in which bubbles rise to the top of the sample container. At this point, the bubble ruptures as the gas-liquid interface between the bubble core and surrounding liquid is no longer present (Figure 2.2b). Further, coalescence of bubbles (i.e. 2 or more bubbles merging) will also drive instability (Figure 2.2c).

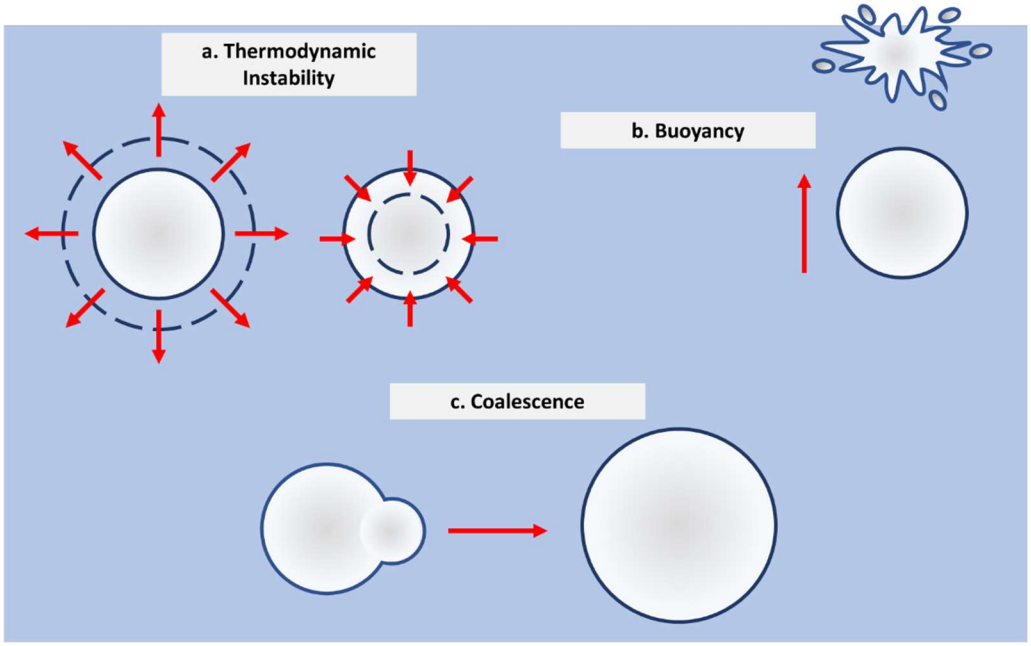

Figure 2.2 - Examples of classical bubble instability mechanisms. a) Thermodynamic instability caused by the "Laplace Catastrophe", in which small changes to bubble radius lead to a positive feedback loop and rapid bubble expansion or contraction. b) The buoyant nature of bubbles in solution leads to bubbles rapidly rising towards the liquid-air interface, at which point they rupture. c) Bubble-bubble coalescence in which two (or more) bubbles merge to form a single bubble. These larger bubbles then typically experience reduced lifetimes due to buoyant effects.

2.6 Evidence of NB Stability

Regardless of their predicted instability, many studies have shown the existence, and, in some cases, somewhat increased stability of NBs compared to MBs. Using DLS, Abdalkader 2017 et al. [82] demonstrated the stability of C_3F_8 NBs for up to 90 hours when stored at 4 ° C. However, due to the nature of DLS, it is unclear whether the proportion of NBs (compared to non-gas particles) is consistent across all measurements. We have also shown that C_4F_{10} NB size and concentration are stable for up to a month using NTA; however, similar to DLS, it is not possible to distinguish between NBs and non-gas particles [56]. Non-shell stabilized NBs generated in pure water were shown to be stable for up to a month by Kanematsu et al. [121],

who observed constant concentrations using NTA. These particles were shown to be NBs, as a subsequent freeze-thaw cycle led to complete NB destruction [116].

Whilst both DLS and NTA are incapable of determining if particles are gas-filled, work by Hernandez et al. [59] was the first to characterize NB stability using RMM, showing stability over 5 hours, although a slight decrease (~20 %) in concentration was observed. From these studies, it is quite clear that NBs are stable, at least on similar timescales to MBs. However, the exact mechanism behind stability is still unknown. Before we enter a deeper discussion, it should be noted that although there have been suggestions that the Laplace equation is not applicable to the nano-scale, molecular dynamics simulations have indicated indeed it does hold, even down to dimensions of several nanometres. [123].

2.7 Suggested Stability Mechanisms

NBs possess non-zero zeta-potentials, and hence net charge, irrespective of the presence of a surfactant shell, therefore leading to the existence of an electric double-layer [95,108]. The electric double-layer at the NB surface may lead to electrostatic pressure, countering the Laplace pressure. The double-layer will also reduce bubble coalescence due to the associated electrostatic repulsion between particles. Hau Tan et al. [66] proposed a modified Epstein-Plesset model incorporating the electrostatic pressure. The assumption of charge conservation of an initially shrinking bubble leads to an increase in surface charge density, increasing the electrostatic pressure. As the bubble continues to shrink, an equilibrium will be reached, at which point the electrostatic pressure balances the Laplace pressure. This model predicted an equilibrium bubble size of approximately 100 – 300 nm, dependent on the Debye length and initial bubble zeta potential, and agreed with the results from dark field microscopy experiments [124]. In a separate study, Yin et al.[125] observed that for anionic-lipid coated bubbles, zeta potential magnitude increased from -2.93 mV to -18.36 mV as bubble size decreased from 1120 nm to 437 nm, consistent with this model. Increasing the concentrations of mono- and multi-valent salts have an adverse effect on non-shelled NB stability, due to electrostatic screening decreasing Zeta potential magnitude [126]. However, work by Michailidi et al. [127] provided conflicting results in which Zeta potential magnitude increases with NaCl concentration, contrary to the prediction of colloidal stability (Section 3.1). The so-called "bulk" effect of high concentrations of NBs, and therefore small inter-bubble distance, may also have a part to play in their stability. Using molecular dynamics simulations and using the Lennard-Jones potential, Weijs et al. [128] showed that provided NB inter-bubble distance was below a critical value, NBs were stable. The small inter-bubble distance (l_0) can provide shielding of gas diffusion due to a high local gas concentration and it was found that a population of 3 nm diameter (d) NBs were stable provided inter-bubble spacing was < 30 nm

or $\frac{l_o}{d} < 10$. Assuming a NB concentration of ~ 10^{11} /mL and d = 100 nm, inter-bubble spacing would be approximately 1 – 2 μm and as such may be within the range for stability.

The buoyant nature of bubbles in solution leads to bubbles rapidly rising towards the liquid-air interface, at which point the bubble ruptures (Figure 2.2b). However, NBs are effectively neutrally buoyant thus effectively increasing their stability (Section 3.6). This can also be demonstrated following an energy approach, by considering the work done by buoyancy ($\sim \Delta\rho g R^3$) , if this is less than, or of a similar magnitude to thermal energy of the particle, $k_B T$, then the particles will undergo random thermal motion. For gas bubbles this turns out to be around a diameter of ~ 1 μm, above which buoyancy effects become non-negligible [66]. Hence, NBs will not rapidly rise to the top of the solution, thereby enhancing NB lifetime.

The presence of so-called "hard" Hydrogen bonds, similar to those found in ice and gas hydrates, have also been postulated to be responsible for NB stability, providing a barrier to gas diffusion. Using ATR-IR spectroscopy, Ohgaki et al.[129] found that shorter, stronger Hydrogen bonds dominated those found in NB samples, due to the lower frequency molecular vibrations of O-H groups. However, this has not been shown for shell-stabilized NBs.

2.8 Nanobubbles for Diagnosis and Therapy

2.8.1 Diagnostic Ultrasound and Acoustic Characterisation

MBs are used clinically as Ultrasound Contrast Agents (UCAs) to improve vascular contrast as they can efficiently scatter US [130]. Diagnostic US typically utilizes frequencies in the range of 1 – 20 MHz, which is concurrent with the predicted resonance of MBs [31]. The harmonic response of MBs allows for the use of non-linear imaging techniques, to further improve contrast, known as contrast-enhanced US (CEUS) [131,132]. Using CEUS, MBs have been able to aid in diagnosing diseases, such as hepatocellular carcinoma, through the quantification of parameters including peak enhancement and wash in/wash out time [133]. Due to the smaller size of NBs, their predicted resonance can be much greater than 20 MHz and at clinical frequencies would be expected to provide reduced contrast compared to MBs, potentially limiting their clinical use for diagnostics [56,134]. An example of this was shown by Sun et al. [135], in which the predicted scattering cross-section of a Definity like NB (d = 0.7 um) is ~ 10^5 times smaller than that of MBs, across the clinical frequency range. The predicted resonance behaviour of an oscillating bubble is described in more detail in Section 3.2.2.

Contrary to these predictions, numerous studies have shown the ability of NBs to acts as UCAs at clinical frequencies. Leon et al. [136] showed that NBs provided contrast enhancement in non-linear imaging whilst Wu et al. [55] showed NBs provide a similar enhancement at 8 MHz as MBs, when administered at matched gas volumes. This potentially suggests that the total void

fraction, and as such impedance mismatch, is the dominant contributor towards contrast enhancement, compared to volumetric oscillations. Pellow et al. [137] also showed that NBs were acoustically active at clinically relevant frequencies. Acoustic emissions from MBs and NBs were compared at matched number density (10^6 bubbles/mL). excited at two different clinical frequencies (2.5 and 8 MHz). It was demonstrated that NBs could produce harmonic emissions at similar magnitudes to MBs, albeit requiring slightly higher pressures (~400 kPa). It was also shown that by further increasing the driving pressure, NBs produced broadband emissions indicative of inertial cavitation. Although the exact reason for this behaviour of NBs at clinical frequencies is not understood, a preliminary study by Jafari Sojahrood et al. [138] suggests that NB resonant frequency decreases with increasing excitation pressure. This is proposed to be due to buckling of the lipid shell and a subsequent decrease in surface tension, as proposed by the Marmottant model [139] (Section 3.2.3).

NBs have also shown increased tumour retention and wash-out times *in vivo* compared to MBs [140]. Yin et al. [125] showed that NBs had a half-time to washout of 1265 ± 60 s compared to 310 ± 20.7 s for MBs. This increased retention is often attributed to the leaky vasculature and poor lymphatic drainage associated with tumours, although it is also possible that the observed increase in acoustic stability of NBs could contribute to longer washout times [55].

Bubbles also show promise for use in US molecular imaging, enabling molecular assessment and identification of disease phenotype and progression [50]. Attachment of ligands, such as antibodies, to the bubble shell, allows for selective targeting to cells with disease-specific molecular-level expressions, leading to increased retention and US signal washout compared to non-targeted bubbles. Due to their size, MBs are limited to targeting molecular markers expressed in the tumour vasculature, such as VEGFR [50,141,142]. As NBs may have the ability to extravasate, they would be able to provide additional molecular information in areas unreachable by MBs [143]. Fan et al. [112] produced NBs that could selectively target PSMA (prostate specific antigen), with *in vivo* models showing increased retention in C33a xenografts compared to non-targeted NBs, whilst no difference was seen for the PSMA negative MDA-MB-468 breast cancer cells. Similar results have also been shown for renal cell carcinoma [109] whilst CAIX (carbonic anhydrase IX) targeting may allow for molecular imaging of multiple organs [106,144]. However, there are currently no studies comparing the effectiveness of NBs compared to MBs for molecular imaging, which would be required for further advancements in this area.

2.8.2 Therapeutic NBs

2.8.2.1 Sonoporation and Co-Delivery

US induced MB oscillations have been shown to locally increase cell permeability in a process known as sonoporation, with potential advantages for the delivery of therapeutics. When driven at low acoustic pressures, MBs undergo stable volumetric oscillations (stable cavitation), which induce localized fluid flow and subsequent shear stresses. Increasing the acoustic pressure can lead to MB destruction, capable of producing violent liquid jets. Both of these interactions can increase local cell membrane porosity, which can be used to increase therapeutic uptake [42,145,146].

NBs in combination with US have been shown to promote cellular uptake of therapeutics such as pDNA and Dox leading to increased treatment effectiveness [82,110]. Abdalkader [82] et al. showed that the combination of NBs and US was required for significant uptake of Luciferase tagged pDNA in C26 colon cells compared to controls and that the delivery efficiency was increased further by integration of pDNA into the NB construct. The topic of NB and gene delivery will be discussed in greater detail in Section 2.8.5. An *in vivo* study of a PC3 prostate murine model by Fan et al. [110] showed that NBs in combination with US are able to locally increase tumour Dox concentration, subsequently decreasing the concentration in non-insonated areas compared to Dox alone.

While both these studies, and others mentioned over the following sections, show the ability of NBs to increase therapeutic uptake locally, no in-depth studies investigating NB sonoporation, optimizing acoustic parameters and NB dosage have been presented to date. Indeed, there is a large variation in NB size and composition, that is likely to lead to different acoustic behaviour and sonoporation efficiencies. Furthermore, although increasing local drug dosage, co-delivery of the therapeutic agent and NBs may still lead to increased systemic toxicity due to the high concentration of drugs that can accumulate in the non-targeted tissue as shown by Fan et al. [110]. As such, it is beneficial to incorporate therapeutics into the NB

complex with targeted release triggered by an external stimulus such as US, to reduce systemic toxicity. This will be discussed further in the following sections.

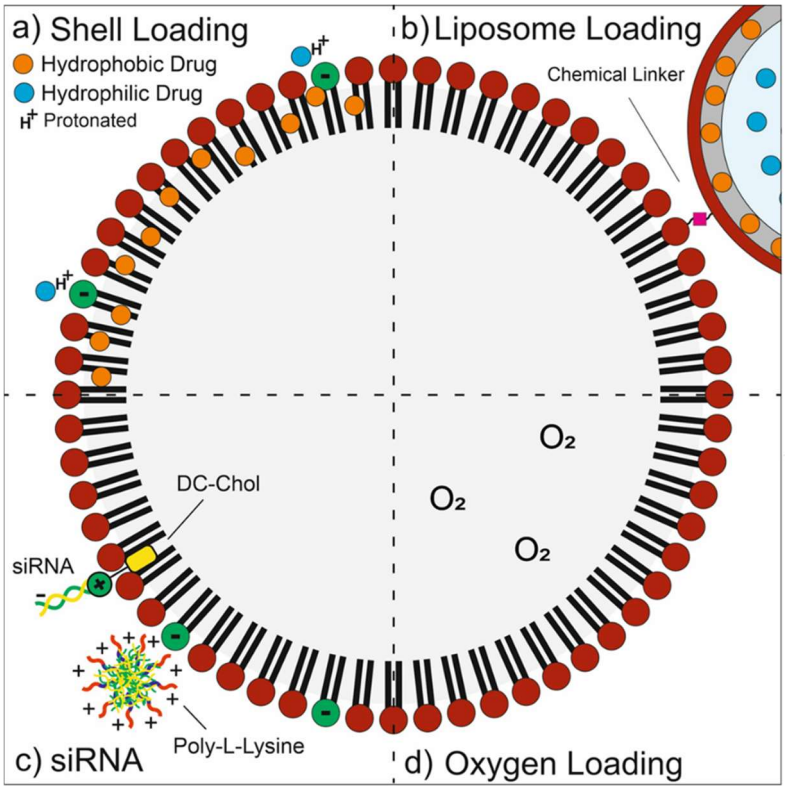

Figure 2.3 – Schematic showing different ways of functionalising NBs for therapeutic delivery. a) Direct loading into the shell of hydrophobic drugs into the lipid monolayer, or by protonation of a hydrophilic drug and electrostatic attraction to anionic lipids. b) Attachment of drug loaded liposomes, in which both hydrophobic and hydrophilic drugs can be loaded, to the NB shell via a chemical linker. c) Attachment of cationic siRNA to the NB shell via electrostatic interaction, either by direction attachment to anionic lipids (DC-Cholesterol) or through the formation of cationic Poly-L-Lysine micelles, and ionic attachment to anionic lipids. d) Loading of therapeutic gases, such as oxygen, directly into the bubble core for treatment of hypoxia.

2.8.2.2 Passive Loading

Chemotherapy agents can be loaded into the NB shell using passive loading techniques, relying on self-assembly via hydrophobic or electrostatic interactions (Figure 2.3a). In this method, therapeutic agents are added to the NB shell components before NB production. This technique preserves the nanoscale dimensions of the bubbles post-loading, with drug loaded NBs typically having diameters ranging 360 – 500 nm [99,147–149].

For example, Peng et al. [108] successfully loaded the hydrophobic chemotherapy agent, paclitaxel (PTX), into lipid shelled NBs by the simple addition of PTX to the lipid solution before NB production. Following a similar method, Yu et al. [88] successfully produced Temsirolimus loaded NBs with these methods. Loading efficiencies of 54 % and 69 %

respectively were determined in these studies, obtained by HPLC (high-performance liquid chromatography).

Xie et al. [150] conjugated a cell-penetrating peptide (CPP) to another hydrophobic drug, Camptothecin (CPT) via a disulfide linker, and CPP-CPT was subsequently loaded into NBs. After the US triggered-release (1 MHz, 1 W/cm^2, 60 s duration) of the CPP-CPT conjugate and subsequent endocytic uptake, it is thought that the disulfide linker would be reduced resulting in the intra-cellular release of the un-modified CPT. Flow cytometry analysis showed a 2-3 fold increase in CPP-CPT uptake of in HeLa cells compared to CPT. However, only a ~ 20 % decrease in viability for CPP-CPT NBs compared to CPP only NBs, potentially suggesting that the CPP-CPT complex is less effective in inducing cell death.

Whilst this technique is effective at loading hydrophobic drugs, some studies have also shown the ability to load hydrophilic drugs. Dox is typically used in its hydrophilic form as an HCl salt. However de-protonation of the amine group yields a non-polar, hydrophobic variant. Nittayacharn et al. (2020) [151] compared the loading efficiency of hydrophilic Dox (Dox HCl) to hydrophobic Dox (hDox) which were loaded with efficiencies of 18.7 ± 2.0 % and 11.4 ± 4.5 % respectively. It was also shown the loading of both types of Dox increase NB stability during insonation likely due to an associated increase in shell stiffness. Despite this, the mechanism in which Dox HCl would actively associate with a lipid membrane is not immediately clear. In work by Nittayacharn et al. (2019,2020) [62,151] NBs contained DPPA and as such, the anionic phosphate head group would electrostatically interact with the protonated amino group of Dox HCl [152]. However, Khan et al. [99] did not incorporate anionic lipids into their bubble shell, which perhaps surprisingly contained cationic DSPE-PEG-Amine, leading to positively charged NBs as shown via zeta potential measurements. Regardless, fluorescence microscopy images of MBs produced via the same method show co-localization of Dox fluorescence with the lipid shell, which may correspond to successful loading. It should also be noted that lipid NB samples will consist of a mixed population of both NBs and liposomes, in which both variants of Dox are known to associate with [49,153]. As such, encapsulation efficiencies measured for this loading method are likely to include drug loaded into liposomes as well as NBs.

In comparison, Lin et al. [154] reported encapsulation efficiencies as high as 93 % for Dox HCl into their non-ionic NBs. Closer inspection of the methodology to determine the loading efficiency shows that Lin et al. used centrifugal washing, compared to molecular filtration techniques mentioned in the previous studies. Whilst standardized molecular filtration techniques can reach cleaning efficiencies of > 98 %, the efficiency of centrifugal cleaning is not standardized and may have a much lower cleaning efficiency due to the nature of the technique. This in turn may contribute to an incorrectly measured high encapsulation

efficiency. The discrepancy in encapsulation efficiencies highlights the importance of the cleaning methodology for accurate determination of NB drug loading capabilities. Additionally, the relatively low efficiencies suggest that other loading methods for hydrophilic drugs may be more appropriate.

In their work, Nittayacharn et al. (2019) [62] show that Dox-NBs in combination with US (3 MHz, 2 W/cm^2, 20% duty cycle, 1 minute) effectively enhance Dox distribution in LS174T xenograft murine models. The application of TUS to Dox-NBs was vital for a statistically significant increase in both Dox fluorescence and mass in the tumour slice, compared to Dox and Dox-NBs only, hence showing the ability of NBs to promote therapeutic uptake. Results also correlated with *in vitro* experiments, showing maximum cell death for Dox-NBs + TUS to other treatment groups. However, the study did not compare to a control group consisting of co-delivery of Dox and NBs, in which sonoporation would be the main mechanism of drug delivery, and hence it is not possible to assess whether Dox loading was beneficial, either in increasing efficacy or reducing toxicity to non-targeted areas.

2.8.2.3 Drug-Loaded Liposome Functionalization

Both hydrophilic and hydrophobic drugs can be efficiently loaded into liposomes and reach encapsulation efficiencies > 90 %. Their aqueous core allows encapsulation of hydrophilic drugs via passive or active techniques whereas, hydrophobic drugs can be loaded into the lipid bilayer. Drug-loaded liposomes are used clinically during chemotherapy, reducing systemic toxicity and likelihood of side effects. However, liposomal delivery is also associated with increased accumulation in the mononuclear phagocyte system, which can reduce the proportion of nanoparticles delivered to the tumour site to as low as 1 % [91].

The ability to trigger liposomal drug delivery would increase both treatment effectiveness and reduce the severity of side effects such as hand-foot syndrome. Liposome-loaded MBs have been widely documented in the literature, where an US pulse was used to locally release the liposomal payload [36,43,46,48]. However, the combination of NBs and liposomes has not yet been widely investigated, with only a handful of published studies at present.

Like traditional therapeutic MBs, Chandan et al. [155] produced paclitaxel liposome-loaded NBs, with liposome conjugation achieved using EDC/NHS chemistry (Figure 2.3b). In combination with an US trigger (1 MHz, 2 W/cm^2, 100% Duty Cycle, 60 s), paclitaxel was successfully released from the NB-liposome complex, whilst in vitro studies showed a concomitant decrease in viability of MCF-7 and MDA-MB-231 cell lines. However, drug release kinetics show that large concentrations of paclitaxel are released passively. Over a 3-hour period, ~ 100 μg of paclitaxel was released passively, compared to 200 μg with an US trigger. These results are also concurrent with viability studies, which showed that the application of an US

trigger induced a relatively small decrease in viability (~10-20%), depending on the dose. Additionally, the attachment of ~ 100 nm liposomes to the outside of the NB increases the size of the delivery complex. Across two studies, NB-Liposome sizes were 756 ± 180 nm and 528 ± 32 nm, significantly larger than the majority of NBs mentioned previously [156]. This increase in size may potentially negate the advantage of the submicron nature of NBs, for improved extravasation.

The lack of NB-liposome complexes is surprising, considering the widespread use of liposomes in combination with MBs or other triggered release mechanisms [16,157]. Furthermore, interactions between NBs with liposomes or bilayers could be used as a well-defined, controllable model to assess NB interactions with cell membranes.

2.8.2.4 Electrostatic Adsorption of siRNA

Short-chain nucleotides, such as siRNA (short interfering RNA) have been studied as a possible cancer treatment, with the ability to silence genes such as those related to drug resistance [90,97] and proliferation [80]. However, siRNA delivery is limited by two factors. Firstly, the need for intracellular delivery and secondly; RNase induced degradation. NBs have been shown to be a promising delivery route for siRNA. Due to its anionic nature, siRNA can be directly attached to a positive charged NB shell. Yin et al. [97,119] utilized self-assembling siRNA/Poly-L-Lysine micelles electrostatically adsorbed to anionic-shelled NBs (Figure 2.3c). Following a similar approach, both Cavalli. et al. [79] and Wu et al. [80] introduced DC-Cholesterol (3ß-[N-(N',N'-dimethylaminoethane)-carbamoyl]cholesterol) into the NB shell, allowing for direct attachment of siRNA. Both of these methods protect siRNA from degradation, whilst attachment to NBs and subsequent US exposure promoted intra-cellular uptake of siRNA.

One of the leading causes of chemotherapy failure can be attributed to drug resistance. A common cause of this is attributed to the MDR-1 (Multi-Drug-Resistant-1) gene. MDR-1 is responsible for producing a P-gp protein drug efflux pump, removing the drug from treated cells and reducing treatment effectiveness. Yang et al. [104] showed that siRNA-NBs could be used to silence MDR-1 and successfully silence P-gp expression, which led to increased efficacy of Dox-loaded NBs. Similarly, expression of BCL-2 has been shown to contribute to resistance of microtubule disrupting drugs, such as Paclitaxel (PTX) by inhibiting apoptosis [158]. Dual functionalized siRNA and PTX loaded NBs were developed by Yin et al. [97]. In combination with US (1 MHz, 500 kPa, 1 kHz pulse repetition frequency (PRF), 50% duty cycle, 60s). These NBs were capable of reducing the expression of BCL-2 mRNA in HepG2 cells *in vitro,* leading to the increased therapeutic effect of PTX-NBs *in vitro* and *in vivo* compared non-siRNA, PTX-only NBs. As such in both of these studies, the dual NB

functionalization of drug and siRNA shows much promise for reversing drug resistance. Xie et al. [159] used a cell-penetrating peptide (CPP)/siRNA conjugate to increase intracellular delivery. Systemic delivery of CPP-siRNA conjugates increased transfection efficiency *in vitro* compared to siRNA alone, whilst NB loading and an US trigger (1 MHz, 1 W/cm^2, alternating 10 s on, 10 off, 60 s total duration) were also successful in siRNA delivery, significantly decreasing mRNA expression. However, a direct comparison was not made between CPP and non-CPP siRNA NBs, and further studies would be needed to properly assess the benefit of CPP conjugation when used in conjunction with NBs. In their study they then moved on to an *in vivo* murine model, in which addition of molecular targeting to EphA2 receptor and use of c-Myc silencing RNA, enhanced the therapeutic effect compared to non-targeted NBs, delaying tumour progression.

2.8.2.5 Oxygen Loaded Nanobubbles for Treatment of Hypoxia

Hypoxic regions in tumours, in which cells have inadequate oxygen (O_2) supply, can reduce treatment effectiveness. These hypoxic regions can lead to overexpression of HIF-1α (hypoxia-inducible factor 1α), which induces angiogenesis and metastasis [4].

Khan et al. [72] produced O_2 loaded NBs by sonication of an oxygen-saturated lipid solution (Figure 2.3d). These O_2 NBs were shown to be successful in reversing hypoxic conditions, and subsequently reducing the expression of HIF-1α in MDA-MB-231 cells cultured in a hypoxic environment. This work was furthered in another study [102], in which O_2 NBs were loaded with Dox for enhanced therapeutic effect. Interestingly in these studies, both O_2 and Dox delivery rely on a passive release mechanism, without an external US trigger. The latter also claimed that NBs are endocytosed and the Dox and O_2 were released inside the cell. However, there was no direct evidence to support this, and it could also be attributed to passive release. NTA concentration measurements of O_2-NBs showed a decrease in concentration of ~ 30 % after 30 days. However, due to the lack of intermediate time points and the nature of NTA, it is unclear whether bubbles still remain and if they are indeed O_2 filled.

Whilst the studies above succeeded in hypoxia reversal, they were conducted on 2D cell monolayers, incubated in a hypoxic environment. *In vivo,* tumours typically possess a hypoxic core as the tumour outgrows its blood supply. In these conditions, tumour cells can alter their metabolism leading to increased occurrence of metastasis. Additionally, many drugs require oxygen to be effective. As such, a better model to assess the potential for hypoxia reversal, would be to use 3D cell models, such as spheroids, due to their natural occurrence of a necrotic core surrounded by a region of hypoxic cells.

To our knowledge there are currently no studies in which the release of O_2 from NBs is triggered by US. However, NBs have potential for hypoxia reversal and that the addition of a drug payload would be expected to further increase the treatment effectiveness.

2.9 Increased Accumulation in Tumours

Due to their sub-micron size, NBs may be able to leave the tumour microvasculature and accumulate in tumour interstitial space (Figure 2.4), with potential benefits for both diagnostic and therapeutic applications. For diagnostics, NBs may allow for molecular imaging in areas previously not reachable by traditional UCAs, whereas for therapy this would allow drugs to be delivered directly to the tumour tissue itself, as opposed to the surrounding vasculature. This is a potential major advantage of NBs over their micron-sized counterparts.

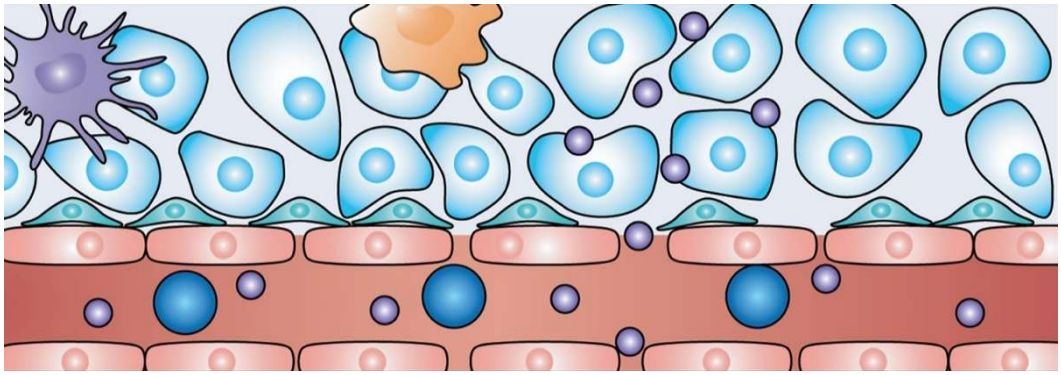

Figure 2.4 – Schematic of how NBs may have improved therapeutic efficacy compared to MBs. MBs are typically confined to the vasculature, due to their larger size. However, the reduced size of NBs opens up potential for their passive extravasation and accumulation in tumour interstitial space, passing through inter-endothelial gaps.

Using fluorescence microscopy, Peng et al. [108] found that NBs could passively accumulate in interstitial space in breast cancer xenograft models, but remained restricted to the vasculature in muscle tissue. Yin et al. [119] showed the application of US (1 MHz, 1 W/cm^2, 1 kHz PRF, 50% duty cycle, 60 s) could further increase extravasation of NB into the tumour whilst another study showed that MBs (~2 μm) did not show any evidence of passive targeting whilst NBs did [54], demonstrating the importance of the reduced NB size. These results also echo those discussed in Section 2.8.1, in which NBs demonstrated increased tumour retention in diagnostic US compared to their MB counterparts.

Using a murine dorsal window chamber, recent works by Pellow et al. [160,161] provided the first acoustic evidence of increased tumour uptake of intact NBs. Fluorescence microscopy showed an increase in passive NB extravasation into the tumour compared to non-tumour controls. Acoustic monitoring, in combination with a high-pressure acoustic pulse (1 MPa peak negative pressure, pulse length of 100 μs, pulse repetition period of 10 ms, 50 times), was

used to trigger NB destruction and generate broadband emissions. A second identical trigger followed this 10 s later to determine if vascular replenishment had occurred and whether NBs were present in the vasculature or tumour interstitial space. Results showed that NBs had been delivered intact to the interstitial space. Additionally, the application of lower pressure US was able to nearly double the increase in NB accumulation compared to passive methods.

The mechanism behind the observed increased passive accumulation is widely hypothesized to be due to the EPR (Enhanced Permeability and Retention) effect [162,163], although there is a broad debate across the research community about its validity [164,165]. Tumour uptake of nanoparticles is often associated with gaps in the endothelial lining, often quoted as ranging from 300 – 700 nm [140]. However, a recent study found that despite inter-endothelial gaps being as large as 2 μm, the vast majority (up to 97 %) of uptake of gold nanoparticles (AuNPs) was due to an active transport mechanism [164]. It was also found that larger AuNPs (100 nm) relied more on endothelial gaps as opposed to an active transport mechanism compared to smaller AuNPs (15 – 50 nm), which also had overall increased uptake compared to larger AuNPs. Whilst this is an important observation, the morphology and surface functionality of AuNPs differs significantly from that of NBs and as such it is not clear whether similar results would be observed for NBs. Furthermore, the effectiveness of the EPR effect varies greatly depending on the tumour type and location, nanoparticle size in addition to the inherent patient to patient variability. This also highlights the importance of NB size in relation to tumour accumulation, suggesting that minimizing NB size would also lead to increased uptake. To date, NB extravasation studies have primarily concerned NBs of ~ 500 nm in size. However, as mentioned previously there is a large variance in NB size across studies.

2.10 Concluding Remarks

The aim of work in this thesis was to highlight and investigate two main gaps in the literature. Firstly, that of combining liposomes and NBs for drug delivery, whilst still maintaining their nanoscale nature that is predicted to enhance their tumour distribution and hence treatment efficacy. In this thesis this was done by encapsulation of NBs within drug-loaded liposomes with a resultant size of ~ 200 nm. Secondly, work addresses challenges in accurately characterising and distinguish NBs. A new method was developed to characterise the size and concentration of NBs and discriminate them from non-gas cored particles, utilising a commercially available NTA system. NBs of varying size were then isolated and characterised, after which their therapeutic capabilities, and the relationship of this to stability, was assessed.

3 Background Theory and Mechanisms

3.1 Colloidal Stability

In this thesis, colloids, and their stability, are a key part of all studies whether this be the liposomal pre-cursor solution used to produce MBs and NBs, or the development of a liposome based drug delivery system. Hence, it is important to understand the theoretical basis behind their stability.

There are four main mechanisms that contribute to the formation and stability of colloidal systems: the hydrophobic effect, Van der Waals interactions, electric double layer forces and steric effects[166]. The hydrophobic effect is the main driving force behind the formation of liposomes and lipid-stabilised bubbles, in which non-polar molecules self-assemble to reduce the surface area exposed to water, and decrease the total entropy of the system [167]. For amphiphilic molecules (those which contain both hydrophobic and hydrophilic portions), self-assembly can lead to the formation of micelles and liposomes. Lipids can also self-assemble to form a monolayer at a liquid-gas interface, acting to reduce surface tensions and decrease the energy cost associated with the interface. In this thesis, phospholipids were used to form therapeutic liposomes, in which the aqueous core can be used to encapsulate hydrophilic molecules and form a stabilizing shell for gas-cored micro- and nanobubbles.

3.1.1 DLVO Theory

The behaviour of colloids (i.e. liposomes, bubbles etc.) is commonly described by the DLVO theory, named after the researchers who developed it (Derjaguin, Landua, Verwey and Overbeek) [168–170]. This theory combines the electrostatic forces and the van der Waals attraction to explain the aggregation and stability of particle interacting throughout a liquid medium. Particles with a charged surface will electrostatically attract ions of the opposite charge, forming an electric double layer at the particle surface. Initially, the repulsive force due to electrostatic interactions is close to zero, but as two particles or colloids approach each other, and their double layers being to overlap the repulsion force begins to grow significantly. Van der Waals attractive forces are nearly always presents, resulting from fluctuating dipoles of atoms and molecules. The DLVO theory assumes that the free energy per unit area can be approximated by the addition of contributions from both van der Waals and electrostatic forces (Equation 3.1), where W_{vdW} and W_{dl} are contributions from van der Waals and double layer interactions.

$$W(h) = W_{vdW}(h) + W_{dl}(h) \qquad \text{Equation 3.1}$$

$$W_{vdW}(h) = -\frac{H}{12\pi h^2}$$ Equation 3.2

$$W_{dl}(h) = \frac{2\sigma_+\sigma_-}{\epsilon_0\epsilon_\kappa}\exp(-\kappa h), \qquad \kappa = \left(\frac{2q^2 N_A I}{k_B T \epsilon \epsilon_0}\right)^{\frac{1}{2}}$$ Equation 3.3

The contribution from van der Waals forces can be assumed by Equation 3.2, where H is the Hamaker constant (which determines the strength), and h is the inter-particle spacing.

Double layer interactions can be approximated as Equation 3.3, where σ_+ and σ_- are the surface charge densities per unit area of each particle, ϵ_0 is the permittivity of vacuum, ϵ the dielectric constant of water. κ is the inverse Debye length, q is elementary charge of an electron, N_A is Avogadro's constant, I is ionic strength of the solution, k_B is Boltzmann's constant and T is absolute temperature. Hence, increasing ionic strength acts to shield the repulsive double layers forces and decrease stability. The force trend with varying particle separation is shown in Figure 3.1a, for double layer and van der Waals forces separately, and combined for the DLVO theory. At large separations, the force is initially dominated by van der Waals, however as the double layer of each particle approaches, the electrostatic repulsion becomes significant. At a separation of approximately the Debye length (κ^{-1}), the potential passes through a maximum, at which point the van der Waals forces dominates, and particles are attracted (Figure 3.1b). The height of this maximum, or potential barrier, indicates how stable the system is, as particles have to overcome the barrier to aggregate. At separations less than this, the potential has a deep attractive well which is referred to as the primary minimum. If particles do not have enough energy to overcome this barrier (i.e. too little momentum), the colloids can remain in the secondary minimum. As a result of this, measurement of particle zeta potential is often used as a metric of stability [18,19,171].

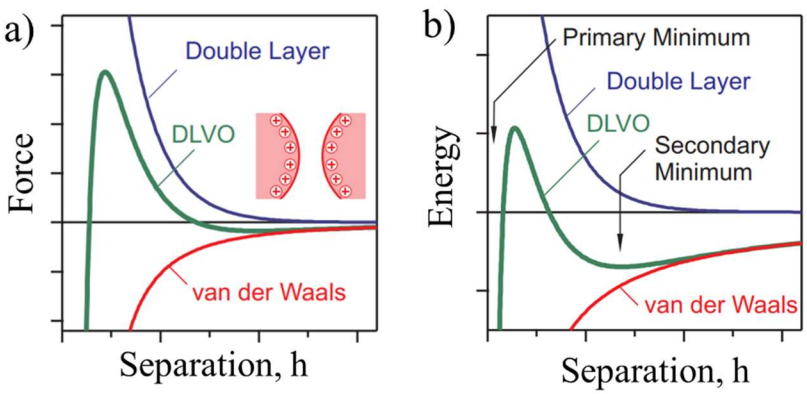

Figure 3.1 – a) Force and (b) energy profiles for the DLVO model for two particles with a separation distance of h, showing the contributions from the double layer electrostatic and van der Waals interactions. Reused under a CC BY 4.0 licence from [253].

3.1.2 Steric Effects

Whilst the DLVO model can be used to predict stability of colloidal systems, steric effects are neglected from the model. Here, the adsorption or conjugation of polymers to the colloid surface can reduce particle aggregation, in what is known as steric hindrance [13]. For a hydrophilic polymer (such as poly-ethylene glycol (PEG)), the polymer chains extend out into the surrounding fluid. As particle approach each other, an osmotic effect acts to separate the particles due to a local increase in polymer concentration. If the polymers start to interpenetrate, thermodynamic effects begin to dominate as polymer chains lose degrees of freedom, and hence decrease in entropy. Phospholipids conjugated to PEG chains (of varying molecular weights) are commonly used to increase nanoparticle stability, whilst also providing 'stealth' properties, reducing opsonisation and an immune response [89,172,173]. In this thesis, PEGylated lipids are used in both the formation and stabilisation of liposomes and MBs and NBs.

3.2 Ultrasound and Bubble Interactions

3.2.1 Ultrasound Basics

Ultrasound describes high frequency sound waves (> 20 kHz) that are above that of human hearing. Medical US typically uses frequencies of 1- 15 MHz with typical US wavelengths are ~10^{-4} m (assuming a speed of sound in tissue of 1540 ms^{-1}). US imaging follows a pulse-echo method where short ultrasonic pulses are emitted by a transducer. Reflection of the incident pulse occur at the boundary between two materials with different acoustic impedances, Z, which are then detected by the transducer. A greater impedance mismatch leads to increased intensity of the reflected pulse. The intensity of the pulse corresponds to the brightness of the image, and time of flight corresponds to the location of the interface. This is known as B-Mode imaging. A more detailed description of B-mode imaging can be found in Section 4.5. US imaging is routinely used clinically for pre-natal sonograms, US-guided interventions, and in combination with contrast agents, echocardiography [174]. US can also be used to monitor blood flow through the use of Doppler imaging, in which moving scatterers (i.e. blood cells) reflect US at a frequency different to that of the incident pulse. In diagnostic US, a unitless metric known as the mechanical index (MI) is used as an index of bio-cavitation effects, and hence safety[175]. MI is defined as a function of peak negative pressure (PNP, MPa) and frequency (f, MHz) (Equation 3.4). The FDA recommends that the MI should not exceed 1.9 in the absence of gas bodies, or no greater than 0.4 in the presence of gas bodies or UCAs [176].

$$\text{Mechanical Index, MI} = \frac{\text{PNP}}{\sqrt{f}} \qquad \text{Equation 3.4}$$

3.2.2 Damped Oscillator

Soft tissue is relatively acoustically homogeneous ($Z \sim 1.6 \times 10^6$ kg.m^{-2}s^{-1}) with approximately 1-2 % of the incident wave being reflected. As such, clinical imaging can suffer from poor contrast. To aid imaging, microbubbles are routinely used as intravascular contrast agents, as their gas core provides a large impedance mismatch ($Z_{air} \sim 4 \times 10^2$ kg.m^{-2}s^{-1}) between surrounding soft tissue and blood [177]. Hence, at the interface between a gas-cored bubble and blood or soft-tissue, ~ 99 % of the incident wave is reflected. However, this is not the only factor that contributes the MB echogenicity. Due to their gas-core, exposure of bubbles to US (an oscillating pressure field) induces volumetric bubble oscillations. At low pressure amplitudes, the displacement of the boundary of a free bubble can be modelled as a one-dimensional spring defined by its mass, a restoring force damping and an applied force (Equation 3.5), where m is the mass of the system, β is mechanical resistance related to dissipation, s is stiffness of the system and F_{drive} is the driving force. Here x(t) is defined as radial displacement from the initial radius. As a result of this, the system has a defined resonance frequency, f_r (Equation 3.6). The definitions of m, β and s as described by Medwin [178] are shown in Equation 3.7, where ρ_L is density of the surrounding liquid, δ_{tot} is total damping of the system, ω is angular frequency, γ is the heat capacity ratio and P is ambient pressure.

$$mx''(t) + \beta x'(t) + sx(t) = F_{drive}(t) \qquad \text{Equation 3.5}$$

$$f_r = \frac{1}{2\pi}\sqrt{\frac{s}{m}} \qquad \text{Equation 3.6}$$

$$m = 4\pi R_0^3 \rho_L, \qquad \beta = \delta_{tot}\omega m, \qquad s = 12\pi\gamma P R_0 \qquad \text{Equation 3.7}$$

$$f_r = \frac{1}{2\pi R_0}\sqrt{\frac{3\gamma P}{\rho_L}} \qquad \text{Equation 3.8}$$

This leads to Equation 3.8 in which it is evident the resonance frequency is inversely proportional to bubble size. Whilst this equation describes the resonance behaviour of a free bubble, the surrounding shell adds an additional restoring force which will then increase the resonance frequency of the bubble. Somewhat fortunately, the resonance frequency of lipid-shelled microbubbles, utilised as contrast agents, lies within the clinically approved frequency range for imaging. When excited on resonance, the acoustic scattering cross section of a bubble rapidly increases, as described by Equation 3.9, where σ is scattering cross-section and f_{drive} is driving frequency [179].

$$\sigma = \frac{4\pi R_0^2}{\left(\frac{f_r^2}{f_{drive}^2} - 1\right)^2 + \delta_{tot}^2} \qquad \text{Equation 3.9}$$

The trend described by this equation is shown in Figure 3.2. Here, an arbitrary bubble was defined as having an initial radius of 2 μm and a resonance frequency of 2 MHz. The value of δ_{tot} was varied between 0.01 and 1 to demonstrate the effect of increased damping on the system. At frequencies below resonance, scattering cross section rapidly increases as it approaches the maximum value at resonance. At frequencies above this however, scattering cross-section decreases to a constant value. Increasing the total damping of the system leads to a decrease in the peak scattering cross section achievable, whilst also producing a broadened

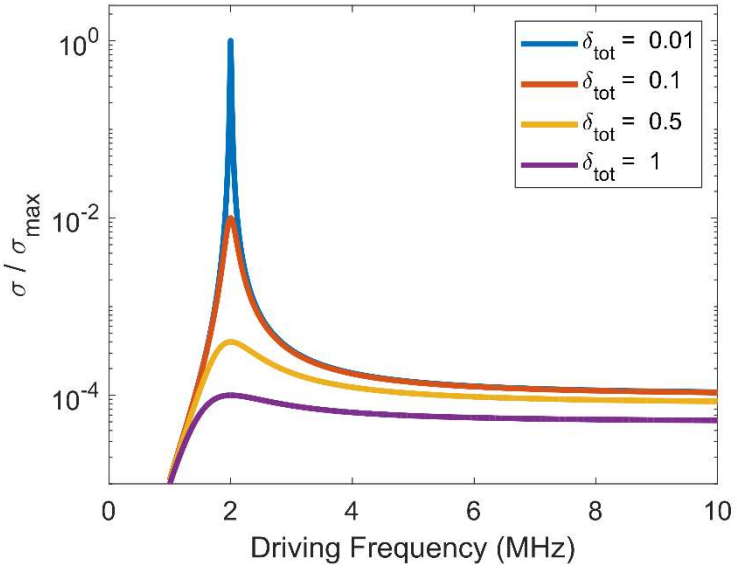

Figure 3.2 – A plot showing the trend between scattering cross section of a bubble, σ, and the driving frequency of the ultrasound. All plots were normalised to the maximum value for δ_{tot} = 10. An arbitrary bubble was defined as having an initial radius of 2 μm, a resonance frequency of 2 MHz and scattering cross section plot for δ_{tot} = 0.01,0.1 0.5 and 1.

frequency response. For a bubble with no damping, the scattering cross-section will tend to infinity on resonance.

3.2.3 Radial Oscillations

At low driving pressures, bubbles will scatter and oscillate at the fundamental driving frequency (i.e. linearly). Volumetric oscillations of a bubble are commonly described by the Rayleigh-Plesset equation [180] (Equation 3.10).

$$R\ddot{\mathrm{R}} + \frac{3}{2}\dot{\mathrm{R}}^2 + \frac{4\nu_{\mathrm{L}}}{\mathrm{R}}\dot{\mathrm{R}} + \frac{2\gamma}{\rho_{\mathrm{L}}\mathrm{R}} + \frac{\Delta\mathrm{P(t)}}{\rho_{\mathrm{L}}} = 0 \qquad \text{Equation 3.10}$$

where R is instantaneous bubble radius, $\ddot{R}$ and $\dot{R}$ denote the first and second order derivative of time, ν is the kinematic viscosity, γ is surface tension and $\Delta P(t) = P_{\infty}(t) - P_B(t)$, the difference between the external pressure infinitely far from the bubble, and internal bubble pressure.

This equation can be derived from first principles. Firstly, by considering mass conservation the radial outward velocity, u, must follow an inverse square law (Equation 3.11a) and be proportional to some function of time f(t). Assuming there is no mass transport at the bubble surface, the velocity is then defined by Equation 3.11b. Substitution of Equation 3.11b into Equation 3.11a yields Equation 3.11c. The assumption of no mass transfer only holds if the density if the surrounding medium is much greater than that of the gas-core.

The velocity definition can then be applied to the Navier-Stokes equation for an incompressible fluid, defined in spherical coordinates (Equation 3.12), which considers conservation of momentum. Substitution of Equation 3.11c into the Navier-Stokes equation yields a differential equation, in which variables (r and t) can be separated and integrated. For this, boundary conditions are required for pressure, P, at the bubble surface (r=R). The normal stress pointing radially outwards from the bubble is described by Equation 3.13a. As it assumed there is no mass transfer across the bubble surface, the force per unit area (at the bubble surface must be zero (Equation 3.13b). This assumption then leads a definition for the pressure at the bubble surface, P(R), (Equation 3.14). This then yields the Rayleigh-Plesset equation. It can be shown from this that under steady conditions (i.e. $\dot{R} = 0$), the Rayleigh-Plesset yields the equation for Laplace pressure.

$$\mathrm{u(r,t)} = \frac{\mathrm{f(t)}}{\mathrm{r}^2}, \qquad \mathrm{u(R,t)} = \dot{\mathrm{R}} = \frac{\mathrm{f(t)}}{\mathrm{R}^2}, \qquad \mathrm{u(r,t)} = \frac{\mathrm{R}^2}{\mathrm{r}^2}\dot{\mathrm{R}} \qquad \text{Equation 3.11a, b, c}$$

$$\rho_L\left(\frac{\partial u}{\partial t}+u\frac{\partial u}{\partial r}\right)=-\frac{\partial P}{\partial r}+\mu_L\left[\frac{1}{r^2}\frac{\partial}{\partial r}\left(r^2\frac{\partial u}{\partial r}-\frac{2u}{r^2}\right)\right] \quad \text{Equation 3.12}$$

$$\sigma_{rr}=-P+2\mu_L\frac{\partial u}{\partial r},\ \ \sigma_{rr}(R)+P_B-\frac{2\gamma}{R}=0, \quad \text{Equation 3.13a, b}$$

$$P(R)=P_B-\frac{4\mu_L\dot{R}}{R}-\frac{2\gamma}{R} \quad \text{Equation 3.14}$$

Although applicable to a free gas bubble, surrounded by an incompressible liquid, the Rayleigh-Plesset equation does not account for elastic and viscous contribution provided by the bubble shell (i.e. lipid, polymer, etc.). Over time terms have generally been added to this equation, to describe the behaviour of lipid-coated microbubbles at low to medium pressures. Perhaps the most notable of these is the Marmottant model [139], which assumes the bubble has a finite, constant number of lipid molecules. Three parameters are used to describe the properties of the shell: a buckling radius, the compressibility of the shell, and a break-up shell tension (Equation 3.15). Each parameter describes at what radius the shell buckles ($\gamma = 0$), an elastic modulus that gives the slope of the elastic regime, and a parameter to describe the surface tension at which the bubble ruptures. The Marmottant modal is achieved by combining the Rayleigh-Plesset equation and the polytropic gas law, and then defining surface tension as a function of radius (Equation 3.16).

$$\rho_l\left(R\ddot{R}+\frac{3}{2}\dot{R}\right)=\left[P_0+\frac{2\gamma(R_0)}{R_0}\right]\left(\frac{R}{R_0}\right)^{-3\kappa}\left(1-\frac{3\kappa}{c}\dot{R}\right)-P_0 -\frac{2}{R}\left(\gamma(R)+2\mu\dot{R}+\frac{2\kappa_s\dot{R}}{R}\right)-P_{ac}(t) \quad \text{Equation 3.15}$$

$$\gamma(R)=\begin{cases}0 \text{ if } R\le R_{buckling}\\ \chi\left(\frac{R^2}{R_{buckling}^2}-1\right) \text{if } R_{buckling}\le R\le R_{break-up}\\ \sigma_{water} \text{ if } R\ge R_{ruptured}\end{cases} \quad \text{Equation 3.16}$$

This piece-wise definition then leads to three discrete regimes of bubble behaviour under changing ambient pressure and bubbles radius, and hence variation in surface tension (Figure 3.3). The buckled regime corresponds to where $\gamma = 0$, due to fast compression of the bubble and lipid monolayer. The elastic regime then corresponds to a small radial region in which the lipid monolayer is assumed to behave as an elastic material. This is then followed by the broken or ruptured state in which, under fast expansion, the lipid monolayer breaks above a

threshold surface tension, $\gamma_{critical}$, exposing areas of bare gas interface to the surrounding medium, and hence $\gamma = \gamma_{water}$.

At higher driving pressures, this model predicts that bubbles will undergo non-linear oscillations. During the compression phase of the incident US field, the bubble will buckle and hence surface tension decrease. However, in the elastic region and during bubble expansion, the surface tension will increase proportional to R^2. This leads to what is known as "compression only" behaviour and non-linear oscillations [181,182].

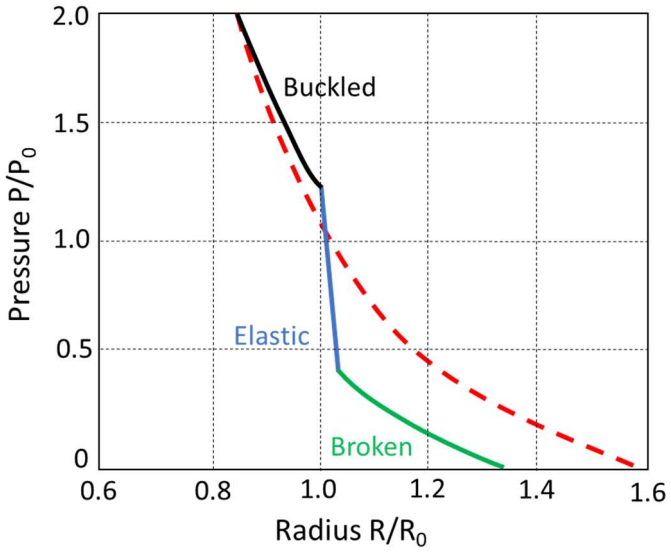

Figure 3.3 – An example plot comparing between the Rayleigh-Plesset (red, dashed) and Marmottant (solid) models, for how bubble size changes with a change in ambient pressure. In the Marmottant model, each coloured section refers to the differing bubble behaviour due to the piece-wise definition of surface tension. Buckled (black), elastic (blue), broken (green).

3.2.4 Non-Linear Oscillations and Acoustic Emissions

At low acoustic pressure, bubbles will oscillate linearly at their fundamental frequency. However, further increasing the acoustic pressure leads to non-linear oscillations, which generate harmonics of the fundamental driving frequency, f_0. These harmonics can either be sub-harmonic (f_0/n), super harmonic (nf_0) or ultra-harmonic ($(2n+1)f_0/n$) where $n \in \mathbb{N}$ [183]. In diagnostic imaging, tissue response is primarily linear (i.e. at the fundamental frequency). Utilising non-linear imaging techniques such as pulse-inversion or amplitude-modulation, the harmonic signal provided by bubbles (or US contrast agents) can be isolated, hence increasing image contrast [184,185]. Whilst at lower driving pressures bubbles will undergo stable volumetric oscillations (stable cavitation), increasing the pressure beyond a threshold can induce total bubble destruction (inertial cavitation). During inertial cavitation, the oscillation bubble expands above a critical radius [186], at which point inertial forces dominate the compression phase leading to bubble destruction and fragmentation (Figure 3.4). Because of this

phenomenon, non-linear/harmonic image modalities typically utilised low acoustic pressures (MI < 0.1) such that stable bubble oscillation, and contrast enhancement, is maintained. Additionally, the FDA recommends that the MI does not exceed 0.4 when using UCAs [176].

As well as producing harmonic emissions, unique to inertial cavitation is the emission of broadband noise [187,188]. Observation of these acoustic emissions can allow for determination of bubble behaviour occurring during insonation, in what is known as cavitation detection. In this thesis, passive cavitation detection is used to acoustically characterise NBs (Section 6.6). It should be noted that as bubble populations are typically polydisperse, under insonation of a tone pulse (i.e. a single frequency) acoustic emissions will consist of bubbles excited to different magnitude of radial oscillation and hence a mixture of both stable and inertial cavitation. As such, harmonic emissions are typically concurrent with broadband noise.

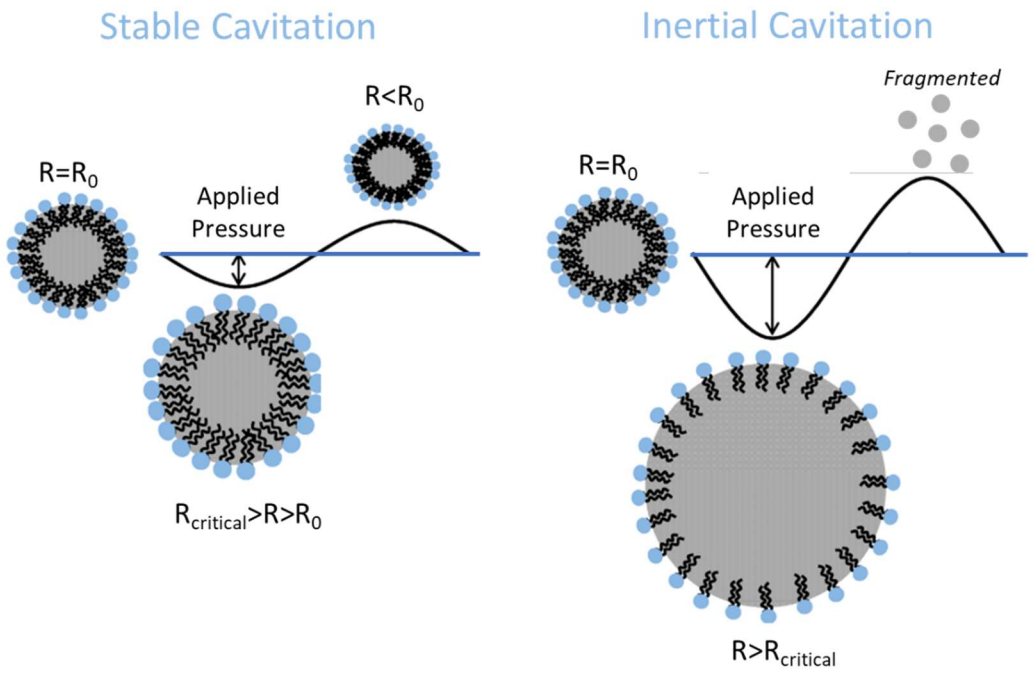

Figure 3.4 – Schematic showing the behaviour of lipid coated bubbles during an incident ultrasound pulse. Here, the bubble is initially at rest ($R=R_0$). At low to medium acoustic pressures, the bubble will volumetrically oscillate in a stable regime (stable cavitation), expanding during the rarefaction phase ($R>R_0$) and contracting during the compression phase ($R<R_0$). At higher acoustic pressures, the bubble will expand above a critical radius ($R_{critical}$), followed by rapid compression leading to bubble destruction and fragmentation. Adapted from [220] under a CC BY-NC 4 licence. Copyright Ivyspring International Publisher 2012.

3.3 Sonoporation Mechanisms

These two discrete bubble behaviours (stable and inertial cavitation) can both be used to transiently increase cell membrane permeability, in a process known as sonoporation. For a

stably oscillating bubble there are two main physical mechanisms that induce membrane poration. Firstly, volumetric oscillation of the bubble induced by the incident US field push and pull on the cell membrane during the expansion and compression phases (Figure 3.5a). These oscillations also induce localised fluid flow (Figure 3.5b). When situated near a surface (i.e. cell membrane), application of the non-slip boundary condition (Equation 3.17) where u is fluid velocity and $\hat{n}$ is the unit normal vector, leads to shear flow and hence shear forces generated across the membrane. Both of these processes affect membrane integrity.

$$u \times \hat{n} = 0 \qquad \text{Equation 3.17}$$

At higher acoustic pressures, when bubbles undergo inertial cavitation, the bubble expansion and subsequent collapse leads causes the formation of a liquid microjet directed towards the cell membrane, and hence creating a pore (Figure 3.5c).

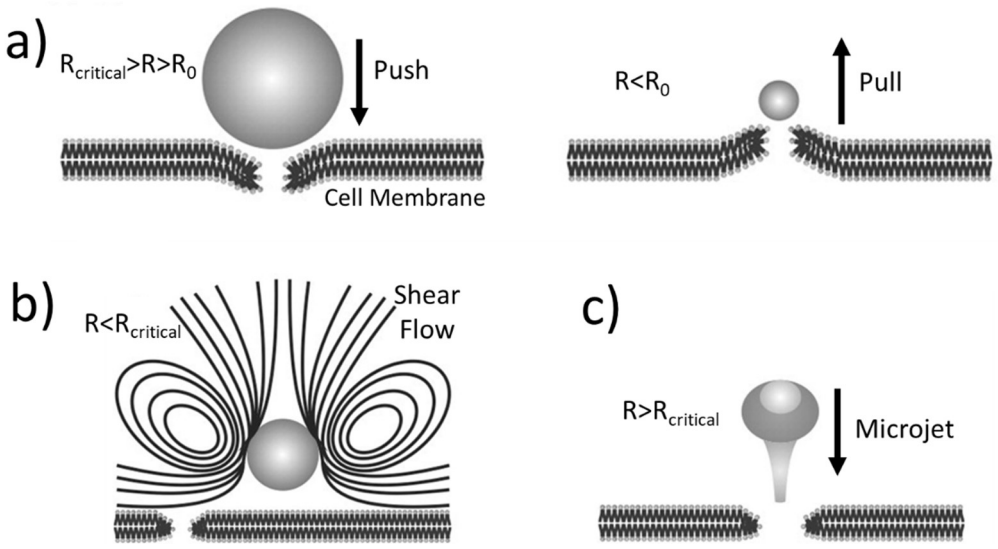

Figure 3.5 – The three main mechanisms in which the combination of bubbles and ultrasound and induce cell membrane poration, known as sonoporation. a) Pushing and pulling effects during stable bubble oscillation. b) The stably oscillating bubble also induces localised fluid flows, exerting a shear force on the membrane. c) During inertial cavitation and bubble collapse, the collapse is asymmetrical and produces a high velocity fluid microjet directed towards the membrane.

3.4 Bubble Stability

For a bubble at rest, the internal pressure must be equal to the sum of the external pressure of the liquid and the induced pressure due to surface tension (i.e. Laplace pressure, Equation 2.1). Whilst this is useful for generally describing the dependence of bubble stability on size and surface tension, it does not describe the motion of bubble dissolution or growth. This was first described by Epstein and Plesset [57] (Equation 3.18), which predicts inherent bubble instability due to the so-called "Laplace catastrophe". For example, a small increase in bubble size

decreases the Laplace pressure. Due to Henry's law (Equation 3.19), this reduces the gas concentration in the bubble's immediate vicinity, causing the gas to diffuse from solution into the bubble and establish a positive feedback loop. Similarly, the reverse holds for a bubble that initially decreases in size. This equation considers the surface tension of the bubble but neglects any stabilising shell and hence any additional elastic or viscous forces.

$$\dot{R} = -H\frac{1 - f + \frac{2\gamma}{P_a R}}{1 + \frac{4\gamma}{3P_a R}}\left(\frac{D_w}{R} + \sqrt{\frac{D_w}{\pi t}}\right) \qquad \text{Equation 3.18}$$

$$C = kP \qquad \text{Equation 3.19}$$

where $\dot{R}$ is the first-order time derivative of bubble radius, R, H is the Ostwald coefficient $H = \frac{c_a}{c_g}$ where c_a and c_g are gas concentration in the aqueous and gas phases, P_a is ambient pressure, D_w is diffusivity of water molecules, $f = \frac{c_i}{c_\infty}$ where c is dissolved gas concentration initially (c_i) or at saturation (c_∞).

Whilst the Epstein-Plesset model is valid for a free bubble, it does not consider the influence of a stabilising shell. This model was further developed by Borden and Longo (Equation 3.20) [83] in which an additional term was added to account for mass transfer resistance of a lipid monolayer, R_{shell}, which acts to slow the rate of bubble dissolution.

$$\dot{R} = -\frac{H}{\frac{R}{D_w} + R_{shell}}\left(\frac{1 + 2\gamma/P_a R) - f}{1 + \frac{4\gamma}{3P_a R}}\right) \qquad \text{Equation 3.20}$$

3.5 Ostwald ripening

Whilst the Epstein-Plesset equation, and its developed models, explain the dissolution and growth of a single bubble they do not consider the behaviour of a population of bubbles with varying size. In a population, particles (i.e. bubbles, emulsions, etc.) of larger size have increased thermodynamic stability, due to the inherent instability of surface molecules, and larger particles have a smaller surface area to volume ratio. This is described by Kelvins equation (Equation 3.21) where μ is the chemical potential (Equation 3.22), γ is surface tension, Ω is the molar volume of the material, r is particle size, P is vapour pressure, P_{sat} is saturated vapour pressure, T is temperature and k is the Boltzman constant.

$$\Delta\mu = \frac{2\gamma\Omega}{r} \qquad \text{Equation 3.21}$$

$$\mu = kT\ln\left(\frac{P}{P_{sat}}\right)$$ Equation 3.22

Smaller particles in solution will begin to shrink and deposit their surface molecules into the solution to reduce the concentration gradient between the interior and exterior of the particle. A proportion of the dissolved phase then induces growth in larger particles, as this is energetically favourable. This net flux of solute can be described by the Gibbs-Thomson equation (Equation 3.23), where C_e is solute concentration at a plane interface, C_r is solubility at the surface of a spherical particle with radius r, γ is the surface tension, and Ω is the molar volume of the particle. Hence, here the difference between C_r and C_e induces a diffusive flux from the smaller to larger particles and average particle size increases.

$$C_r = C_e \exp\left[\frac{2\gamma\Omega}{R_B T}\frac{1}{r}\right]$$ Equation 3.23

As a result of this, there is a defined critical radius in which particles below this size will shrink and dissolve, and particles larger in size will continue to grow [189]. In the case of bubbles (both MBs and NBs) Ostwald ripening occurs when bubbles shrink as a result of their high Laplace pressure, and thus create areas of supersaturation in the local environment that cause larger bubbles to grow. Work by Lifshitz and Slyozov, and separately by Wagner, in what is now known as LSW theory[190,191], quantitatively predicts that the average radius of particles in solution $\langle R \rangle$, grows over time (Equation 3.24), where c_∞ is solubility of the particle material, D is diffusion coefficient, R is the ideal gas constant, and t is time.

$$\langle R \rangle^3 - \langle R \rangle_0^3 = \frac{8\gamma c_\infty v^2 D}{9RT} t$$ Equation 3.24

3.6 Bubble Buoyancy

The terminal velocity of a particle in solution (either rising or sinking) can be calculated by Equation 3.25, where U is the ascension velocity, g is the gravitational acceleration, d is the diameter, $\Delta\rho$ is the difference in density between the medium and the core, μ is the dynamic viscosity of the suspending fluid.

$$U = \frac{g d^2 \Delta\rho}{18\mu}$$ Equation 3.25

By assuming that the particle is spherical and rigid, this can be derived by applying a force balance between the Stokes drag force (Equation 3.26), and the buoyant force, which is equivalent to the mass of displaced fluid (Equation 3.27).

$$F_d = 6\pi\mu RU$$ Equation 3.26

$$F_b = \frac{4\Delta\rho\pi g R^3}{3}$$ Equation 3.27

3.7 Fluorescence

Fluorescence is the emission of light from a substance, after absorption of light of higher energy (i.e. lower wavelength). Molecule energy levels consist of electronic, vibrational and rotational levels. At room temperature most molecules occupy the lowest vibrational level of the ground electronic state. Excitation of a molecule occurs when an incident photon interacts with a substance and causes it to enter an excited vibrational state. Energy from a photon, E, is directly proportional to frequency, ν, and hence inversely proportional to wavelength, λ, and is quantized as shown by Equation 3.28, where c is speed of light and h is Planck's constant.

$$E = h\nu = \frac{hc}{\lambda}$$ Equation 3.28

For absorbance, and hence excitation, to occur the energy of the photon must correspond to the gap between the molecules ground state energy levels (S_0), or the highest occupied molecular orbital (HOMO), and the energy level of the first (S_1) or second (S_2) electronic vibrational state orbitals. Fluorescence is the emission of a photon accompanying relaxation of the excited state to the ground state. After absorption, vibrational relaxation of the excited state occurs followed by emission of a lower energy photon and return of the molecule to the ground state. This can be demonstrated by the Jablonski diagram shown in Figure 3.6.

The efficiency of this process (i.e. how many of the absorbed photons undergo this process) is defined by the quantum yield, Φ, (Equation 3.29) and can be used estimate how "bright" a fluorophore is, an aspect that is important to consider during fluorescence imaging.

$$\Phi = \frac{\mathrm{N(photons\ emitted)}}{\mathrm{N(photons\ absorbed)}}$$ Equation 3.29

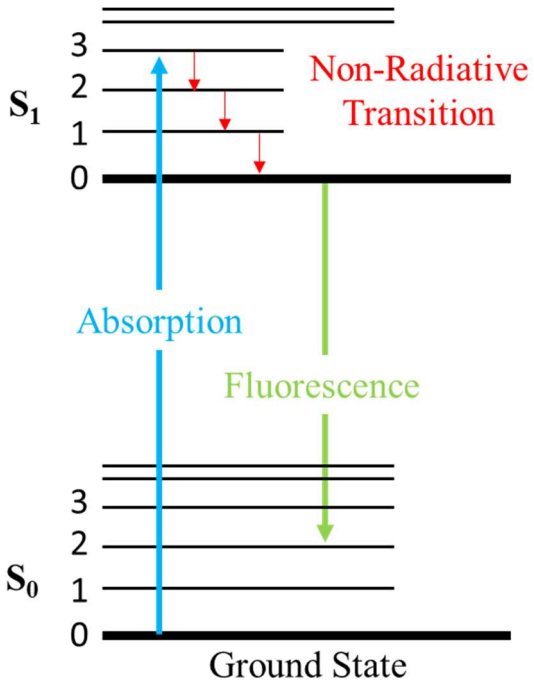

Figure 3.6 – Jablonski diagram showing excited states of a fluorescence molecule. Electronic states (thick black lines) consist of vibrational sub-states (thin black lines). Fluorescence occurs when a molecule in the ground state (S_0) absorbs a photon and is excited to a higher electronic state (here, S_1). Non-radiative transitions (red) can occur until the molecule is in the lowest vibrational state of the excited electronic state. When the molecule relaxes into a lower electronic state (green line) it subsequently emits a photon of lower energy than the absorbed photon (i.e. fluorescence emissions).

3.8 Light Scattering

In this thesis, light scattering techniques are routinely used to characterise the size of nanoparticles (liposomes, NBs). The following sections describes two theories that can be used to describe the interaction of nanoparticles with light: Rayleigh scattering, and Mie theory.

3.8.1 Rayleigh Scattering

Rayleigh scattering is the elastic scattering of light by particles much smaller than the wavelength. The small size approximation can be parametrized by Equation 3.30, where r is particle radius, k is wavenumber and λ is wavelength.

$$x = \frac{2\pi r}{\lambda} \qquad \text{Equation 3.30}$$

Rayleigh scattering occurs when x ≪1, when the particle size is approximately 10 x smaller than the wavelength. Here, the particle experiences a uniform electric field that oscillates slowly in time. Reradiated light is all in the same phase, but as the particles are randomly positioned in the solution, the scattered light arrives at a detector with random collection of

phases. As a result, the intensity is neither periodically constructive nor destructive. The amplitude of scattered light will be proportional to the particles volume, and hence the intensity proportional to r^6. The scattering intensity of a sphere, as a function of position, is shown in Equation 3.31, where I_0 is incident light intensity, R is distance to the particle, θ is scattering angle, m is the relative refractive index ($n_{particle}/n_{medium}$), and d is particle diameter.

$$I = I_0 \frac{1 + \cos^2 \theta}{2R^2} \left(\frac{2\pi}{\lambda}\right)^4 \left(\frac{m^2 - 1}{m^2 + 2}\right)^2 \left(\frac{d}{2}\right)^6 \qquad \text{Equation 3.31}$$

Averaged over all angles, the scattering cross section, σ_s can be given by Equation 3.32 [192].

$$\sigma_s = \frac{2\pi^5}{3} \frac{d^6}{\lambda^4} \left(\frac{m^2 - 1}{m^2 + 2}\right)^2 \qquad \text{Equation 3.32}$$

The intensity of Rayleigh scattered light is dependent on particle size, refractive index and wavelength of incident light.

3.8.2 Mie Theory

In this thesis, light scattering techniques are used to characterise the sizes of particles > 100 nm in diameter, and hence does not satisfy the limits of $x \ll 1$. Mie theory, formulated in 1908, considers interactions between an electromagnetic field and a particle, including any absorption of the incident light by the particle. Such effects become more important for particles that are plasmonically active, such as gold nanoparticles utilised for photothermal therapy [193,194]. Without derivation, which is beyond the scope of this thesis, the scattering cross-section of a sphere can be predicted by Equation 3.33, in which only dipolar contributions (i.e. first harmonic) are considered, in what is known as the quasistatic approximation [195,196]. Here, k is the wavevector, in which ϵ_m is the permittivity of the medium and α is defined in Equation 3.34, where ϵ is the permittivity of the particle. Hence, it is clear the scattering scales with a^6 and hence the square of particle volume, similar to that in Rayleigh scattering.

$$\sigma_s = \frac{k^4}{2\pi} |\alpha|^2, \qquad k = \frac{2\pi\epsilon_m}{\lambda} \qquad \text{Equation 3.33}$$

$$\alpha = 4\pi a^3 \frac{\epsilon - \epsilon_m}{\epsilon + 2\epsilon_m} \qquad \text{Equation 3.34}$$

For a non or lowly absorbing material (hence the imaginary refractive index = 0), the permittivity or dielectric constant is equal to the square of the refractive index, and the scattering cross-section is proportional to $|n^2 - n_m^2|^2$.

3.9 Microfluidics and Fluid Flow

Microfluidics is the manipulation of fluid flow on the microscale. The reduction in length scale from macro- to micro- provides increased control over the fluid due to a phenomenon known as laminar flow. Additionally, microfluidics requires low sample volumes, reducing reagent cost, whilst also providing scope for automation and high throughput measurements and production.

The Navier-Stokes equation describes conservation of momentum of a fluid under flow, and can be used to predict fluid behaviour (Equation 3.35) where ρ is fluid density, u is fluid velocity, p is fluid pressure and F is an externally applied force (e.g., gravitational, magnetic). Here, fluid inertial forces are balanced by forces provided by an external pressure gradient, viscous forces and any other external forces (e.g. gravitational, electromagnetic) [197].

$$\rho\left(\frac{\partial u}{\partial t} + u \cdot \nabla u\right) = -\Delta p + \mu\nabla^2 u + F \qquad \text{Equation 3.35}$$

$$\frac{\partial \rho}{\partial t} + \nabla \cdot (\rho u) = 0 \qquad \text{Equation 3.36}$$

The Navier-Stokes equation can be combined with the continuity equation (Equation 3.36), which defines conservation of mass. Assuming the fluid is incompressible, this reduces to $\nabla \cdot u = 0$, as fluid density is assumed to be constant. Whilst able to predict the motion of fluid flow, there are few situations in which the Navier-Stokes equation can be solved analytically (e.g., a cylindrical pipe). Numerical simulation techniques such as finite element method can be used to predict fluid flow with the application of appropriate boundary conditions, however these can be computationally expensive and temporally slow.

To predict the behaviour of fluid flow, multiple dimensionless quantities have been described and are typically composed quickly and efficiently by scaling the magnitude of different forces that act on the fluid. Most commonly, the Reynolds number (Re) is used to predict the dominance of either inertial or viscous forces (Equation 3.37), where L is a characteristic length scale of the system, dependent on flow geometry.

$$Re = \frac{F_{inertial}}{F_{viscous}} = \frac{\rho u L}{\mu} \qquad \text{Equation 3.37}$$

For a square or rectangular geometry, commonly used in microfluidics, this is defined by the hydraulic diameter, $D_{H,}$ where A is channel area, P is channel perimeter, and w and h are channel height and width (Equation 3.38) [198].

$$D_H = \frac{4A}{P} = \frac{2wh}{w + h} \qquad \text{Equation 3.38}$$

At low Re (< 2300), flow is described as laminar during which viscous forces dominate the behaviour of the fluid [199]. Here, the fluid follows smooth continuous streamlines and particle velocity is predictable. At higher Re (> 4000), fluid becomes turbulent at which point the flow becomes erratic and unstable, forming eddy currents and vortices, making it increasingly difficult to predict fluid behaviour [200]. Due to the dependence on fluid velocity, u, and channel geometry, microfluidics nearly always operates within the laminar regime. For very low Reynolds numbers (Re $\ll$ 1) the behaviour can be modelled as Stokes flow, in which inertial forces are negligible, simplifying the Navier-Stokes equation ($-\Delta p - \mu \nabla^2 u = 0$).

In this thesis, microfluidics was used in two ways. Firstly, to produce MBs and NBs using the microspray regime, which utilizes a multi-phase flow (liquid and gas). Microfluidics was also used as a method to culture colorectal cancer cells, to help facilitate sonoporation studies and reduce reagent volume consumption.

3.10 Cell Structure and Cancer Progression

Cells are the basic biological unit that make up living organisms and can be split into two types: prokaryotic and eukaryotic. Prokaryotes lack a nucleus and are typically between 1 – 10 μm in size. An example of a prokaryote is bacteria. Eukaryotic cells are vastly more complex, possessing a nucleus, and can form multicellular organisms such as plants and animals. Depending on the individual cell type, eukaryotes are typically between 10- 20 μm in size. Cells are enclosed by a cell membrane, consisting of a lipid bilayer and membrane proteins, which control movements of ions and molecules in and out of the cell. Enclosed within the cell membrane is the cytoplasm. Organelles are sub-units within the cytoplasm each with their own specialised functions and are surrounded by a liquid known as the cytosol. Organelles which can either be enclosed within their own lipid bilayers (membrane bound), or as distinct units without this surrounding bilayer (non-membrane bound). Eukaryotes contain a nucleus containing DNA, which is arranged into chromosomes.

Cells can undergo mitosis, in which the cell reproduces asexually, creating an identical copy of itself via DNA replication. However, during this process mistakes can occur, leading to genetic mutations. The relative number of mutations is typically very low, and cells have mechanisms in place to repair DNA, or if a cell is irreparably damaged then programmed cell

death is triggered (apoptosis) to prevent further mutations. The main feature of a cancerous cell is that of uncontrolled proliferation, in which the mechanisms to prevent mutated cells proliferating have failed. If multiple mutations occur within genes responsible for controlling cell replication, as well as those which control safeguarding and induced apoptosis, a cancerous growth known as a primary tumour will form. To continue proliferating and growing, the tumour requires a blood supply. This can either happen by encompassing pre-existing vasculature or by inducing formation of new blood vessels (angiogenesis). The formation of blood vessels is regulated by pro- and anti-angiogenic factors, which when in balance, prevents over-proliferation of endothelial cells, and new vasculature does not form. In a process known as the "angiogenic switch" tumours begin rapid growth of malignant cells due to the formation of new vasculature [201].

Cancer can become metastatic when cells from the primary tumour break away and move into a blood vessel or lymph node situated elsewhere in the body. An example of this is the SW480 and SW620 immortalised cell lines, which represent primary colorectal cancer, and a metastasized tumour located in the lymph nodes [202].

4 Experimental Theory

4.1 Microscopy Techniques

4.1.1 Epi-fluorescence Microscopy

Fluorophores are molecules which when excited with a light source, absorb and re-emit light at a higher wavelength than the incident light (Section 3.7). Epi-fluorescence microscopy produces an image by illuminating a sample containing a fluorophore with near-monochromatic light. An excitation filter (Ex) is placed in the path of the incident light, removing all light except that of the desired excitation wavelength bandwidth. A dichroic mirror is used to direct light onto the sample, allowing the re-mitted light to reach an emission filter (Em), removing undesired wavelengths, and finally to a photodetector (Figure 4.1).

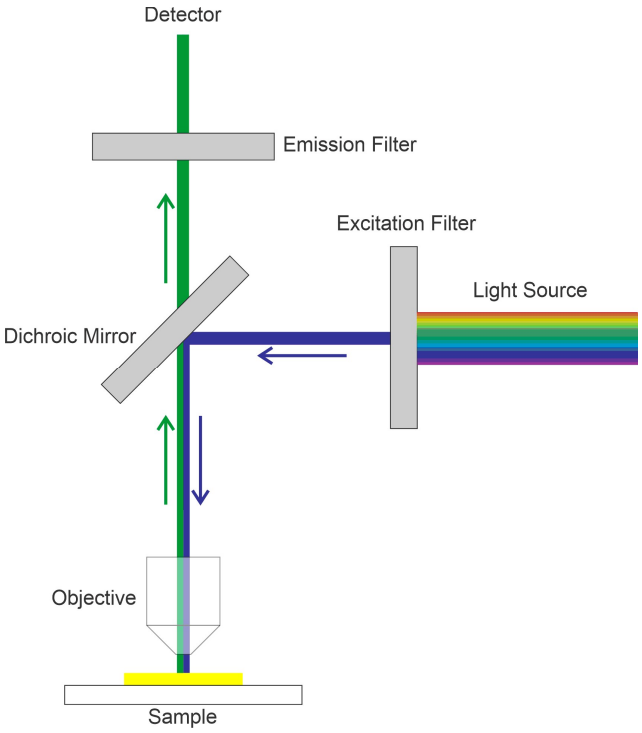

Figure 4.1 - Schematic of an upright epifluorescence microscope. A white light source is passed through an excitation filter matching that of the desired excitation wavelength, A dichroic mirror directs the incident light to illuminate the sample. The emitted light then passes through the dichroic mirror, through an emission filter to the detector.

4.1.2 Confocal Laser Scanning Microscopy

Confocal microscopy is a fluorescence imaging technique that uses a pinhole to remove out of focus light and hence improve spatial resolution (Figure 4.2). In traditional epifluorescence microscopy, light throughout the sample depth is collected, including out of focus, and hence

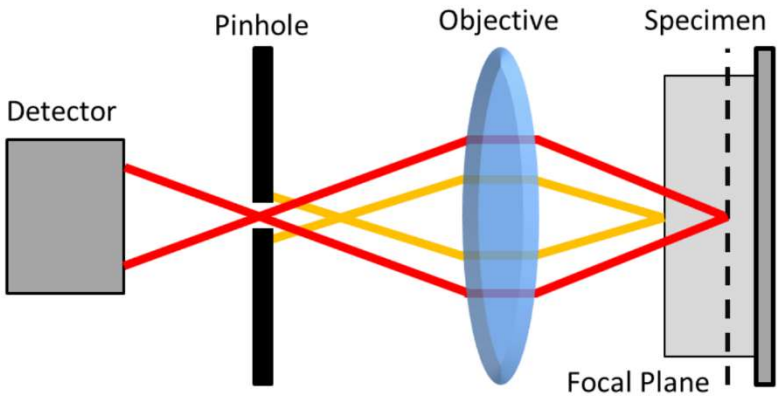

Figure 4.2 - Schematic showing the working principle of a confocal microscope. The use of a pinhole allows for collection of focussed light (red) from the sample, whilst omitting unfocused light (orange), reducing background fluorescence, and allowing imaging at a defined depth. Reused with permission from [202] under a CC BY-NC-SA 2.0 licence.

limiting resolution. The use of a pinhole allows for only in-focus light to be collected (i.e. from the same plane), reducing background fluorescence that would be associated with out of focus specimens. Confocal microscopes, or commonly confocal laser scanning microscopes (CLSM), utilise multiple monochromatic lasers to illuminate the sample and excite fluorophores. During image acquisition, multiple mirrors are used to linearly raster scan across the x and y axis, collecting light from individual elements and producing an image. The size of the scanning element, and hence resolution, is typically close to that of the diffraction limit, hence increasing resolution compared to wide-field microscopy. Samples can also be mapped in 3D through the use of a z-stack, in which multiple x-y images are acquired at varying focal depths. Further, the size of the pinhole can be reduced, increasing confocality but at the cost of total image brightness. During imaging, resolution and scan speed of the acquisition can be adjusted to increase image quality, at the expense of imaging time which may lead to motion blur in live samples. In this thesis, confocal microscopy was primarily used to image cell monolayers to assess the uptake of a fluorescent membrane probe.

4.1.3 Transmission Electron Microscopy

Transmission Electron Microscopy (TEM) utilises a focused, high-energy beam of electrons to produce an image following a similar principle to that of bright field microscopy. The Abbe diffraction limit for a microscopy system can be described by Equation 4.1, where d is minimum resolution, λ is wavelength, n is the refractive index of the medium and NA is the numerical aperture of the system.

$$d = \frac{\lambda}{2NA} \qquad \text{Equation 4.1}$$

Optical microscopy typically utilises wavelengths of 400 – 600 nm, and hence even for a typical NA (~ 0.6) resolution is limited to the order of 10^2 nm. The wave-particle duality of electrons, with a De Broglie wavelength defined by Equation 4.2, and hence a greatly reduced wavelength (~2.5 pm at 200 keV) leads to imaging resolutions of ~ 10^{-10} m.

$$\lambda = \frac{h}{p} \qquad \text{Equation 4.2}$$

where λ is wavelength, h is the Planck constant (6.63 x10^{-34} m^2 $kg.s^{-1}$) and p is momentum of the particle. Hence, the effective resolution of TEM is governed by the velocity of the electrons. To reach the required energy (10^3 eV), electrons are accelerated across a potential difference and focused using a pair of condensing lenses, before passing through an objective aperture and striking the sample. Incident electrons can be scattered or absorbed by atomic nuclei, or pass through the sample unimpeded, at which point they are collected by a fluorescent screen or camera forming an image. Biological samples (i.e. lipids, proteins) have low electron densities and hence to increase contrast heavy metal stains are commonly used. Throughout this thesis, 1 % uranyl acetate was used, in which uranyl ions bind to proteins and lipids in the sample. Samples were prepared in a phosphate free buffer to prevent precipitation of salts and hence unwanted diffraction events [203] and dried onto carbon coated copper grids prior to imaging.

4.2 Nanoparticle Tracking Analysis

Nanoparticle Tracking Analysis (NTA) is a technique to characterise both size and concentration of sub-micron particles, tracking light scattered from individual particles in solution to determine their diffusion constant, related to their Brownian motion by the Einstein-Stokes (Equation 4.3). A dilute suspension of sample is driven through a low volume flow cell at a constant flow rate using a syringe pump, where a 488 nm laser is incident to the

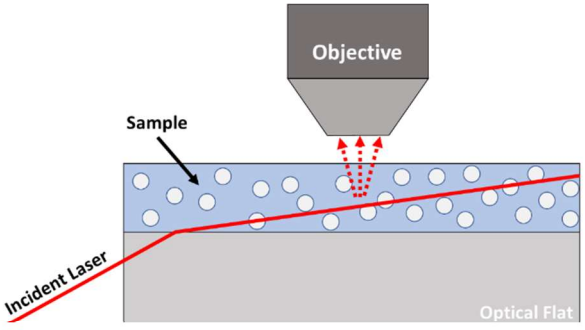

Figure 4.3- Schematic showing the working principle of Nanoparticle Tracking Analysis. A sample is illuminated using a 488 nm laser incident at a 45 °, and scattered light collection by a 20 x objective, prior to post processing.

sample at a 45 ° angle. Light scattered by each individual particle is collected using a 20 x objective and a camera used to record videos of the sample (Figure 4.3).

These videos are then analysed post video collection to determine particle size and concentration for individual particles. NanoSight NS300 (Malvern Panalytical, UK) was used for all measurements and videos were analysed using NTA Software 3.3.

$$\frac{\overline{< x,y >}^2}{4} = Dt = \frac{k_b T}{6\pi\eta r} t \qquad \text{Equation 4.3}$$

Where $\overline{< x,y >}^2$ is the mean square displacement, D is translation diffusion coefficient of the particle, t is time, k_b is Boltzmann's constant, T is temperature, η is dynamic viscosity of the solution and r is the hydrodynamic radius of the particle.

4.3 Dynamic Light Scattering

Dynamic Light Scattering (DLS) is another light scattering technique that can be used to determine nanoparticle size, and follows a similar principle of operation to NTA, with the exception that rather than tracking scattered light from individual particles, the scattered light from a bulk sample is analysed. A sample is irradiated with a monochromatic, coherent light source which is subsequently scattered by the particles in solution (Figure 4.4a). Due to the Brownian motion of the particles, the scattered light intensity fluctuates and analysis using an autocorrelation function can be applied to determine particle size. For example, comparing intensity at an initial time, I(t), with that a short time later, I(t + δt), the signals would be very similar and as such have strong correlation. If intensity at a much later time, T, is considered,

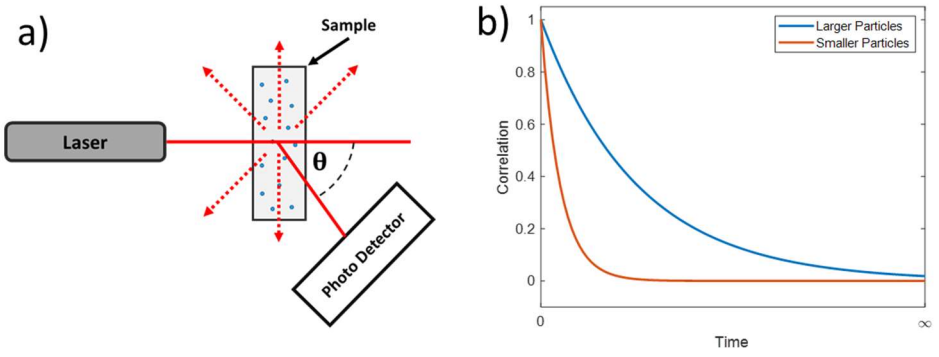

Figure 4.4 - Schematic showing the principle of Dynamic Light Scattering. a) Scattered light from an illuminated sample is collected using a photo detector. This is then followed by processing using an auto-correlator. b) Example of auto-correlation functions of intensity data from dynamic light scattering (DLS). The plot shows example decays of larger and smaller particles which have differing decay constants, τ.

I(T), there would be very little correlation with I(t), due to the random Brownian motion of the particles. The rate at which the correlation decays is related to particle size. For example, smaller particles will decorrelate in a shorter time compared to larger particles (Figure 4.4b).

In the simplest case of a monodisperse sample, this correlation follows a single exponential decay which can be related to the diffusion coefficient of the particles (Equation 4.4).

$$C = e^{-2Dq^2\tau} \qquad \text{Equation 4.4}$$

where D is the diffusion coefficient of the particles, q is scattering vector and τ is the decay rate. $q = \frac{4\pi n}{\lambda}\sin\frac{\theta}{2}$ where n is refractive index of the medium, λ is incident light wavelength and θ is the scattering angle.

From this, the hydrodynamic radius of the suspended particles can be determined using Equation 4.3.

Throughout this thesis, DLS measurements were performed using a Zetasizer Nano ZS (Malvern Panalytical, UK) equipped with a 633 nm He-Ne laser and scattered light measured at a backscatter angle of 173 °, using cuvettes with a path length of 10 mm. Measurement conditions were optimised automatically by the system and three measurements performed on each sample allowing for calculation of mean and standard error for distributions. Additionally, a polydispersity index (PDI) is calculated for each measurement providing a measure of sample monodispersity in addition to reliability of the measurement, determined by cumulants analysis of the correlation function.

Populations are displayed either as an intensity, number, or volume weighted distribution where appropriate. An intensity-weighted distribution is the raw data provided from the instrument. However, due to the relationship between particle size and scattering cross-section described by Rayleigh and Mie theory (Section 3.8), an intensity-based distribution is inherently biased towards larger particles. For example, a 100 nm sphere will scatter 10^6 times more than a 10 nm sphere. If the optical properties of the particle are known (refractive index and absorption), then a number-weighted or volume-weighted distribution can be calculated. In general, for a distribution with an average particle size d, d(intensity) > d(volume) > d(number). An example of this is shown in Figure 4.5. Due to this, in a mixed sample containing very large and very small particles (e.g. 1000 nm vs 10 nm), the scattered light from the larger particles can overrule that from the small particles, resulting in an inaccurate distribution.

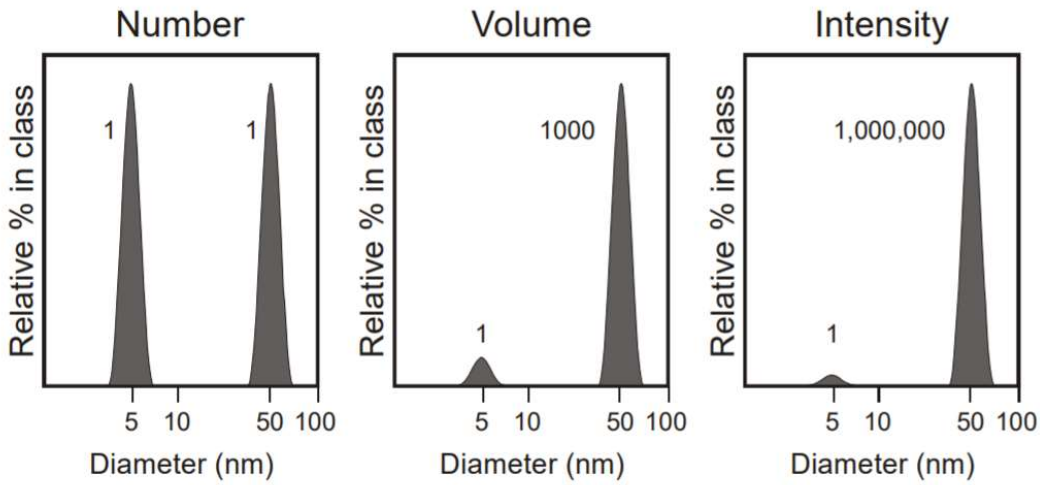

Figure 4.5 - Comparison between a number, volume and intensity weighted distribution generated from Dynamic Light Scattering for an equal number of 5 and 50 nm particles. This demonstrates the different bias associated with each distribution. Adapted from the Zetasizer Nano User Manual [254].

4.4 Resonant Mass Measurement

Resonant mass measurement (RMM) is a single particle measurement technique that can measure size, concentration and additionally determine whether the particle is negatively buoyant (sinks) or positively buoyant (floats) in the suspension medium. As such, RMM can separate population distributions between bubbles (positively buoyant) and non-bubbles (negatively buoyant). RMM works on the principle of buoyant mass. M_B, and the effective change in mass of a self-oscillating cantilever. The self-oscillating cantilever contains a microfluidic channel in which sample can flow through and flow rates are adjusted accordingly as such that in an optimal scenario a single particle is present on the cantilever. If this particle has a different density to that of the suspension medium, the mass of the cantilever changes, subsequently changing the frequency of oscillation, Δf. The oscillating frequency of the cantilever is recorded using a light source incident onto the tip of the cantilever and reflected light collected by a photodiode. Depending on whether the particle has a density higher or lower than the medium, i.e. sinks or floats, the frequency will decrease or increase respectively. The magnitude and direction of the frequency shift can be used to determine particle size (Equation 4.5 - 4.7). Whilst this technique requires particle density to be known, particle density only has a small effect on analysed size ($D \propto \rho^{-1/3}$).

$$M_B = \frac{\Delta f}{S} \qquad \text{Equation 4.5}$$

$$M = M_B\left(1 - \frac{\rho_f}{\rho_p}\right)^{-1} \qquad \text{Equation 4.6}$$

$$D = \left(\frac{6M}{\pi\rho_p}\right)^{\frac{1}{3}} \qquad \text{Equation 4.7}$$

where f is frequency, S is calibration constant, M is 'dry mass', ρ_f and ρ_p is fluid and particle density respectively and D is diameter.

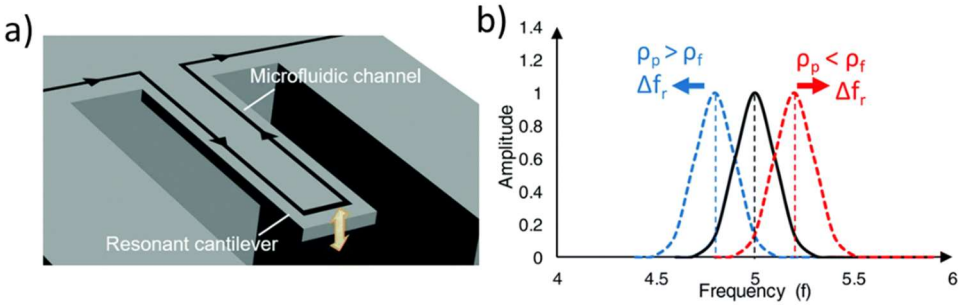

Figure 4.6 -– Schematic showing the principle of operation of resonant mass measurement (RMM). As a particle of density differing to that of the suspension fluid flows across the self-resonating cantilever, the resonant frequency changes producing a frequency shift depending on whether particle density, ρ_p, is greater or less than fluid density, ρ_f. Adapted from [59] under a CC BY-NC 3.0 licence. Copyright Royal Society of Chemistry 2019.

The RMM instrument used throughout this thesis (Archimedes, Malvern Panalytical, UK) was provided by Malvern Analytical on an initial trial basis.

4.5 Ultrasound Imaging

US imaging works on the principle of pulse-echo, in which reflections from an incident US pulse are used to form an image. All US imaging in this thesis was B-Mode (brightness mode) in which the brightness of the image is directly linked to the intensity of the received pulse. The intensity of the received pulse is determined by the change in acoustic impedance between two materials (Equation 4.8), I_r and I_i are the intensities of the reflected and incident beam and z_1 and z_2 are the acoustic impedances of the two materials.

$$\frac{I_r}{I_i} = \left(\frac{z_2 - z_1}{z_1 + z_2}\right)^2 \qquad \text{Equation 4.8}$$

The time of flight (i.e. time between pulse and echo) can be used to determine the position of material or tissue boundaries (i.e. where reflections occur) if the speed of sound is known. For soft tissue this is relatively constant (~ 1540 m/s). Transducers are typically composed of a

piezoelectric plate, a matching layer and a backing layer. The piezoelectric plate is commonly constructed out of lead zirconate titanate (PZT). Application of a positive or negative voltage to the PZT layer causes it to stretch or compress, producing ultrasonic waves. When receiving acoustic emissions, the reflected US causes the PZT to contract/stretch which is converted into a corresponding voltage. Due to the impedance mismatch at the PZT-tissue boundary, only about 20 % of the intensity would be transmitted.[177] The presence of a matching layer, of thickness of a quarter wavelength, can increase transmission by up to 100 % due to constructive interference of reflected and transmitted waves. Additionally, the matching layer

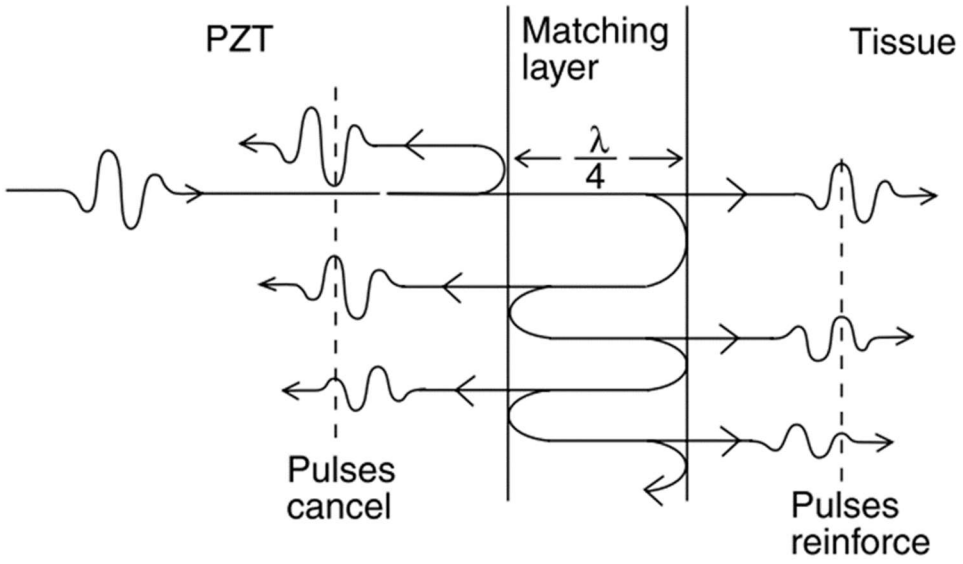

Figure 4.7 – Schematic showing how the matching layer, of one-quarter wavelength (λ/4) in thickness. This allows for increased transmission into tissue and reduced reflection of acoustic waves back into the PZT by constructive and destructive interference respectively.

also prevents reflections heading back into the PZT due to destructive interference (Figure 4.7). The backing layer, composed of a material with high acoustic attenuation, helps to damp any reflected wave and prevent ringing in the PZT.

A full B-mode image consists of a cross-sectional representation of the imaged area. To produce this 2D image, a multi-element transducer is required in which each element generates a scan line to form the total image. In this thesis, a clinically approved US imaging system (3-8 MHz, V-Scan, GE Healthcare, US) was used to image NBs in an acoustic phantom, using a linear array probe.

4.6 Optical Spectroscopy

4.6.1 Fluorescence Excitation and Emission Spectroscopy

Steady state fluorescence spectroscopy is a technique that determines the intensity of fluorescent emissions from a sample. Excitation at a fixed wavelength, and measurement of

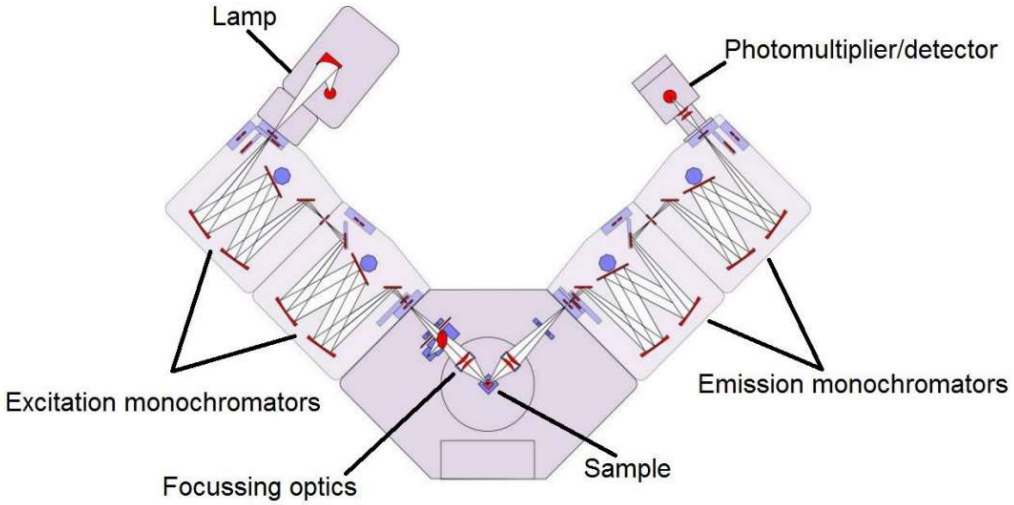

Figure 4.8 - Schematic of the Edinburgh Instruments FLS 980 spectrometer used in this thesis. The location of the illuminating light source (Xenon arc lamp), monochromators, sample chamber and PMT detector are shown. Reused from [255] *under a CC BY-NC-SA 2.0 licence.*

the fluorescence emissions over a range of wavelengths is known as fluorescence emission spectroscopy. Sample fluorescence emissions can also be measured at a fixed wavelength, whilst varying the excitation wavelength, in what is known as fluorescence excitation spectroscopy. The combination of both excitation and emission spectra allows for characterisation of the fluorescent properties of a fluorophore or sample. In this thesis, fluorescence spectroscopy was used to quantify the amount of drug release from a sample after various treatment conditions (Section 5.6). A fluorescence spectrometer consists of multiple components, to allow control over both the excitation and emission wavelengths, as well as their bandwidth. A schematic of the fluorescence spectrometer used throughout this thesis (FLS 980, Edinburgh Instruments, UK) is shown in Figure 4.8. A white lamp (450 W Xenon arc lamp), providing a large range of wavelengths, passes through adjustable excitation monochromators to determine the excitation wavelength, as well as the bandwidth of this excitation. The monochromatic light is then directed towards the sample chamber, containing the sample in a cuvette. Fluorescence emission from the sample is collected at a 90 ° angle, where the emission beam passes through an additional set of monochromators to control the collected emission wavelengths, prior to reaching the detector (R928, Hamamatsu, JA). The system was also equipped with a thermoelectrically cooled cuvette holder with magnetic stirring abilities (TC 1 Temperature Controller, Quantum Northwest, US).

In this thesis a well-plate based fluorescence spectrometer (SpectraMax M2e, Molecular Devices, US) was also used to measure fluorescence emission from multiple samples. Whilst typically less accurate than a cuvette-based spectrometer, measurements in a 96-well plate allow for rapid measurement of samples with different treatment conditions as well as over multiple repeats.

4.6.2 UV-Vis-NIR

Ultraviolet/Visible/Near-Infrared (UV-Vis-NIR) absorption spectroscopy is a technique used to measure how a given sample absorbs light as a function of wavelength. This can be used to determine the concentration of an absorbing sample in solution, based on a calibration curve, that is described by the Beer-Lambert law (Equation 4.9), in which sample absorbance is linearly related to concentration.

The spectrometer throughout this thesis (Cary Series UV-Vis-NIR, Agilent Technologies, US) was equipped with a dual-beam functionality, in which a beam of light with controlled wavelength is split into two. One beam then passes through the sample of interest, whilst the other through a control (or blank) sample containing just the dispersant. For cuvettes with known path length, the absorbance due to the solute can then be determined by comparing the difference in intensity of detected light. It is important to note that the Beer-Lambert law only holds for low sample concentrations, in which scattering events (as opposed to radiative interactions) have negligible effect on beam intensity.

Similar to fluorescence spectroscopy measurements, absorbance measurements were also performed using a well-plate based spectrometer.

$$A = \varepsilon c l \qquad \text{Equation 4.9}$$

where A is absorbance, ε is the molar extinction coefficient ($M^{-1}cm^{-1}$), c is concentration (M), and l is path length (cm).

4.7 Flow Cytometry

Flow cytometry is a technique in which single cells, focused by a sheath fluid flow, are illuminated by a laser light source and the forward scatter, side scatter and fluorescence emission are measured. Physical properties of the cells can be determined by observing the forward (size) and side scatter (granularity) of the incident light. Cells can be stained with fluorescent dyes (e.g., live/dead staining), conjugated with antibodies (e.g., VEGFR2-FITC), or transfected with fluorescent proteins (Green Fluorescent Protein), and flow cytometry used to quantify fluorescence emissions. In this thesis, a flow cytometer (CytoFlex S, Beckman Coulter, US) was used to quantify fluorescence from a FITC live stain and 7-AAD, a membrane impermeable DNA stain, to determine the occurrence of sonoporation.

5 Experimental Procedures 1

5.1 Microfluidic Production of Nano- and Microbubbles

Nano- and microbubbles were prepared from a mixture of DPPC (1,2-dipalmitoyl-sn-glycero-3-phosphocholine) and DPSE-PEG2000 (1,2-distearoyl-sn-glycero-3-phosphoethanolamine-N-[methoxy(polyethylene glycol)-2000]) in a 95:5 molar ratio and a total lipid concentration of 2 mg/mL (Avanti Polar Lipids, AL, US). Lipids were dissolved in a 1:1 mixture of chloroform and methanol and dried under nitrogen to remove the solvent and subsequently resuspended in PBS solution containing 1 % (v/v) glycerol. The lipid solution was then combined with C_4F_{10} (perfluorobutane, PFB) gas in a multiplexed micro-spray microfluidic device for bubble production as described in Peyman et al.[46,204] using the Horizon system. This was developed in house in Leeds, combining the microfluidics, flow control and brightfield microscopy into one system [205]. Microfluidic chips were produced externally (Epigem, UK) out of PMMA (Poly(methyl methacrylate) and SU-8 photoresist using photolithography. Liquid and gas were interfaced to the microfluidic chip using a custom made PMMA manifold containing PTFE (Polytetrafluoroethylene) tubing, which through the use of a clamping mechanism created a gas tight seal between the manifold and the chip (Figure 5.1). Both liquid and gas flows were controlled using pressure-pumps (Mitos P-Pump, Dolomite, US).

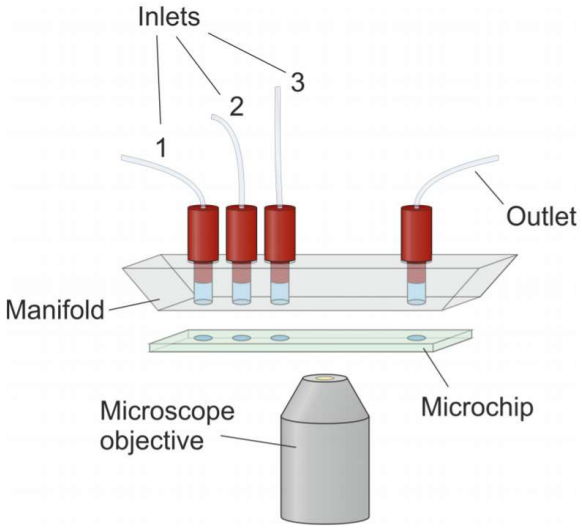

Figure 5.1 - Schematic showing the microfluidic set up used for micro- and nanobubble production using the Horizon system. Liquid and gas inlets fit into a custom-made manifold which is then clamped to the microchip to create a gas tight seal. The system is situated above a microscope objective to allow observation of the fluidics during use. Inlets 1 and 3 were used for liquid and gas phases respectively, where Inlet 2 is used for alternative microfluidic chips not used in this body of work. Reused from [256] *under a CC BY-NC-SA 2.0 UK licence.*

Microfluidic devices were mounted on a movable x-y stage situated above an inverted brightfield microscope, allowing observation of the fluidics during use.

Microfluidic device geometry is shown in Figure 5.2 containing 4 separate, or multiplexed, microbubble production devices to allow for rapid microbubble production. The chip contains two inlets, one for each liquid and gas flows, and an outlet for sample collection. Microbubble production devices consisted of modified flow focusing geometry with liquid channel width of 50 um and gas channel width of 30 um, fabricated to an initial height of 25 um and an additional 25 um expansion situated after the nozzle, allowing production of the desired microspray regime [46].

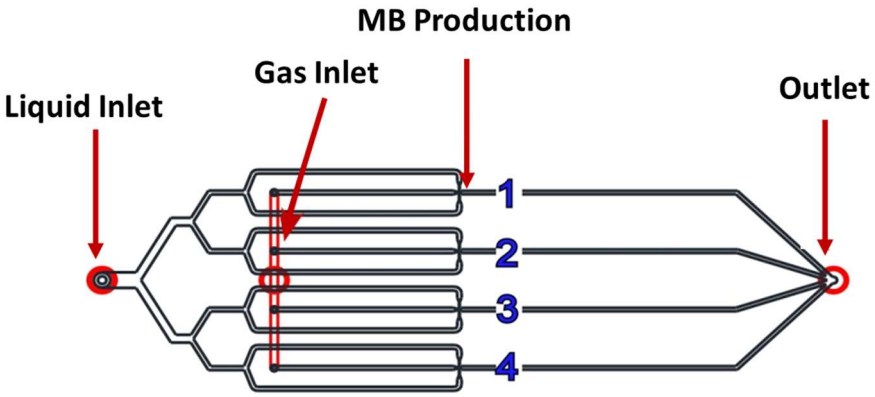

Figure 5.2 - Geometry of microfluidic device used for microspray microbubble production. The device contains 4 separate microbubble production devices. Both liquid and gas inlets are split into 4 separate channels to allow multiplexing of the device and sample collected from a single outlet.

5.1.1 Nanobubble Isolation

NBs were passively isolated from MBs via flotation due intrinsic MB buoyancy. A spherical bubble in a medium has an ascension velocity, described by Equation 3.24. For a PFB bubble with radius of 1 μm it would take 47 minutes to travel 1 cm. For a bubble in the same medium with diameter of 150 nm it would take 840 minutes to travel the same distance and as such can be regarded as neutrally buoyant. After 1 hour, a syringe and fine needle was used to remove NB sample from the bottom of the vial and subsequently filtered through 800 nm PTFE membrane to remove any large bubbles.

5.2 Nanobubble size and concentration determination

5.2.1 Nanoparticle Tracking Analysis (NTA)

Single particle tracking was used to analyse NB populations using NanoSight Nanoparticle Tracking Analysis (NanoSight NS300, Malvern Panalytical, UK). Samples were illuminated with a 488 nm laser and individual particles tracked using NTA 3.3 software. Samples were diluted 1:1000 in PBS prior to measurement and measurements repeated in triplicate.

Measurements were performed under flow using a PC controlled syringe pump at infusion rates of between 20 – 40 a.u., as defined by the NTA 3.3 software.

5.2.2 Resonant Mass Measurement (RMM)

Resonant mass measurement (Archimedes, Malvern Panalytical, UK) was used to demonstrate and analyse populations of positively buoyant (bubbles) and negatively buoyant particles in NB solutions. Archimedes was equipped with a MicroH sensor capable of measurement of particle diameters of between 150 – 5000 nm and pre-calibrated with 1 μm polystyrene beads (ThermoScientific Microsphere Size Standards 4010A). Samples were diluted 1:500 in PBS prior to measurements. During the measurement, NB sample was loaded initially for 120 seconds and analysed at pressures of 3, 2 and 3 psi for sample, reference, and experiment values. The limit of detection was set to 25 mHz to provide consistency for all measurements. Particle densities were set to 0.0112 and 1.3 g/mL for positively buoyant and negatively buoyant particles respectively, corresponding to the density of PFB gas and lipid vesicles [59].

5.3 Liposome and Nested-Nanobubble Production

A combination of DSPC, Cholesterol and DSPE-PEG2000 were dried under Nitrogen in round bottom flasks in a 63:32:5 molar ratio at a total lipid concentration of 15 mg/mL. The lipid film was resuspended in either PBS buffer for liposome (LS) production or with NBs at stock concentration for Nested-NB production and rehydrated via stirring for 1 hour. For calcein loading, solution pH was adjusted using 10 M NaOH to pH 10.5 and calcein added to a final concentration of 100 mM prior to rehydration. Rehydrated lipid solution was homogenized via extrusion by passing through a 400 nm PTFE membrane. Free calcein and NBs were removed via centrifugation at 17,000 g for 20 minutes, washed with PBS and centrifugation and washing repeated (Figure 5.3).

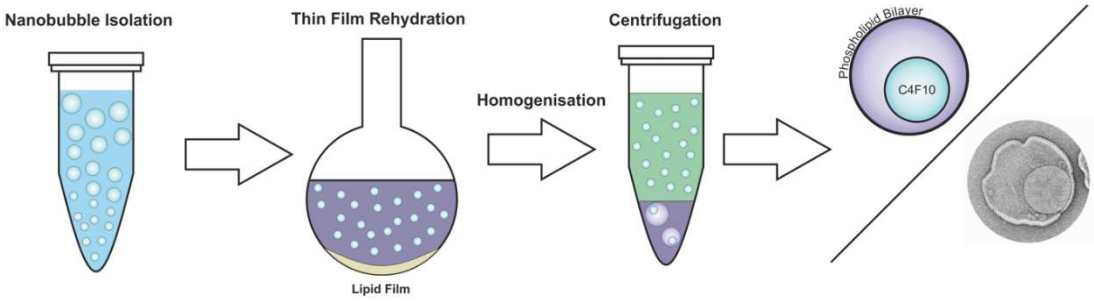

Figure 5.3 - Schematic showing preparation of Nested-NBs. NBs are isolated from a mixed population via flotation. A NB solution containing 100 mM calcein is then used to rehydrate a thin film lipid film. The solution is homogenised via extrusion through a 400 nm membrane, during which NBs and calcein are encapsulated within a liposomal shell. Un-encapsulated calcein and NBs are then removed via centrifugation, yielding the final Nested-NB product.

5.4 Transmission Electron Microscopy

For Transmission Electron Microscopy (TEM), samples were prepared in a phosphate free buffer and 5 uL of sample pipetted onto glow discharged carbon grids. After 30 seconds incubation, sample was washed with buffer and 5 uL of 1 % uranyl acetate added for 30 seconds, then removed and left to air dry. Images were taken at a range of magnifications ranging from 11,000 to 46,000 x using a FEI T12 transmission electron microscope (FEI Tecnai T12, USA). Images were analysed manually using ImageJ (NIH, US) to determine particle diameter.

5.5 Optical Characterisation of Calcein

5.5.1 UV-Vis-NIR Spectroscopy

UV-Vis-NIR measurements of calcein were performed such to determine the molar extinction of calcein, using both cuvette and well-plate based methods. For the cuvette (10 mm path length) based system, absorbance was measured for wavelengths of 200 - 800 nm for calcein concentrations of 0.001 – 10 mM. Well-plate based measurements were performed using a multi-mode well plate based reader, capable of both fluorescence and absorbance measurements (SpectraMax M2E, Molecular Devices, US). Each well in a clear 96 well plate contained 200 uL and peak absorbance was measured at 460 nm.

5.5.2 Fluorescence Spectroscopy

Fluorescence excitation and emission spectra of calcein were determined using a cuvette-based spectrometer (FLS 980, Edinburgh Instruments, UK). Cuvettes were made of quartz and had a path length of 10 mm. For emission spectra, calcein was excited off-peak at 460 nm and emission intensity measured for wavelengths of 470 – 700 nm. For excitation spectra, emission was fixed a 515 nm and excitation wavelength varied between 400 and 600 nm. These spectra were determined with a dwell time of 0.2 s and slit width of 1.0 nm. Calcein fluorescence was also measured using the multi-mode well plate reader, with excitation wavelengths of 460 nm and 490 nm, and emission of 515 nm, performed in opaque well plates to minimize interference between wells.

5.6 Nested-Nanobubble Drug Release and Stability

5.6.1 Thermal Stability

To determine the drug-loading stability of Nested-NBs at various temperatures, fluorescence measurements were conducted using a thermoelectrically cooled cuvette-holder, maintaining the sample at various temperatures. Due to the high concentration of encapsulated calcein, fluorescence was initially quenched. However, when released from the liposome into the bulk

medium, calcein concentration decreases and fluorescence subsequently unquenches. During measurements, the sample was gently stirred ~ 300 RPM using a magnetic stirrer. Samples were diluted 1:25 in PBS and fluorescence emission intensity was recorded in 5-minute intervals for a total duration of 30 min (21 ° C and 37 ° C) and 180 min (4 ° C). To further investigate the thermal stability, a temperature ramp was performed, with an initial temperature of 22 ° C, and fluorescence emission of Nested-NBs was measured in 5 ° C intervals up to 62 ° C, with the sample remaining at each temperature for 2 minutes. Total fluorescence emission for all experiments was determined by integration of the emission spectra. To determine the percentage of release/leakage from samples, fluorescence was measured for non-treated samples (negative control), treated samples and samples lysed with 0.1 % Triton-X (positive control) to calculate the percentage of calcein released from the sample (Equation 5.1). Percentage release was calculated by Equation 5.1, where $FL_{treated}$, $FL_{+control}$ and $FL_{-control}$ are fluorescence intensities for treated, positive and negative control samples respectively.

$$\%\ \text{Release} = 100\ \text{x}\ (\text{FL}_{\text{HIFU}} - \text{FL}_{-\ \text{control}})/(\text{FL}_{+\text{control}} - \text{FL}_{-\text{control}}) \quad \text{Equation 5.1}$$

5.6.2 Quantifying HIFU Triggered Release

Drug release after HIFU exposure was quantified using the multi-mode well-plate based reader. NB and liposome samples were diluted 1:25 in PBS, and fluorescence measured at excitation and emission wavelengths of 460 and 515 nm respectively and percentage release determined using Equation 5.1.

5.7 Ultrasound Imaging

B-mode diagnostic US images of NBs and Nested-NB populations were produced using a 3-8 MHz linear array probe (V-Scan, GE Healthcare, US). Samples were imaged in a wall-less agar flow phantom, produced by mixing 3 % by mass agar and 8 % by mass glycerol with degassed water [206]. The mixture was heated in a microwave and manually stirred intermittently until a homogenous solution was produced. The mixture was poured into a 3D printed mould containing a 4 mm outer diameter tube and left to cool. The tube was removed after the agar had set and Luer lock fittings attached for sample loading. The mean grayscale intensity of B-mode images within the region of interest were calculated using MATLAB (Mathworks Inc, US).

5.8 High Intensity Focused Ultrasound (HIFU) and Passive Cavitation Detection (PCD)

A single element High Intensity Focused Ultrasound (HIFU) transducer was used for US mediated NB destruction. A 1.1 MHz centre frequency HIFU transducer (H-102, Sonic

Concepts, US) was used for all HIFU experiments. The transducer was connected to a +55 dB power amplifier (A300, E&I Ltd, US) via an impedance matching circuit. A computer-controlled function generator (33220A, Agilent, US) was used to provide sinusoidal burst cycles to the transducer. Free field pressure was measured using a membrane hydrophone (Precision Acoustic Ltd, Dorchester, UK) with a 400 μm sensitive element, calibrated by the National Physics Laboratory (Middlesex, UK) [188] All pressures stated are based from their free field calibrations with errors of ± 0.1 MPa. The HIFU transducer was coupled to the sample using a coupling cone containing degassed Milli-Q water. A TTL digital delay pulse generator (9524, Quantum Composers, MT, USA) was used to synchronize the HIFU pulse and data acquisition system. A broadband focused detection (Y-102, Sonic Concepts, WA, USA) was positioned in the central aperture of the HIFU transducer and co-aligned with its focal region. It was connected to a 5 MHz high pass filter (Allen Avionics, US) and a 40 dB pre-amplifier (Spectrum GmbH, Germany). A 14-bit data acquisition (DAQ) card (M4i.4420-x8, Spectrum GmbH, Germany) was used to record acoustic emissions. A desktop PC was used to control all hardware and post-processing using MATLAB. For each HIFU pulse, 163 μs of cavitation data was recorded and Fast Fourier Transformed into the frequency domain. Frequency data was comb filtered to remove harmonics, leaving only broadband emissions. [188] Additionally, the inverse comb filter was applied to remove broadband emissions, leaving only ultra-harmonic emissions. Data was recorded for 0.5 s either side of the 5 s HIFU exposure with initial values before HIFU used as a noise baseline. To maximise the magnitude of acoustic emissions, the concentration of Nested-NBs and Liposomes were maintained as high as possible whilst remaining constant between the two samples at 1.56×10^{11} particles/mL.

6 Development of Nested-Nanobubbles for Ultrasound Triggered Drug Release

Motivation

The effectiveness of chemotherapy treatment is determined by the total dose of drug delivered to the diseased tumour site, which in turn is limited by side effects associated with systemic delivery and the required dose. NBs in combination with US have been used to enhance intracellular delivery of therapeutics [82,110] and triggered release of chemotherapeutic agents [97,99,150,207]. However, there has been little focus on the combination of NBs and drug-loaded liposomes, of which the latter are already in clinical use, reducing the exposure of healthy tissue to drugs. This is somewhat puzzling as the attachment of drug-loaded liposomes to microbubbles (therapeutic MBs), is arguably the most prevalent method of MB functionalisation [46,205,208], with various examples of their *in vitro* and *in vivo* effectiveness [48,50] and are currently approved for Phase 2 clinical trials. However, one of the limitations of MB-based therapeutics is that they suffer from vascular confinement, which can limit drug penetration into the tumour. As such, minimizing the size of the drug delivery complex may improve drug distribution by taking advantage of the leaky vasculature and reduced lymphatic clearance associated with tumours [55,160].

In this chapter, Nested-Nanobubbles (Nested-NBs) are introduced as submicron drug delivery vehicles, consisting of an outer liposomal shell containing both the encapsulated drug payload and one or more NBs that can act as internal nuclei for an US-triggered release (Figure 6.1). The use of a liposomal shell provides a well-documented platform for loading and delivery of both hydrophilic and hydrophobic compounds and compared to traditional bubble-liposome conjugates, Nested-NBs maintain their nanoscale nature (< 300 nm), potentially promoting extravasation and retention.

The production and characterisation of microfluidically produced NBs, and their development into triggered drug delivery vehicles is described. NB populations were characterized via light scattering, electron microscopy, resonant mass measurement, and acoustic techniques. The development and formation of Nested-NBs via extrusion is then documented, and their hydrophilic drug loading capabilities quantified using self-quenched calcein, and fluorescence spectroscopy. Electron microscopy was used to assess successful NB encapsulation and high intensity focused ultrasound (HIFU) used to trigger NB destruction, and release of calcein. Acoustic monitoring via passive cavitation detection (PCD) in combination with thermal monitoring was used to observe interactions between NBs and US, and aid understanding of

the triggered release mechanism. Finally, acoustic radiation force in combination with light scattering was used to try to isolate Nested-NBs from non-acoustically active liposomes.

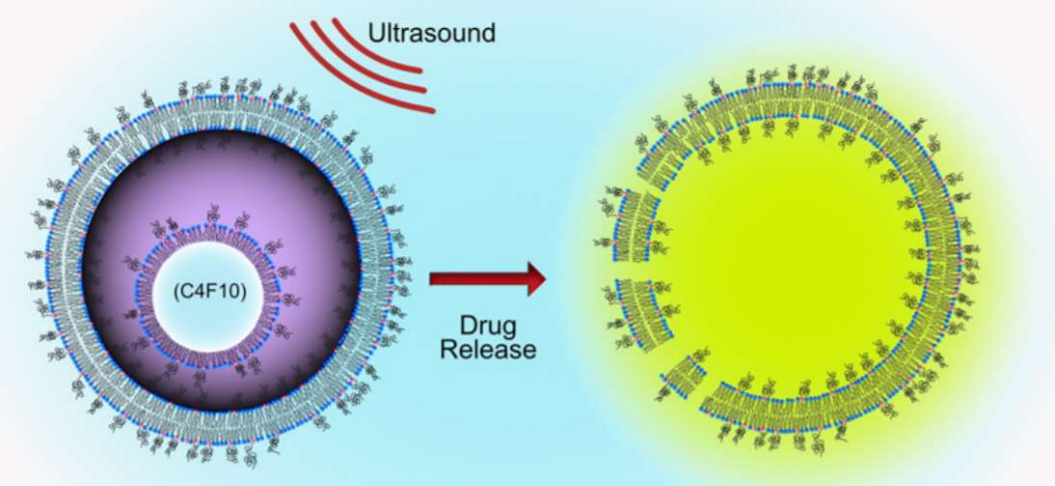

Figure 6.1 - Schematic representation of a Nested-Nanobubble, with a liposomal shell encapsulating a C_4F_{10} NB and self-quenched calcein, acting as a model drug. An external US stimulus is able to destroy the NB, subsequently rupturing the encapsulating liposome and triggering drug release.

6.1 Characterisation of Microfluidically Produced Nanobubbles

Initial NB production was based on previous work within our group described by Peyman et al. [46,204], in which a microfluidic platform (Horizon) was developed with the aim for point of care production of therapeutic functionalised micro- and nanobubbles [205]. Typical microfluidic production geometries such as flow focusing [209] and T-junction [210] allow for control over microbubble size (1 – 20 μm) and dispersity. However, resultant bubble concentrations typically range from 10^6-10^8 /mL. Furthermore, these techniques can be difficult to use in practice, requiring careful balancing of liquid and gas flow rate as well as complex experimental set ups. The Horizon system introduced a new microfluidic platform for micro- and NB production in one all-encompassing system allowing for control over liquid and gas flow rates and visualisation of production via optical microscopy. Horizon utilises the 'microspray' production regime, capable of producing microbubbles at concentrations up to 10^9 /mL with modal size of ~ 2 μm. The microspray geometry is similar to that of a flow focusing device, however the addition of a 3D vertical expansion situated after the production nozzle is predicted to facilitate a vaporisation-like break-up of the central gas jet, compared to the steady stream typically associated with flow focusing.

The microspray regime also concurrently produces nanoparticles of 100 - 300 nm in size, at a concentrations of ~ 10^{11} /mL, when characterised via Nanoparticle Tracking Analysis and electrical conductance methods (qNano) [56]. However, the exact physical properties of these particles are difficult to determine through standard nanoparticle characterisation methods.

Namely, are they liquid-core droplets, gas-core NBs, liposomes or a combination? Regardless, in this section these nanoparticles will be referred to as microspray NBs (MS-NBs). All MS-NBs in this chapter were fabricated with a lipid formulation of DPPC/DSPE-PEG2000 in a 95:5 molar ratio, shown to provide optimum microbubble stability due to the brush-like conformation of the PEG layer [11].

6.1.1 Dynamic Light Scattering

MS-NB populations were characterised using two different light scattering techniques: Dynamic Light Scattering (DLS) and Nanoparticle Tracking Analysis (NTA). Both techniques follow similar principles, measuring particle Brownian motion and hence particle size, using the Stokes-Einstein equation (Section 4.2, 4.3). However, DLS uses auto-correlation of scattered light from the bulk sample, whereas NTA measures the motion of individually tracked particles. Hence, whilst DLS can determine only size, NTA can also determine particle concentration. Comparing between both intensity-weighted and number-weighted distributions enables greater insight into the sample population, due to the non-linear relationship between particle size and scattering intensity (Section 3.8). Because of this,

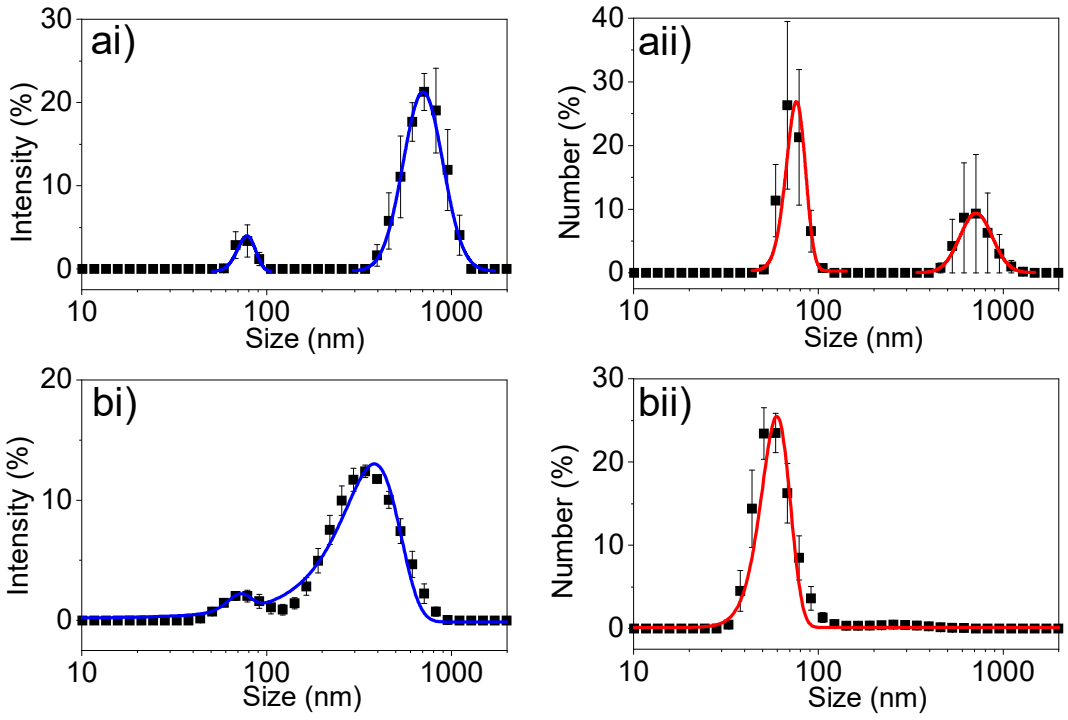

Figure 6.2 - Size distribution of MS-NBs measured via Dynamic Light Scattering. Populations (a) before and (b) after filtration through 800 nm membrane, for both (i) intensity-weighted and (ii) number-weighted distributions.

intensity-based distributions are biased towards larger particles, especially those with a bi-modal population.

This is demonstrated in Figure 6.2a, where NBs isolated from a MB population were measured via DLS, prior to filtration to remove larger bubbles. Un-filtered MS-NBs demonstrated a bi-modal distribution with a primary intensity peak at 719 nm and a secondary intensity peak at 79 nm. Conversion of this to a number-based distribution, shows peaks at similar positions (729 and 76 nm respectively), however with the intensity of the peaks switched (i.e. 76 nm peak has the highest intensity). This suggests that un-filtered MS-NBs contain primarily particles of ~ 100 nm in size, with a smaller population of larger particles that are the primary contributors to scattering. This also highlights that there is a dual population of particles present in our MS-NB samples, likely to be a combination of aqueous core liposomes and gas-core bubbles. Filtration of this sample through an 800 nm filter (Figure 6.2bi) removes particles greater than the filter size as well as a significant decrease in size to ~ 400 nm as larger particles are removed during the filtration process. Comparing this to the number-based distribution (Figure 6.2bii), shows that the sample is now primarily composed of ~ 100 nm particles, and a small population of larger particles (~400 nm) as shown by the intensity distribution.

6.1.2 Nanoparticle Tracking Analysis

Figure 6.3 shows MS-NB populations characterised via NTA, after isolation and filtration. Over 5 separate sample preparations, the average particle concentration was (5.79 ± 0.66) x 10^{11}/mL, with a modal size of 106 ± 4 nm, in agreement with Peyman et al. [56]. Few particles below the modal values were detected, suggesting the limit of detection (LOD) of the NTA

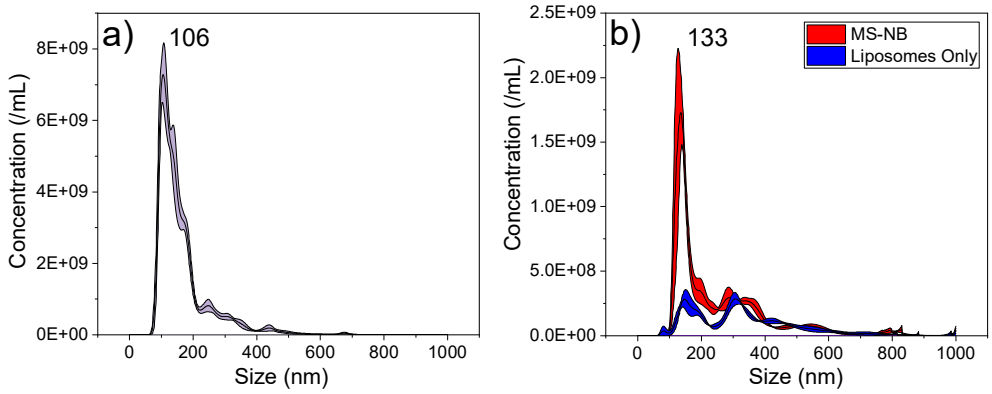

Figure 6.3 - Size and concentration distribution of MS-NBs characterised via NTA. a) Over 5 separate sample preparations the average the average particle concentration was (5.79 ± 0.66) x 10^{11}/mL, with a modal size of 106 ± 4 nm. b) Comparison of NTA distributions between MS-NBs and their liposome pre-cursor solution, showing an increase in total particle concentration from (7.0 ± 0.6) x 10^{10} /mL to (1.5 ± 0.3) x 10^{11} /mL, as well as an increased proportion of particles ~ 100 nm in size.

system has been reached. Comparison between MS-NBs and their liposome pre-cursor solution shows an increase concentration from (7.0 ± 0.6) x 10^{10} /mL to (1.5 ± 0.3) x 10^{11} /mL, suggesting formation of new nanoparticles through the microspray regime, with modal size of 133 nm (Figure 6.3b). The change in population distribution also suggests that particles ~ 100 nm in diameter are produced during the MS regime, whilst those > 100 nm are a sub-population of lipid vesicles, present in the pre-cursor solution. These results also mimic those seen via DLS (Figure 6.2b).

6.1.3 Transmission Electron Microscopy

MS-NBs were also imaged using TEM, and their size distribution analysed over a total of 252 particles across 31 images. Particles had a spherical morphology, and the population demonstrated a log-normal distribution with an average size of 120 ± 48 nm (Figure 6.4a) similar to that as measured by NTA and DLS. A sub-population of particles < 100 nm was also measured, previously undetected by NTA. As this population is discrete from the particles produced during the microspray regime, it is likely these are lipid vesicles as opposed to NBs or particles produced during the microspray process.

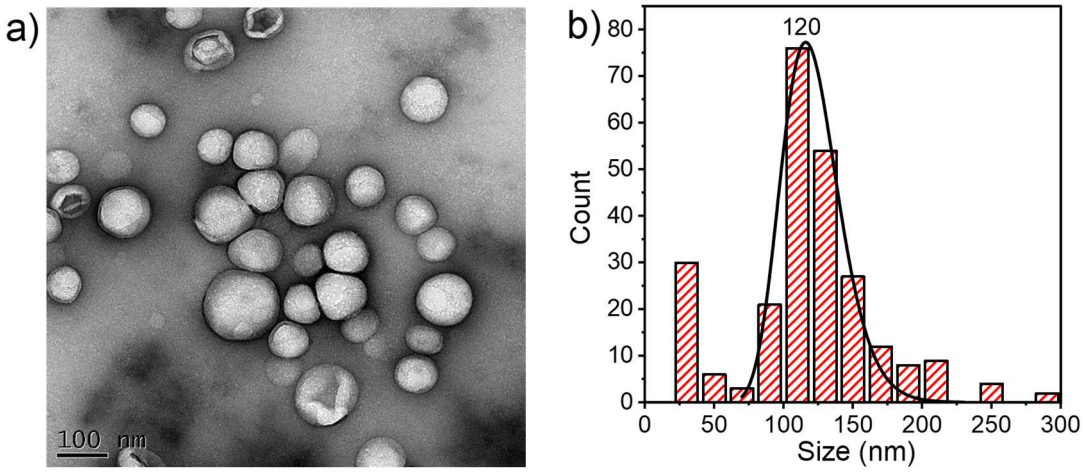

Figure 6.4 - Characterisation of MS-NBs via TEM showing (a) their spherical morphology and (b) particle size distribution.

6.1.4 Resonant Mass Measurement

However, a limiting factor with TEM, NTA and DLS is that they fail to distinguish between particles with different physical properties (i.e. liposomes, NBs and droplets). Due to the relationship between particle size and Laplace pressure, smaller NBs may condense into liquid core C_4F_{10} droplets, and hence data shown in Figure 6.2 - Figure 6.4 cannot be used exclusively to confirm the presence of gas-core NBs. and alternative techniques are required.

Resonant Mass Measurement (RMM) is a technique that allows buoyant (e.g., NBs) and non-buoyant (e.g., liposomes, droplets) particles to be distinguished, through the use of a self-resonating cantilever containing a microfluidic channel. When a particle of differing density

to that of the medium passes through the channel, the cantilever resonance frequency shifts proportional to particle mass, with the direction dependent on whether the particle is negatively or positively buoyant.

RMM was used to characterise MS-NBs (Figure 6.5) and shows that both (a) positively and (b) negatively buoyant populations exist in the MS-NB sample. Averaged over 3 samples, concentrations were found to be (1.17 ± 0.68) x 10^9/mL and (3.54 ± 1.20) x 10^9/mL with modal sizes of 212 ± 12 nm and 321 ± 32 nm for the positively and negatively buoyant particles, respectively. The negatively buoyant population likely consists of a combination of lipid vesicles that were not converted into bubbles during production, as well as potentially containing PFB droplets, which due to their small size have condensed from a gas into liquid PFB droplets. It should be noted that the modal size here may be erroneous and is likely dictated by the LOD of the RMM system, which was higher than that of the modal particle size determined via DLS, NTA and TEM thus excluding a large proportion of the population. The LOD of the RMM system is determined by the change in density between medium and particle. Here, the LOD is around 200 nm, below which particles smaller than this cannot be discriminated from background noise, and thus RMM fails to determine the nature of the particles below this, which make up the largest contribution to the NTA data circa 100 nm. This is reflected in the decreased total particle concentration recorded by RMM (~5x10^9/mL) compared to NTA (~6 x 10^{11}/mL). Additionally, NTA suggests the majority (~95 %) of the population consist of particles produced during the microspray process whilst for RMM only this value is only ~ 25 %.

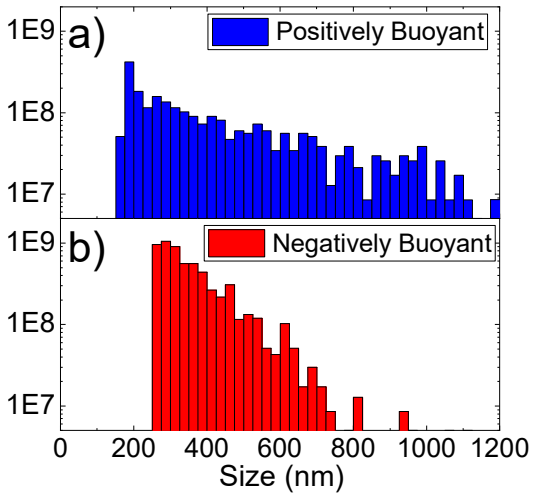

Figure 6.5 - Resonant Mass Measurement characterisation of MS-NBs. a) Positively buoyant and b) negatively buoyant populations with concentration of (1.17 ± 0.68) × 10^9/mL and (3.54 ± 1.20) × 10^9/mL respectively.

Notwithstanding, RMM is still useful for confirming the presence of submicron bubbles, as opposed to just droplets or liposomes, present in MS-NBs. It should be noted that a MicroH

sensor was used in this study, with a LOD of ~ 200 nm. Sensors with reduced cantilever dimensions, and hence higher sensitivity (NanoH), are available, and have previously demonstrated the existence of C_3F_8 cored bubbles approximately 100 nm in size [59]. However, the bubbles in our study are produced using a higher molecular weight gas (C_4F_{10}) and hence have a higher probability of condensing into liquid droplets. In direct communication with the manufacturer, Malvern Panalytical, a NanoH sensor was trialled in this study, however the system and results proved unreliable due to blockages. Regardless, RMM has demonstrated the existence of nanoscale buoyant particles (i.e. bubbles) produced microfluidically via the microspray regime.

6.2 Acoustic Behaviour of MS-NBs

Previously, MS-NBs have been shown to increase US imaging contrast at frequencies ≥ 15 MHz, and as such outside the clinically useful range. Firstly, it was shown that MS-NBs had increased acoustic response compared to liposomes, and a frequency sweep predicted the resonance frequency of MS-NBs to be ~ 55 MHz. Secondly, their ability to enhance contrast *in vivo* was shown with a pre-clinical Vevo 770 system using a 40 MHz centre frequency transducer and harmonic imaging modality [204]. In this section, the diagnostic capabilities of MS-NBs using a clinically approved B-mode US imaging system were investigated. NBs destruction was then triggered using high intensity focused US (HIFU), to further investigate their use as triggered drug delivery agents.

6.2.1 Diagnostic Ultrasound

MS-NBs were imaged in an agar flow phantom using a 3-8 MHz linear array probe, as part of a GE V-Scan imaging system with a mechanical index of 0.8. The flow phantom used here consists purely of agar, and hence shows minimal acoustic scattering and attenuation. B-Mode images shows the circular cross section of the phantom. Mean grayscale intensity (MGI) of a region of interest (ROI) in the B-mode image was measured for MS-NBs at total particle concentrations ranging from $\sim 10^9$ to 10^{11} NBs/mL, determined via NTA. A representative image of MS-NBs in the phantom is shown in Figure 6.6ai, showing contrast enhancement in the ROI compared to a PBS control containing no NBs. A linear increase in MGI with increasing concentration was observed (Figure 6.6aii). This trend was typically expected up to a critical NB concentration, after which a decrease in contrast may be observed due to increased attenuation as the void fraction increases [59]. As this was not seen with MS-NBs at their yield concentration, they may have potential benefits for dual therapeutic and diagnostic use, where higher NB concentration may be required.

It is also notable that the MI used for this experiment was larger than that typically used for micron-scale UCAs (MI<0.4) [175,176], as greater than this typically induces MB destruction. However, the observed stability of NBs may be due to being driven off resonance and hence inducing smaller volumetric oscillations, reducing the rate of gas dissolution. The increased driving pressures may also offset the effects of off-resonance excitation, consistent with work by Pellow et al. [137] where NBs exhibited fundamental and harmonic emissions at clinical frequencies (2.5 and 8 MHz), but requiring an increased pressure threshold of ~ 500 kPa compared to MBs (< 100 kPa). Further, a study by Sojahrood et al. [138] stipulates that at higher driving pressures, buckling of the NB lipid shell induces a decrease in surface tension. This would then subsequently reduce NB resonance frequency, potentially explain why NBs have high contrast at driving frequencies an order of magnitude lower than their predicted resonance. Whilst comparisons can be made between results, the nature of the V-Scan imaging system limits control and knowledge of the precise US parameters used for imaging and any further conclusions being drawn.

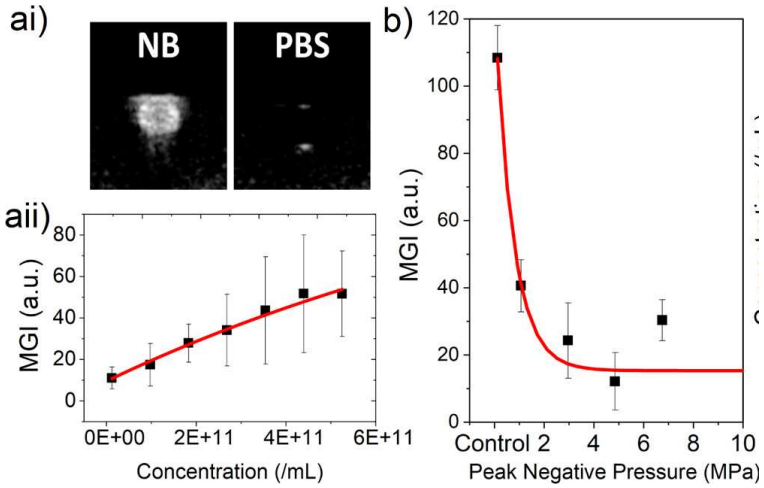

Figure 6.6 - Characterisation of NBs using clinically relevant B-mode imaging. a) Demonstrating their diagnostic capabilities in a flow phantom showing (ai) contrast enhancement compared to a PBS control and (aii) the relationship between particle concentration and mean grayscale intensity (MGI). b) MGI of MS-NBs after application of high intensity focused ultrasound (HIFU) across a range of peak negative pressures, demonstrating the ability to destroy MS-NBs with an acoustic trigger. All experiments were repeated in triplicate.

6.2.2 HIFU-mediated Nanobubble Destruction

MS-NBs were then treated with HIFU aiming towards NB destruction necessary for triggered drug release from Nested-NBs. The mean grayscale intensity (MGI) of MS-NBs was measured prior and post HIFU exposure at peak negative pressures (PNPs) ranging from 1.06 – 6.75 MPa. MGI decreased exponentially with increasing pressure reaching a minimum MGI after exposure at 4.83 MPa (Figure 6.6b). At PNP = 6.75 MPa, there was a slight increase in

MGI, which may be attributed to cavitation and bubble formation induced by the increased pressure. The loss in contrast can be attributed either to complete NB destruction (e.g., inertial cavitation) or by bubble gas loss due to disruption to the lipid shell.

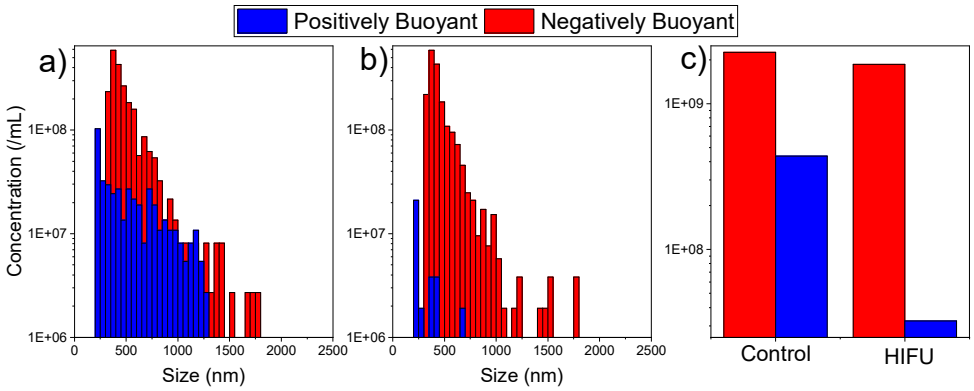

Figure 6.7 - MS-NBs populations measured by RMM (a) before and (b) after HIFU exposure. c) Concentrations of positively and negatively buoyant particles pre and post HIFU.

A similar experiment was performed using RMM to characterise MS-NB populations before and after HIFU exposure shown in Figure 6.7a and b respectively. Positively buoyant particle concentration decreased by an order of magnitude, from 4.38×10^8 to 3.24×10^7 /mL whereas the negatively buoyant particle concentration remained unchanged (Figure 6.7c). A small population of smaller NBs remain, which may be due to their higher resonance frequency and as such, the magnitude of their volumetric oscillations may not be sufficient to initiate NB destruction. Larger MS-NBs may also decrease in size via gas dissolution during US exposure. These results are similar to those shown by Hernandez et al. [59] requiring similar pressures albeit at a higher driving frequency (12 MHz, MI = 1.52). In this study a small increase in the concentration of the negatively buoyant population was also observed, attributed to remnant bubble shells re-assembling to form other lipid particles.

This experiment was repeated, and samples characterised via DLS before and after HIFU exposure. Initially, MS-NBs primarily consist of particles ~ 80 nm in size, with a small population of particles ~ 400 nm (Figure 6.8a). After HIFU exposure, the peak situated at ~ 80 nm in both number and intensity distributions disappears, leaving behind a mono-modal sample of ~ 240 and 200 nm in size, dependent on intensity and number distributions (Figure 6.8b). This suggests that the acoustically active particles in the MS-NB distribution are those ~ 80 nm in size, and the larger sub-population of particles are likely lipid aggregates, in agreement with our NTA data (Figure 6.3).

As such, a combination of characterisation techniques has been used to characterise the size and concentration of MS-NBs, and RMM demonstrated the existence of microfluidically produced sub-micron bubbles. MS-NBs were shown to have diagnostic potential, providing contrast enhancement for diagnostic US imaging, as well as therapeutic potential shown via US triggered destruction.

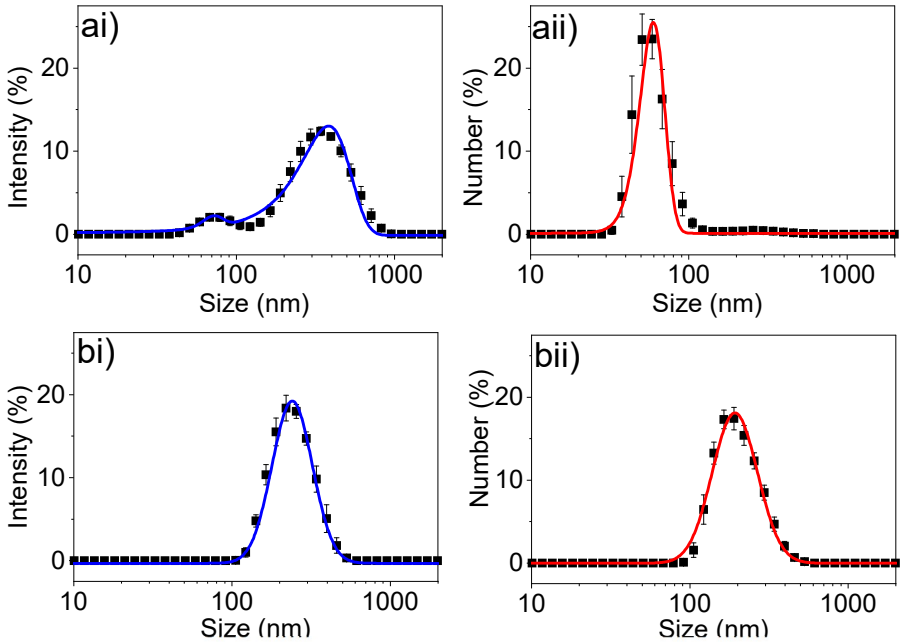

Figure 6.8 - DLS measurements of MS-NBs (a) before and (b) after exposure to high intensity focused ultrasound (HIFU) showing both (i) intensity and (ii) number weighted distributions.

6.3 UV-Vis and Fluorescence Spectroscopy of Calcein

To enable quantification of drug release from Nested-NBs, self-quenched calcein is used as a model drug, encapsulated within the liposome aqueous core. Calcein is a fluorescent dye with similar properties to fluorescein with peak fluorescence Excitation and Emission (Ex/Em) wavelengths (λ) of 495/515 nm respectively. At high concentrations, calcein self-quenches due to the primary inner-filter effect, in which high sample absorbance provides attenuation of the excitation light. Additionally due to the overlap in calcein excitation and emission spectra, calcein can also quench due to the secondary inner-filter effect, where emitted light is re-absorbed in the sample itself. Liposomal encapsulation of high concentrations of calcein allows for quantification of liposomal leakage, as when released from the liposome into the bulk medium, calcein concentration decreases and fluorescence increases due to un-quenching. Comparison between a treated sample, a negative control (untreated) and a fully lysed sample (e.g., treated with Triton-X) allows percentage leakage to be determined.

To characterise the optical properties of calcein, both UV-Vis and fluorescence spectroscopy were used. Firstly, UV-Vis was used to determine calcein absorbance, and determine the molar extinction coefficient. Fluorescence spectroscopy measurements then observed the relationship between fluorescence intensity and concentration. Calcein optical density was measured using UV-Vis spectroscopy in a cuvette with a path length of 10 mm, at concentrations between 0.001 – 10 mM and wavelengths of 200 – 800 nm (Figure 6.9a). Peak absorbance was determined to be ~ 495 nm across all concentrations, in agreement with accepted values.

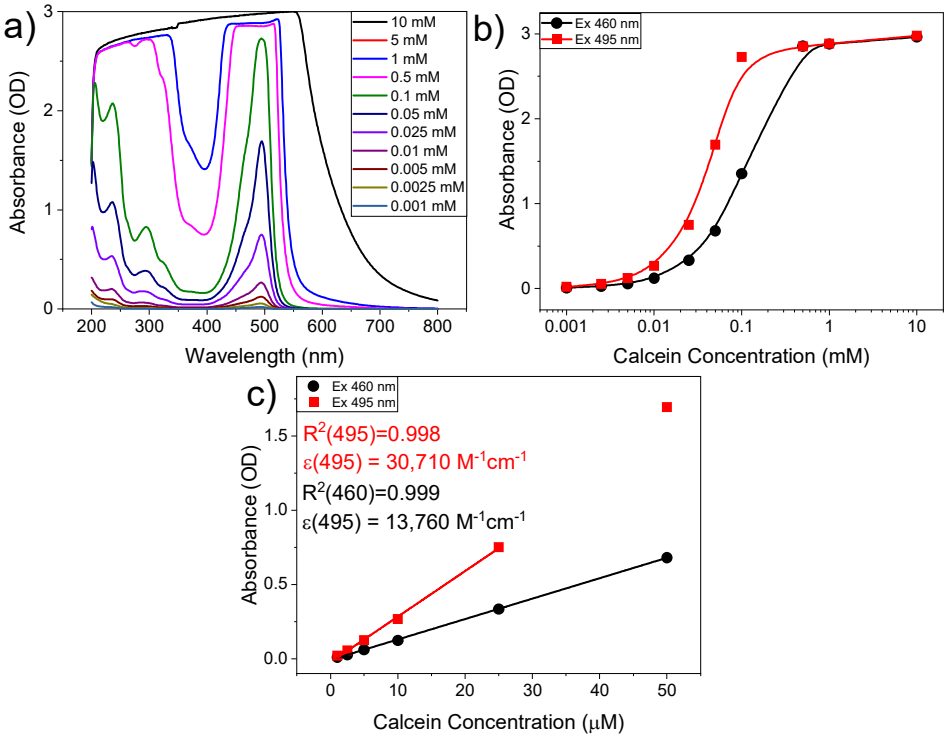

Figure 6.9 - Calcein absorbance measured at concentration of 0.001 – 10 mM. a) Absorbance (OD) spectra between 200 – 800 nm Absorbance measured at 460 nm and 495 nm between b) 0.001 – 10 mM, showing a non-linear trend and c) showing a linear trend obeying the Beer-Lambert law for concentrations up to 50 μM

Absorbance values on-peak (λ = 495 nm) and off-peak (λ = 460 nm) were measured (Figure 6.9b), showing that at higher concentrations, the relationship between absorbance and concentration is non-linear. However, at lower concentrations (< 50 μM) the relationship between absorbance and concentration is linear, as described by the Beer-Lambert law (Equation 4.8)[211]. As such, fitting a linear trend to Figure 6.9c allows determination of the molar extinction coefficient, ε.

For a path-length, l, of 10 mm, $\varepsilon(460\ \text{nm}) = 13{,}760\ \text{M}^{-1}\text{cm}^{-1}$ and $\varepsilon(495\ \text{nm}) = 30{,}710\ \text{M}^{-1}\text{cm}^{-1}$ with R^2 values of 0.999 and 0.998 respectively. Additionally, for λ = 495 nm the relationship between absorbance and concentration becomes non-linear at a lower concentration than λ = 460 nm (>25 μM compared to > 50 μM respectively). Hence, the use of λ = 460 nm allows for higher concentrations to be measured whilst still following the linear regime.

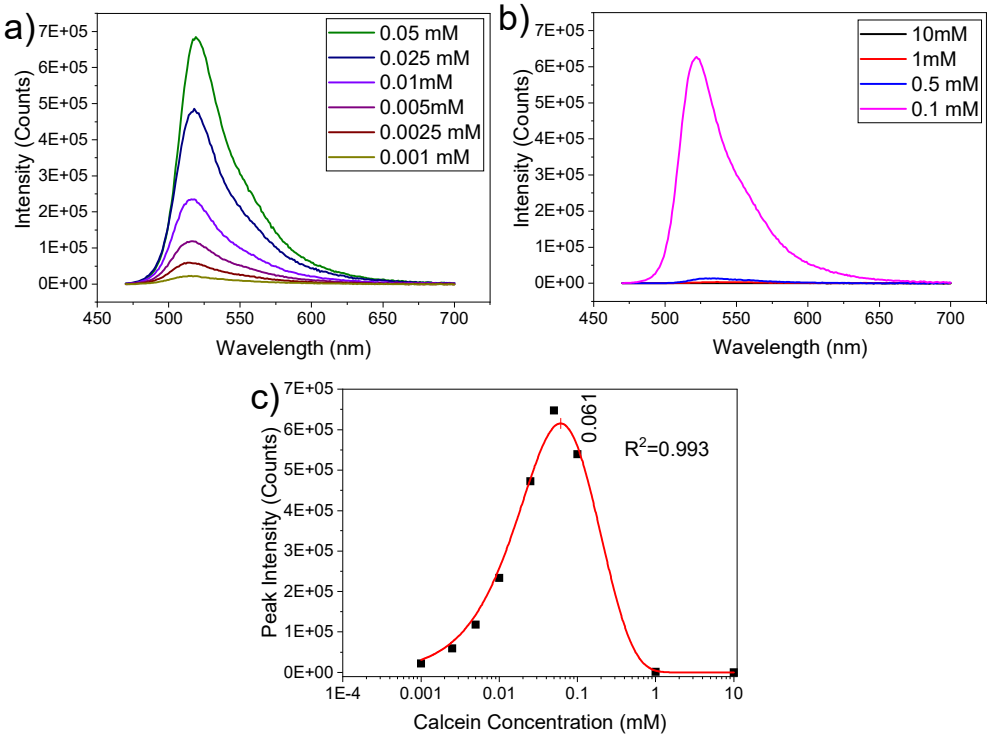

Figure 6.10 - Fluorescence emission spectra of calcein, across a range of concentrations after excitation at 460 nm. Emission spectra for a concentration range of a) 0.001 – 0.05 mM and b) 0.1 – 10 mM. c) Peak fluorescence intensity of calcein between 0.001 – 10 mM, highlighting self-quenching at high concentrations due to the inner filter effect. Data was fit using a modified Stern-Volmer equation, with peak emission intensity at a calcein concentration of 0.061 mM.

Calcein fluorescence emission spectra were measured using a cuvette based fluorescence spectrometer. The fluorescence emission spectra of calcein between wavelengths of 470 – 700 nm, after excitation at 460 nm, is shown in Figure 6.10. Fluorescence was measured at a range of calcein concentrations (0.001 – 10 mM) in a 10 mm path length cuvette, demonstrating self-quenching due to the inner filter effect [212].

Figure 6.10a shows increasing emission intensity with increasing concentration, between 0.001 – 0.05 mM. Increasing calcein concentration ≥ 0.1 mM, the fluorescence emission begins to decrease, and decreases rapidly at concentrations > 0.5 mM (Figure 6.10b). The effect of concentration on peak fluorescence at 515 nm is shown in Figure 6.10c. The

relationship between concentration, fluorescence intensity and self-quenching can be described by the Stern Volmer equation, requiring a modified version to account for the inner-filter effect (Equation 6.1a,b). Here, B_f is a proportionality constant for intensity, [Ct] is molar concentration of calcein, k_{ife} is a constant representing decrease of fluorescence due to inner filter effect, and ε is molar extinction coefficient. Fitting the modified Stern-Volmer equation to the data in Figure 6.10*c* and including the value of ε(460 nm) determined a peak fluorescence at a calcein concentration of 0.061 mM, as well as $R^2 = 0.993$, signifying good agreement between experimental results and theory.

$$I_0 = B_f\left(1 - 10^{-\varepsilon[C_t]}\right) \qquad \text{Equation 6.1a}$$

$$I = I_0 e^{-k_{ife}[C_t]} \qquad \text{Equation 6.1b}$$

A fluorescence excitation scan was also performed on calcein at a range of concentrations, between 0.001 – 10 mM. In this scan, calcein was excited across a range of wavelengths (400 – 600 nm), with emitted light collected at a fixed wavelength of 515 nm. Calcein exhibited a peak excitation wavelength of ~ 495 nm, with fluorescence intensity increasing with concentration for values of 0.001 – 0.025 mM (Figure 6.11a). At

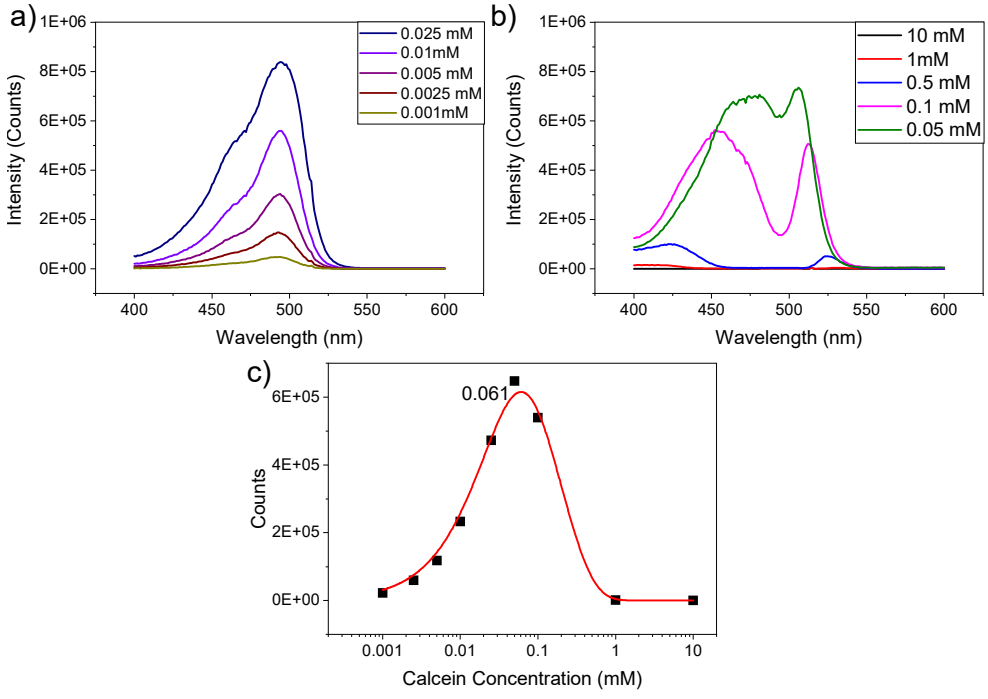

Figure 6.11 - Excitation spectra for calcein with a fixed emission of 515 nm. Fluorescence excitation spectra are shown for wavelengths of 400 – 600 nm, for calcein concentrations of a) 0.001 – 0.25 mM showing concurrent increase in emission with concentration, and b) concentrations of 0.05 – 10 mM, demonstrating self-quenching of calcein due to the inner filter effect. c) Effect of calcein concentration on excitation counts, showing calcein self-quenching.

concentrations between 0.05 – 10 mM, fluorescence decreased due to self-quenching with a noticeable trough visible in the spectra at ~ 495 nm (Figure 6.11b). Figure 6.11c shows the trend between calcein concentration and fluorescence intensity, similar to that shown in Figure 6.10c. Data was fit using the Stern-Volmer equation, and a molar extinction coefficient of $\varepsilon(460\ \text{nm}) = 13{,}760\ \text{M}^{-1}\text{cm}^{-1}$ determined.

For experiments involving multiple samples (i.e. triggered release with multiple parameters) a micro well plate based spectrometer was used to increase sample throughput. Calcein molar extinction coefficient calculated using microplate reader was determined via absorbance measurements, as shown in Figure 6.12a. By default, the system normalizes absorbance values for a 10 mm path length. From this, the molar extinction coefficient, with an excitation wavelength of 460 nm, was determined to be 7502 ± 180 $M^{-1}cm^{-1}$. For fluorescence emission experiments, calcein was excited at 460 nm and point emission intensity recorded at 515 nm (Figure 6.12b). Data was fit using the Stern-Volmer equation (Equation 6.1) and peak calcein fluorescence determine to be at 0.33 mM, at which point self-quenching begins.

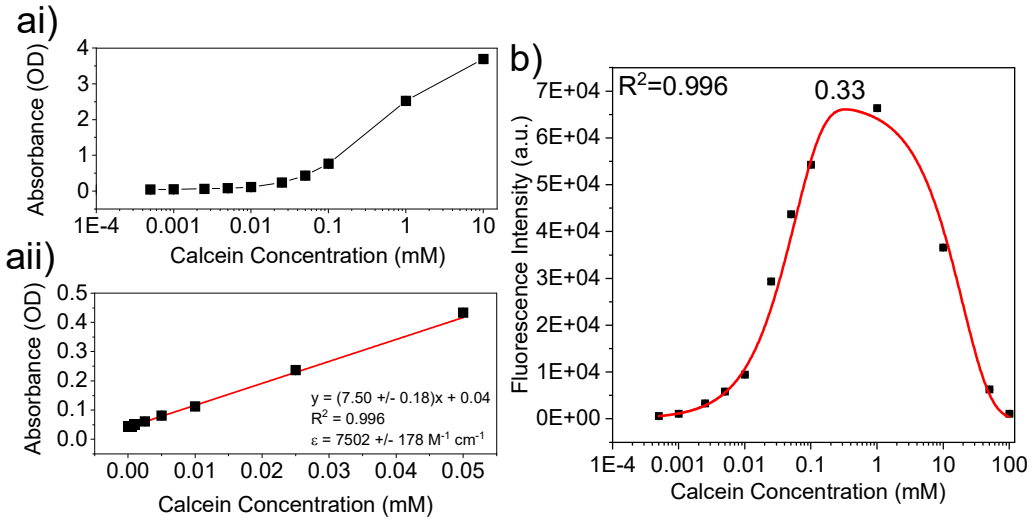

Figure 6.12 - UV-Vis and fluorescence spectroscopy characterisation of calcein, measured using a microplate reader. a) Trend between absorbance and concentration for (i) concentrations up to 10 mM, showing a non-linear trend and (ii) up to 0.05 mM showing a linear trend, fit to determine the molar extinction coefficient of 7502 $M^{-1}cm^{-1}$. b) Fluorescence spectroscopy measurements showing self-quenching of calcein at high concentration, and peak fluorescence at 0.33 mM. Data was fit following the Stern-Volmer equation.

6.4 Optimisation of Nested-NB Fabrication

The liposomes used to encapsulate NBs, and hence form Nested-NBs consisted of DSPC, Cholesterol and DSPE-PEG2000 with a molar ratio of 63:32:5 unless stated. This composition is similar to that used in the clinic liposomal formulation of Doxorubicin, Doxil, and identical

to that used in previous therapeutic liposomes used in our group [16,46,48]. The inclusion of a high Cholesterol percentage provides drug loading stability, in which Cholesterol molecules sit between the lipid hydrocarbon chains, increasing membrane rigidity. Multilamellar vesicles (MLVs) were formed by a thin film rehydration method, in which a thin lipid film is rehydrated by an aqueous buffer. Homogenisation of the sample is achieved by repeated extrusion through membranes with a pore size similar to that of the desired resultant liposome diameter (in this case 400 nm). With each extrusion, the proportion of liposomes smaller than the pore size increases resulting in unilamellar vesicles with a monomodal distribution. To load calcein into liposomes, the lipid film was rehydrated using a solution of PBS containing 100 mM calcein. Full experimental methodology is described in Section 5.3. Following rehydration and extrusion, free, unencapsulated calcein requires removal from the solution.

In this thesis, two different cleaning techniques were investigated for removal of free calcein: gel filtration chromatography (GFC) and centrifugal (CF) washing. In GFC, particles and molecules are separated by size and on their differing ability to enter the pores of the gel-filtration medium. Hence this enables liposomes to pass through the column, prior to calcein. In the CF method, liposomes are centrifuged at high speed such that they form a pellet, of which the remaining calcein super-natant can be removed, and pellet redispersed. After cleaning, successful encapsulation of calcein can be confirmed by full liposome lysis using 0.1 % Triton-X, releasing calcein into the bulk medium and subsequently un-quenching. This also allows calcein release or leakage to be quantified by comparison to a baseline, and fully lysed sample. Hence, to increase sensitivity of the release assay the dynamic range between these two samples should be maximised. GFC was used initially as proof a of concept to demonstrate successful calcein encapsulation, building upon a previously developed protocol in our group.

6.4.1 Cleaning by Gel Filtration Chromatography

To optimize GFC, 50 μL aliquots were collected throughout sample elution (maximum of 1 mL), to determine in which aliquots contained the cleaned liposomes, and at which point the eluted sample contained high concentrations of free calcein and hence are undesirable. The first 3 aliquots from this study were noticeably transparent, indicating little to no liposomes or free calcein and as such were not analysed further. For nearly all subsequent aliquots, fluorescence increased after addition of Triton-X (lysed vs unlysed) indicating successful encapsulation of calcein (Figure 6.13). Background fluorescence due to free calcein increased with increasing aliquots (Figure 6.13a), as expected via the GFC process. Aliquots 5 – 9 showed the largest increase in fluorescence compared to their background value, and hence larger dynamic range (Figure 6.13b), whilst when combined providing a usable sample volume for triggered release experiments (~ 250 uL). It should be noted that all samples were

diluted 25 x prior to fluorescence measurements, reducing the sample absorbance and ensuring the relationship between fluorescence intensity and calcein concentration is linear. This is reflected by the maximum fluorescence intensity measured in Figure 6.13 of ~10^4, corresponding to calcein concentrations within the linear absorbance range (Figure 6.12).

Following this, Nested-NBs were formed as described in Section 5.3, by rehydration of a thin lipid film using a solution containing MS-NBs and 100 mM calcein. After formation and cleaning via GFC (collected in 100 uL aliquots in the elution stage), the change in fluorescence intensity between Nested-NBs and liposomes was compared after addition of Triton-X, and hence full lysis.

Results showed that in the Nested-NB sample, calcein was successfully encapsulated signified by an increase in fluorescence after addition of Triton-X (Figure 6.14). For all aliquots, the change in fluorescence for Nested-NBs was less than that seen in the liposome only sample. This could be due to reduced aqueous volume inside the liposome core, due to successful NB encapsulation, however, is not absolute confirmation of encapsulation. It is also possible that the presence of NBs during fluorescence measurements may influence the fluorescence intensity. Kopechek et al. [213] found that the presence of microbubbles decreases the overall fluorescence reading, due to scattering of incident and emitted light. To investigate this, fluorescence intensity of a liposome sample with and without free NBs was measured, finding negligible change between fluorescence readings (2874 vs 2924 a.u.). This may be due to the

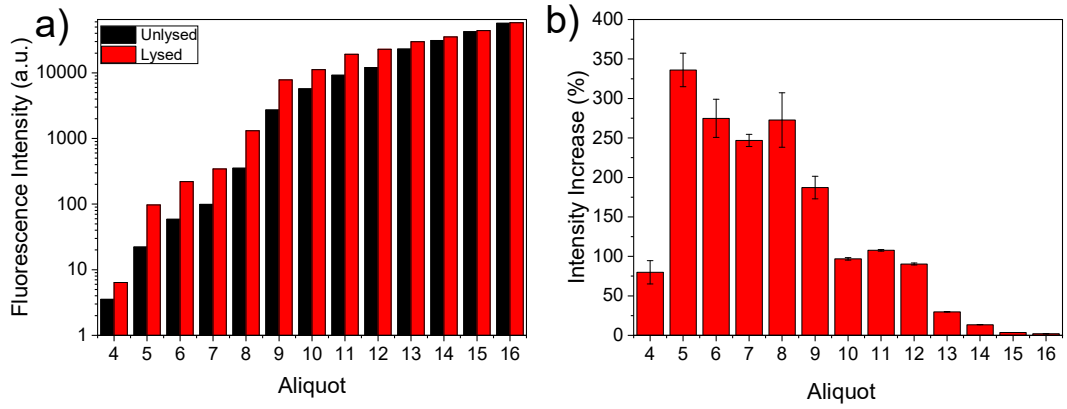

Figure 6.13 - Fluorescence characterisation of calcein-loaded liposome samples, cleaned via gel filtration chromatography. a) Fluorescence intensity (Ex/Em 460/515 nm) of 50 µL aliquots collected during the cleaning process, before and after lysis with Triton-X. b) The percentage intensity increase after lysis, for each aliquot showing a noticeable peak between aliquots 5 – 9.

reduced size of NBs, and the non-linear relationship between particle size and optical scattering cross section.

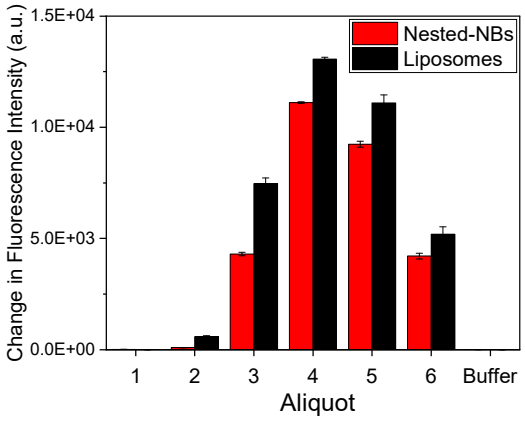

Figure 6.14 - Change in Fluorescence Intensity after addition of Triton-X to Nested-NBs and Liposomes, for each 100 µL aliquot collected during the elution step of gel filtration chromatography.

Transmission Electron Microscopy (TEM) was used to observe Nested-NB morphology and determine whether NBs were successfully encapsulated (Figure 6.15a). Images show potential encapsulation of 100 – 200 nm particles within ~ 400 nm particles, as we all as many 100 nm un-encapsulated particles of similar size to MS-NBs. NTA measurements also showed similar results (Figure 6.15b), in which an increased population of ~ 100 nm particles were present in the Nested-NB sample compared to liposomes only. Due to the nature of TEM, it is possible that some of the nested particles are not truly encapsulated but dried directly on-top of another particle during preparation of the TEM grid. This, combined with the high concentration of

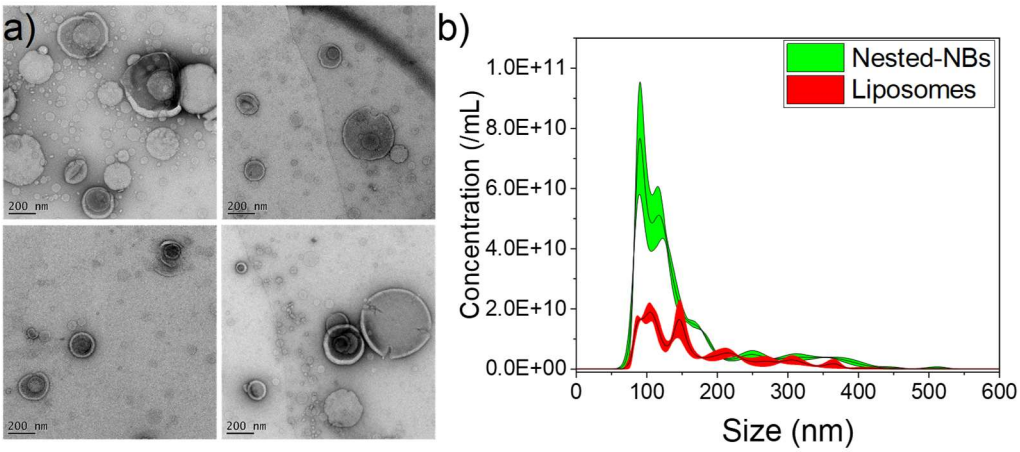

Figure 6.15 - a) Transmission Electron Microscopy micrographs of Nested-NBs, after cleaning via gel filtration chromatography showing potential encapsulation of NBs within liposomes. b) NTA population data of Nested-NBs and liposomes, showing an increased population of free NBs (~ 100 nm) in the Nested-NB sample

free particles, makes it difficult to confirm whether NBs were successfully encapsulated within the liposomal aqueous core.

6.4.2 Cleaning by Centrifugation

Following these results, the use of centrifugation (CF) as an alternative cleaning technique was investigated. Firstly, to remove free NBs, and as such provide clearer evidence of successful NB encapsulation, and secondly to provide a more consistent cleaning process compared to GFC, due to the nature of the elution process. Nested-NB and liposome samples were centrifuged (Section 5.3) forming a pellet at the bottom of the Eppendorf. This can subsequently be washed with PBS and the pellet redispersed, removing free calcein and NBs. CF also enables Nested-NB concentration to be adjusted above the initial yield concentration. The efficiency of the CF cleaning process was compared to GFC, by synthesizing one bulk sample which is split into two, and each cleaned either by CF or GFC.

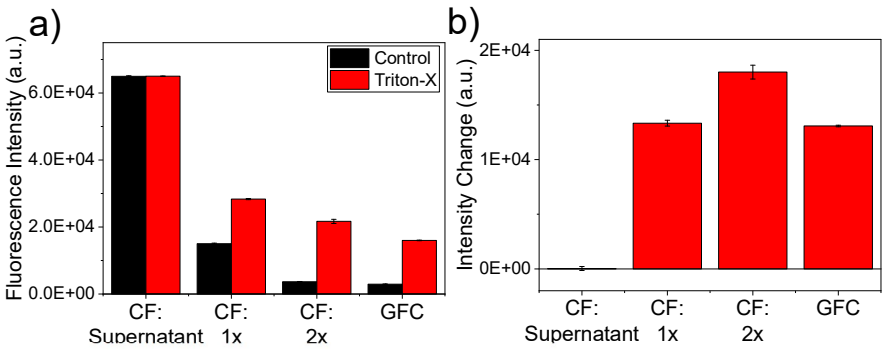

Figure 6.16 - Fluorescence intensity measurements of Nested-NB samples cleaned via centrifugation (CF) and gel filtration chromatography (GFC)(a) before and after addition of Triton-X and (b) the associated intensity change.

Figure 6.16a shows the fluorescence intensity for the supernatant collected post CF, Nested-NB samples cleaned after 1 or 2 CF cycles, and Nested-NBs cleaned via GFC. The supernatant initially had a high fluorescence intensity ($6.49 \pm 0.2 \times 10^4$ a.u.), due to the free calcein in solution. After one cycle, CF cleaning effectively removed free calcein, signified by a decrease in fluorescence compared to the supernatant ($1.50 \pm 0.02 \times 10^4$ a.u.). A second cycle further decreasing the fluorescent background, to similar values as seen for GFC ($3.67 \pm 0.01 \times 10^3$ a.u. compared to $2.92 \pm 0.01 \times 10^3$ a.u). Addition of Triton-X triggered an increase in fluorescence for all cleaned samples. The change in intensity after addition of Triton-X was also considered (Figure 6.16b), as sensitivity of the measurement technique is improved by maximizing the dynamic range between control and full lysis. After one CF cleaning cycle, the change in fluorescence was like that of GFC (~1.3×10^4 a.u.). A second cleaning cycle further increased the change in fluorescence to $1.80 \pm 0.06 \times 10^4$ a.u., hence increasing dynamic range.

After optimising calcein removal using CF, the next process was to remove free, un-encapsulated NBs. CF cleaned Nested-NBs were characterised using NTA and TEM. Compared to the GFC cleaned sample (Figure 6.15) modal size increased from 183 ± 1 to 319 ± 7 nm, showing that smaller particles are removed (Figure 6.17a). This coincided with a decrease in total particle concentration from $1.82 \pm 0.09 \times 10^{12}$ to $2.45 \pm 0.10 \times 10^{11}$ /mL. These results agreed with analysis of TEM images, in which a total of 124 individual liposomes were analysed across 38 images, and the size of liposomes and any nested particles were determined. The population distribution followed a normal distribution with modal sizes of nesting particles and liposomes at 140 ± 69 and of 251 ± 130 nm, respectively (Figure 6.17b). From this it was also determined that 22 ± 2% of liposomes encapsulated single or multiple NBs. Images of Nested-NBs and that on average, each Nested-NB contained 1.29 ± 0.01 NBs. Representative TEM micrographs (7c & d) showed clear encapsulation of particles within liposomes, as well as the absence of large quantities of small, un-encapsulated particles. This reduction in particle size of an order of magnitude compared to traditional therapeutic microbubbles (~ 2 μm)[50,214] and other liposome-NB complexes (500 - 800 nm)[156] holds promise for increased accumulation and uptake of Nested-NBs into tumour microvasculature.

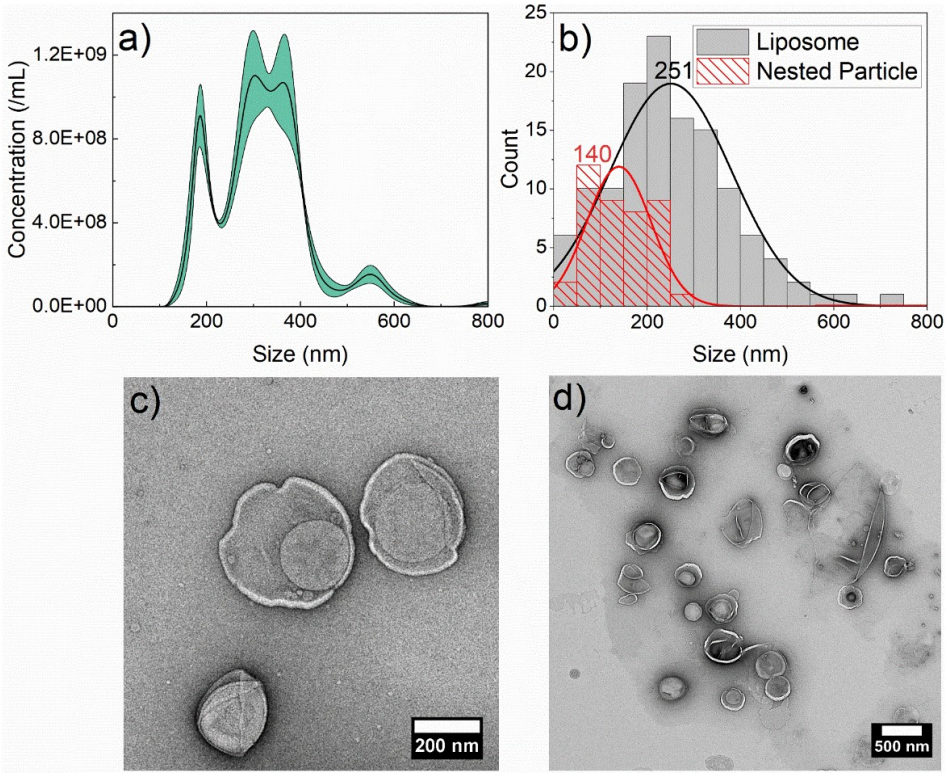

Figure 6.177 - Nested-NB population distribution measured by (a) NTA and (b) TEM, showing distribution for both the Nested-NB and the encapsulating liposome. (c, d) Representative TEM images of Nested-NBs showing two individual Nested-NBs and a larger field of view, respectively

The B-mode MGI of Nested-NBs was also monitored throughout their production (Figure 6.19) from the initial MS-NB stock, through to thin film rehydration, extrusion and cleaning by either GFC or CF. Prior to cleaning, MGI remained relatively constant throughout. Immediately after extrusion, MGI was 74.8 ± 2.0 a.u, similar to that for MS-NBs at stock concentration (Figure 6.6a) which decreased to 30.5 ± 1.9 a.u. and 11.3 ± 0.7 a.u. after cleaning by GFC and CF respectively. This decrease in MGI between GFC and CF cleaning is consistent with the removal of free NBs.

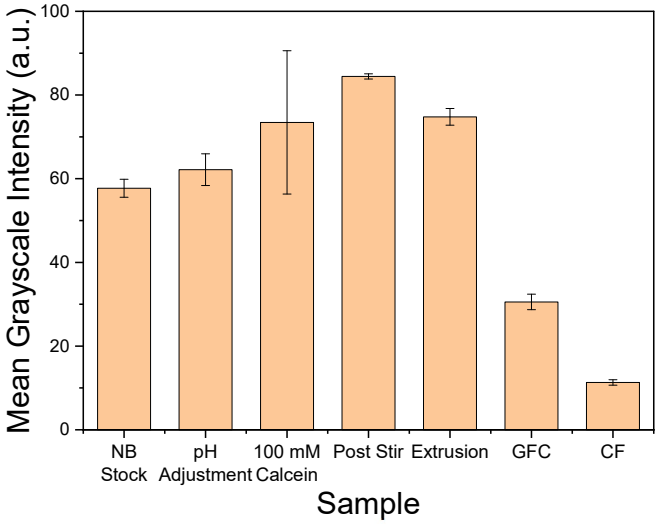

Figure 6.188 - Mean Grayscale Intensity (MGI) of B-Mode ultrasound images of Nested-NBs throughout each stage of their production. Initial MS-NB stock solution, after pH adjustment, after addition of calcein to a concentration of 100 mM, post stirring and rehydration of a thin lipid film, after extrusion and after cleaning either by gel filtration chromatography or centrifugation.

6.4.3 Drug Loading Stability in Varying Thermal Conditions

A triggered drug delivery vehicle should demonstrate drug loading stability at a range of temperatures: at 37 ° C (physiological temperature) such that minimal drug payload is released until the applied trigger, at 21 ° C (room temperature) such that experiments are reliable and reproducible, and at 4 ° C (fridge temperature) such that they remain stable for use in the short to medium term. Hence, the temporal stability of calcein loading into Nested-NBs at these 3 temperatures was measured via fluorescence spectroscopy. All measurements were conducted using a thermoelectrically cooled cuvette-holder, and sample gently stirred ~ 300 RPM using a magnetic stirrer. For all conditions, fluorescence values were recorded in 5-minute intervals for a total duration of 30 min (21 ° C and 37 ° C) and 180 min (4 ° C).

The percentage release of calcein was calculated by comparing temporal values to a negative control (t=0) and positive control corresponding to full release (Triton X). Across all temperatures and timescales measured (Figure 6.19), no significant calcein release was recorded. After 180 min at 4 ° C, calcein leakage of 0.81 % was recorded (N=1), compared to -1.1 ± 0.95 % and 0.1 ± 3.2 % after 30 mins at 21 (N=3) and 37 ° C (N=3) respectively. As such, Nested-NBs were found to be stable over time scales of at least 3 hours, over which a typical US triggered release experiment is performed. Further, at physiological temperature drug loading is stable for at least 30 mins, exceeding typical bubble lifetime *in vivo* (~10 min) [215] and would therefore be considered suitable as a triggered release agent.

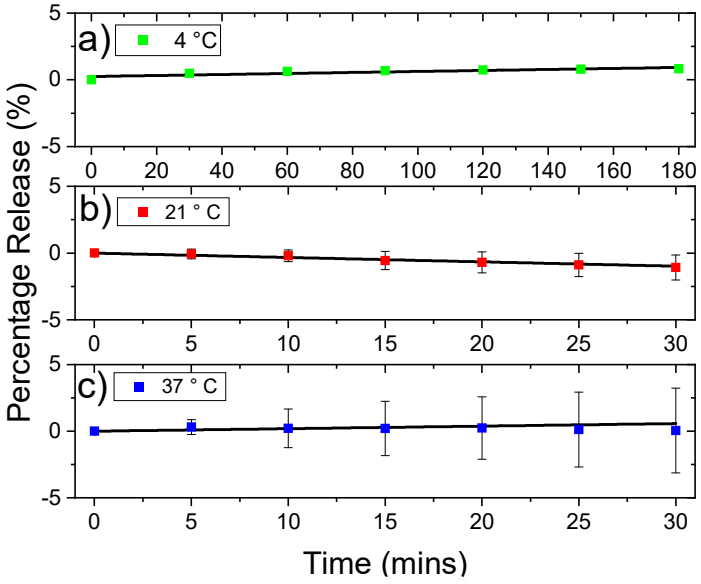

Figure 6.19 - Thermal stability of drug loading in Nested-NBs. a) Over 180 minutes at 4 ° C (N=1) and over 30 minutes at b) 21 ° C (N=3) and c) 37 ° C (N=3). Each data set was fit with a linear trend.

6.5 Pulsed Wave HIFU for Triggered Release

Nested-NBs were exposed to HIFU to provide a mechanism for triggered NB destruction and subsequent payload release. Full experimental protocol is described in Section 5.8 but briefly Nested-NBs were contained within an Eppendorf, and the HIFU transducer was coupled to the sample using a coupling cone containing degassed Milli-Q water. Calcein-loaded liposomes containing no NBs were also used as a control sample to determine whether release was due to encapsulated NBs, or thermal effects associated with HIFU. Following HIFU exposure, sample fluorescence was measured using a well plate-based fluorescence spectrometer. Percentage release was determined by measuring fluorescence of non-exposed

samples (negative control), exposed samples, and samples lysed with 0.1% Triton-X (positive control).

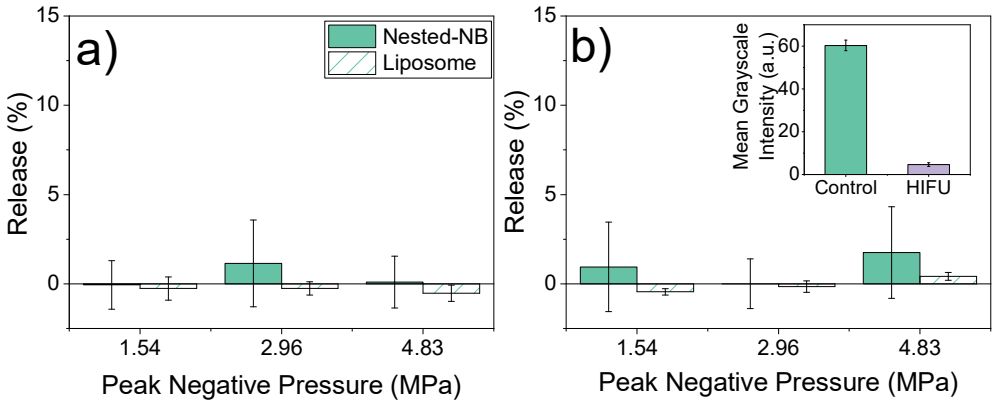

Figure 6.20 - Release profiles for Nested-NBs and liposome controls after ultrasound exposure at PNPs ranging from 1.54 to 4.83 MPa. (a) 1% duty cycle and (b) 50% duty cycle. Inset: MGI of B-mode imaging of Nested-NBs before and after HIFU exposure at 4.83 MPa at 50% duty cycle.

Nested-NBs were initially treated using pulsed-wave HIFU, at peak negative pressures (PNPs) of 1.54, 2.96 and 4.83 MPa and at either 1 % or 50 % duty cycle for a total of 5 s, and release profiles are shown in Figure 6.20a & b respectively. At these exposure parameters, no significant calcein release was observed from Nested-NBs compared to liposome-only controls. To determine whether these exposures were inducing destruction of the encapsulated NBs, Nested- NBs were imaged using B-mode US before and after HIFU exposure. Nested-NBs initially demonstrated echogenicity, which after insonation at 4.83 MPa at 50% duty cycle, their MGI decreased by 92.4 ± 5.6% from 60.3 ± 2.4 to 4.6 ± 0.8 (a.u.), suggesting NB destruction (Figure 6.20b inset).

One possible explanation for the lack of release may be that although NBs are being destroyed, the resultant shear stresses from their oscillations are not capable of suitably disrupting the surrounding lipid bilayer to trigger drug release. In previous experiments, liposomes contained a molar cholesterol content of 32 %. This value was chosen as this provides good liposomal and drug-loading stability, and is similar to clinically used liposomal formulations[216]. Cholesterol has a concentration dependent effect on membrane permeability, by sitting within the hydrocarbon chains and at higher concentrations inducing a conformational order [217]. Increasing cholesterol content reduces membrane permeability [16], and hence the effect of varying the cholesterol content of Nested-NBs on their HIFU-triggered calcein release was investigated.

Nested-NBs were formulated with cholesterol content of either 32, 22 or 12 %, maintaining the 5 % molar content of DSPE-PEG2000 and varying the DSPC content to account for this. Firstly, DLS was used to confirm the production of Nested-NBs with these formulations and to determine the effect of this on particle size (Figure 6.21a). For the initial formulation, Nested-NBs had a modal size of 328 nm, which increased with decreasing cholesterol content to 573 and 585 nm for 22 % and 12 % cholesterol content, respectively. This may be due to the reduced membrane fluidity with lower cholesterol content and as such, larger MLVs may be present in the hydrated solution, which then are not fully homogenized during the extrusion process. Regardless, after HIFU exposure no significant release was recorded for any of the Nested-NB samples, irrespective of cholesterol content (Figure 6.21b).

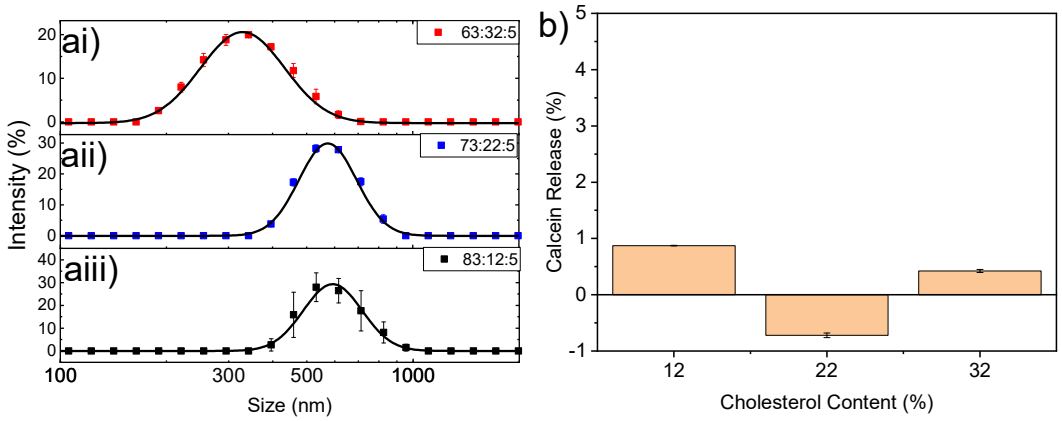

Figure 6.21 - Characterisation of Nested-NBs formulated with varying molar cholesterol content. a) Populations measured via DLS for formulations containing molar ratios of DSPC:Cholesterol:DSPE-PEG2000 of i) 63:32:5, ii) 73:22:5 and iii) 83:12:5 with modal sizes of 328, 573 and 585 nm respectively. All distributions were fit using a lognormal function. b) Percentage calcein release after HIFU exposure (4.83 MPa, 50 % duty cycle) for the varying formulations, corresponding to cholesterol content of 12, 22 and 32 %.

6.6 Passive Cavitation Detection

The lack of observed release from HIFU-mediated NB destruction, as confirmed by DLS and RMM, led us to further investigate the interaction between Nested-NBs and the applied HIFU field. Passive cavitation detection (PCD) was used to observe acoustic emissions during insonation. Observation of acoustic emissions allows for bubble acoustic activity to be detected, and determine the nature of this activity i.e. whether NBs are oscillating in a stable regime or an unstable regime, leading to destruction. A broad-band-focused detector was positioned in the central aperture of the HIFU transducer, coaligned with its focal region. During insonation, acoustic emissions from the focal point are received by the detector and passed through a 5 MHz high-pass filter to suppress detection of the HIFU drive frequency.

6.6.1 Passive Cavitation Detection of Nanobubbles

To determine the noise baseline and system sensitivity, MS-NBs at concentrations between 10^{10} – 10^{12} /mL were exposed to HIFU (f_0 = 1.1 MHz, PNP = 4.83 MPa, 50 % duty cycle) and acoustic emissions monitored, and compared to a PBS baseline. Figure 6.22a shows the recorded frequency spectrum for varying NB concentration, averaged over the total exposure duration and across 3 separate samples for each concentration, except for 9 x 10^{11} /mL, due to sample volume constraints. Across all spectra, magnitude increases above 5 MHz, due to the high pass frequency filter present in the system.

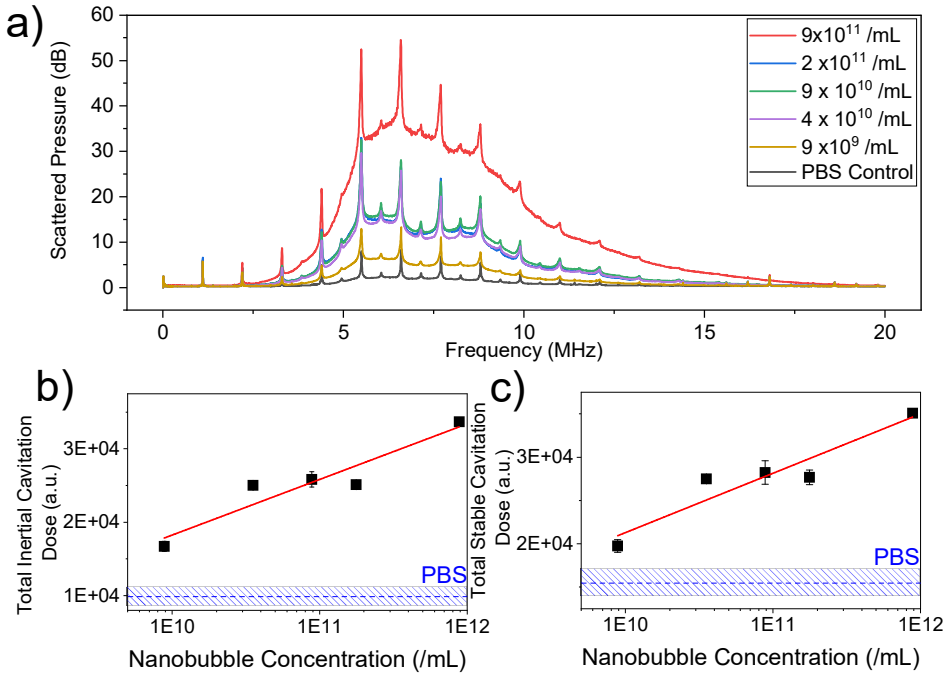

Figure 6.22 Acoustic emissions from MS-NBs during HIFU insonation (4.83 MPa, 50 % duty cycle) measured for MS-NBs at concentrations of 10^{10} – 10^{12} /mL. a) Scattered Pressure (dB) across the frequency spectrum (0 – 20 MHz) showing the presence of super and ultraharmonics, increasing with MS-NB concentration. b) Total Inertial Cavitation Dose (TICD) and (c) Total Stable Cavitation Dose across all concentrations. Data was fit using a 3-parameter logarithmic function (y = a – bln(x+c)).

For all spectra, including that of the PBS baseline, peaks located at the superharmonics ($nf_0, n \in \mathbb{N}$) are clearly visible, as well as those for the ultraharmonics ($f_0(2n+1)/2$), commonly associated with stable bubble cavitation. However, it should be noted that these were also present at a lower magnitude in the PBS control. Broadband noise is also present and increasing with NB concentration, indicative of inertial cavitation and suggesting bubble destruction, in agreement with our previous findings. Broadband and harmonic emissions were then quantified by integration of spectra that was frequency analysed to either remove (broadband only) or isolate harmonic frequencies. These values for varying NB concentrations are shown in Figure 6.22b & c respectively, quantified as the Total Inertial Cavitation Dose

(TICD) and Total Stable Cavitation Dose (TSCD) [188]. For MS-NB concentrations of $\geq 10^{10}$ /mL, MS-NBs were acoustically distinguishable from the baseline with TICD and TSCD of (1.7 ± 0.7) x 10^4 and (2.0 ± 0.7) x 10^4 a.u. compared to PBS values of ~ (0.99 ± 0.12) x 10^4 and (1.55 ± 0.19) x 10^4 a.u. respectively. With increasing MS-NB concentration, both TICD and TCSD followed a logarithmic trend up to the maximum concentration of MS-NBs (9 x 10^{11} /mL) at which point TICD = 3.4 x10^4 and TSCD = 3.5 x10^4 a.u. The relatively high value of the PBS controls maybe attributed to a combination of both cavitation induced within the solution and acoustic reflections from the sample holder because of the relatively high PNP. As such, this data confirms the ability to distinguish acoustically active MS-NBs from the PBS only background using PCD.

6.6.2 Passive Cavitation Detection of Nested-NBs

These results are similar to those shown by Pellow et al. [137] in which both harmonic and broadband acoustic emissions of NBs were observed, dependent on excitation pressure. Following these results, acoustic emissions of Nested-NBs were monitored. From NTA characterisation of Nested-NBs, their average concentration is 2.45 ± 0.10 × 10^{11} with ~ 20 % of these containing a nested particle. As such, the total NB concentration can be assumed to be 5 x 10^{10} /mL, slightly greater than the limit of detection of the PCD system (~10^{10} NBs/mL). Hence for Nested-NB PCD experiments, their concentration was maintained as high as consistently possible at 1.56 × 10^{11} /mL, to ensure NB acoustic activity could be detected. Based on the encapsulation efficiency of NBs within Nested-NBs, this is equivalent to ~3 x 10^{10} NBs/mL.

Nested-NBs were then exposed to HIFU, and acoustic emissions monitored, as previously described. The scattered pressure spectra for Nested-NBs, liposomes and PBS are shown in Figure 6.23a. All samples demonstrated the presence of both harmonic emissions and broadband noise, with N-NB and LS having increased magnitude compared to PBS control.

To help distinguish between Nested-NBs and liposomes (LS), the Inertial Cavitation Dose (ICD) was plotted against time (Figure 6.23b), where t = 0 corresponds to the beginning of the US exposure. At this point, all samples demonstrated broadband emissions. For LS and PBS, this remained relatively constant across the total duration, however for Nested-NB activity peaked at the beginning of the exposure, until reaching a constant value after ~ 2 s. The Total Inertial Cavitation Dose (TICD) was for each sample was (2.70 ± 0.06) x 10^4, (2.60 ± 0.07) x 10^4 and (2.14 ± 0.13) x 10^4 a.u. for Nested-NB, LS and PBS respectively (Figure 6.23c). By summarising across the total duration of the exposure, Nested-NB and LS are indistinguishable. Due to the high PNP, NB destruction was expected to occur during the initial pulse cycles of the HIFU exposure, which correlates with the increased broadband noise

at the beginning of the N-NB exposure. To distinguish between N-NBs and LS, the change in magnitude of emissions over time was quantified (Pulse Normalised TICD, PN-TICD). Broadband emissions were cumulatively integrated with increasing pulse number and then normalized per pulse (Figure 6.23d), calculating a cumulative average. Using this metric, Nested-NBs demonstrated increased activity at the beginning of the exposure compared to LS. As this exposure progressed, the PN-TICD decreased such that at the end of the exposure they are indistinguishable from non-acoustically active LS (Figure 6.23d). This suggests that the NBs present in the Nested-NB sample initially provide an increase in both broadband emissions, as NBs undergo inertial cavitation. As the exposure progresses, the PN-TICD decreased until eventually by the end of the exposure, Nested-NB and liposome samples are indistinguishable from each other, indicative of no NBs remaining. This is also in agreement with the near-total loss of contrast shown by B-mode imaging (Figure 6.18b).

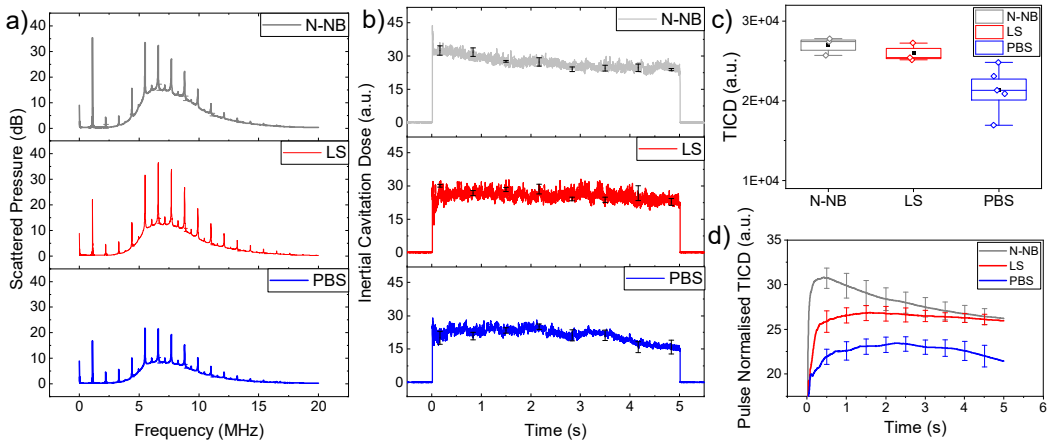

Figure 6.23 - a) Passive cavitation detection data characterising Nested-NBs (N-NB, N=3), liposomes (LS,N=3) and PBS(N=5) during exposure to HIFU (PNP = 4.83 MPa, Duty Cycle = 50 %, PRF = 1 kHz, Duration = 5 s). a) Frequency spectrum showing the scattered pressure between 0-20 MHz, averaged across the 5 s duration of the ultrasound exposure, and then averaged over multiple samples. b) Inertial Cavitation Dose quantifying the total broadband emissions for 0.5s before and after the 5 s exposure, averaged over all samples. c) Total Inertial Cavitation Dose (TICD) calculated by integration of Inertial Cavitation Dose throughout the exposure. Data is shown as a box plot, showing values for each repeat (diamond), median (central line), mean (black square) standard error (box) and 5th and 95th percentile (whiskers). d) Pulse normalised TICD, where the cumulative TICD is normalised by number of pulses. All error bars are the standard error across all measurements, and some are omitted for clarity.

As both broadband and harmonic response is detected, it is likely that the reduction in B-mode contrast is due to a combination of both rapid bubble fragmentation (i.e. inertial cavitation) as well as acoustically driven diffusion (stable cavitation) over the course of the HIFU exposure. Hence, the lack of release observed from Nested-NBs is noteworthy in understanding

interactions between the applied US field and encapsulated NBs. During stable cavitation, volumetric oscillations of the encapsulated NB, and hence localised fluid flow may be expected to induce liposomal poration, similar to that shown *in vitro* on cell membranes[41,48,218]. For effective sonoporation and promotion of intracellular drug uptake, the bubble-membrane distance should be minimized, and only effective across length scales similar to that of bubble size (approximately 1-2 bubble diameters) [218,219]. Our system contains a ~ 100 nm NB nested within a ~250 nm liposome, with a membrane comparable to that of a cell. As such, the average bubble-membrane distance is ~ 75 nm comparable to that of NB size, and at these length scales it is unclear to what extent membrane poration would occur. Another mechanism is also proposed in which volumetric NB oscillations would induce a "slinky-effect" on the encapsulating liposome [220]. This would induce dilation in the lipid-bilayer, increasing the inter-molecular distance between phospholipid molecules and hence increasing membrane permeability. It should be noted that a critical factor in our system is that the NB oscillations are not free and will in turn be damped by the presence of the encapsulating liposome. The damping provided by the nesting shell may also inhibit the occurrence of inertial cavitation (i.e. bubble collapse). The threshold for the occurrence of inertial cavitation is commonly defined by a critical bubble expansion ratio r_c/r_0 , where r_0 is initial bubble radius and r_c is the critical radius required for bubble collapse, with the threshold typically between $3 \leq (r_c/r_0) \leq 8$ [220,221]. As our MS-NBs are nested within liposomes approximately 2-3 times greater than their diameter, the existence of the nesting shell may provide additional resistance to bubble expansion, and hence hinder the occurrence of inertial cavitation.

Similar to the Nested-NB system, Wallace et al. investigated the use of MBs encapsulated within polymer [222] and liposomal shells [222]. It was found that the presence of an encapsulating polymer shell increased the threshold for MB destruction and increased as nesting shell size decreased. Similarly, the efficiency of drug release decreased concurrently with the size of the nesting liposomal shell. The use of low pressure (0.54 MPa) and high pressure (3.74 MPa) US treatment was investigated as a release trigger, with the respective regimes being attributed to inertial and stable cavitation, although the occurrence of cavitation was not acoustically characterised. Whilst both regimes induced increased liposomal drug release, prolonged US exposure (~ 25 min) was required for significant release, with minimal release observed in the initial 5 minutes of exposure (~ 5 %). This may go some way to explaining the lack of release observed in Nested-NBs, where we utilised high pressure (4.83 MPa) but only for short durations (5 s). However, based on the observed acoustic emissions it is apparent that by the end of the 5 s exposure, Nested-NBs are indistinguishable from a control sample and are no longer acoustically active. Hence it seems clear that the mechanisms associated with stable

and inertial cavitation are incapable of inducing liposomal drug release in Nested-NBs, at clinically relevant frequencies.

6.7 Triggered Release using Continuous Wave HIFU

To trigger drug release from Nested-NBs, the duty cycle of the HIFU exposure was changed from pulsed to continuous wave (CW), such that the total acoustic energy is increased. By doing this, Nested-NBs demonstrated calcein release over a range of PNPs (2.01 to 3.90 MPa) with a total exposure time of 5s. Figure 6.24a shows the release profiles for both Nested-NBs (solid) and liposomes (hashed). The amount of release increased with increasing PNP for both samples up to a maximum Nested-NB release of 52.9 ± 10.3% with a corresponding liposome-only release of 35.3 ± 9.2% at PNP = 3.90 MPa. Considering only the difference in release between Nested- NBs and liposomes, a maximum difference of 26.2 ± 10.3% was achieved at 2.96 MPa (Figure 6.24b). The difference in release is comparable to the encapsulation efficiency of NBs within Nested-NBs (22 ± 2%), which would suggest that the efficacy of release of the Nested-NB is approaching 100%. Increasing the PNP further led to a decrease in the difference in the release profiles, as maximum Nested-NB release is achieved, whilst the increased acoustic energy may continue to contribute to thermal release. As no release was previously observed with pulsed HIFU exposures, the ability of CW HIFU to induce release is useful in identifying the release mechanism.

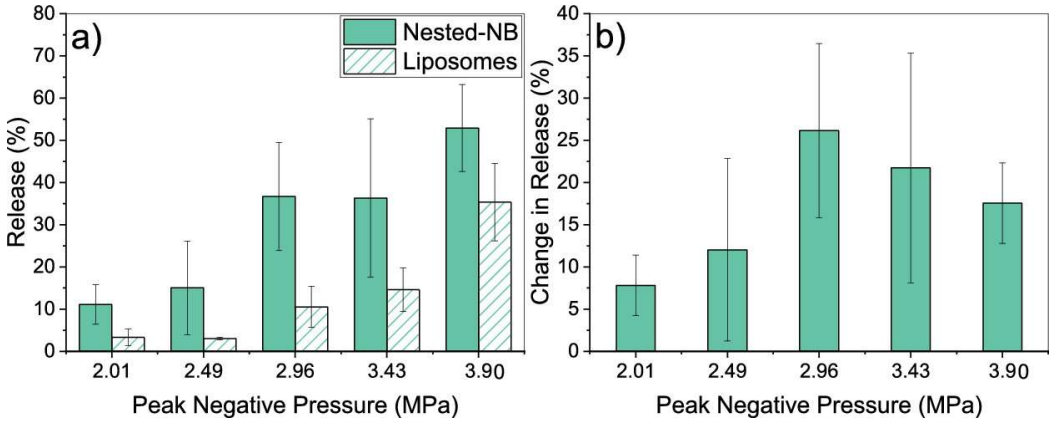

Figure 6.24 a) Release profile of Nested-NBs and liposome controls after continuous wave (CW) HIFU exposure at PNPs ranging from 2.01 to 3.90 MPa. (b) Difference in the release of Nested-NBs compared to liposome controls.

6.7.1 Contribution of Thermal Effects to Release

To determine the influence of any thermal effects on drug release, a thermocouple was used to measure the maximum temperature of the solution during CW HIFU exposures (Figure 6.25a). For PNPs of 2.01 – 3.43 MPa, maximum temperature remained constant at 35-40 ° C, before an increase to 58.2 ± 6.5 ° C at 3.90 MPa.

The effect of these temperatures alone, in the absence of an acoustic trigger, was investigated using a fluorescence spectrometer equipped with a temperature-controlled cuvette holder. A temperature ramp was performed, with an initial temperature of 22 ° C, and fluorescence of Nested-NBs was measured in 5 ° C intervals up to 62 ° C, with the sample remaining at each temperature for 2 minutes (Figure 6.25b). Minimal release (< 2 %) was observed up to 37 ° C, at which point release increases following a sigmoidal trend. Using parameters from the sigmoidal trend, release plateaus at 43.6 ± 4.2 % for temperatures > 55 ° C. This value corresponds to the phase transition temperature of the primary lipid in Nested-NB liposomal bilayer (DSPC, T_m = 55 ° C). At this point, the closely packed, gel-phase lipids in the bilayer being to transition to a disordered liquid crystalline phase. This transition is commonly associated with leakage of the liposomal content due to reduced lipid packing, and hence reduced van der Waals interactions by acyl chains. These results also agree with those in the literature for calcein-loaded phosphatidylcholine liposomes[223], where maximal leakage occurs as the gel-phase transition temperature is approached. Minimal thermal release is observed for temperatures < 40 ° C, which correspond to PNPs of 2.01 – 3.43 MPa, similar to the trend shown in Figure 6.25a in which liposome only samples show no, or only small amounts, of calcein release. When temperatures increase above 40°C, i.e. for PNP of 3.90 MPa (T_{max} = 58 ° C), calcein release rapidly increases and this is again reflected in Figure 6.25, in which liposome only release increases significantly.

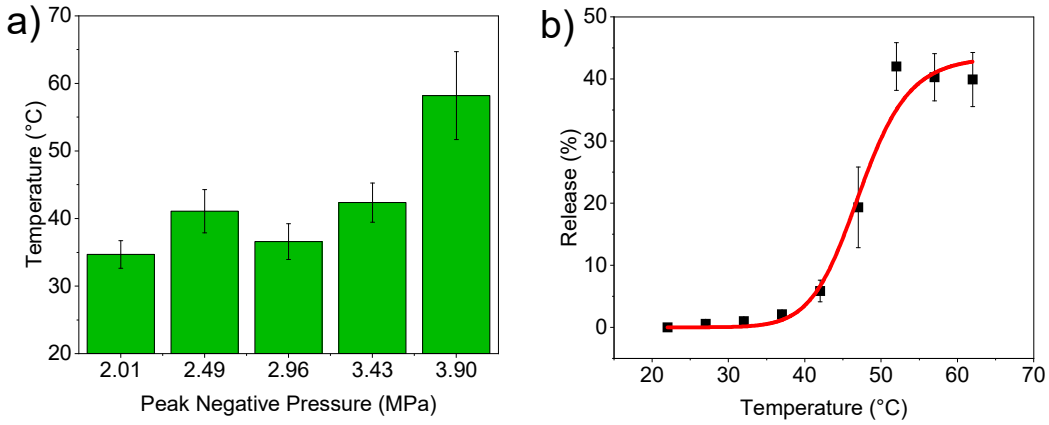

Figure 6.25 - a) Maximum temperature of Nested-NBs during CW HIFU exposure for PNP of 2.01 – 3.90 MPa, measured using a thermocouple. b) Percentage calcein release from Nested-NBs during a temperature ramp starting initially at 22 °C and increasing in 5 ° C intervals up to 62 °C, with the sample remaining at each temperature for 2 minutes.

6.7.2 Vaporisation Dynamics of Perfluorocarbon Droplets

Although NBs are present in the Nested-NB sample, RMM identified that 79 ± 4% of the population concentration consists of negatively buoyant particles, which may be a combination of liposomes and C_4F_{10} droplets (Figure 6.5). As such, it is reasonable to assume

that a similar proportion of encapsulated particles within the Nested-NBs would be negatively buoyant. Additionally, because the modal size of encapsulated particles (~140 nm) is less than the limit of detection of RMM (~200 nm), the existence of bubbles of this size cannot be confirmed. Because of the inverse relationship between the Laplace pressure and bubble radius, in addition to the density of the C_4F_{10} gas core used in our experiments compared to more commonly utilised perfluoropentane (C_3F_8) (11.2 vs 8.2 kg/m^3), it is increasingly likely that as particle size decreases, a subpopulation of PFB droplets would exist.

The bulk boiling point of C_4F_{10} is −1.7° C; however, confinement into either a bubble or a droplet will elevate this boiling temperature because of the associated pressure increase due to the Laplace pressure. The Clausius−Clapeyron relation, modified to include the Laplace effect (Equation 6.2) describes the change in boiling point of a liquid from confinement into a droplet. Using this, we can investigate the hypothesis that our Nested-NBs contain encapsulated C_4F_{10} droplets, which undergo rapid phase conversion during CW-HIFU exposure, triggering liposomal drug release.

$$T_1 = \left[\frac{1}{T_0} - \frac{R}{M_w \Delta_{vap} H} \ln\left(1 + \frac{2\sigma}{r_d P_0}\right)\right]^{-1} \qquad \text{Equation 6.2}$$

where T_1 is the elevated boiling temperature, T_0 is boiling point (271.4K) at atmospheric pressure P_0 (101.3 kPa), M_w is molecular weight of PFB (238.03 g/mol) , $\Delta_{vap}H$ is enthalpy of vaporisation (100 kJ/mol), σ is surface tension and r_d is droplet radius.

The predicted elevated boiling temperature for PFB particles of varying diameter is shown in Figure 6.26a for surface tensions ranging from 5 to 20 mN/m, covering expected values for fluorocarbon droplets and bubbles.[215] For PFB particles at room temperature (21 °C) with diameters between 100 and 200 nm, the majority of particles lie below the vaporization curve and hence would be expected to exist as liquid droplets.

This is in agreement with previous work published in our group, in which MS-NBs experience a rapid increase in size, measured via DLS, when heated above a threshold temperature of 57 °C, suggesting the occurrence of a phase transition from liquid to gas.[204] This transition temperature matches closely to the predicted value in Figure 6.26a for a surface tension of 10−15 mN/m. Considering a PFB droplet of 140 nm in size, corresponding to the modal encapsulated particle size determined by TEM, temperatures of 22.9 °C and 37.7 °C would be required for vaporisation for droplets with σ = 5 and σ = 10 mN/m, respectively. As such all PNPs investigated would be capable of vaporisation at surface tensions like those expected for PFB droplets, supporting our hypothesis of a phase change trigger. These results are also

concurrent with those from Wu et al. [224] in which increasing the pulse duration was found to lower the threshold for acoustic vaporisation of PFB droplets, using similar US parameters (1 MHz, ≤ 5MPa).

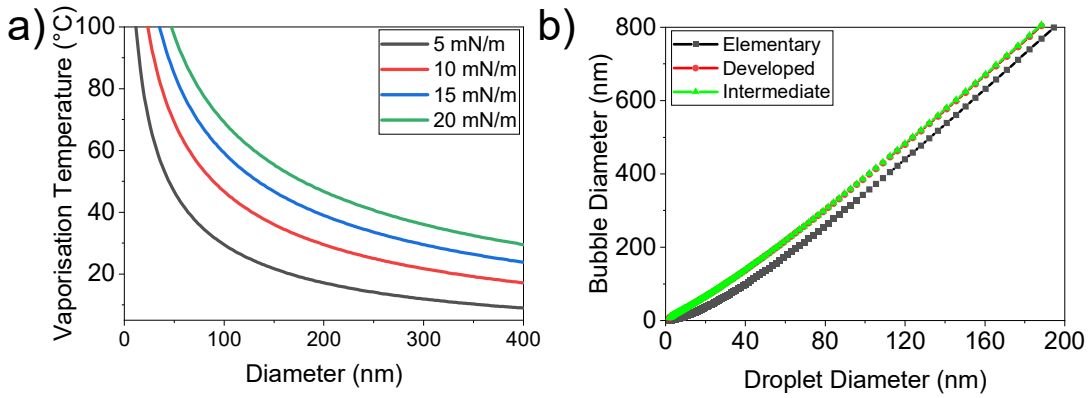

Figure 6.26 - a) Vaporization temperature of a PFB droplet with varying surface tension calculated using the Clausius−Clapeyron relationship (Equation 4). b) Predicted final bubble diameter after vaporization of a PFB droplet comparing three models documented from ref[225].

To determine whether droplet vaporization would be capable of inducing liposomal drug release, a model developed by Evans et al. [225] was used to predict the expected diameter increase of the resultant bubble post-vaporization. There are three models with increasing complexity, which we have labelled elementary, developed, and intermediate.

For all models, it is assumed that after phase-change, the number of bubbles is equal to the number of droplets before i.e. there is no coalescence. The elementary model assumes that post-vaporisation, the number of molecules of the volatile phase remains constant, such that there is no change in solubility. This neglects the fact that as bubble or droplet size varies, the Laplace pressure too will change, and hence too will solubility. A consequence of this is that for larger droplets ($r_d > 10^{-6}$ m), the activated volume ratio ($\frac{v_b}{v_d}$, where v_b and v_d are volumes of the bubble and droplet respectively), is independent of initial droplet size. For our system where $r_d \sim 10^{-7}$ m, this may have little influence on results. The intermediate models adds additional complexity by accounting for a change in solubility, and assuming partial equilibration of the core with a surrounding region of the particle.

The change in solubility is described by the Kelvin equation (Equation 6.3), where R is the ideal gas constant (8.32 $J.mol^{-1}K^{-1}$) T is temperature, S_0 is bulk solubility of the volatile material, S_t is enhanced solubility of the material under confinement inside the bubble or droplet, γ_t is surface tension where the subscript refers to either droplet (t = d) or bubble (t = b). Similarly, $V_{m,t}$ is molar volume of the bubble or droplet and r_t is radius. Assuming no change in the number of droplets and bubbles post-vaporisation, the effect of this is to supress the volume increase as solubility inside the confined volume decreases, and gas is drawn out of the bubble into the surrounding liquid. The predicted bubble size post-vaporization is shown in Figure 6.26b for all the three models, assuming a droplet surface tension of σ_d = 10 mN/m and bubble surface tension of σ_b = 20 mN/m. For droplets of 100−200 nm diameter, all models produced similar results with an expected bubble diameter post-vaporization of >300 nm, that is, larger than the modal size of our encapsulating liposomes. This in turn suggests that this expansion may lead to liposomal rupture, and hence triggered drug release, consistent with our results.

$$RT \ln\left(\frac{S_t}{S_0}\right) = \frac{2\gamma_t V_{m,t}}{r_t} \qquad \text{Equation 6.3}$$

6.8 Conclusion

In this chapter, NBs were produced using microfluidics (MS-NBs), determining their size and concentration using transmission electron microscopy and light scattering, whilst the use of resonant mass measurement confirmed the presence of sub-micron gas bubbles. MS-NBs demonstrated diagnostic potential, providing contrast for clinically relevant B-mode imaging. Their therapeutic potential was also shown through the use of HIFU to trigger the destruction of MS-NBs. This was further investigated by their encapsulation within model-drug loaded liposomes to form Nested-NBs.

The resultant Nested-NBs displayed good echogenicity and drug loading stability. Triggered release of the drug payload was investigated using HIFU in combination with PCD, such to cause destruction of the encapsulated NB and trigger liposomal rupture. During PW-HIFU (1 % and 50 % duty cycle) exposure, MS-NBs and Nested-NBs both demonstrated harmonic and broadband acoustic emissions, indicating the occurrence of stable and inertial bubble cavitation. It would be expected that these interactions would lead to triggered release of the encapsulated drug payload within Nested-NBs, however no drug release was observed even for PNPs of between 1.54 - 4.83 MPa. The cholesterol content of the Nested-NB was reduced from 32 % to 22 % and 12 % to reduce membrane stiffness, and promote drug release, but had little effect on the release profile.

In contrast, the change of modality to CW-HIFU produced drug release across a range of PNPs (2.01 – 3.90 MPa). The maximum difference in release compared to a liposome only control is comparable to the encapsulation efficiency of NBs within Nested-NBs (22 ± 2%), which would suggest that the efficacy of release of the Nested-NB is approaching 100%. This is likely associated with the increase in heating due to CW-HIFU, and suggests that a synergistic effect of an acoustic and thermal trigger required for release from Nested-NBs. Increasing the PNP further led to a decrease in the difference between the release profiles, as maximum Nested-NB release is achieved, whilst the increased PNP may continue to contribute to thermal release. These observations can be understood if, at room temperature, our Nested-NBs contain a mix of both encapsulated PFB NBs and PFB droplets. During CW HIFU, the sample temperature was found to increase above a predicted threshold such that the PFB droplets underwent a phase change from the liquid to gas state. The subsequent increase in their diameter, predicted to be by a factor of 3, could then lead to liposome rupture and drug release. The fact that PW US does not trigger drug release from Nested-NBs may prove beneficial, as drug loading will be stable during diagnostic imaging and release not triggered until the application of CW-HIFU. Thus, Nested- NBs have diagnostic potential, providing contrast enhancement for clinically relevant US frequencies, and the ability to trigger drug release through the vaporization of PFB droplets.

7 Experimental Procedures 2

7.1 NB Preparation, Production and Isolation

Due to the relationship between bubble diameter and terminal rise velocity (Equation 3.25), centrifugation can be used to isolate bubbles of varying size. [226] As such, a MB suspension was initially produced, and then centrifuged at different relative centrifugal force (RCF) to separate desired bubble populations.

The initial MB suspension was prepared using 95:5 molar ratio of the lipids DPPC (1,2-dipalmitoyl-sn-glycero-3-phosphocholine) and DSPE-PEG2000 (1,2-distearoyl-sn-glycero-3-phosphoethanolamine-N-[methoxy(polyethylene glycol)-2000]) to form the stabilizing shell. Lipids were initially dissolved in 50:50 chloroform:methanol solution, and the solvent removed under nitrogen for ~ 60 mins, followed by vacuum desiccation overnight. The resultant lipid film was then rehydrated with PBS containing 1 % (v/v) glycerol, by stirring and heating at 55 °C for 20 min, to a final lipid concentration of 2 mg/mL. The lipid solution was then tip sonicated (20 kHz, 150 W, Sonifier 250, Branson, USA) for 40 min at 4 °C to produce small lipid vesicles (~ 100 nm). This solution was then centrifuged at 17,000 g for 30 mins and aspirated, firstly to remove any titanium deposited during the tip sonication process, and secondly to ensure the absence of any large lipid aggregates.

To produce the initial MB suspension, 1 mL of vesicle solution was added to a 1.5 mL glass vial and the solution and vial headspace was saturated with C_3F_8 (perfluoropropane) gas, maintaining a gas pressure of 300 mBar for 2 min. Gas flow was controlled using a p-pump (Mitos P-pumps, Dolomite, UK) and a PC using the Dolomite Flow Control Centre [205]. The vial lid was then replaced and sealed with parafilm, prior to mechanical agitation for 45 s (VialMix, Bristol Myers Squibb, US). This solution was then added to 9 mL of PBS in a 15 mL centrifuge tube and centrifuged at RCFs of 100, 500 or 1,000 g to isolate NBs of varying size. Post-centrifugation, NBs were isolated by removal of the lower 6 mL of solution using a long, fine needle (19g x 2.0", Terumo) and 5 mL syringe (total volume > 6 mL), taking care to avoid cross-contamination of the NB sample and MB foam layer.

7.2 NB Population Characterization

To determine the size and concentration of sub-micron bubble populations, the light scattering techniques of Nanoparticle Tracking Analysis (NTA, size and concentration) and Dynamic Light Scattering (DLS, size only) were used.

7.2.1 Nanoparticle Tracking Analysis

For NTA measurements (NanoSight NS300, Malvern Panalytical, UK), NB samples were measured at between 1- 50 x dilution in PBS (lipid concentrations of ~ 4 – 200 μg/mL), depending on the initial sample concentration, such that recorded videos were at optimal particle concentration for particle tracking (i.e. ~ 10^8-10^9 particles /mL). Samples were illuminated with a 488 nm laser, and individual particles were tracked and analysed using NTA 3.3 software. During data acquisition, the camera level (a marker of image intensity) was set to between values of 3-4, such that highly scattering particles (i.e. NBs) were detected, but particles with a lower scattering intensity (i.e. lipid vesicles) were not.

Measurements consisted of 5 x 60 s videos, between which the sample was advanced to observe and track a unique set of particles. Each video was then post processed using a software detection threshold of 20, and the mean and standard error for each sample calculated.

7.2.2 Dynamic Light Scattering

DLS (Zetasizer NanoZS, Malvern Panalytical, UK) measurements were conducted using NBs at their yield concentration, corresponding to a lipid concentration of ~ 0.2 mg/mL. Samples were illuminated with a 633 nm and backscattered light detected at an angle of 173 °. Distributions shown are based on an intensity distribution due to NB samples containing a mixed population with different optical properties. As such, it should be noted that sizing data will be weighted towards larger particle sizes.

7.2.3 Brightfield Microscopy

Brightfield microscopy was used to determine the concentration of optically visible bubbles in NB samples. 30 uL of sample was introduced into a 50 μm deep chamber on a glass slide, and NBs allowed to rise for 5 mins to ensure they were all in the same focal plane. An inverted microscope (Nikon 90i, Japan) was used to image MBs with a 40 x objective (NA = 0.6) and a CCD camera (DS-Fil 5Mega pixel, Nikon, Japan) was used to take 10 images for each sample. Due to the resolution limit of our microscopy system (~ 600 nm, 0.16 μm/pixel), determination of NB size is not reliable. Image analysis was performed using a custom ImageJ script, to determine the total number of particles in each image, and then converted to a concentration value.

7.3 Cell Culture

Cells were stored in a moisture-controlled incubator at 37 °C with a 5% CO2 atmosphere and cultured in 25 cm^2 flasks. Cells were handled following aseptic technique, inside a Class II A1 Biosafety Cabinet. The SW480 colorectal cancer cell line was provided by European

Collection of Authenticated Cell Cultures (ECACC). Cells were cultured in Dulbecco's Modified Eagle Medium (DMEM/F-12; Gibco, US) supplemented with 10% fetal bovine serum, 2 mM GlutaMax. Passage numbers were kept below 50 for all experiments. For sonoporation studies, cells were seeded onto a microfluidic device (μ-Slide VI 0.4, iBidi, Germany).

7.3.1 Well Plate Culture

For well-plate experiments, SW480 cells were cultured at an initial seeding density of 2 x 10^6 cells per well. Cells were cultured for 48 hours prior to all experiments. During acoustic exposure, a total volume of 2.5 mL of the uptake assay (with or without MBs) was added to couple to the transducer element.

7.3.2 Microfluidic Culture

Each microfluidic device consisted of 6 individual channels with a channel height of 0.4 mm, length of 17 mm, and width of 3.8 mm. Channels were pre-treated with iBiTreat for culture of adherent cell lines. Cells were detached from the culture flask by incubation with TrypLE (Thermo Fisher Scientific) for 5 mins and counted using a hemocytometer. The cell suspension was adjusted to a concentration of 7 x 10^5 cells/mL and 30 μL of this suspension pipetted directly into the microfluidic channels. Devices were then inverted such that cells adhered to the top of the microfluidic channel. After 2 hours, the devices were righted and 60 μL of DMEM added to each reservoir simultaneously. Cells were cultured on-chip for 48 hours prior to sonoporation studies. During on-chip culture, devices were placed on a raised surface to promote gas exchange.

7.4 Acoustic Set-Up and Ultrasound Exposure

An unfocused, 2.25 MHz central frequency transducer (V323-SM, Olympus, US), with an element diameter of 6.35 mm, was used for sonoporation studies. The transducer was driven by a +53 dB power amplifier (A150, E&I Ltd, USA) and a computer-controlled function generator (TG5011A, Agilent, USA) was used to provide sinusoidal burst cycles to the amplifier. Free-field pressure of the transducer was determined using a needle hydrophone (0.2 mm, Precision Acoustics Ltd, UK), calibrated by the National Physics Laboratory (Middlesex, UK). Each US exposure consisted of the following parameters: Mechanical Index = 0.6, Driving Frequency = 2.25 MHz, Peak Negative Pressure = 900 kPa, Pulse Repetition Frequency = 1 kHz, Duty Cycle = 1 %, Total Duration = 5 s. The US transducer was coupled to the top of the microfluidic chip using a 20 mm gel stand-off pad (AquaFlex, Parker, US) ensuring the channel was situated in the far-field of the US beam [48]. Here, the US beam width can be defined by Equation 7.1 [227], where α is half angle beam spread, k is a constant, c is speed of sound, f is frequency and D is element diameter. k is a constant depending on the

point that the beam spread is calculated. For – 6 dB (i.e. 50 % reduction) and for – 20 dB (90 % reduction) k = 0.56 and 1.08 respectively.

$$\sin\left(\frac{\alpha}{2}\right) = \frac{kc}{fD} \qquad \text{Equation 7.1}$$

For our system, the beam width is then predicted to be 2.3 mm (-6 dB) and 4.50 mm (- 20 dB), and hence the majority of acoustic energy will be localised to a region in the microfluidic channel. The microfluidic chip was positioned above a water bath with an acoustic absorber positioned at a 45 ° angle to reduce acoustic reflections and the formation of standing waves (Figure 7.1a).

7.5 Sonoporation Studies

For the sonoporation studies, a red fluorescence membrane probe (70 kDa Texas-Red Dextran, ThermoFisher) was used to quantify uptake, whilst a green fluorescence live stain (CellTracker Green CMFDA) was used to determine cell viability post treatment 18. NB samples were prepared as described previously and mixed with TexasRed-Dextran to reach the desired NB concentration and a final Dextran concentration of 14 μM. For control samples (no treatment and US only), PBS containing 14 μM Dextran was used. NBs were then added to the microfluidic channels by pipetting 60 μL of sample directly into a reservoir, and then withdrawal of 60 μL from the opposing reservoir. This was repeated in triplicate to ensure the channel contained only NB solution. Chips were then covered with foil and left for 60 mins at 21 °C to aid sonoporation by allowing NBs to rise to the top of the channel and hence in contact with the cell monolayer (Figure 7.1).

For all treatment conditions, the adjacent channel was left blank to avoid cross over between of US treatment between channels. Channels were then treated with US (where appropriate) and left for a further 10 minutes to promote uptake. Channels were then washed with DMEM (5 x 100 μL), followed by CellTracker Green (5 x 100 μL, 2 μM) and incubated at 37 °C for 30 min. Channels were then washed with DMEM (5 x 100 μL) prior to confocal fluorescence imaging.

7.6 Confocal Fluorescence Imaging

Microfluidic chips were imaged using a laser scanning confocal microscope (Leica DMi8/SP8) to determine the location of live cells and quantify Dextran fluorescence. Due to the confocality of the microscope (1 Airy Unit), it was possible to image exclusively cells adhered to the top of the microfluidic device, and hence exposed to NBs. It should be noted that cells along the bottom of the channel did not show any evidence of uptake and the large majority of cells remained adhered to the top of the channel. Images were taken in sequential mode using and 488 nm and 532 nm lasers with emission windows of 493 – 749 nm and 557

– 781 nm corresponding to the CellTracker Green and TexasRed-Dextran respectively. These values were determined by the in-built DyeAssistant software to maximize fluorescence intensity and minimize cross talk.

Full fluorescence and brightfield maps of each microfluidic channel were taken using the TileScan feature, consisting of multiple images (512 x 512 px) which were then combined to create the final image. The autofocus setting was used in between each image location, determining the focal plane with the maximum intensity in the green fluorescence channel across 5 steps within a user-centred 60 µm window.

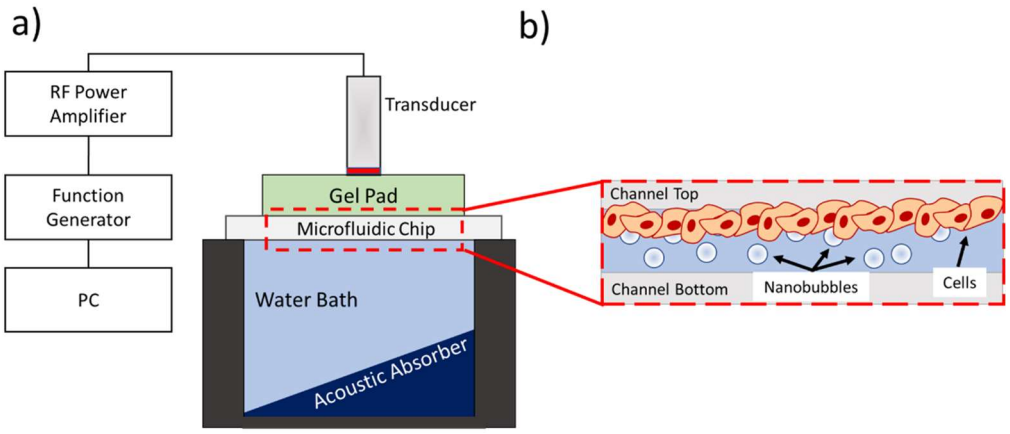

Figure 7.1 - Schematic showing the acoustic and microfluidic set-up used for sonoporation experiments. (a) The transducer was driven by a +53 dB power amplifier and a computer-controlled function generator was used to provide sinusoidal burst cycles. The transducer was coupled to the top of the microfluidic chip using a gel stand-off pad, positioned above a water bath with an acoustic absorber positioned at a 45 ° angle. (b) Schematic describing how cells were cultured on the top of the microfluidic channel so that the intrinsic buoyancy of bubbles resulted in them being in direct contact with cells. Not to scale.

7.7 Fluorescence Image Analysis and Quantification of Uptake

Confocal fluorescence maps were analysed using image processing tools in MATLAB (2019b, Mathworks Inc, USA) to determine the Dextran fluorescence intensity inside viable cells. An image mask was generated from the CellTracker Green image and then applied to a background subtracted Dextran image. As the US exposure is constrained to a discrete region in the centre of the microfluidic channel, an average red fluorescence profile in the x-direction along the chip was calculated to identify this region. The fluorescence profile was smoothed using a Savitzy-Golay filter (2 mm window) followed by a baseline subtraction [228]. From these profiles, the total fluorescence intensity was quantified. Initially, a Gaussian distribution was fit to the smoothed data to determine the peak centre, x_c, and standard deviation, σ. If successful, the background subtracted, non-smoothed profile was integrated between (x_c - 2σ) and (x_c + 2σ) to determine the total intensity. If the fit was unsuccessful (i.e. no clear uptake

detected) then the data was integrated across a 7 mm window situated in the centre of the profile.

7.8 Flow Cytometry

A flow cytometer (CytoFlex S, Beckman Coulter, US) was used to quantify fluorescence from a FITC live stain and 7-AAD, a membrane impermeable DNA stain, to determine the occurrence of sonoporation. The flow cytometer was equipped with a 488 nm and 561 nm laser, and band pass filters of 525 nm/40 nm and 690 nm/50 nm. All flow cytometry measurements were performed by Dr Sally Boxall and Dr Ruth Hughes of the Bio-imaging and Flow Cytometry suite, University of Leeds. A minimum of 10,000 valid events were collected for each sample.

8 The Influence of Nanobubble Size on Sonoporation and Stability

Motivation

NBs are typically produced at the same time as polydisperse MBs and are subsequently separated either by flotation or centrifugation [229]. Throughout the literature the NB isolation techniques and subsequently the size of the NBs collected varies greatly (100 – 800 nm) [207] making it difficult to compare their effectiveness as therapeutic delivery vehicles. Further, many of these NB populations contain a proportion of large microscale bubbles (> 5 μm). As described by Doinikov and Bouakaz [230] the shear stress exerted by an oscillating bubble on a cell membrane is non-linearly proportional to initial diameter. Depending on the model used, an 800 nm NB will produce shear stresses between 10^2 - 10^4 times greater than that of a 100 nm NB. Additionally, the variation in bubble diameter will also lead to changes in resonance frequency ($f_0 \propto 1/r_0$), which will greatly affect the magnitude of their volumetric oscillations dependent on the driving frequency, and hence influence their performance for both therapy and diagnosis. The size of the NB will also affect their ability to extravasate and accumulate in tumour interstitial space, one of the most appealing aspects of NBs.

Variation in reported NB size may also be associated with the challenge of accurately determining NB size and concentration. Due to their sub-micron nature, typical sizing techniques used to characterize MBs (brightfield microscopy, Coulter counters) are unsuitable. Light scattering techniques such as DLS and NTA are routinely used to determine nanoparticle size by observing their Brownian motion, with these techniques often applied to NBs. However, a typical NB sample contains a mixed population of aqueous-cored liposomes and gas-cored NBs, which these techniques do not overtly distinguish. This, coupled with classical bubble theories that predict NB lifetimes should be on the order of microseconds, has led to some scepticism in the research community over the existence of stable NBs. Whilst some techniques (Resonant Mass Measurement, holographic NTA[117]) can distinguish between bubbles and non-bubbles, either by comparing particle density to the medium, or by measuring particle phase contrast, they are not yet widely available.

For effective translation into clinical use, the size and concentration of NBs should be able to be accurately and reproducibly measured, allowing for determination of their therapeutic effectiveness. In this chapter, the relationship between NB size and their therapeutic capability (i.e. to promote drug uptake) is investigated. Firstly, acquisition settings for a commercially

available NTA system are optimized, such that sub-populations (bubbles and liposomes) in a NB sample can be distinguished, and that the size and concentration of NBs is measured exclusively. This method is then used in combination with DLS and optical microscopy to characterise 3 NB populations of varying mean size, isolated via centrifugation. The effectiveness of these different NB populations across a range of concentrations was then compared in uptake experiments, using clinically relevant ultrasound frequencies, and by observing uptake of fluorescent Dextran into SW480 cell monolayers in a microfluidic device. NTA was also used to measure the stability of different sized NBs, at either matched NB or lipid concentration, revealing the link between their therapeutic performance and stability, and highlighting potential mechanisms behind their stability.

8.1 Nanobubble Isolation and Characterization

8.1.1 NB Isolation by Centrifugation

NBs in this section were prepared by mechanical agitation and with a C_3F_8 gas core, increasing the likelihood they remain as gas-cored NBs, as opposed to droplets, due to the reduced molecular weight. This method also closely mimics many published NB studies [80,85,101,110,112,150,231], and as such has increased relevance to the field. The liposome solution used to produce NBs was homogenized via tip-sonication such that the resultant population was monodisperse and free of large aggregates, facilitating discrimination between liposomes and larger NBs. The size distribution of this liposome pre-cursor solution is shown in Figure 8.1, measured by (a) NTA and (b) DLS, with both techniques showing a monodisperse population.

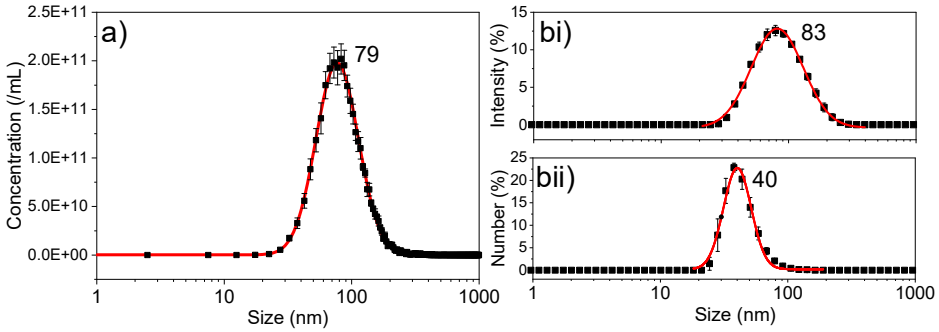

Figure 8.1 – Size distribution of tip-sonicated liposomes used as a pre-cursor solution to produce NBs. Characterised by a) Nanoparticle Tracking Analysis and b) Dynamic Light Scattering showing (i) Intensity and (ii) Number weighted distributions.

Liposome concentration determined by NTA was 3.19 ± 0.23 x 10^{12} /mL and a modal size of 79.4 ± 36.1 nm, compared to sizes of 83.2 ± 46.6 nm and 40.0 ± 12.1 nm determined by DLS for intensity and number weighted distributions respectively. The variance in modal size between methods can be attributed to the increased LOD associated with the NTA system (i.e. > 50 nm), and hence a potentially erroneous increase in modal size, as smaller particles in the

population are not detected by the technique. Additionally, the decrease in modal size between the intensity and number based DLS distributions is to be expected due to the non-linear relationship between particle size causing intensity-based distributions to be weighted towards larger particles.

To investigate the effect of NB size on sonoporation, control over the size of NB populations is required. Here, polydisperse populations of MBs were produced and centrifugation used to isolate different size NBs. As the terminal rise velocity of NBs is dependent on their size, as well as gravitation acceleration, varying the Relative Centrifugal Force (RCF) and isolating NBs from set heights will allow isolation of NBs of different sizes. To do this, MB samples (1 mL total volume) were diluted by a factor of 10 and centrifuged in a 15 mL sample tube, facilitating NB isolation from different heights. For each RCF, samples were labelled 1-5 based on their height and consisted of 2 mL aliquots where Sample 1 refers to the bottom sample and 5 refers to the top (Figure 8.2a).

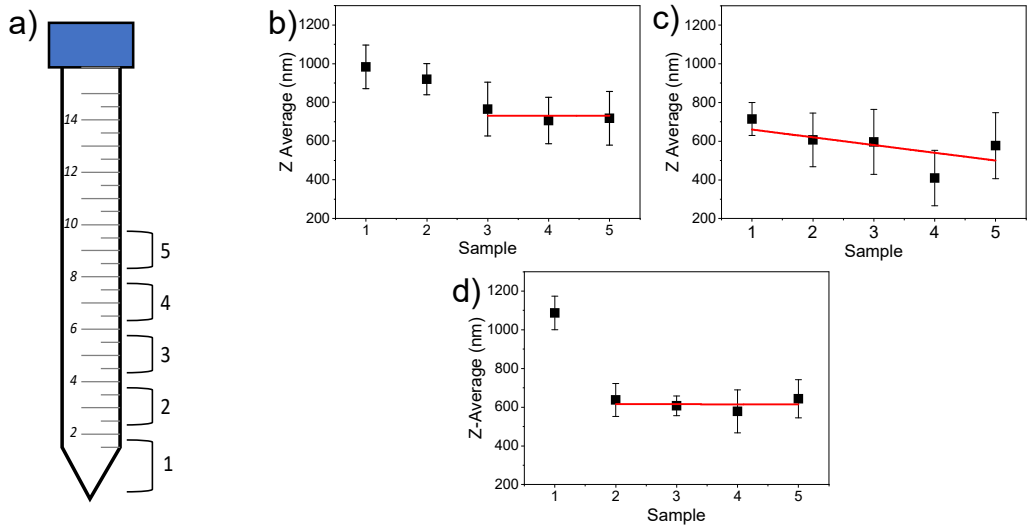

Figure 8.2 – a) Schematic of how NB samples were isolated from varying heights after centrifugation, for samples labelled 1-5. (b-d) DLS data showing the Z-Average size of NB samples separated by centrifugation at RCFs of (b) 100 g, (c) 500 g and (d) 1,000 g (N=3 for all).

The size distribution of each sample was then characterised using DLS. Although unable to distinguish between liposomes and NBs, DLS has a larger measurable size range (10 – 10,000 nm), providing additional information on the presence of the total bubble population (i.e. both NBs and MBs). Additionally, by measuring samples at relatively high bubble concentration, and hence optical density, gas-cored bubbles would be expected to dominate scattering events due to their increased size (i.e. > 100 nm) and scattering cross section. The Z-Average size (determined by the exponential decay of the autocorrelation function) for NBs separated using RCFs of 100 g, 500 g and 1,000 g are shown in Figure 8.2b, c & d respectively. For RCF = 100 g, the size of NB samples steadily decreased from 984 ± 113 nm for sample 1 down to

718 ± 139 nm for Sample 5. For samples 3-5 the average size also appeared to plateau demonstrated by the linear fit shown in Figure 8.2b, in which the gradient was fixed at 0, yielding a y intercept of 730 ± 18 nm. For RCF = 500 g, NB size was initially smaller (sample 1, Z-Average = 715 ± 85 nm) as expected, although NB size remained relatively constant regardless of the height of isolation. For RCF = 1,000 g, the initial size of sample 1 was 1087 ± 87 nm, larger than that for any other measured populations, which may be due to the formation of a bubble "foam" at the top of the tube, and subsequent bubble coalescence. For samples 2-5, size rapidly decreased to a constant value of 616 ± 54 nm, as determined by the linear fit shown in Figure 8.2c. Whilst the RCF and the height at which the sample is isolated influenced NB size, the change in size between samples was not significant enough to warrant this as reproducible isolation technique. However, using this isolation technique samples 3-5 across all RCFs demonstrated constant size. As such, following these experiments NBs were isolated using only samples 3-5 (i.e. isolation of NBs below the 6 mL line) to isolate 3 NB populations of distinct size.

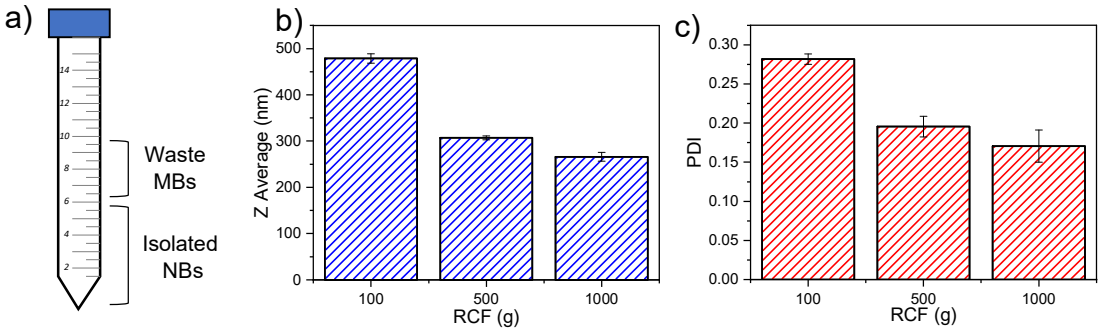

Figure 8.3 – a) Schematic showing the isolation process of NBs after centrifugation. DLS sizing data of NBs separated using the lower 3 samples after centrifugation at varying RCF of 100, 500 and 1,000 g. b) Z-Average and (c) Polydispersity Index (PDI) of each sample.

Results of populations for each RCF (100 g, 500 g, 1,000 g) after isolation of samples 3-5 characterised by DLS, are shown in Figure 8.3. Average size decreased with increasing RCF, with each population size distinct from one another, and respective sizes of 479 ± 10 nm, 307 ± 4 nm and 266 ± 10 nm. Additionally, the polydispersity index (PDI), decreased with increasing RCF, as a greater proportion of larger bubbles are removed from the sample leading to a more monodisperse population.

Following this, RCF was further increased to isolate a fourth, smaller (< 200 nm) NB population for comparison. As terminal rise velocity is inversely proportion to the square of the particle size, RCF will also need to be increased accordingly. Figure 8.4 shows DLS sizing data for NB samples isolated at RCFs of 1,700 g, 2,500 g and 4,000 g, resulting in average sizes of 544 ± 355 nm, 275 ± 25 nm and 285 ± 184 nm respectively over two repeats. Compared to our previous smallest NB sample (RCF = 1,000 g, Z-Average = 266 ± 10 nm), there is no considerable decrease in size observed. The large error associated with these higher RCF samples also suggests a lack of reproducibility. Additionally, the PDI of each population significant increased compared to previous values to values > 0.4, suggesting a polydisperse population distribution. This may be due to increased RCF promoting bubble coalescence or decreased optical density of samples and non-negligible contribution from smaller liposomes to the scattering.

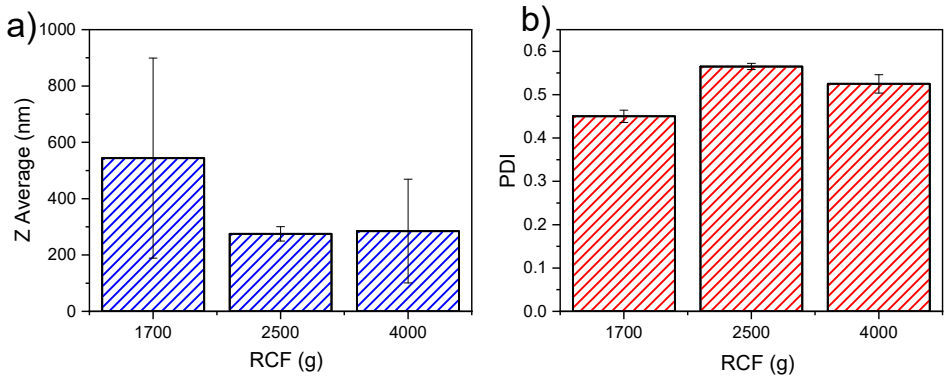

Figure 8.4 – DLS sizing data of NBs separated using higher RCF values (1700, 2500 and 4000 g) to isolate a smaller, fourth discrete NB population. A) Z-Average and (b) Polydispersity Index (PDI) of each sample. Error bars represent the standard error over 3 independent samples.

Although useful for determining the average size of a bulk population, DLS does not directly measure individual particles and hence cannot determine particle concentration or distinguish between particles with different optical or physical properties. To assess the therapeutic and diagnostic effectiveness of NBs, accurate concentration determination is required, to compare populations at matched particle concentration or gas volume. Hence, development of a technique that can accurately quantify the concentration of gas-cored NBs is crucial for the pre-clinical and clinical translation of therapeutic NBs.

8.1.2 Nanoparticle Tracking Analysis to Distinguish Nanobubbles

Nanoparticle Tracking Analysis (NTA) is a light scattering technique in which the Brownian motion of individual particles is tracked, diffusion coefficient determined, and particle size calculated. As individual particles are tracked, total particle concentration can also be determined. However, typically this system cannot distinguish between sub-populations with differing physical properties, such as the mixed population of liposomes and NBs present in

NB samples. An example of this is shown in Figure 8.5, in which NBs and their liposome precursor solution were both characterised using NTA. For both measurements, samples were measured at a matched dilution (1,000 x) and approximate lipid concentration (2 µg/mL) and acquisition settings (camera level = 12). It should be noted that the high dilution ratio is required such that samples are at the required particle concentration for NTA measurements (~ 10^9 /mL). Both NB and liposome samples had a modal size of 90 nm with respective concentrations of (3.09 ± 0.6) x 10^{12} /mL and (2.26 ± 0.11) ± 10^{12} /mL. This is in contrast to DLS data (Figure 8.1, Figure 8.2) where a marked increase in particle size is found. As such, the two populations are indistinguishable from each other, and it would be easy to conclude from NTA the absence (or a low concentration) of any NBs or sub-micron particles produced during mechanical agitation.

The relationship between scattered light intensity, I_s, and the change in refractive index between the medium (n_{water} = 1.33) and the particle, Δn, as well as size, r, is described in Equation 3.32. Due to their gas-core, NBs of equivalent size will scatter light more efficiently than liposomes. Assuming that the refractive index of NBs is close to that of air (n_{air} = 1) and the refractive index of liposomes to be $n_{liposomes}$ = 1.38 [232], the intensity of scattered light will be ~40 x greater compared to that from an equivalent size liposome (Equation 3.32, Equation 3.34). Previously shown DLS data also identified the average population size to be greater than this (300 – 500 nm) hence would be expected to be optically distinct from the sub-100 nm liposomes. As NTA measurements are not weighted towards scattering intensity, it is likely that the NB populations consistent mostly of small, low scattering particles (i.e. liposomes) with a sub-population of highly scattering, larger particles at a lower concentration

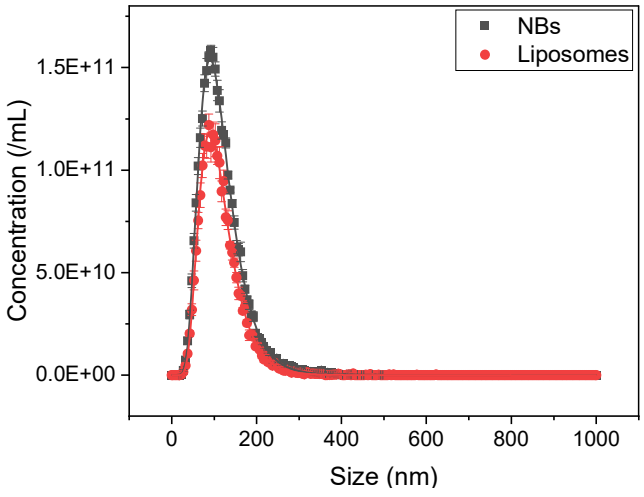

Figure 8.5 – Nanobubble (NBs) and liposome populations measured using NTA, measured at a dilution of 1,000 x in PBS and a camera level of 12. Both populations had a modal size of 90 nm, and total particle concentration of (3.09 ± 0.6) x 10^{12} and (2.26 ± 0.11) x 10^{12} /mL for NBs and liposomes respectively.

(i.e. bubbles), that are identified via DLS. During video acquisition on the NTA system, the camera level can be adjusted to increase or decrease the intensity of the acquired image.

To attempt to distinguish between NBs and liposomes, samples were measured at a higher concentration (100 x dilution, 20 μg/mL lipid concentration) and a reduced camera level (3), such that only highly scattering particles will be detected, and omit lower scattering particles. Images taken during NTA acquisition for characterisation of liposomes and NBs are shown in Figure 8.6, in which highly scattering particles are visible in the NB samples, but not in the liposome only sample. This indeed suggests that NB samples contains particles with an increased scattering cross-section compared to liposomes, although it is not clear whether this is due to differing optical properties, or simply size alone.

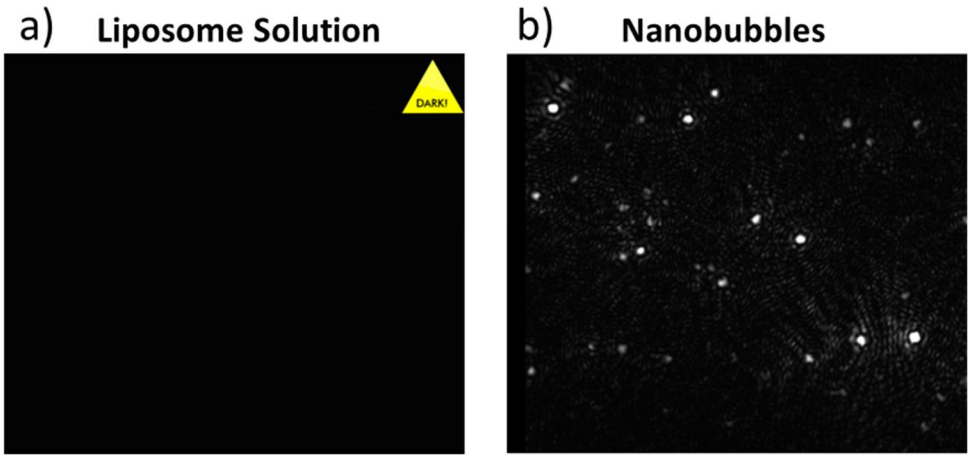

Figure 8.6 – Images taken during NTA acquisition with sample dilution of 100 x and camera level of 3 for (a) liposome and (b) nanobubble solution. At these acquisition settings, highly scattering NBs can be detected and subsequently tracked, whereas lower scattering liposomes are omitted from the measurement.

As a control, liposome only samples were imaged across a range of camera levels at a lipid concentration of 20 μg/mL, to determine the threshold at which they are visible. The mean intensity of the image NTA system was measured for camera levels ranging from 3 – 13, with the lower and upper bounds corresponding to acquisition settings where NBs and liposomes can and cannot be determined, respectively. As shown in Figure 8.7a, image intensity increased exponentially with increasing camera level and no signal was detected until a camera level of 8 (Figure 8.7g) whilst image intensity did not reach values that would be considered optimum until a camera level of 12 (Figure 8.7k), signified by the absence of the "dark" warning label on the image. Hence, variation of camera level for values < 8 are unlikely to affect population distributions when measuring NBs. In images where the camera level is ≥ 11, it becomes difficult to distinguish individual scattering events, likely due to the increased

total particle concentration compared to optimal measurements (i.e. 1,000 x dilution, Figure 8.5).

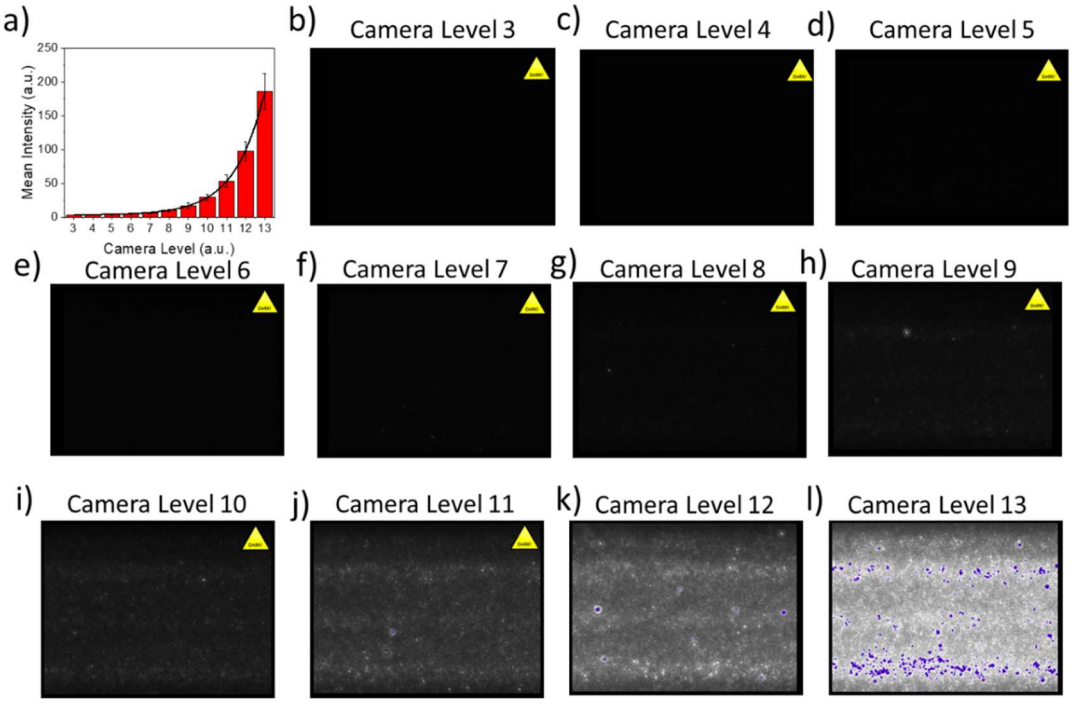

Figure 8.7 The effect of varying Camera Level on NTA image acquisition during measurement of the pre-cursor liposome solution at a lipid concentration of 20 µg/mL, similar to NB measurements. A plot of mean intensity (a) in a central area of each image (b-l) for camera levels varying between 3-13, showing no detectable scattering from liposomes until the camera level is > 9, in comparison to typical values of 3-5 used for NB measurements. Hence this shows that at lower camera levels, only NBs are detectable. Further, this also shows exponential relationship between camera level and image intensity using the NTA system.

Whilst it is evident that increasing camera level correlates with an increase in recorded image intensity, the exact parameters and values varied within the NTA system are not clear. Whilst it is not stated in the manual for the instrument, various parameters are saved in the meta data after a measurement. Namely, these are the unitless camera gain, shutter time in ms and upper limit of the intensity histogram. The values for each of these parameters at camera levels ranging from 1 – 16 is shown in Figure 8.8. For the camera levels that NBs are measured at (3-5) the camera gain remains constant (15 a.u.) whilst the associated increase in brightness is attributed to an increase in the shutter time (0.33, 0.58 and 1.13 ms respectively). At higher camera levels (11-13), such as those to measure primarily liposomes, the increase in intensity is a combination of increasing camera gain, shutter time and a reduction in the upper limit of the intensity histogram.

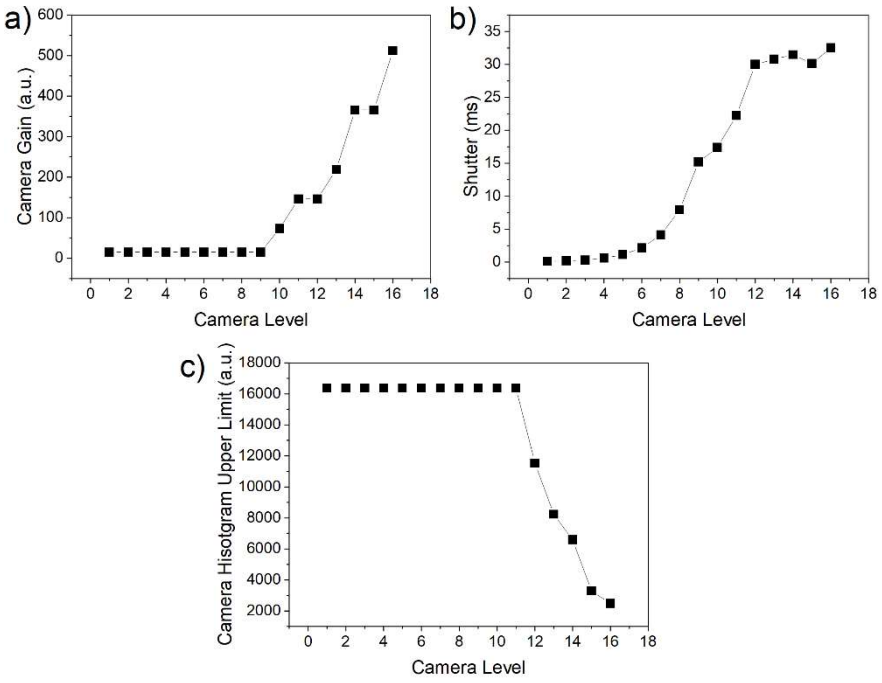

Figure 8.8 – The effect on changing the camera level on various parameters of the NTA system during data acquisition. a) Camera Gain b) Shutter (ms) and c) Camera Histogram upper limit.

Although these NTA measurements do not confirm the presence of gas-cored NBs, recent publications used a similar NB production method and gas-core, and Resonant Mass Measurement was used to demonstrate the presence of sub-micron buoyant particles [59,118], and hence it is likely NBs are present. Using this method, the three NB populations isolated with varying RCF were characterised using NTA. Figure 8.9 shows the NTA measured populations of NBs isolated via centrifugation at a) 100 g, b) 500 g and c) 1000 g, in which all populations follow a log-normal distribution. As RCF is increased, larger bubbles are progressively removed from the population, as shown in the cumulative distribution plot (Figure 8.9d) whilst the modal size of the population remains constant (Figure 8.9e). The initial NB concentration also decreases with increasing RCF, from $(4.91 \pm 0.53) \times 10^{10}$ /mL (RCF = 100 g) compared to $(0.93 \pm 0.10) \times 10^{10}$ /mL (RCF = 1,000 g) (Figure 8.9f). This observed decrease in NB yield is likely due to a combination of removal of larger bubbles from populations, in addition to NB instability and coalescence driven by higher RCFs.

To determine whether these particles were acoustically active, NBs (RCF = 100 g) were treated with high intensity focused ultrasound (HIFU, frequency = 1.1 MHz, PNP = 4.83 MPa, PRF = 1 kHz, Duty Cycle 1 %, 5 s duration), after which NB concentration decreased by 98.3 ± 0.26 % from (3.03 ± 0.30) x 10^9 /mL to (2.90 ± 0.50) x 10^8 /mL. Hence, it is highly likely that the increased scattering intensity observed from NTA measurements can be attributed to gas-cored NBs.

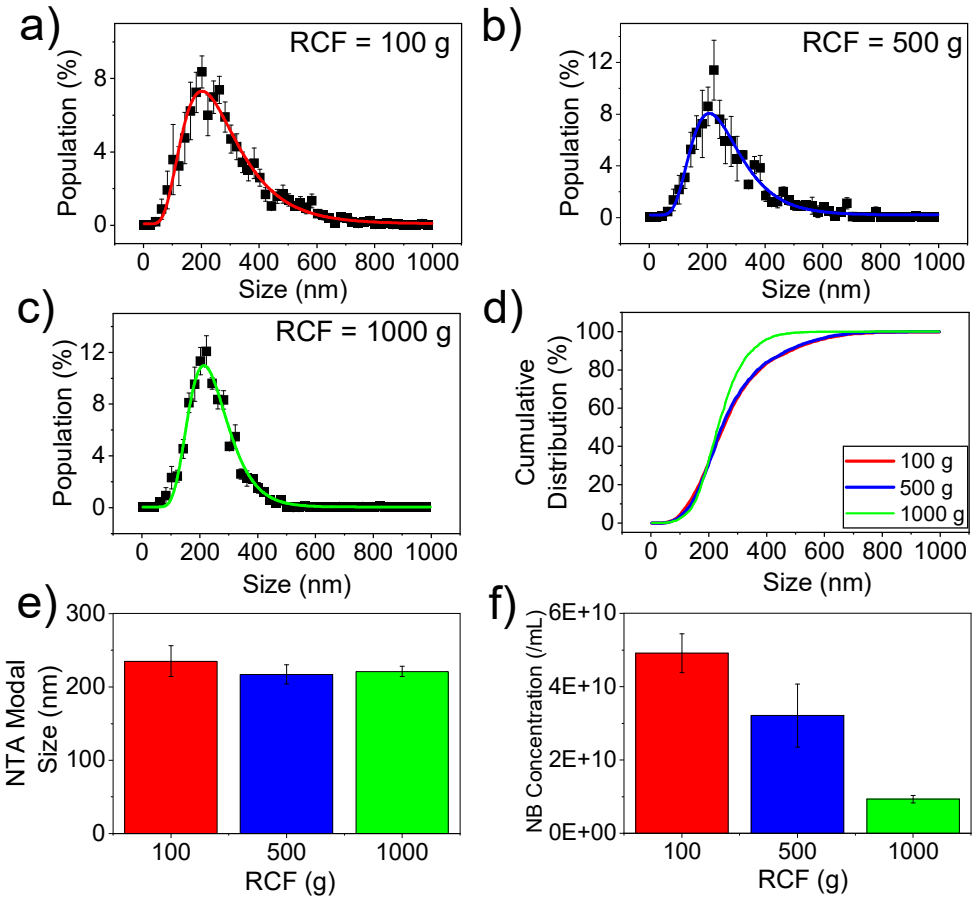

Figure 8.9 – Characterisation of NB populations using NTA such that only highly scattering, gas-cored NBs are detected. Populations distributions are shown for NBs isolated at RCF of (a) 100 g, (b) 500 g and (c) 1,000 g and (d) their cumulative distribution function. e) Modal size and (f) concentration of NB populations.

8.1.3 Characterisation of Larger NBs

Using the light scattering techniques discussed so far, it is simple to assume that all bubbles in the sample are NBs (< 1 μm). However, NB populations characterised exclusively using these techniques can still retain a proportion of microbubbles [101,112,140], which would be

expected to contribute, dependent on their concentration, to any therapeutic or diagnostic effect at clinically relevant frequencies.

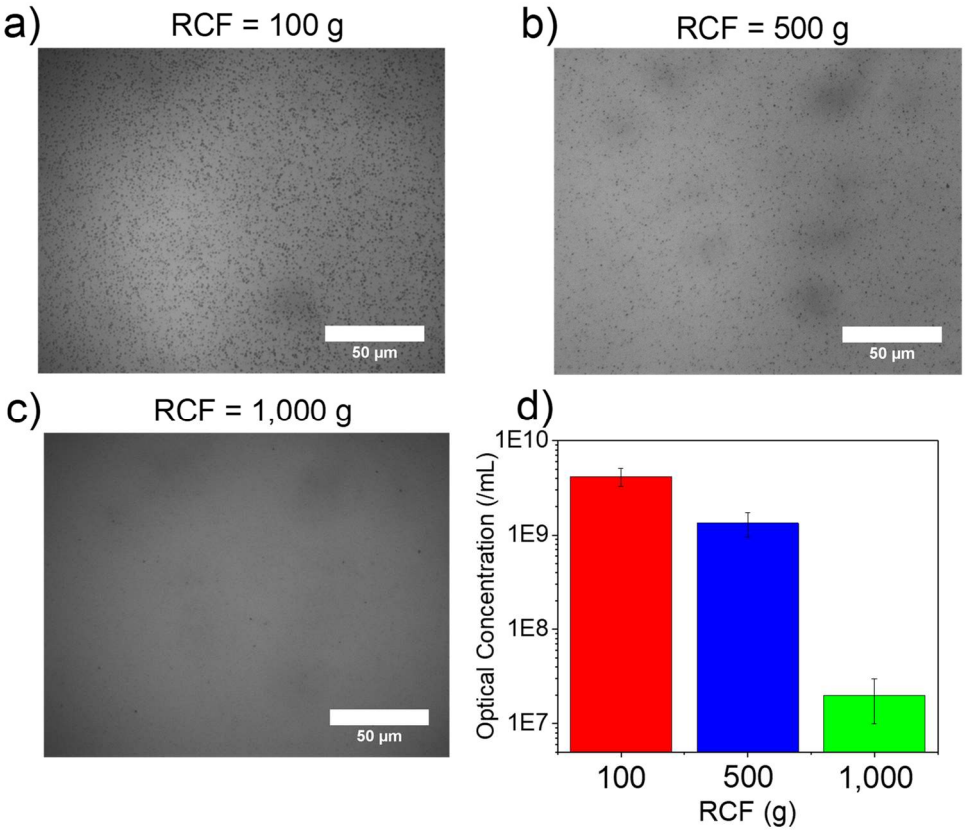

Figure 8.10 – Brightfield microscopy images of NB samples. a) RF = 100 g b) 500 g and c) 1,000 g at their yield concentrations. A decrease in optically visible bubbles with increasing RCF was observed, as larger bubbles are removed during the isolation process.

To determine the presence, and concentration, of any larger bubbles, images of the three NB populations were taken using brightfield microscopy. Due to the resolution limit of the microscopy system used (Numerical Aperture = 0.60, r ~ 600 nm), as well as the scaling resolution of the camera (0.16 µm/pixel), the size of bubbles ≤ 1 µm in diameter cannot accurately be determined. Regardless, a proportion of particles below this threshold would still be expected to be observable due to their intrinsic scattering, and hence this method was used purely to determine the concentration of larger, optically visible bubbles. Brightfield images of each NB population at their yield concentration are shown in Figure 8.10a, b, and c for RCF = 100 g, 500 g and 1,000 g respectively. Images showed the presence of optically visible bubbles in all 3 samples, whilst also demonstrating the lack of any larger microbubbles (i.e. > 1 µm). Prior to centrifugation, MB concentration was ~ 5 x 10^{10} /mL, which decreased as RCF increased as progressively smaller bubbles are removed from the population (Figure 8.10d). For RCF = 1,000 g, optically visible bubbles are nearly completely removed from the sample (2 ± 1 x 10^{7} /mL) approaching the lower limit of detectible bubble concentration (~ 10^{6} /mL) assuming one bubble per image.

When assessing the therapeutic and diagnostic performance of NBs, it is important to consider the ratio between NBs and MBs. Larger bubbles would be expected to have a large contribution to therapy and diagnosis, due to the relationship between bubble size, r, and predicted shear stress exerted on a cell membrane ($\tau \propto r^4$), and resonance frequency ($f_0 \propto 1/r$), especially within the clinically approved US frequency range (1 – 15 MHz). To highlight the ability of increasing RCF to selectively remove larger bubbles from the population, the ratio between optically visible bubbles (MBs) and NBs was analysed (Figure 8.11). Initially the NB/MB ratio was 11.7 ± 2.8 (RCF = 100 g), which increased to 24.0 ± 9.5 and 465 ± 238 for an RCF of 500 g and 1,000 g respectively

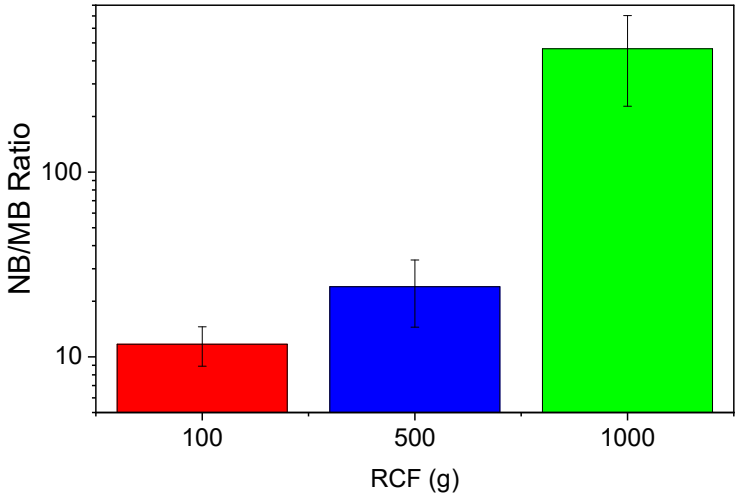

Figure 8.11 – Ratio of NB to MB concentration for NB samples isolated by centrifugation at RCF of 100 g, 500 g and 1,000 g. NB concentration was determined by NTA and MB concentration by optical microscopy.

Whilst it is evident that larger bubbles are being removed from the population, it should be noted that few NBs > 600 nm were detected in NTA measurements, yet ~10^9 /mL larger bubbles were detected via optical microscopy. To determine why, the ability of NTA to characterise larger particles (i.e. > 600 nm) was assessed. Monodisperse NIST standard polystyrene beads with nominal diameters of 600 (Figure 8.12a) and 800 nm (Figure 8.12b) were analysed. Beads had actual diameters of 620 ± 24 nm and 788 ± 26 nm according to the data sheet (determined by electron microscopy) and were characterised via both DLS and NTA, providing an additional comparison between the two techniques. DLS slightly oversized the standards (modal size 653 nm and 852 nm) whilst low PDI values (0.03 and 0.10 respectively) indicated monodispersity of the sample. Although determined by a number-weighted distribution, the oversizing by the DLS may be explained by the dependency of scattering intensity on size and hence increased contribution to the population. In comparison, NTA slightly undersized the particles, with modal sizes of 526 nm and 711 nm. This observed

decrease in size may suggest that a fraction of larger particles is omitted but regardless, confirms the ability of NTA to detect and accurately size larger particles.

Another consideration may be that larger bubbles exist at a concentration below the threshold for detection by NTA (~10^9 particles/mL). For RCF = 100 g (i.e. the sample containing the highest concentration of MBs), samples were typically diluted 10 x for NTA analysis. Hence, the concentration of MBs during measurement would be ~ 10^8 MB/mL, an order of magnitude below the optimal range for NTA. Another consideration may be that the increased size and hence increased scattering intensity associated with larger bubbles may also prove difficult for the NTA system to track and require optimisation of acquisition parameters for larger bubbles. As such, this section demonstrates that due to varying measurable size ranges of techniques, a combination of light scattering and optical microscopy is currently required to properly characterise NB populations.

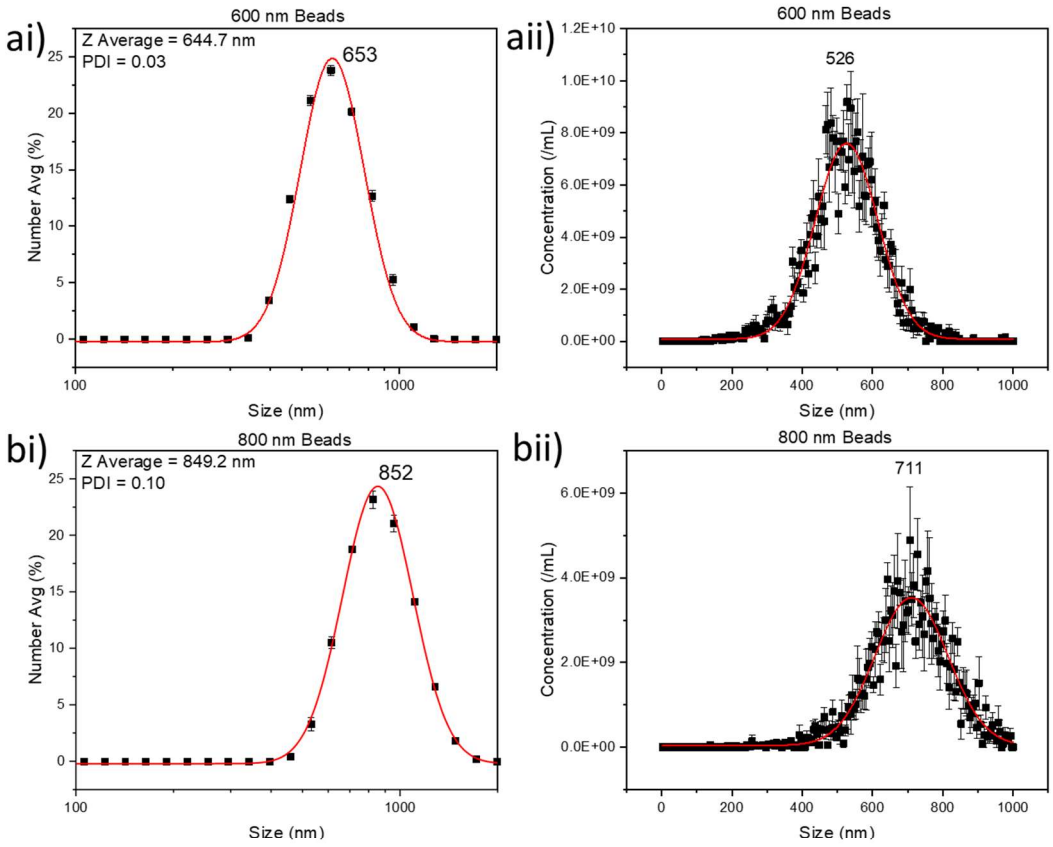

Figure 8.12 - Population distribution of NIST standard (a) 600 nm and(b) 800 nm polystyrene spheres. Populations were measured via (i) DLS and (ii) NTA. Modal values were determined by a log-normal distribution fit.

8.2 Proof of Concept: Microbubble Mediated Sonoporation

NBs in combination with US have been shown to locally increase cellular uptake of small molecules, such as chemotherapeutics and model drugs [62,119], via a process known as

sonoporation. In this chapter we aim to investigate the effect of NB size and concentration on their sonoporation efficiency, using clinically relevant US and *in vitro* culture of cell monolayers. As a proof-of-concept study, MBs were initially used in combination with US to promote uptake as their sonoporation capabilities are well documented, and would provide a good assessment of the acoustic and *in vitro* experimental set-up (e.g., acoustic parameters, cell culture conditions, uptake assay).

Throughout sonoporation studies, SW480 colorectal cancer cell lines were used. These cells are primary human cells taken from adenocarcinoma (Dukes stage B, T2-3 N0 M0 grade) of the colon and have been used in therapeutic microbubble studies [50,233], as well as those characterising their mechanical properties [234]. Further, a metastatic cell line taken from the lymph nodes of same patient exists (SW620, Dukes Stage C, T2-4 N1 M0 grade), in which the mechanical structure is shown to evolve with disease progression [202], and hence could provide a second cell line for additional comparison. SW480 cells were cultured as a monolayer and after treatment with US and MBs, were located using CellTracker Green. This fluorescent green stain is able to freely pass through the cell membrane, and once inside a viable cell becomes membrane impermeant. Fluorescence and brightfield images of cells were acquired using a confocal microscope, with an example image SW480 cells after live staining shown in Figure 8.13. No further optimisation of staining parameters (i.e. concentration and time) was required as the fluorescence images were deemed of sufficient quality and contrast.

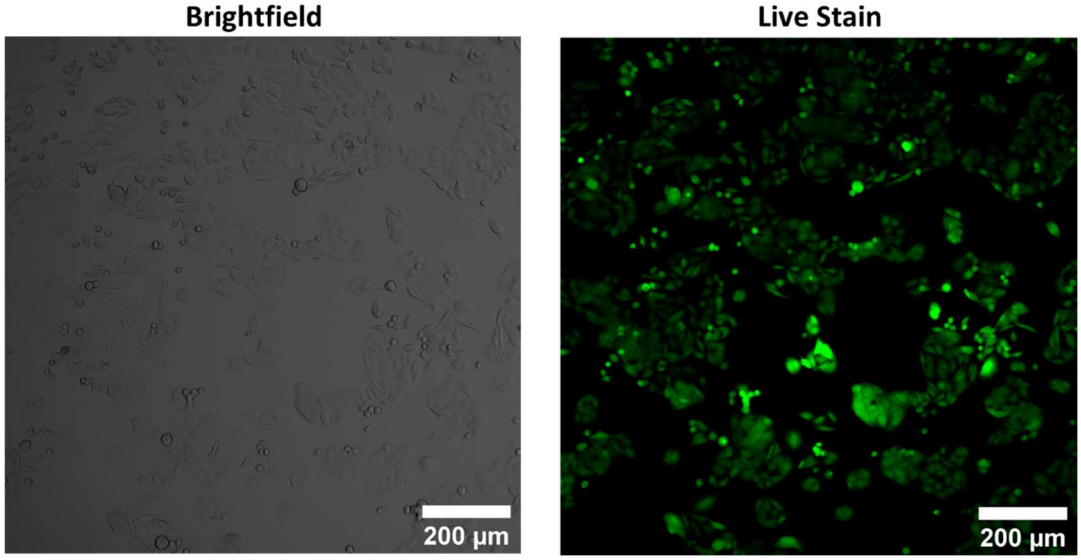

Figure 8.13 – Fluorescence images of an SW480 cell monolayer taking using a confocal microscope showing both brightfield and live stain images.

The poor contrast evident for brightfield images can be attributed to the absence of phase-contrast from the system, and hence are excluded from further analysis. To determine and quantify the occurrence of sonoporation, fluorescent membrane probes are commonly used,

and as such allows for co-localisation of fluorescence between a live cell and the membrane probe indicating successful sonoporation.

8.2.1 Well Plate Experimental Set Up

Sonoporation experiments initially consisted of the use of well plate based assays, in which a monolayer of SW480 colorectal cancer cells were cultured in a 24-well plate, similar to a study by McLaughlan et al. [40]. Wells had a diameter of 10 mm and hence were appropriate for use with an unfocused 2.25 MHz central frequency transducer, with an element size of 6.35 mm. This allowed for US to be incident from above, towards the cell monolayer and bubble population, utilising the acoustic radiation force such to push bubbles into contact with the cells (Figure 8.14). The distance between the transducer element and cell monolayer was kept constant for all exposures using a 3D printed adaptor, such that cells and bubbles were situated in the far-field of the transducer (13.5 mm).

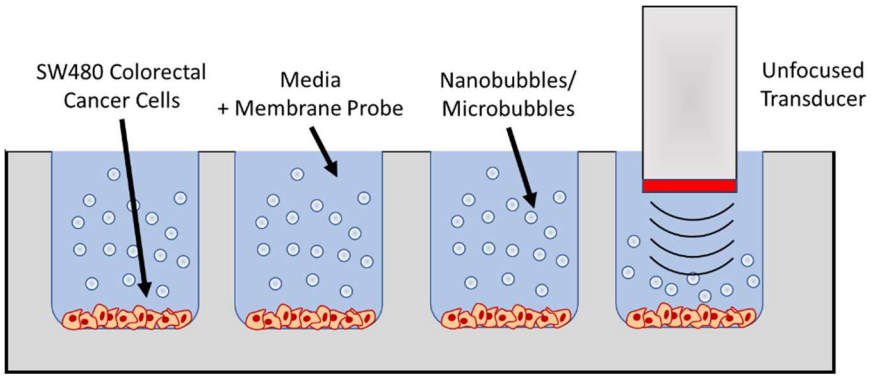

Figure 8.14 – Schematic of the well plate-based experimental set up used for initial sonoporation studies. SW480 cells were cultured as a monolayer and microbubbles/nanobubbles added in the presence of a membrane probe prior to insonation.

Initially, 7-AAD was used as a membrane probe and indicator of sonoporation. Similar to Propidium Iodide (PI) [235], 7-AAD is commonly used to detect dead cells in a population as it is membrane impermeable but can freely enter dead cells with a compromised membrane [236]. Upon entering a cell, 7-AAD binds to DNA and fluoresces with peak excitation and emission wavelengths of 535 nm and 647 nm respectively, and hence can be used as membrane probe to quantify sonoporation. Compared to PI (Ex/Em 535/617 nm) it has a greater stokes shift and hence reduced spectral overlap with FITC (Ex/Em 490/525 nm). To test the functionality of 7-AAD and optimize the staining assay, cells were killed using 20 % EtOH exposure [237], followed by staining with 7-AAD over a range of concentrations (0.1 – 5.0 µM, 30 mins). After EtOH treatment, cells displayed a noticeable change in morphology whilst the 7-AAD stained nearly all cells, and with fluorescence intensity increasing with concentration (Figure 8.15). At a concentration of 5 µM, staining intensity was the brightest whilst no signs of

cytotoxicity were observed in a control sample (no EtOH treatment) and hence this concentration was used for sonoporation experiments.

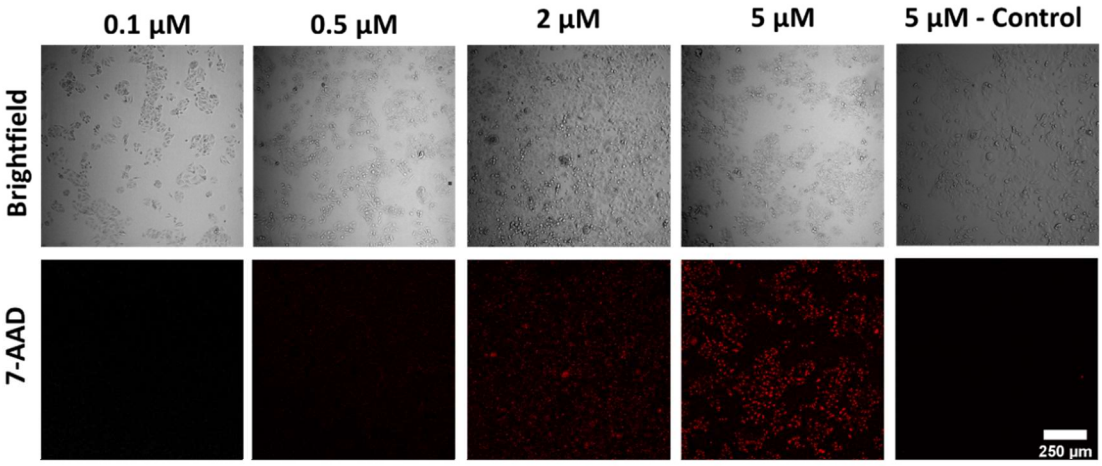

Figure 8.15 – Fluorescence images of SW480 cells after staining using 7-AAD across a range of concentrations (0.1 – 5 µM) after treatment with 20 % EtOH. Control cells (no EtOH) treatment showed no noticeable signs of cytotoxicity from a 7-AAD concentration of 5 µM.

Prior to sonoporation experiments, the effect of US at different Mechanical Index (MI) on MB populations was investigated. MBs at a concentration of 10^8/mL were exposed to US at MI of 0.1, 0.2 and 0.6 and concentration before and after US measured. For MI of 0.1 and 0.2, MB concentration remained relatively constant changing by -36.4 % and +10.3 % respectively, suggesting the occurrence of stable cavitation. However, increasing MI to 0.6 facilitated MB destruction, and a decrease in concentration of 98.3 %, similar to those observed on-chip by Bourn et al. [48]. The lack of destruction or change in concentration for MI = 0.1, 0.2 may also be attributed to some degree of acoustic attenuation and scattering provided by the relatively high MB concentration.

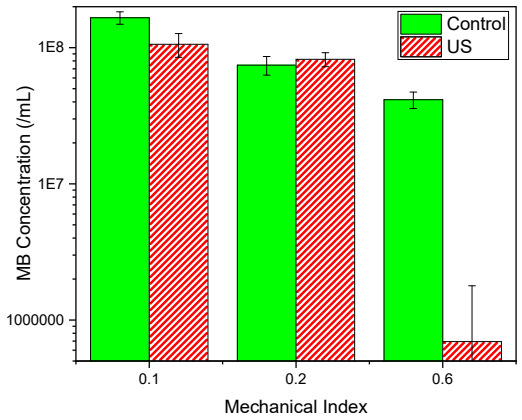

Figure 8.16 – Microbubble concentration before and after exposure to US at a Mechanical Index of 0.1, 0.2 and 0.6. Initial MB concentration was ~10^8 /mL for all samples.

As MB destruction was confirmed, an initial experiment utilized an MI of 0.6 and MBs at a concentration of either 10^7 or 10^8 MBs/mL. Whilst after exposure at this MI, MB concentration decreases significantly, it would be expected for a combination of both stable cavitation (and hence microstreaming) and inertial cavitation (and hence micro-jetting) to be occurring, with both mechanisms capable of inducing sonoporation. Based on work by van Rooij et al. [235], sonoporation and pore-resealing is typically expected to occur over the timescale of a few minutes. Hence after treatment, SW480 cells were incubated for a further 10 mins before washing, followed by live staining.

Composite fluorescent images (live stain and 7-AAD) of SW480 cells are shown in Figure 8.17 after treatment with US only, and US + MBs at concentration of either 10^7 or 10^8 MBs/mL. No significant fluorescence in the 7-AAD channel was observed for any of the samples, and hence MBs + US had no effect on the cells (i.e. sonoporation or cell death). To induce sonoporation, the bubble-cell distance must be minimized (approximately 1-2 bubble diameters) [218,219]. The mean inter-particle distance of suspended particles can be approximated by $n^{-1/3}$ where n is the number density of the particles. For free MBs at a concentration of 10^8 /mL distributed homogeneously throughout the well, the average inter-bubble distance, and hence approximate distance between the MBs and the cell monolayer would be ~20 µm. Hence bubbles with an average of diameter of 1-2 µm would be out of the effective sonoporation range. One way to rectify this would be to further increase the MB concentration (i.e. 10^9 - 10^{10} /mL) however these high concentrations may strongly attenuate and scatter the incident US (i.e. acoustic shadowing).

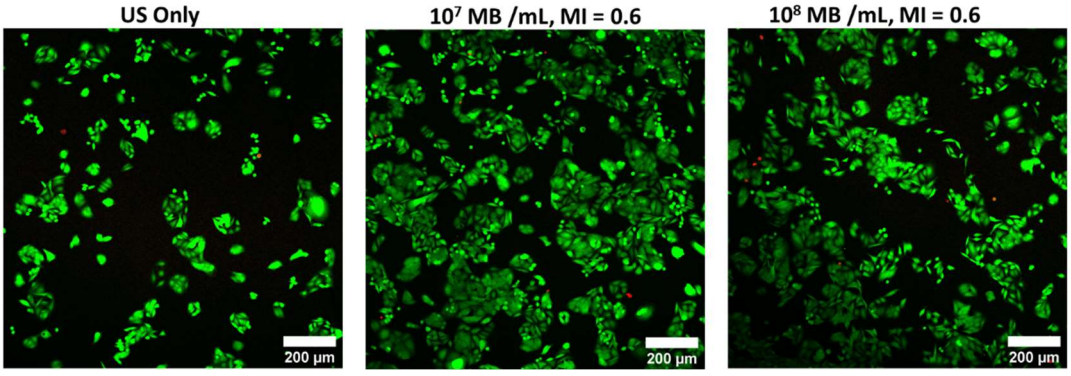

Figure 8.17 – Composite images of SW480 cells showing live stain and 7-AAD channels after exposure to (a) US only (MI 0.6) or combined with (b) 10^7MB/mL or (c) 10^8 MB/mL. For all exposure conditions, no significant uptake was observed.

An alternative solution is to utilise the acoustic radiation force to push MBs into direct contact with the cell monolayer [238]. The MI of the US was reduced (MI = 0.1, 0.2) and the total US duration increased (120 s) such that MBs are no longer being destroyed (i.e. stable cavitation). The MB concentration was also reduced (10^6, 10^7 MB/mL) to reduce acoustic attenuation and scattering, and more closely mimic the study performed by McLaughlan et al. [40], which utilized concentrations of 10^6 MBs/mL and an MI of ~ 0.07, observing sonoporation of 5-10 % of the total population. Despite these changes, SW480 cells still showed no evidence of either 7-AAD uptake, or cell death induced by the mechanical stress provided by the oscillating bubbles (Figure 8.18).

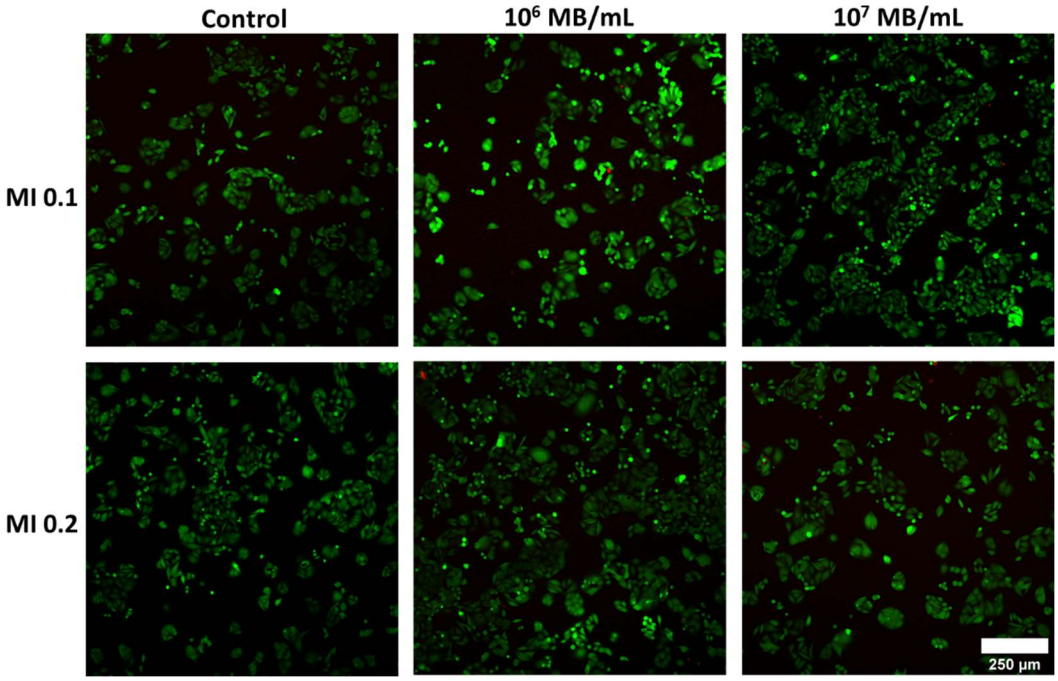

Figure 8.18 - Composite images of SW480 cells showing live stain and 7-AAD channels after US exposure at an MI of either 0.1 or 0.2, and at MB concentrations of 10^6 or 10^7 MB/mL.

8.2.1.1 Flow Cytometry

As a final test of MBs in this experimental set up, sonoporation was quantified using flow cytometry: a technique that can quantify fluorescence emissions of single cells to a high degree of sensitivity. It is possible that the SW480 cells are indeed being sonoporated, but the amount of uptake is below the sensitivity limit of the confocal microscopy system. This may also be exacerbated by the reduced quantum yield of 7-AAD (0.02 %), compared to PI (0.2 %). The use of flow cytometry also provides quantitative data, as opposed to qualitative fluorescence images that would require further analysis to quantify uptake. In these experiments, after US treatment and staining, cells were detached from the surface of the well plate via trypsinization and handled in suspension, to enable analysis of the sample using flow cytometry. For each sample, a minimum of 10,000 valid cells events were collected. All operation of the flow

cytometry system was performed by and under the supervision of Dr. Sally Boxall and Dr. Ruth Hughes of the Bioimaging and FACS Facility, University of Leeds.

A control (no treatment) SW480 cell sample with no staining was first measured to provide a reference to which the gating was applied for side and forward scatter (Figure 8.19a) containing 36.55 % of the total recorded events. For all measurements, a minimum of 10,000 valid events were recorded. Gating was applied such that results consisted mainly of viable cells, to identify cells that are both viable and have experienced sonoporation. This gate was then applied to all samples for further analysis.

To observe fluorescence emission from both the live stain and 7-AAD, cells were excited sequentially with a laser wavelength of 488 nm and 561 nm, and emitted light collected using bandpass filters of 525/40 nm and 690/50 nm respectively. The system has a maximum fluorescence intensity of 10^7 a.u., above which any saturated events are discarded. Figure 8.19b and c show histograms of fluorescence emission intensity for unstained and stained control samples respectively, for both live stain (i) and 7-AAD (ii) emission. Prior to staining, cells had mean fluorescence intensities of 4.16 x 10^3 a.u. & 1.50 x 10^3 a.u. for live stain and 7-AAD emission. Post staining, the 7-AAD staining remained relatively unchanged (2.19 x 10^3 a.u.) whilst live stain emission increased by 3 orders of magnitude (4.42 x 10^6 a.u.),

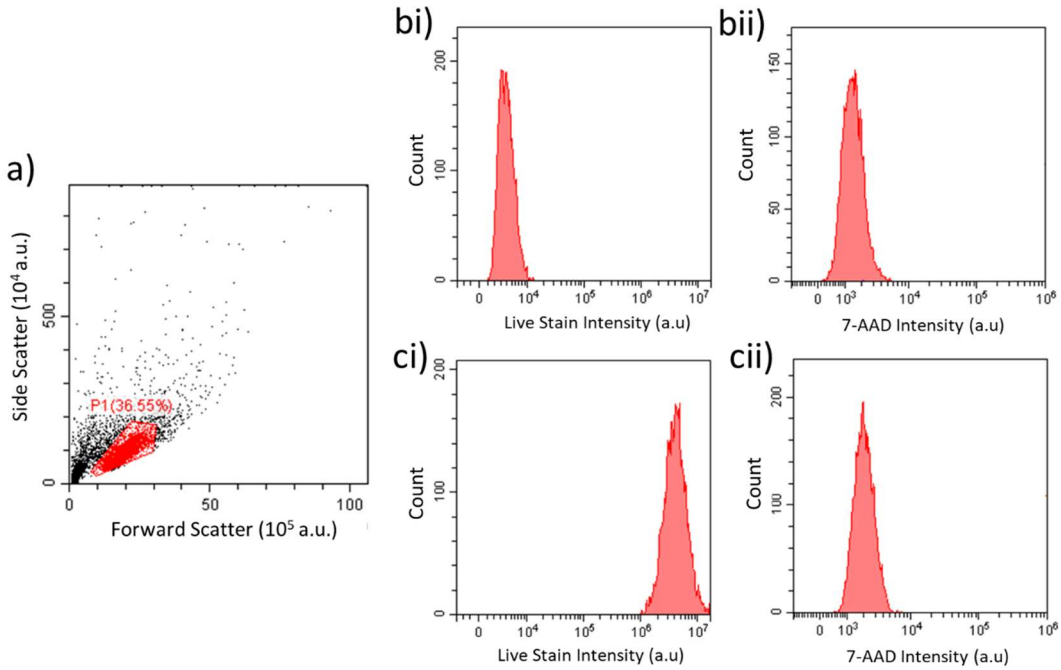

Figure 8.19 – Flow cytometry data collected for control SW480 cells. (a) Scattering data showing side scatter and forward scatter intensity of a control sample with no fluorescence staining. The gating was then applied to all subsequent samples. Live stain and 7-AAD intensity shown for (b) a non-stained control sample and (c) control sample stained with both live stain and 7-AAD.

showing successful staining of live cells, and minimal dead cells included in our analysed populations.

To identify any change in membrane permeability, the intensity of 7-AAD emission from cells was compared after US and MB treatment. Figure 8.20 shows 7-AAD emission for cells after treatment for a range of US conditions (MI = 0.1, 0.2, 0.6) and MB concentrations (10^6, 10^7 /mL). Figure 8.20 (a – d) shows histograms of 7-AAD fluorescence intensity for no treatment, MI 0.6 only, MI 0.6 and 10^6 MB/mL and MI 0.6 and 10^7 MB/mL. Fluorescence intensity for condition each were 2.19 x 10^3 a.u., 2.06 x 10^3 a.u, 1.54 x 10^3 a.u and 1.79 x 10^3 a.u respectively, showing no change in 7-AAD uptake and in agreement with previous analysis using fluorescence microscopy.

Similar results were observed for all other treatment conditions, summarised in Figure 8.20e. An intensity threshold was applied post-processing to the control, stained sample such that the majority of the cell population is contained below the threshold (99.86 %). For each treatment condition, the percentage of cell population above this threshold was determined, to quantify the change in 7-AAD fluorescence. For all treatment conditions, there was no discernible change in the proportion of the population containing 7-AAD (all values < 0.2 %) and hence no evidence of sonoporation. This goes some way to eliminating the possibility that the confocal fluorescence system is not sensitive enough to detect sonoporation and provides conclusive evidence that sonoporation is not occurring or at least not observable in this system.

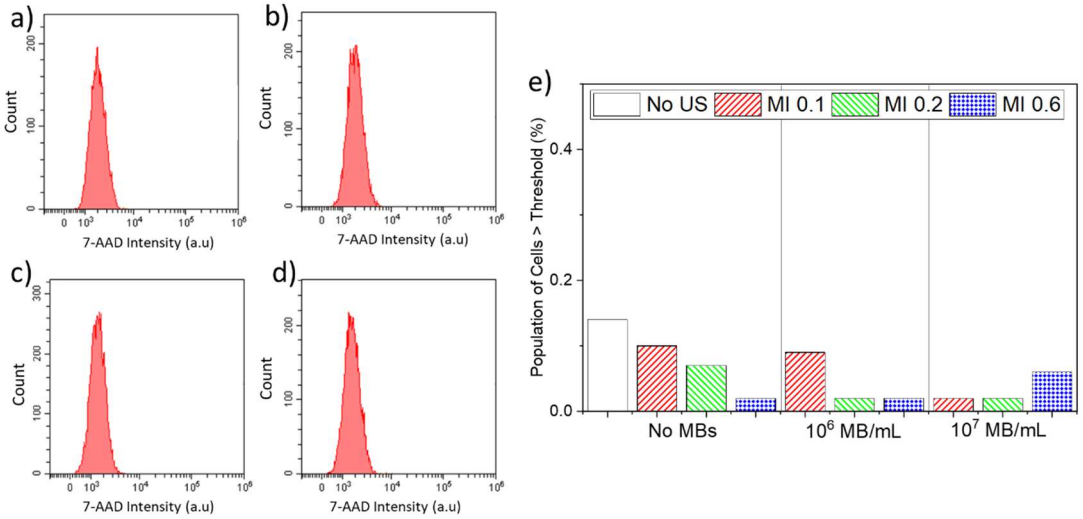

Figure 8.20 - Flow cytometry data of SW480 cells showing fluorescence intensity of the 7-AAD stain/membrane probe after different treatment conditions. All ultrasound treatment had an MI of 0.6 and total duration of 60 s. (a) Control (no treatment), (b) US only (c) US and 10^6 MB/mL and d) US and 10^7 MB/mL. (e) Summary of flow cytometry data showing the population of cells with 7-AAD fluorescence higher than the threshold applied to the control, no US sample for a range of parameters: MI of 0.1, 0.2, 0.6 and MB concentrations of 10^6 and 10^7 MB/mL.

Hence, this raises the question as to why sonoporation is not occurring in this system. Even though the quantum yield of 7-AAD is lower than that of PI, the high MB concentration and MI used in these experiments would be expected to induce irreversible sonoporation, and hence cell death, to some amount of the population. As shown in Figure 8.13, 7-AAD would then be able to successfully identify these cells. Closer assessment of results from McLaughlan et al.[40] highlight the importance of bubble-cell distance, in which targeted MBs had greatly improved sonoporation efficiency compared to free MBs (~ a 4 fold increase). Using the well-plate based system, the cell monolayer is situated at the bottom of the well. Naturally, bubbles will rise away from the cell monolayer, hence reducing the chance of sonoporation. In this section, we investigated the use of a lower MI so to not decrease the concentration of MBs, and also facilitate movement of MBs towards the monolayer and induce sonoporation. In many studies where the effect of a single MB on single cell membrane integrity, a commonly used system is that of an OptiCell: a hermetically sealed chamber for cell growth consisting of two membranes upon which cells can be cultured. In this set-up, the OptiCell can be inverted such that MBs can rise towards the cell monolayer, promoting sonoporation and molecular targeting [239,240].

8.2.2 On-Chip Sonoporation Assay

To minimize the bubble-cell distance, the acoustic and cell culture set up was changed. SW480 cells were cultured on the top of a microfluidic channel, such that sonoporation can be facilitated by allowing bubbles to rise to the top of the channel, hence be minimizing cell-

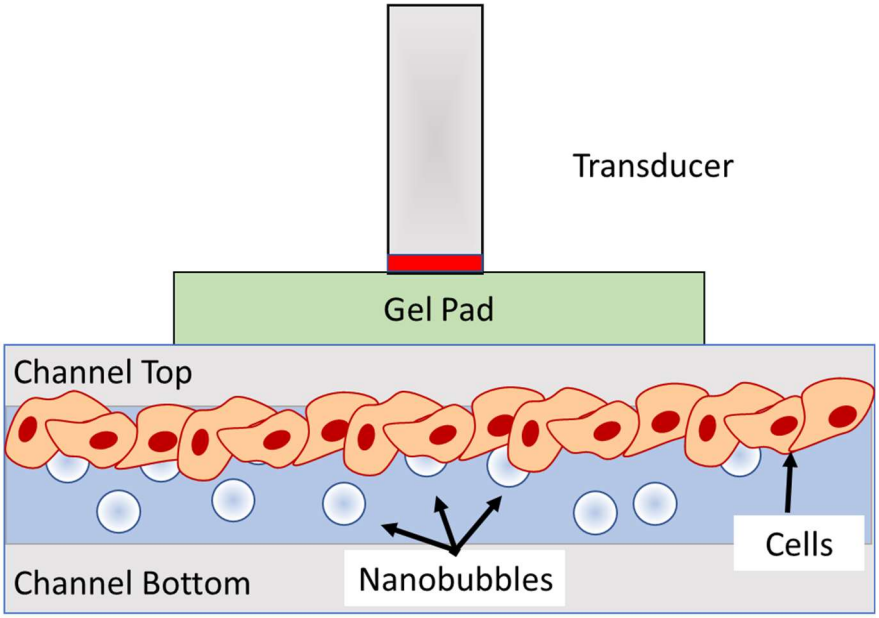

Figure 8.21 – Schematic of the cell culture and acoustic set up for sonoporation studies using a microfluidic chip. SW480 cells were cultured on the top of the microfluidic channel, such that nanobubbles can float towards the monolayer and facilitate sonoporation.

bubble distance (Figure 8.21). Full experimental set up is described in Section 7.3. The small volumes associated with microfluidics also allows a cost-effective increasing in assay concentrations, increasing sensitivity. Initial on-chip experiments used PI as the membrane probe due to the increased quantum yield, as well as being commonly used in other sonoporation studies[240–242].

Figure 8.22 shows confocal fluorescence images of SW480 cells, cultured on the top of the microfluidic channel, treated with MBs at a concentration of 10^8 MBs/mL and with a MI of 0.1 or 0.6, corresponding to stable or inertial cavitation regimes. For control samples (no treatment or US only) minimal signal was seen from the PI channel. The combination of MBs and US together promoted uptake of PI for both MI of 0.1 and 0.6, with PI signal found for an MI of 0.6. Closer analysis of a composite fluorescence image of this treatment condition (Figure 8.23) shows that nearly all cells that are stained with PI lack a live stain and hence likely have been killed during sonoporation. The PI is also highly localised to the nucleus of the cells, as opposed to the cytoplasm. For future work where quantitative image analysis will be required, this may introduce additional complexity and limit the reliability of simple co-localisation between live stain and uptake marker. Regardless, this result is positive in the fact that the combination of MBs and US has induced physical changes in the cell monolayer, as opposed to previous experiments where no changes were seen.

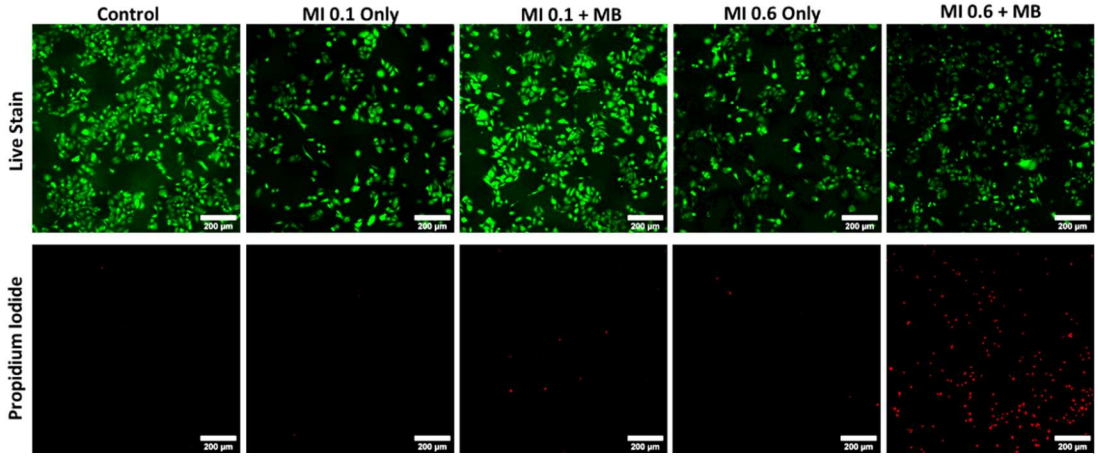

Figure 8.22 – Confocal fluorescence images of SW480 cells cultured on-chip treatment with US (MI 0.1 & 0.6) and MBs (10^8 /mL) showing live stain and propidium iodide fluorescence, which was used as a membrane probe. Images were taken from the top plane of the microfluidic channel.

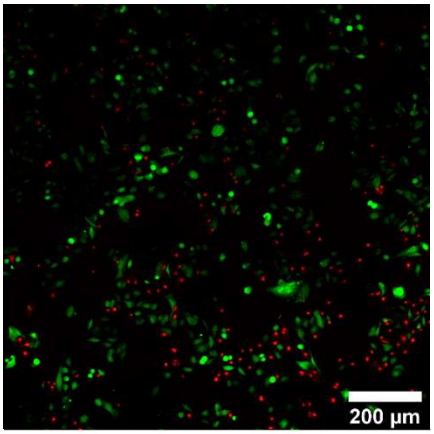

Figure 8.23 – Composite fluorescence image of SW480 cells treated with MBs (10^8/mL) and US (MI 0.6) showing live stain (green) and propidium iodide (red).

Following this, the use of dextran as a membrane probe was investigated. Dextran is a polysaccharide that is available in varying molecular weights, and is commonly used as a membrane probe [243,244]. In these studies, TexasRed-Dextran (TR-Dextran) with an average molecular weight of 70 kDa was used, but there is also scope to investigate varying molecular weight influences uptake, and hence the size of pores generated in sonoporation [245]. Unlike 7-AAD and PI, Dextran is not a biological stain and does not bind to any specific molecules (i.e. DNA). Initially membrane impermeable (dependent on molecular weight), Dextran will only enter cells with a compromised membrane and fluoresce inside the cytosol, beneficial for quantitative analysis where fluorescence from Dextran and the live stain is co-localised.

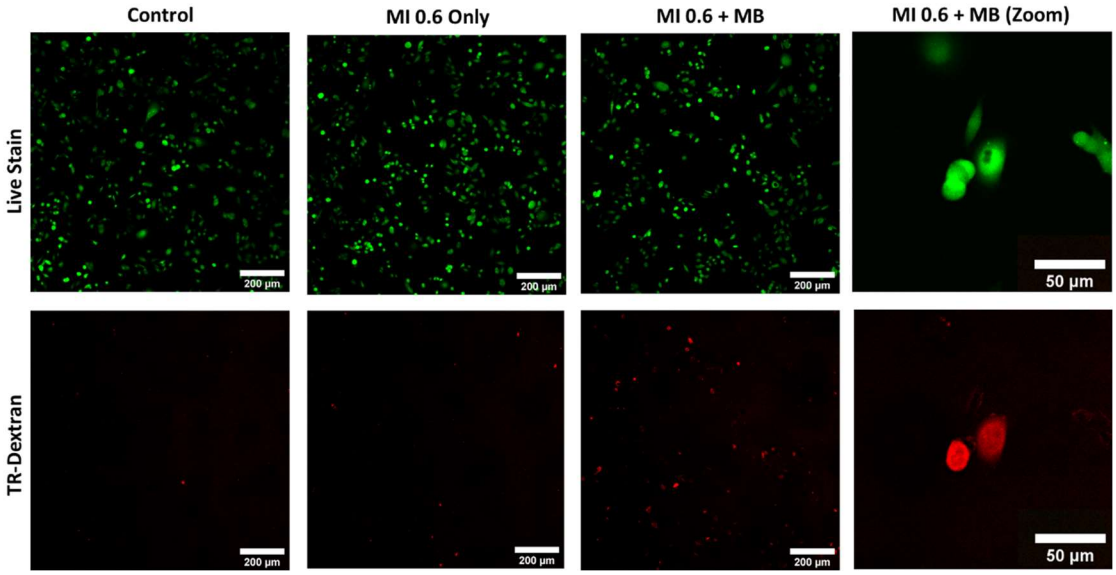

Figure 8.24 – Confocal fluorescence images of SW480 cells treated with MBs (10^8/mL) and US (MI 0.6) showing live stain and 70 kDa TexasRed Dextran, used as a fluorescent membrane probe. MI 0.6 + MB zoom image shows the co-localisation of fluorescence between the live stain and TR-Dextran due to membrane permeation and cytosolic uptake.

SW480 cells were treated with a combination of US (MI 0.6) and 10^8 MBs/mL using 70 kDa Dextran as the fluorescent membrane probe at an initial concentration of 1.5 µM (Figure 8.24). No uptake was observed for control samples (no treatment and US only); however, uptake of Dextran was observed for the combination of MBs and US. Closer analysis of the images shows clear co-localisation between the live stain and Dextran fluorescence (Figure 8.24 zoom). Following this result, Dextran was used as a membrane probe for all future experiments in which NB-based sonoporation was investigated.

8.3 Nanobubble Mediated Sonoporation

In this section, the sonoporation capability of the three different NB populations developed in Section 8.1 were assessed, such to evaluate the influence of NB size on sonoporation efficiency. The largest of the three populations, (RCF = 100 g) was used as an initial test to demonstrate the ability of NBs to induce sonoporation. NBs were administered at their yield concentration (~ 10^{11} NB/mL), as characterised by NTA and treated with US (MI 0.6). Figure 8.25 shows both the live stain and TR-Dextran channels, showing fluorescence co-localisation and hence sonoporation, compared to US only controls (Figure 8.23). Whilst the occurrence of sonoporation is evident, the size of the US beam compared to the microfluidic channel needs to be considered. The microfluidic channels have a length and width of 17 mm and 3.8 mm respectively. On-chip, the FWHM (-6 dB) of the US beam will be 2.24 mm and as such mostly localised to a region with this approximate diameter (Section 7.4). Additionally, the typical field of view of a single confocal image using this system

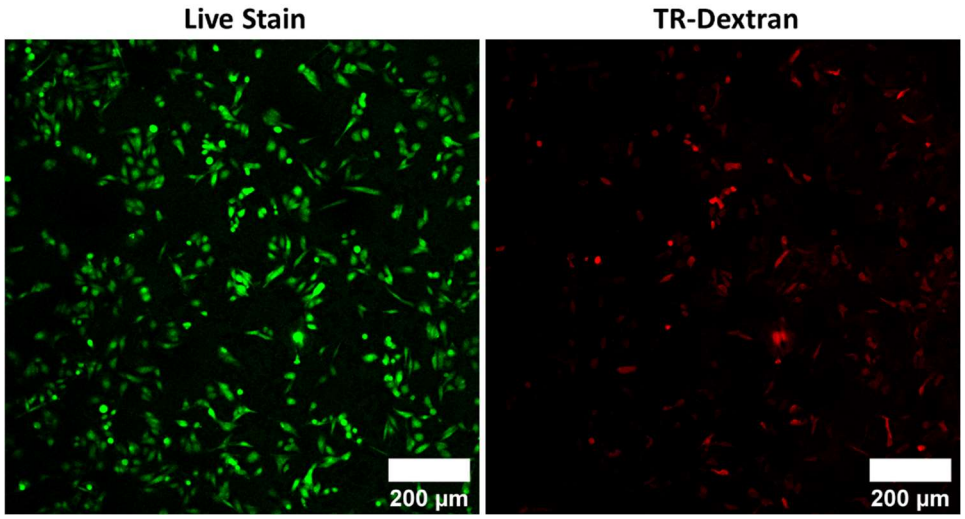

Figure 8.25 – Confocal fluorescence images of SW480 cells treated with US (MI 0.6) and Sample I NBs, isolated by centrifugation at an RCF of 100 g, showing live stain and TexasRed Dextran channels. NBs were administered at their yield concentration.

(1.2 x 1.2 mm), means that a single, or a combination of randomly spatially oriented acquisitions will not provide a reliable means of comparing uptake between samples.

To quantitatively assess total Dextran uptake, and hence sonoporation, full confocal maps encompassing the full microfluidic channel were acquired. These images were taken using the Leica confocal system "TileScan" method and utilized autofocus for each image, based on the intensity of the live stain channel (Section 7.6). Example images are shown in Figure 8.26 for samples treated with NBs and US (a), or just US (b), in which a clear localised area of Dextran fluorescence is visible in the centre of the channel and the majority of signal confined with a region bounding the -20 dB (i.e. 90 % pressure reduction) beam profile. Additional images at increased zoom show clearer evidence of co-localisation and Dextran fluorescence.

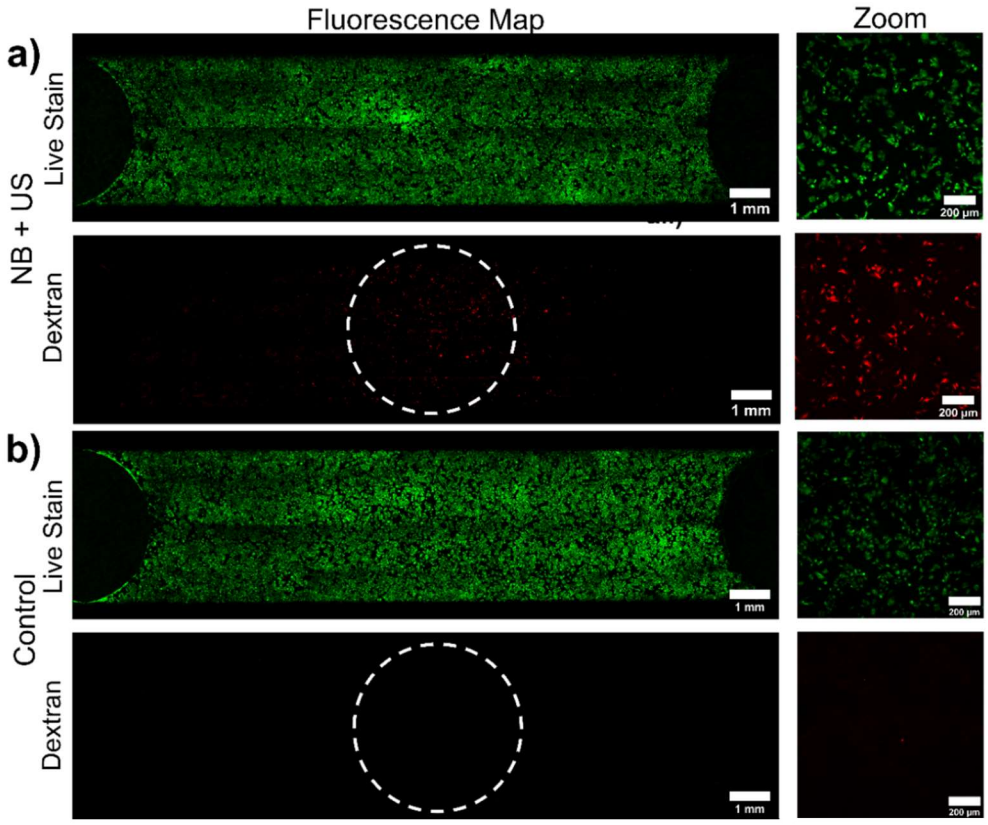

Figure 8.26 –Confocal fluorescence map scans showing live stain and Dextran fluorescence emissions from SW480 cell monolayers. Images show cells after treatment with NBs and US (a) or a control sample of US only (b). Full fluorescence maps of the microfluidic chip were used for quantitative analysis of uptake, and increased zoom images show clear co-localisation of fluorescence between Dextran and the live stain indicative of sonoporation in viable cells. White dashed circle represents the -20 dB point of the pressure field.

Images were analysed such to determine the total fluorescence of Dextran inside live cells within the central insonated region of interest. Full details are described in Section 7.7 but briefly, an image mask was generated from the live stain image and then applied to a background subtracted Dextran image. An average red fluorescence profile in the x-direction along the chip was calculated to identify the region corresponding to insonation and hence uptake. From these profiles, the Total Fluorescence Intensity (TFI) was quantified; either by fitting a Gaussian distribution and integrating to calculate the TFI, or if no uptake was detected, data was integrated across a 7 mm window situated in the centre of the profile (Figure 8.27).

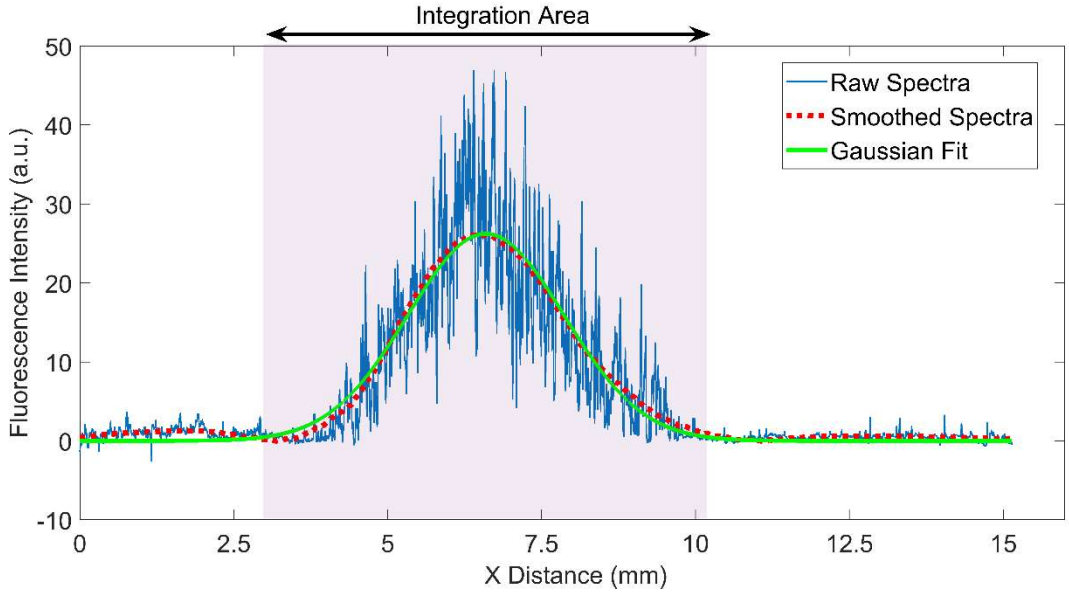

Figure 8.27 - Example of the image processing used to determine total fluorescence intensity, indicative of total Dextran uptake post sonoporation of SW480 cells. Plot shows the average fluorescence intensity of Dextran inside live cells in the x-direction. The raw spectra were smoothed (2 mm window, Savitzy-Golay) and then fit with a Gaussian distribution, to determine the location of the uptake. This was then integrated between $x_c - 2\sigma$ and $x_c + 2\sigma$, where x_c is the peak centre and σ is standard deviation, to determine the total fluorescence intensity. For those where no uptake was detected (i.e. unable to fit a Gaussian distribution), the profile was integrated over a central 7 mm window.

8.3.1 Dextran Concentration Optimisation

As microfluidics typically utilizes low sample volumes, higher concentrations of reagents can be used without dramatically increasing cost. Hence, the effect of increasing the concentration of the membrane probe (TR-Dextran) was investigated, towards increasing assay sensitivity. Experiments were performed using NBs separated by centrifugation with an RCF of 500 g, to provide an intermediate for comparison to future experiments utilising different NB sizes and their expected sonoporation performance (i.e. larger bubbles will induce increased sonoporation). TR-Dextran concentration was varied between 1.5 – 14 μM, and SW480 cells treated with NBs and US (MI 0.6), and compared to controls (no treatment, US only) where the highest Dextran concentration was used (14 μM). It should be noted that from here onwards in this chapter, all control values are averaged over multiple repeats and are consistent throughout with TFI's of 0.92 ± 0.62 a.u. and 0.66 ± 0.64 a.u. for no treatment and US only respectively. At lower TR-Dextran concentrations (1.5 and 3 μM), TFI is not significantly increased compared to control samples (Figure 8.28) with TFI's of 1.65 a.u. and 1.37 a.u. respectively. Further increases of concentration correlated with an increase of TFI to 7.27 a.u. and 20.1 a.u. for concentration of 7 and 14 μM respectively, demonstrating an increase in assay sensitivity. Hence, for further experiments a TR-Dextran concentration of 14 μM was used.

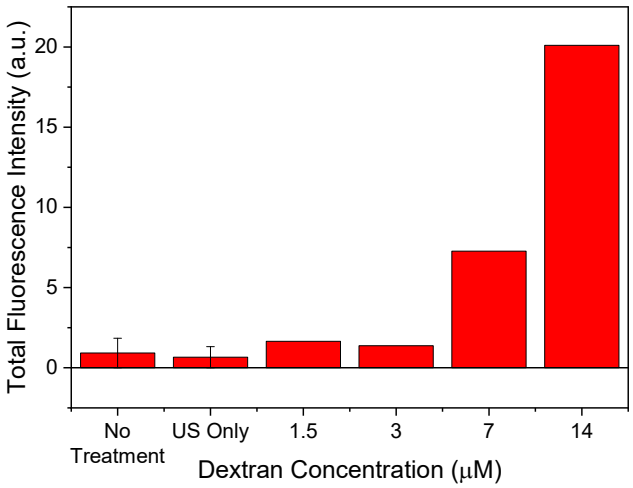

Figure 8.28 – Effect of Dextran concentration on Total Fluorescence Intensity (TFI), a quantitative measure of Dextran uptake based on co-localisation between live cells and dextran fluorescence signal. SW480 cells were treated with US (MI 0.6) and (RCF = 500 g) at a concentration of 10^{11} /mL.

8.3.2 Effect of Nanobubble Rise Time on Sonoporation

Another factor to consider in the on-chip set-up is the duration of time NBs are allowed to rise towards the cell monolayer, prior to US, as this will affect the bubble-cell distance and hence magnitude of sonoporation. The height of the microfluidic channel is 400 μm, with

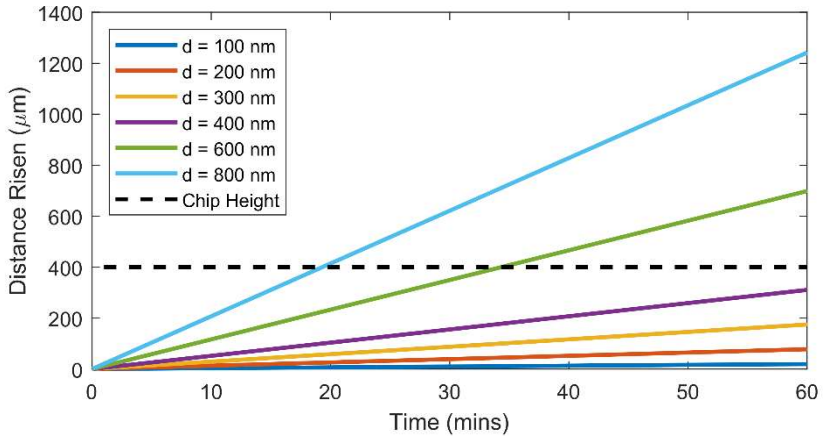

Figure 8.29 - Predicted distance risen for bubbles of varying diameter, d, over 60 minutes. Dashed line represents the channel height in the microfluidic device (400 μm).

SW480 cell monolayers cultured on the top plane. The distance risen over time for NBs of varying size can be predicted using Equation 3.25, and compared to the chip height (Figure 8.29). Although the chip height is 400 μm, assuming initially NBs are homogenously distributed on-chip, on average a bubble would need to rise 200 μm to reach the cell monolayer. In the three NB populations, the majority of NBs are between 200 and 400 nm in diameter and would take between 40 and 150 minutes to rise 200 μm. As such, an increased rise time would expect to increase the occurrence of sonoporation. NBs (RCF = 100 g) were first filtered through an 800 nm membrane, such to remove any bubbles that would be expected to rise rapidly to the top of the channel (~ 10 mins).

Filtered NBs were administered at their yield concentration (1.57 ± 0.05) x 10^{10} /mL (Figure 8.30a) with the observed decrease in yield compared to a typical RCF = 100 g sample (decrease by a factor of 5) is likely due to bubble destruction and coalescence induced by the filtration process. Although the filtration process had a detrimental effect on NB

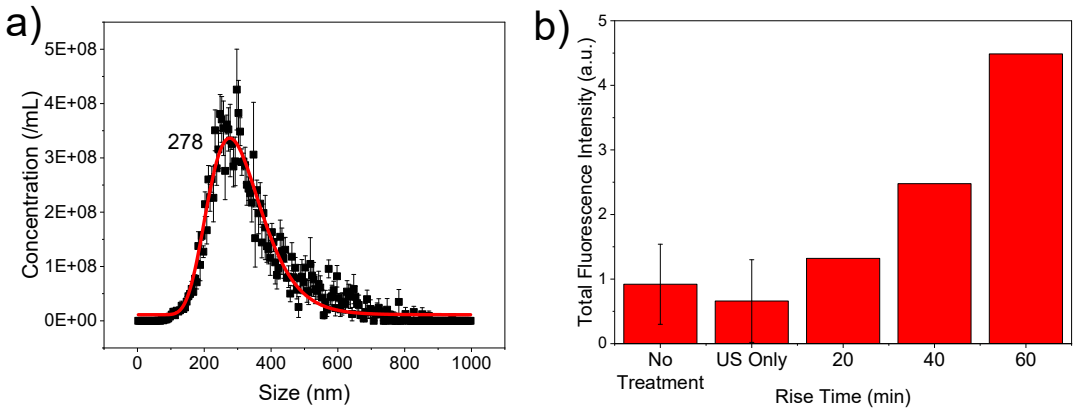

Figure 8.30 – Influence of NB on-chip rise time on Total Fluorescence Uptake, and hence sonoporation. NBs were isolated via centrifugation at an RCF of 100 g and filtered through an 800 nm membrane. Concentration = (1.57 ± 0.05) x 10^{10} /mL.

concentration, the modal size remained consistent with those expected for RCF = 100 g. Filtered NBs were incubated on-chip for 20, 40 and 60 min. prior to insonation and their TFI calculated, compared to control samples of no treatment or US only (incubation time = 60 min.). Little to no uptake was observed for the control samples and increasing rise time led to an increase in sonoporation and TFI (with TFI of 1.32 a.u., 2.48 a.u. and 4.49 a.u. for 20, 40 and 60 mins (Figure 8.30b)). As such, for all following experiments, NBs were left for 60 min on-chip prior to insonation, to maximize the change compared to control samples.

8.3.3 Influence of Nanobubble Size and Concentration on Sonoporation

Using the optimized experimental conditions, the influence of NB size and concentration on sonoporation was investigated. Three NB samples (previously described in Section 8.1) of different sizes were compared, after isolation at an RCF of 100, 500 or 1,000 g.

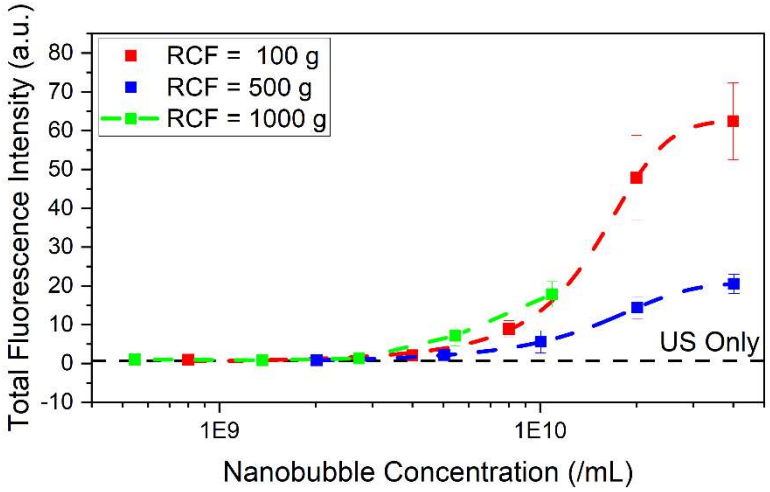

Figure 8.31 - Total Fluorescence Intensity (TFI) inside live cells due to ultrasound and NB mediated uptake, determined via confocal fluorescence microscopy, for three NB samples isolated via centrifugation at RCF = 100 g, 500 g and 1,000 g. Dashed line represents the TFI for the ultrasound (US) only control.

Figure 8.31 shows the TFI plot against initial NB concentration (i.e. the concentration NBs were initially delivered on chip). As values between the no treatment and US only controls are relatively similar, only the US only control is shown in the figure (dashed line). All three NB populations initially demonstrate sonoporation capability at their highest/yield concentration, which for RCF = 100 g, 500 g was ~ 4 x 10^{10} NBs/mL, and ~ 1 x 10^{10} NBs/mL for RCF = 1,000 g, due to their lower initial yield. Decreasing NB concentration led to a corresponding decrease in TFI in all three samples, as would be expected. Comparing directly between samples (i.e. differing size) at matched NB concentration, the larger NBs of RCF = 100 g had increased sonoporation capability compared to RCF = 500 g. However, comparison between RCF = 500 g and 1,000 g at matched NB concentration of 1 x 10^{10} NBs/mL, the

smaller NB population (RCF = 1,000 g) outperforms, with higher TFI (17.8 ± 3.3 compared to 5.6 ± 2.9) contrary to what would be expected.

8.4 Effect of Nanobubble Size on Stability

8.4.1 Matched Nanobubble Concentration

As NBs are left on-chip for 60 min to facilitate sonoporation by NB flotation, the stability of these NBs, and hence actual concentration at the time of insonation, is not known. Whilst this is not directly measurable on-chip, the temporal stability of NBs was investigated in situ in the NTA system to mimic the on-chip conditions (i.e. flow cell). NB concentration was measured over 60 min in 5 min intervals, at an initial concentration of ~ 10^9 NBs/mL, corresponding to the optimal concentration for NTA measurements. Although on the lower end of the NB concentration ranges characterised, higher concentrations (i.e. 10^{10} /mL) would result in increased scattering and noise, and hence unreliable measurements.

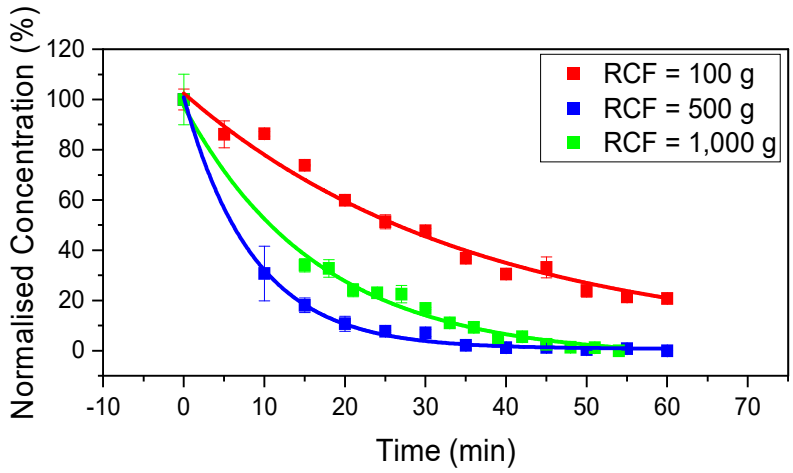

Figure 8.32 - Stability of Nanobubbles samples after separation via centrifugation at different RCF values. Normalised NB concentration measured in situ – "on-chip" over 60 min at matched initial nanobubble concentration of 10^9 bubbles/mL, fitted with an exponential decay function.

Figure 8.32 shows the trend between normalized NB concentration and time, fit with an exponential decay function. The half-life, $\tau_{1/2}$, of this exponential decay for each sample was 24.7 ± 2.5, 6.0 ± 0.2 and 11.6 ± 0.7 min for RCF of 100 g, 500 g and 1,000 g respectively. As the RCF = 1,000 g sample has increased stability compared to RCF = 500 g, these results might go some way towards explaining the sonoporation data. Although there is no universally agreed theory for NB stability, one contributing factor is the Laplace pressure, which is inversely proportional to size, and hence would predict to be largest for the smallest of the three NB samples.

However, results in show Figure 8.32 that the smallest NB sample (RCF = 1,000g) exhibits increased lifetime compared to RCF = 500 g, albeit with RCF = 100 g being the most stable. This suggests that (in the steady state) Laplace pressure is not the only mechanism at play that contribute to NB stability and lifetime. It was also found that the average (mean and mode) size of all samples remained constant over 60 min (Figure 8.33). This may suggest that bubbles are either coalescing and no longer within the measurable size range of NTA, or that there is an occurrence of rapid bubble dissolution.

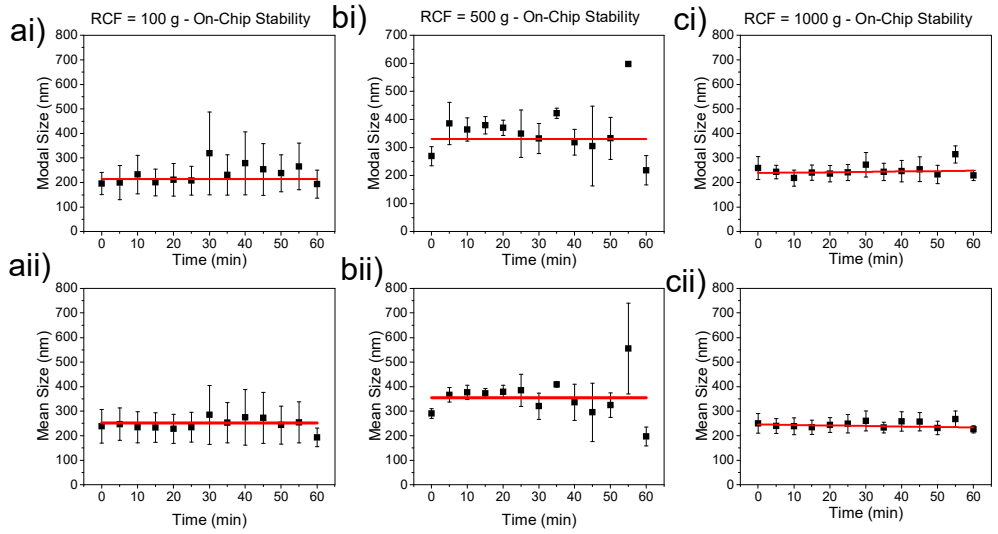

Figure 8.33 - NB stability measured in situ on the NTA system at a concentration of ~10^9 NBs/mL. (a) RCF = 100 g, (b) 500 g and (c) 1,000 g for modal (i) and mean (ii) sizes over 60 min. All results were repeated in triplicate over 3 independent NB productions, and were fit using a linear fit.

8.4.2 Matched Lipid Concentration

Measurements in Figure 8.32 were performed at matched NB concentration, however due to the differing yields in the initial samples, the sample dilution required to reach a set concentration varies. For example, less dilution was required for RCF = 1,000 g NBs compared to RCF = 100 g NBs to reach the matched NB concentration used in the *in situ* stability measurements. As RCF = 1,000 g NBs demonstrated increased stability compared to RCF = 500 g, it may suggest that sample dilution has an influence on NB stability and life-time. As such, the stability of NBs after various dilutions factors was investigated. NB samples were prepared and diluted at varying dilution factors (1 – 50, where 1 is stock concentration) and their concentration measured at t = 0 and t = 60 mins. Results are shown in Figure 8.34a. Here, final concentrations were normalized to their initial values to allow comparison between all 3 samples which had different initial NB concentrations. Across all samples, normalized NB concentration decreased with an increasing dilution factor, and

hence suggesting that dilute NB samples are less stable. Comparison of stability between samples followed showed that larger NBs (i.e. RCF = 100 g) have increased stability, compared to RCF = 500 g, 1,000 g, in agreement with predictions from the Laplace pressure.

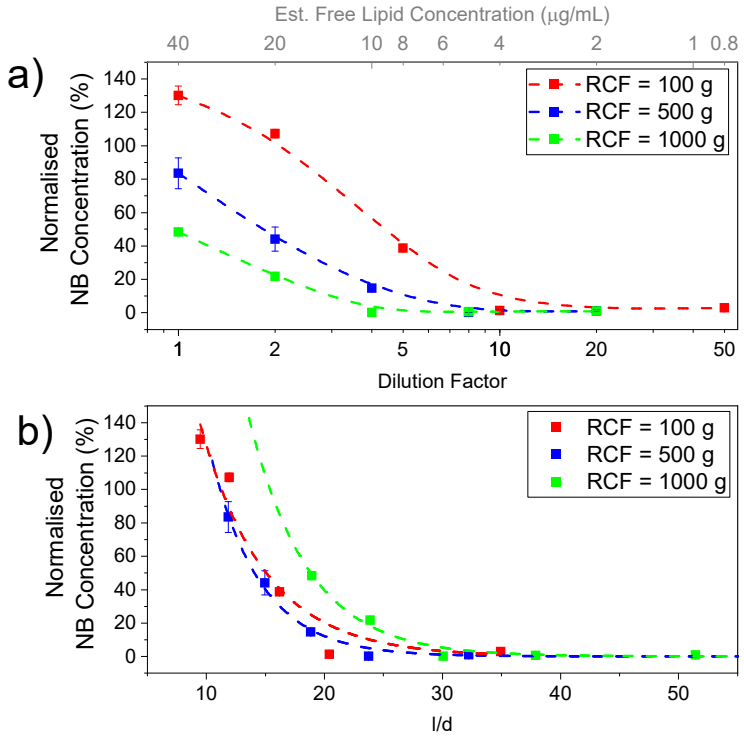

Figure 8.34 - Stability of NBs samples after separation via centrifugation at different RCF values, after storage for 60 minutes at varying dilution factors. NB concentration is expressed as normalised NB concentration, relative to the initial concentration a) Normalised NB concentration for dilution factors ranging from 1 (stock concentration) to 50 (i.e. 50 x diluted). The top x-axis also shows the estimated free lipid concentration in the NB sample. Data is fit with a spline curve to guide the eye. b) Normalised NB concentration as a function of the ratio of the interbubble distance, l, and mean NB diameter, d, achieved by dilutions.

Recently, theories have been proposed that both of these factors will influence the lifetime of lipid-shelled bubbles. Segers et al. [246,247] show that the use of higher lipid concentrations can aid short-term and long-term MB stability. The presence of liposomes in a thin liquid film between colliding bubbles can provide additional colloidal and surface forces, reducing coalescence probability. Here, diluting the NB sample will vary the total free lipid concentration. Here, this was initially assumed to be 40 μg/mL for all samples based on the following calculations. Initially, the produced MB sample will have a lipid concentration of 2 mg/mL. This sample is then diluted 10 x (i.e. 0.2 mg/mL) prior to isolation of NBs. Based off the 95:5 molar ratio of DPPC (M_w=734 g/mol) and DSPE-PEG2000 (M_w = 2805 g/mol), the MB solution will contain 1.44×10^{17} lipid molecules in total. Assuming a lipid head group area of 0.5 nm^2 and MB size of 1 μm at a concentration of 5×10^9 /mL (after dilution), MBs

would contribute to $6.28x10^{16}$ lipids/mL. This sample would also be expected to contain a proportion of NBs. Assuming this NB population is identical in size and concentration to that of Sample I, this would account for $5.12x10^{16}$ lipids/mL. Here, the remaining lipids ($2.98x10^{16}$ lipids/mL) can be accounted for by "free" liposomes in solution. This value of liposomal lipids would be expected to remain constant throughout the NB isolation process, as the vertical distance travelled during centrifugation at 1,000 g over 5 min is negligible (~ 50 μm). When considering the contribution of free liposomes/lipid to NB stability by preventing coalescence via steric effects, it is only this concentration that is important. Here, the free lipid concentration of $2.98x10^{16}$ lipids/mL is equivalent to a mass concentration of 40 μg/mL, which will be consistent throughout all NB samples. This is reflected by the data shown in Figure 8.34a, in which increasing dilution will reduce the concentration of free lipid, which leads to a decrease in NB stability.

Additionally, molecular dynamics simulations by Weijs et al. [128] predicted that small inter-bubble distances, can shield gas diffusion due to high local gas concentrations, and hence enhance NB lifetime. Two systems were investigated in which inter-bubble spacing, l, (or box size in their periodic MD simulations) was varied, where l = 15 nm or 30 nm for a bubble with initial diameter of 3.64 nm. The total number of gas molecules inside the bubble remain constant (Nb = 333) whilst different conditions are investigated for different amounts of gas dissolved in the liquid surrounding the bubble. For all conditions in which l = 15 nm (i.e. l/d = 4.12) bubbles were shown to be stable. For those in which l = 30 nm (I.e. l/d = 8.24) bubbles were unstable unless a large quantity of gas was dissolved in the surrounding medium. Assuming that this prediction holds for all sizes of NBs, this predicts that there exists some ratio between inter-bubble spacing and bubble diameter that will yield stability, regardless of dissolved gas content.

Further analysis of the data presented in Figure 8.34a, to consider the ratio of inter-bubble distance and diameter (l/d) is presented in Figure 8.34b, in which normalised NB concentration is shown after storage for 60 min for $9.5 < l/d < 51.4$. Data was fit using an exponential decay function, and extrapolated to interpret behaviour at l/d values outside the measured range, and above the minimum achievable inter-bubble spacing restricted by initial NB yield. As in Weijs et al. the inter-bubble distance, l, was defined as the distance between the centre of each particle, and hence $l = n^{-1/3}$ where n is volume density of the particles. Across all samples, NB lifetime decreases with increased l/d, in agreement with the proposed model. Interestingly, RCF = 1,000 g NBs (the smallest NB sample) displays enhanced stability at increased l/d values compared to Sample I and II, which follow a similar trend. For example, for NB stability of RCF = 1,000 g NBs over 60 min (i.e. normalised NB concentration = 100 %) an l/d value of 15.4 would be required, compared to 11.1 and 11.3 for RCF = 100g and 500 g

NBs respectively. Hence, for RCF = 1,000 g NBs inter-bubble spacing along cannot explain the increased stability, but which may be attributed to a higher free lipid concentration approximately 5 and 3 times greater than RCF = 100 g and 500 g NBs. Hence, these data suggests that both inter-bubble distance and free lipid concentration influence NB lifetime and stability.

In this study and many others [56,99,109,150,248], the main component of the NB stabilizing shell consists of phosphatidylcholine lipids and as such is zwitterionic. Whilst our NBs are stable for ~ 60 min, dependent on their size and concentration, the rapid decay of concentration at lower lipid concentration and NB concentration would need to be improved for translation into *in vivo* use. Many studies have incorporated combinations of non-ionic poloxamers[55], cross-linked polymers [62] and anionic lipids [54,113] into the NB shell to increase lifetime. Traditionally these methods act to either reduce surface tension to prevent dissolution or reduce bubble coalescence via electrostatic repulsion. A recent theory proposed by Hau Tan et al. [66] suggests that the incorporation of ionic-lipids, and hence NBs possessing a non-zero zeta potential, may provide an electrostatic pressure which acts to counter the Laplace pressure of a collapsing bubble. As such, our use of NTA to successfully characterize NBs is promising for the future development of stable NBs, opening a range of studies to investigate the effect of varying NB shell composition on stability and *in vitro* and *in vivo* performance.

8.5 Conclusion

Accurate characterization of NB size and population has proved challenging in the research community and may limit their transition into clinical studies. In this chapter, a commercially available NTA system was used to determine the size and concentration of exclusively NBs, in a mixed population containing NBs and liposomes. By considering the difference in optical properties between gas-cored bubbles and aqueous cored liposomes, and the associated change in intensity of scattered light, use of a high particle concentration and low camera level allowed measurement of exclusively highly scattering particles. The evidence that these particles were gas-cored, or at the least acoustically active, was marked by a decrease in concentration after exposure to a HIFU destruction pulse. NBs of varying size were then isolated via centrifugation, and their sonoporation capabilities compared across a range of concentrations. Initially studies using a well plate-based set up yielded no evidence of any sonoporation, however change of acoustic and cell culture set up to an on-chip method yielded results, likely due to reducing the average bubble-cell distance.

Confocal fluorescence microscopy and image analysis were used to determine the occurrence of sonoporation. Although sonoporation efficiency was dependent on NB concentration, and the size of the NBs, the expected trends were not followed in which larger

NBs would be expected to have increased therapeutic performance. Instead, at certain NB concentrations, the smallest NB sample outperformed all other samples which then raised questions about their on-chip stability. It was found that in on-chip conditions and at matched NB concentration, the smallest NB sample demonstrated enhanced stability likely due to an increased lipid concentration during measurement. The effect of lipid concentration on stability was then investigated, in which samples were diluted by varying amounts and stored for 1 hour at room temperature. The storage lipid concentration had a significant influence on NB stability where below a threshold concentration there was an almost total loss in NBs across all samples. As the lipid concentration is analogous to sample dilution and hence NB concentration, this also suggests that inter-bubble distance is a governing factor in stability.

These results were then compared to established theories behind bubble stability. In one of which it is hypothesized that increased free lipid concentration can reduce the probability of coalescence as liposomes present between colliding bubbles can provide additional colloidal and surface forces. Another study based on molecular dynamics simulations suggests that small inter-bubble distances can increase NB stability by providing a shield to gas diffusion due to high local gas concentrations and hence there exists critical inter-bubble distance (l_0) at which NBs are found to be stable. This predicted threshold was concurrent with our results across all three NB sizes and the concentration ranges that were measured.

As such, the importance of fully characterizing a therapeutic NB based system is highlighted in which key physical differences between samples have an influence on their stability, and hence their sonoporation performance.

9 Conclusions and Future Work

9.1 Concluding Remarks

Chapter 2 consisted of a literature review, outlining the current state of the therapeutic and diagnostic NB field. A multitude of studies demonstrate the diagnostic and therapeutic potential of NBs, at both clinical and pre-clinical US frequencies. This is a key finding, as one potential hurdle for the clinical translation of NBs is their high predicted resonance frequency, and the associated increase in acoustic attenuation. Despite debate over the validity of the EPR effect, there is growing evidence that the sub-micron nature of NBs promotes extravasation and increased retention in tumour tissue, demonstrated via diagnostic imaging, fluorescence microscopy and acoustic techniques. The therapeutic capability of NBs in combination with US, either by co-delivery or loading of therapeutics, is also widely described in the literature, in which nearly all studies show an increased in efficacy compared to control experiments. However, accurate characterisation of NB size and concentration still remains challenging and makes comparison between studies difficult. Further, few studies compare the therapeutic efficacy of NBs compared to their larger MB counterparts. In reality, it may prove beneficial to administer a mixed population of both MBs and NBs, in which drug loading and bio-effects of MBs are advantageous, but where NBs can increase drug penetration into the solid tumour. The main aim of this project, and thesis, was to investigate the diagnostic and therapeutic capabilities of lipid-shelled NBs. Here, two main gaps in the literature were investigated.

Firstly, Chapter 6 addresses the lack of liposome-NB systems, in which the well-defined drug-loading properties of liposomes are combined with the acoustic release trigger provided by NBs. Here, NBs were encapsulated within a drug-loaded liposome, whilst maintaining their nanoscale (~ 250 nm) nature, forming "Nested-NBs". NBs with a C_4F_{10} core were produced using the microfluidic microspray regime, as described in previous publications. The size and concentration of these NBs were determined using multiple techniques: DLS and TEM (size only), and NTA and RMM (size and concentration). Across all techniques, modal size was consistent whilst the RMM identified the presence of positively buoyant particles down to ~ 150 nm in size. NBs showed good echogenicity using a clinically approved B-mode US scanner, with no signs of acoustic shielding at higher concentrations. Further evidence of NBs being acoustically active was demonstrated using a HIFU destruction pulse, signified by a near total loss in echogenicity.

Loading of the model drug calcein into liposomes was quantified using fluorescence spectroscopy, in which the self-quenching of calcein can be used to quantify liposomal release. NBs were then encapsulated within the liposomal shell via a passive method. Here, two cleaning techniques were investigated: gel filtration chromatography and centrifugation. It

was identified that not only was centrifugation more efficient at removing free calcein, but also removed un-encapsulated NBs. Loading of calcein into Nested-NBs was shown to be stable for at least 30 min at physiological temperatures, and for at least 3 hours during storage at 4 °C.

Nested-NBs were treated with a pulsed-wave HIFU (1.1 MHz) trigger, however for duty cycles of 1% and 50 %, and at peak negative pressures of up to 4.83 MPa no calcein release was observed, despite B-mode imaging showing a loss of echogenicity, indicative of NB destruction. To further observe the acoustic activity of Nested-NBs during insonation, passive cavitation detection (PCD) was used to monitor acoustic emissions. Here, the occurrence of stable and inertial cavitation across the insonation period was quantified. During insonation, Nested-NBs underwent both stable and inertial cavitation but did not induce any drug release. Changing modality to continuous wave was capable of triggering release over a range of pressures, compared to liposome only controls. These observations posed the question of what the true release mechanism is in the Nested-NB system, as it is apparent that NB oscillation or destruction was incapable of inducing drug release. It was hypothesized that smaller NB below the limit of detection of RMM, may exist as phase-condensed liquid droplets. The change of modality to continuous wave, and the associated increase in both acoustic and thermal energy, may provide a synergistic effect to vaporise the encapsulated droplet, and hence trigger release. This hypothesis was in agreement with theoretical models of acoustic droplet vaporisation, in which the acoustic and thermal conditions used were predicted to induce vaporisation, and the resultant bubble post vaporisation large enough to rupture the liposomal shell. As such, this study shows the diagnostic and therapeutic potential of the Nested-NB system.

Chapter 8 investigates the behaviour of NBs of varying sizes and assesses their therapeutic performance as well as more fundamentally studying their stability. In this chapter, NBs were produced by mechanical agitation, and with a C_3F_8gas core. To characterise the different sizes of NBs, a commercial NTA system was utilized such that highly scattering NBs (due to their gas core) can be distinguished from lower scattering liposomes (aqueous core). This method was successfully able to detect and measure exclusively NBs, by requiring a lower camera level setting on the NTA system, such that scattering from liposomes is not visible. NBs of different sizes were isolate via centrifugation at varying RCF, due to the relationship between terminal rise velocity, gravitational acceleration and size. The therapeutic efficiency of these 3 different sized NBs was compared in co-delivery experiments where 70 kDa Dextran was used as a membrane probe, and a clinically relevant US trigger (2.2 MHz, MI 0.6) used to induce bubble cavitation. Colorectal cancer cells (SW480) were cultured as a monolayer within a microfluidic device. All different sizes of NBs were capable of inducing intracellular

uptake of Dextran, in which an increased NB concentration correlated to an increase in fluorescence intensity inside cells.

However, the trend between varying NB size and therapeutic capability did not scale as would be expected, in which larger NBs would be expected to have an increased contribution to any bio-effects, and interaction with the clinically relevant US. In fact, at certain NB concentrations, the smallest of the three NB samples had increased therapeutic performance. The mechanism behind this was investigated by assessing NB stability at matched NB concentration, in an *in situ* mimicking environment mimicking that on-chip, The stability and life-time trend of NBs measured *in situ* mimicked that of the on-chip therapeutic studies, in which NBs were incubated on-chip for 60 min to facilitate sonoporation, by minimizing NB-cell distances. These results then disagreed with initial predictions, in that smaller NBs should be less stable due to an increased contribution from the Laplace pressure, which drives dissolution. A potential explanation is that due to a lower initial NB yield for the smaller sample, when measured at matched NB concentration the resultant lipid concentration is higher compared to other samples. This hypothesis was tested by storing NBs for 1 hour under different conditions, (i.e. varying lipids and NB concentration) achieved by sample dilution.

The storage conditions had a significant influence NB lifetime in which increasing dilution factors had a negative effect on stability. These results suggested that total NB concentration, and hence inter-bubble distance is another factor influencing NB lifetime. The stability results in this thesis agreed with a theory in which it is proposed there exists a critical inter-bubble distance to which NBs are stable. As a result, this chapter highlights that small variations in NB size, as is commonplace in the literature, has a significant influence on their therapeutic performance, although this is not simply linked to size. Hence, it is crucial that NB size, concentration and stability is assessed for successful translation from pre-clinical to clinical studies.

Overall, is it clear that lipid-shelled NBs have much promise as diagnostic and therapeutic agent, but work is still in infancy and standardization over production, characterization and treatment parameters is required.

9.2 Future Work

Whilst the work in this thesis appears as two distinct and complete studies, there remains many routes for further optimisation and investigation.

9.2.1 Further Development of Liposome-NB Systems

Nested-NBs described in this thesis were capable of triggered-drug release, after application of HIFU. Here, relatively high pressures were required (2 – 4 MPa) were required to induce significant drug release. Additionally, continuous wave exposure was required, which would

lead to increase thermal effects *in vivo*. Whilst HIFU is used clinically to treat prostate cancer via thermal ablation, treatments can last multiple hours due to the small focal region (~ 1 mm) and high focal gain of the system. The high pressures required here are attributed to the fact that the release mechanism is acoustic vaporisation of phase condensed PFB droplets, as opposed to gas bubbles. Here, one potential route could be to repeat encapsulation of NBs following the described protocols, but using NBs with a C_3F_8gas-core, such that they are more likely to exist in a gaseous state.

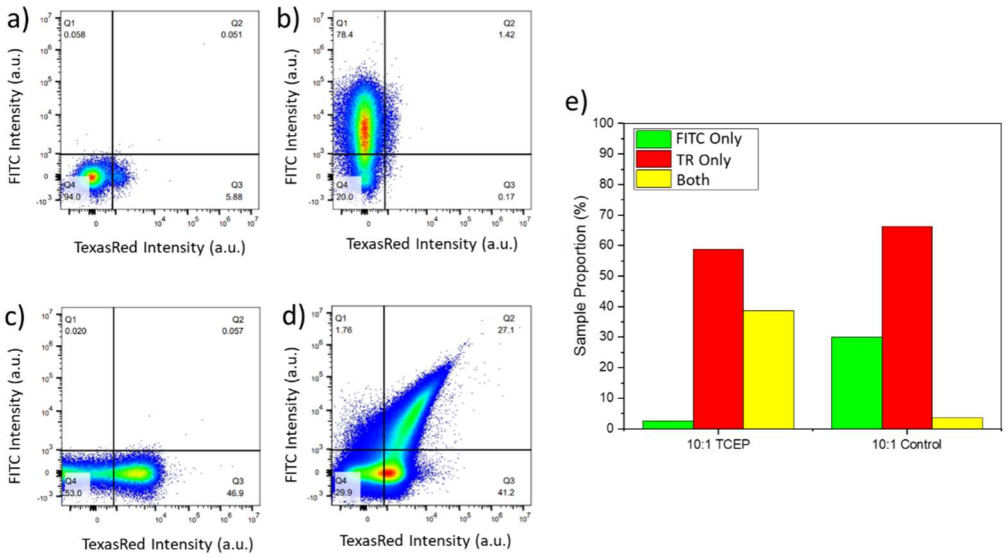

Figure 9.1 - Flow cytometry data quantifying FITC and TexasRed emissions from MS-NB and liposome samples. a) A PBS buffer control to determine gating. b) FITC-Liposomes only. c) TexasRed MS-NBs only. d) MS-NBs and Liposomes combined at a 10:1 ratio and conjugated using maleimide-PDP binding.

Preliminary work in this project investigated the ability to conjugate multiple smaller NBs (~ 100 nm) in diameter to a central drug loading liposome, in which during insonation oscillation of the attached NBs may induce drug release. This work is not so dissimilar from that described by Banerjee group [155,156], in which multiple drug-loaded liposomes (~200 nm) were conjugated to a central NB (~ 400 nm). However, in their results, the release profile is not so dissimilar between the application of US and controls. In fact, in traditional MB-liposome conjugate systems, pressure of up to 7 MPa are required to induce drug release [47]. This may be attributed to 'sonoprinting', in which liposomes are displaced from the central bubble shell after application of US [249]. The conjugation of multiple NBs to a central liposome may bypass this, as multiple oscillating bubbles will be exerting shear stress and pushing-pulling forces on the liposome bilayer. To achieve this, PEGylated lipids conjugated to PDP (pyridyldithiol propionate) and maleimide were incorporated into the shell of MS-NBs and liposomes (~ 400 nm), respectively. Here, the addition of TCEP (tris(2-carboxyethyl)phosphine) can cleave the

disulphide bonding in PDP, and the resultant thiol group bond to the maleimide. Fluorescent lipids were also used to identify MS-NBs (FITC) and liposomes (TexasRed), and flow cytometry used to quantify the fluorescence intensity from each fluorophore, and where co-localisation is indicative of binding. Here, the larger liposome sample was mixed in a 1:10 ratio with MS-NBs and left to incubate for 30 mins to facilitate binding. Flow cytometry data is shown in Figure 9.1, compared to a control sample where PDP was not reduced using TCEP. Here, the addition of TCEP significantly increased the percentage of events with fluorescence co-localisation from 3.6 % to 38.7 %. Hence, this method shows initial promise for the development of a new NB-liposome conjugate. There may also be beneficial diagnostic properties to this system, in which the magnitude of sub-harmonic emissions may be increased, compared to bare NBs[132]. The progression of this work was halted by the COVID-19 pandemic and closure of facilities.

9.2.2 Isolation of Nested-NBs

Work in Chapter 6 developed Nested-NBs, in which drug release from liposomes was triggered by an encapsulated PFB NB in combination with a HIFU destruction pulse. Here, release efficiency from each Nested-NB was approaching 100 %. However only approximately 20 % of the sample population consisted of Nested-NBs, with the remainder being drug-loaded liposomes without an encapsulated NB. As such the majority of the population contains liposomes that do not release drug in response to an US trigger, and may still lead to side effects associated with liposomal drug delivery (i.e. HFS syndrome). To rectify this, a method could be developed to isolate only those liposomes that contain a NB and are acoustically active. The acoustic radiation force has been utilised previously either to translate bubbles into contact with a cell monolayer and promote sonoporation, or to selectively isolate MBs of varying size after production of a polydisperse population using microfluidics.

Preliminary experiments undertaken in this project investigated the ability of the acoustic radiation force to translate. A cuvette based, experimental set up was utilised, in which scattered light emitted by a photodiode is detected at a 90 ° angle by a photodiode (Figure 9.1). A 1 MHz unfocused transducer (MI 0.6, 1 kHz PRF, 1 % Duty Cycle) was placed below the cuvette, such that the acoustic radiation force will translate bubbles towards the top of the cuvette. Here, the light path from the photodiode and detector were positioned at the top of the cuvette, such that scattered light intensity will increase as bubbles approach the top of the cuvette.

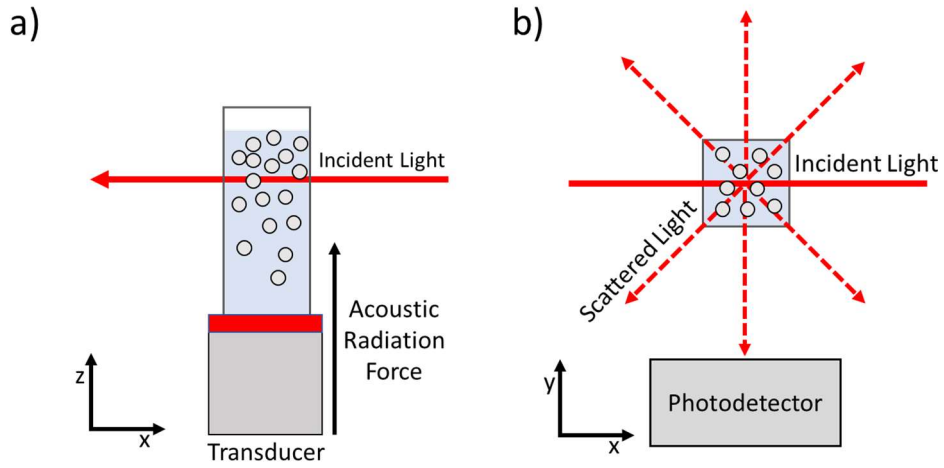

Figure 9.2 – Schematic of the acoustic and optical experimental set up to determine the translation of bubbles via the acoustic radiation force. a) Shown in the x-z plane (side on view) in which a transducer is positioned below a cuvette containing bubbles, with an incident light beam passing through the top of the cuvette. b) Shown in the x-y plane (from above) in which light scattered by bubbles is detected at 90 ° by a photodetector.

Preliminary results shown in Figure 9.3a show the voltage recorded by the photodetector, quantifying scattered light, as MBs (10^8 /mL) are translated to the top of the cuvette and into the light path, by the incident US and associated acoustic radiation force. Application of the US (time = 10 s) is marked by a significant increase in voltage as MBs move from the bottom to the top of the cuvette. The signal begins to plateau at time = 30 s as the US is turned off. To determine whether NBs could be detected by this set up, the magnitude of light scattered by an MS-NB sample (no US) was measured in which voltage is found to increase exponentially with MS-NB concentration (Figure 9.2b).

The translation experiment was repeated with MS-NBs however no change in voltage was observed, likely due to the proportionality of the acoustic radiation force with volume. This system does also not account for the formation of standing waves due to the liquid-air interface associated at the top of the cuvette, in which MB/NBs may assemble at pressure nodes/anti-nodes dependent on their size and resonance frequency. The progression of this work was limited by the COVID-19 pandemic and closure of facilities. Future work may investigate this phenomenon utilizing microfluidics for increased fidelity, following an acoustic method described by Segers et al. [250]. Here, a piezo is integrated into a microfluidic chip to displace bubbles that are then separated hydrodynamically, as displacement is dependent on the driving frequency and bubble resonance frequency. In the case of Nested-NBs, high frequency US could be used to displace the liposomes containing a NB and then be isolated downstream.

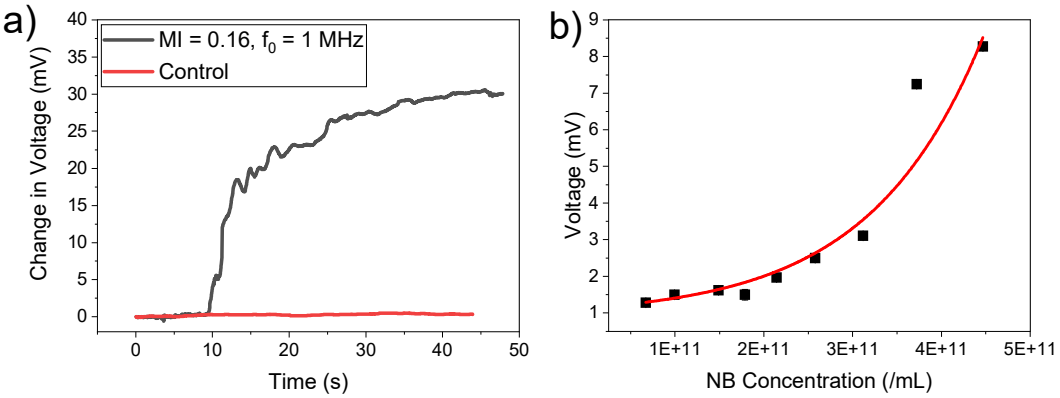

Figure 9.3 – Detected voltage from scattered light in a light scattering set up, used to quantify the motion and concentration of bubbles. a) Change in voltage from the initial reading for a MB sample (10^8 MB/mL) after application of ultrasound, such that MBs translate to the top of the cuvette. b) Voltage of scattered light for NBs at concentrations ranging from 1 – 5 x 10^{10} /mL.

9.2.3 High Frequency NB Sonoporation

The work described in Chapter 8 demonstrated the ability of NBs and US to locally induce cell membrane poration and increase uptake of a model therapeutic. In that study, the US trigger used had clinically relevant pressures (MI = 0.6) and driving frequency (2.25 MHz). Whilst it is predicted the NB resonance frequency will decrease with increasing driving pressure, even under the assumption of lipid shell buckling, their resonance is still predicted to be > 20 MHz [185]. Hence insonation at lower, clinically relevant frequencies is not optimized to drive their oscillation, and hence induce sonoporation. Despite this, few studies across the literature utilize higher frequencies with therapeutic NBs. A potential drawback of higher frequencies is the associated increase in acoustic attenuation, hence limiting the penetration into tissue. However, for treatment of certain disease, invasive transducers and probes are already commonly utilised (e.g., HIFU treatment of prostate cancer, as previously discussed),

in which the distance to the target site is reduced, and attenuation becomes less of a limiting factor. It would be interesting, and beneficial, to investigate the sonoporation capabilities of NBs at higher frequencies, such that they are excited on resonance, and also optimize other acoustic parameters (PRF, duration etc.).

9.2.4 Influence of NB Size on Zeta Potential

There is no agreed universal theory that describes and explains the stability and lifetime of NBs. Whilst many factors may play a role in governing lifetime, one recently proposed theory is that of an electrostatic pressure to offset the Laplace pressure, which may describe the dynamics of both shelled and shell-less NBs. In the model proposed by Hau Tan et al. [66], an additional term due to the zeta potential of a NB is added to the Epstein-Plesset equation, such to balance the Laplace pressure. Here, assuming charge conservation, the surface charge density of a shrinking bubble will progressively increase until the electrostatic pressure balances the Laplace pressure. The model here predicts that bubbles will reach equilibrium at diameters of ~10^7 m. Whilst this model partially agrees with experimental data published prior, an interesting route could be to investigate the influence of NB size on their zeta potential. Here, for NBs with a constant proportion of charged anionic lipids (e.g., DPPA) smaller NBs would be expected to have increased zeta potential. Hence, the NB isolation methods described in this thesis could be used to isolate and measure the zeta potential of NBs of varying size, testing the hypothesis of the model.

9.2.5 Holographic NTA

Recently, Midvedt and Eklund et al. [117,251] developed a methodology termed as "holographic NTA". This method follows a principle similar to standard NTA but differing in that an external reference beam is used to determine particle refractive index, by observing changes in the amplitude and phase of scattered light. Whilst so far this technique has been used to accurately determine the refractive index and size of polystyrene and latex spheres, and those of shell-less NBs. Further work could involve a collaboration with the group to characterise the lipid-shelled, theranostic NBs developed throughout this thesis, as well as characterising the different size NBs described in Chapter 8.

9.2.6 Freeze Dried NBs

Whilst it is evident NBs (and MBs) have potential for both diagnosis and therapy, their limited lifetime (typically a few hours) is one hurdle that needs to be overcome for successful clinical translation. Clinically used MBs (e.g., Definity) are supplied as a lyophilized (or freeze dried) powder, in which the headspace is saturated with the desired gas for the core. This powder is then rehydrated using a saline solution, prior to mechanical agitation to form the result contrast agents. In our group, we recently demonstrated the ability to successfully freeze dry and

reconstitute therapeutic MBs (i.e. those with a conjugated drug payload)[252]. Hence, the ability to freeze dry and reconstitute NBs would be advantageous, not just for clinical translation, but also for their continued use and research pre-clinically. As this thesis described methodology to isolate NBs of varying size, it would be interesting to see whether freeze drying would preserve NB size and hence eliminate the need for repeated production and isolation.

References

(1) Shapiro, C. L.; Recht, A. Side Effects of Adjuvant Treatment of Breast Cancer. *J. Med.* **2001**, *344* (26), 1997–2008.

(2) Wargo, J. A.; Reuben, A.; Cooper, Z. A.; Oh, K. S.; Sullivan, R. J. Immune Effects of Chemorapy, Radiation, and Targeted Rapy and Opportunities for Combination with Immunorapy. *Semin. Oncol.* **2015**, *42* (4), 601–616. https://doi.org/10.1053/j.seminoncol.2015.05.007.

(3) Boucher, Y.; Baxter, L. T.; Jain, R. K. Interstitial Pressure Gradients in Tissue-Isolated and Subcutaneous Tumors: Implications for Therapy. *Cancer Res.* **1990**, *50* (15), 4478–4484.

(4) Baronzio, G.; Parmar, G.; Baronzio, M. Overview of Methods for Overcoming Hindrance to Drug Delivery to Tumors, with Special Attention to Tumor Interstitial Fluid. *Front. Oncol.* **2015**, *5* (JUL), 1–17. https://doi.org/10.3389/fonc.2015.00165.

(5) Minchinton, A. I.; Tannock, I. F. Drug Penetration in Solid Tumours. *Nat. Rev. Cancer* **2006**, *6* (8), 583–592. https://doi.org/10.1038/nrc1893.

(6) Mico, V.; Charalambous, A.; Peyman, S. A.; Abou-Saleh, R. H.; Markham, A. F.; Coletta, P. L.; Evans, S. D. Evaluation of Lipid-Stabilised Tripropionin Nanodroplets as a Delivery Route for Combretastatin A4. *Int. J. Pharm.* **2017**, *526* (1–2), 547–555. https://doi.org/10.1016/j.ijpharm.2017.05.009.

(7) Müller, R. H.; Jacobs, C.; Kayser, O. Nanosuspensions as Particulate Drug Formulations in Therapy: Rationale for Development and What We Can Expect for the Future. *Adv. Drug Deliv. Rev.* **2001**, *47* (1), 3–19. https://doi.org/10.1016/S0169-409X(00)00118-6.

(8) Alyane, M.; Barratt, G.; Lahouel, M. Remote Loading of Doxorubicin into Liposomes by Transmembrane PH Gradient to Reduce Toxicity toward H9c2 Cells. *Saudi Pharm. J.* **2016**, *24* (2), 165–175. https://doi.org/10.1016/j.jsps.2015.02.014.

(9) Bixner, O.; Kurzhals, S.; Virk, M.; Reimhult, E. Triggered Release from Thermoresponsive Polymersomes with Superparamagnetic Membranes. *Materials (Basel).* **2016**, *9* (1), 1–14. https://doi.org/10.3390/ma9010029.

(10) Beltrán-Gracia, E.; López-Camacho, A.; Higuera-Ciapara, I.; Velázquez-Fernández, J. B.; Vallejo-Cardona, A. A. *Nanomedicine Review: Clinical Developments in Liposomal Applications*; Springer Vienna, 2019; Vol. 10. https://doi.org/10.1186/s12645-019-0055-y.

(11) Abou-Saleh, R. H.; Swain, M.; Evans, S. D.; Thomson, N. H. Poly(Ethylene Glycol) Lipid-Shelled Microbubbles: Abundance, Stability, and Mechanical Properties. *Langmuir* **2014**, *30* (19), 5557–5563. https://doi.org/10.1021/la404804u.

(12) Bozzuto, G.; Molinari, A. Liposomes as Nanomedical Devices. *Int. J. Nanomedicine* **2015**, *10*, 975–999. https://doi.org/10.2147/IJN.S68861.

(13) Ishida, T.; Harashima, H.; Kiwada, H. Liposome Clearance. *Biosci. Rep.* **2002**, *22* (2), 197–224. https://doi.org/10.1023/A:1020134521778.

(14) Michelle Longmire, Peter L. Choyke, M.D., and Hisataka Kobayashi, M.D., P. . Clearance Properties of Nano-Sized Particles and Molecules as Imagin Agents: Consideration and Caveats. **2012**, *3* (5), 703–717. https://doi.org/10.2217/17435889.3.5.703.Clearance.

(15) Luo, R.; Li, Y.; He, M.; Zhang, H.; Yuan, H.; Johnson, M.; Palmisano, M.; Zhou, S.; Sun, D. Distinct Biodistribution of Doxorubicin and the Altered Dispositions Mediated by Different Liposomal Formulations. *Int. J. Pharm.* **2017**, *519* (1–2), 1–10. https://doi.org/10.1016/j.ijpharm.2017.01.002.

(16) Moorcroft, S. C. T.; Roach, L.; Jayne, D. G.; Ong, Z. Y.; Ong, Z. Y.; Evans, S. D. Nanoparticle-Loaded Hydrogel for the Light-Activated Release and Photothermal Enhancement of Antimicrobial Peptides. *ACS Appl. Mater. Interfaces* **2020**, *12* (22), 24544–24554. https://doi.org/10.1021/acsami.9b22587.

(17) Vines, J. B.; Yoon, J. H.; Ryu, N. E.; Lim, D. J.; Park, H. Gold Nanoparticles for Photothermal Cancer Therapy. *Front. Chem.* **2019**, *7* (APR), 1–16. https://doi.org/10.3389/fchem.2019.00167.

(18) Roach, L.; Booth, M. E.; Ingram, N.; Paterson, D. A.; Batchelor, D. V. B.; Moorcroft, S. C. T.; Bushby, R. J.; Critchley, K.; Coletta, P. L.; Evans, S. D. Evaluating Phospholipid-Functionalized Gold Nanorods for In Vivo Applications. *Small* **2021**, *2006797*. https://doi.org/10.1002/smll.202006797.

(19) Newham, G.; Mathew, R. K.; Wurdak, H.; Evans, S. D.; Ong, Z. Y. Polyelectrolyte Complex Templated Synthesis of Monodisperse, Sub-100 Nm Porous Silica Nanoparticles for Cancer Targeted and Stimuli-Responsive Drug Delivery. *J. Colloid Interface Sci.* **2021**, *584*, 669–683. https://doi.org/10.1016/j.jcis.2020.10.133.

(20) Yang, K. N.; Zhang, C. Q.; Wang, W.; Wang, P. C.; Zhou, J. P.; Liang, X. J. PH-Responsive Mesoporous Silica Nanoparticles Employed in Controlled Drug Delivery Systems for Cancer Treatment. *Cancer Biol. Med.* **2014**, *11* (1), 34–43. https://doi.org/10.7497/j.issn.2095-3941.2014.01.003.

(21) Noh, S. hyun; Moon, S. H.; Shin, T. H.; Lim, Y.; Cheon, J. Recent Advances of Magneto-Thermal Capabilities of Nanoparticles: From Design Principles to Biomedical Applications. *Nano Today* **2017**, *13*, 61–76. https://doi.org/10.1016/j.nantod.2017.02.006.

(22) Moorcroft, S. C. T.; Jayne, D. G.; Evans, S. D.; Ong, Z. Y. Stimuli-Responsive Release of Antimicrobials Using Hybrid Inorganic Nanoparticle-Associated Drug-Delivery

Systems. *Macromol. Biosci.* **2018**, *1800207*, 1800207. https://doi.org/10.1002/mabi.201800207.

(23) de Leon, A.; Perera, R.; Nittayacharn, P.; Cooley, M.; Jung, O.; Exner, A. A. *Ultrasound Contrast Agents and Delivery Systems in Cancer Detection and Therapy*, 1st ed.; Elsevier Inc., 2018; Vol. 139. https://doi.org/10.1016/bs.acr.2018.04.002.

(24) Ibsen, S.; Benchimol, M.; Simberg, D.; Schutt, C.; Steiner, J.; Esener, S. A Novel Nested Liposome Drug Delivery Vehicle Capable of Ultrasound Triggered Release of Its Payload. *J. Control. Release* **2011**, *155* (3), 358–366. https://doi.org/10.1016/j.jconrel.2011.06.032.

(25) Nesbitt, H.; Sheng, Y.; Kamila, S.; Logan, K.; Thomas, K.; Callan, B.; Taylor, M. A.; Love, M.; O'Rourke, D.; Kelly, P.; Beguin, E.; Stride, E.; McHale, A. P.; Callan, J. F. Gemcitabine Loaded Microbubbles for Targeted Chemo-Sonodynamic Therapy of Pancreatic Cancer. *J. Control. Release* **2018**, *279* (December 2017), 8–16. https://doi.org/10.1016/j.jconrel.2018.04.018.

(26) Javadi, M.; Pitt, W. G.; Belnap, D. M.; Tsosie, N. H.; Hartley, J. M. Encapsulating Nanoemulsions inside Eliposomes for Ultrasonic Drug Delivery. *Langmuir* **2012**, *28* (41), 14720–14729. https://doi.org/10.1021/la303464v.

(27) Lin, S.; Shah, A.; Hernández-Gil, J.; Stanziola, A.; Harriss, B. I.; Matsunaga, T. O.; Long, N.; Bamber, J.; Tang, M. X. Optically and Acoustically Triggerable Sub-Micron Phase-Change Contrast Agents for Enhanced Photoacoustic and Ultrasound Imaging. *Photoacoustics* **2017**, *6*, 26–36. https://doi.org/10.1016/j.pacs.2017.04.001.

(28) Laing, S. T.; Moody, M. R.; Kim, H.; Smulevitz, B.; Huang, S. L.; Holland, C. K.; McPherson, D. D.; Klegerman, M. E. Thrombolytic Efficacy of Tissue Plasminogen Activator-Loaded Echogenic Liposomes in a Rabbit Thrombus Model. *Thromb. Res.* **2012**, *130* (4), 629–635. https://doi.org/10.1016/j.thromres.2011.11.010.

(29) Klegerman, M. E.; Naji, A. K.; Haworth, K. J.; Zou, Y.; Golunski, E.; Peng, T.; Britton, G. L.; Huang, S. L.; Holland, C. K.; McPherson, D. D. Ultrasound-Enhanced Bevacizumab Release from Echogenic Liposomes for Inhibition of Atheroma Progression. *J. Liposome Res.* **2016**, *26* (1), 47–56. https://doi.org/10.3109/08982104.2015.1029494.

(30) Murthi, S. B.; Ferguson, M.; Sisley, A. C. *Diagnostic Ultrasound - Physics and Equipment*; 2010. https://doi.org/10.1007/978-0-387-79830-1_4.

(31) Dietrich, C. F.; Nolsøe, C. P.; Barr, R. G.; Berzigotti, A.; Burns, P. N.; Cantisani, V.; Chammas, M. C.; Chaubal, N.; Choi, B. I.; Clevert, D. A.; Cui, X.; Dong, Y.; D'Onofrio, M.; Fowlkes, J. B.; Gilja, O. H.; Huang, P.; Ignee, A.; Jenssen, C.; Kono, Y.; Kudo, M.; Lassau, N.; Lee, W. J.; Lee, J. Y.; Liang, P.; Lim, A.; Lyshchik, A.; Meloni, M. F.; Correas, J. M.; Minami, Y.; Moriyasu, F.; Nicolau, C.; Piscaglia, F.;

Saftoiu, A.; Sidhu, P. S.; Sporea, I.; Torzilli, G.; Xie, X.; Zheng, R. Guidelines and Good Clinical Practice Recommendations for Contrast-Enhanced Ultrasound (CEUS) in the Liver–Update 2020 WFUMB in Cooperation with EFSUMB, AFSUMB, AIUM, and FLAUS: WFUMB in Cooperation with EFSUMB, AFSUMB, AIUM and FLAUS. *Ultrasound Med. Biol.* **2020**, *46* (10), 2579–2604. https://doi.org/10.1016/j.ultrasmedbio.2020.04.030.

(32) de Jong, N.; Bouakaz, A.; Frinking, P. Basic Acoustic Properties of Microbubbles. *Echocardiography* **2002**, *19* (3), 229–240. https://doi.org/10.1046/j.1540-8175.2002.00229.x.

(33) Lauterborn, W.; Kurz, T. Physics of Bubble Oscillations. *Reports Prog. Phys.* **2010**, *73* (10). https://doi.org/10.1088/0034-4885/73/10/106501.

(34) Schinkel, A. F. L.; Kaspar, M.; Staub, D. Contrast-Enhanced Ultrasound: Clinical Applications in Patients with Atherosclerosis. *Int. J. Cardiovasc. Imaging* **2016**, *32* (1), 35–48. https://doi.org/10.1007/s10554-015-0713-z.

(35) Feinstein, S. B.; Cheirif, J.; Ten Cate, F. J.; Silverman, P. R.; Heidenreich, P. A.; Dick, C.; Desir, R. M.; Armstrong, W. F.; Quinones, M. A.; Shah, P. M. Safety and Efficacy of a New Transpulmonary Ultrasound Contrast Agent: Initial Multicenter Clinical Results. *J. Am. Coll. Cardiol.* **1990**, *16* (2), 316–324. https://doi.org/10.1016/0735-1097(90)90580-I.

(36) Nesbitt, H.; Sheng, Y.; Kamila, S.; Logan, K.; Thomas, K.; Callan, B.; Taylor, M. A.; Love, M.; O'Rourke, D.; Kelly, P.; Beguin, E.; Stride, E.; McHale, A. P.; Callan, J. F. Gemcitabine Loaded Microbubbles for Targeted Chemo-Sonodynamic Therapy of Pancreatic Cancer. *J. Control. Release* **2018**, *279* (April), 8–16. https://doi.org/10.1016/j.jconrel.2018.04.018.

(37) Stride, E.; Saffari, N. Microbubble Ultrasound Contrast Agents: A Review. *Proc. Inst. Mech. Eng. Part H J. Eng. Med.* **2003**, *217* (6), 429–447. https://doi.org/10.1243/09544110360729072.

(38) Faez, T.; Emmer, M.; Kooiman, K.; Versluis, M.; Van Der Steen, A.; De Jong, N. 20 Years of Ultrasound Contrast Agent Modeling. *IEEE Trans. Ultrason. Ferroelectr. Freq. Control* **2013**, *60* (1), 7–20. https://doi.org/10.1109/TUFFC.2013.2533.

(39) Mullick Chowdhury, S.; Lee, T.; Willmann, J. K. Ultrasound-Guided Drug Delivery in Cancer. *Ultrason. (Seoul, Korea)* **2017**, *36* (3), 171–184. https://doi.org/10.14366/usg.17021.

(40) McLaughlan, J.; Ingram, N.; Smith, P. R.; Harput, S.; Coletta, P. L.; Evans, S.; Freear, S. Increasing the Sonoporation Efficiency of Targeted Polydisperse Microbubble Populations Using Chirp Excitation. *IEEE Trans. Ultrason. Ferroelectr. Freq. Control* **2013**, *60* (12), 2511–2520. https://doi.org/10.1109/TUFFC.2013.2850.

(41) van Wamel, A.; Kooiman, K.; Harteveld, M.; Emmer, M.; ten Cate, F. J.; Versluis, M.; de Jong, N. Vibrating Microbubbles Poking Individual Cells: Drug Transfer into Cells via Sonoporation. *J. Control. Release* **2006**, *112* (2), 149–155. https://doi.org/10.1016/j.jconrel.2006.02.007.

(42) Kooiman, K.; Emmer, M.; Foppen-Harteveld, M.; Van Wamel, A.; De Jong, N. Increasing the Endothelial Layer Permeability through Ultrasound-Activated Microbubbles. *IEEE Trans. Biomed. Eng.* **2010**, *57* (1), 29–32. https://doi.org/10.1109/TBME.2009.2030335.

(43) Browning, R.; Stride, E. Microbubble-Mediated Delivery for Cancer Therapy. *Fluids* **2018**, *3* (4), 74. https://doi.org/10.3390/fluids3040074.

(44) Kooiman, K.; Böhmer, M. R.; Emmer, M.; Vos, H. J.; Chlon, C.; Shi, W. T.; Hall, C. S.; de Winter, S. H. P. M.; Schro??n, K.; Versluis, M.; de Jong, N.; van Wamel, A. Oil-Filled Polymer Microcapsules for Ultrasound-Mediated Delivery of Lipophilic Drugs. *J. Control. Release* **2009**, *133* (2), 109–118. https://doi.org/10.1016/j.jconrel.2008.09.085.

(45) Tinkov, S.; Coester, C.; Serba, S.; Geis, N. A.; Katus, H. A.; Winter, G.; Bekeredjian, R. New Doxorubicin-Loaded Phospholipid Microbubbles for Targeted Tumor Therapy: In-Vivo Characterization. *J. Control. Release* **2010**, *148* (3), 368–372. https://doi.org/10.1016/j.jconrel.2010.09.004.

(46) Peyman, S. A.; Abou-Saleh, R. H.; McLaughlan, J. R.; Ingram, N.; Johnson, B. R. G.; Critchley, K.; Freear, S.; Evans, J. A.; Markham, A. F.; Coletta, P. L.; Evans, S. D. Expanding 3D Geometry for Enhanced On-Chip Microbubble Production and Single Step Formation of Liposome Modified Microbubbles. *Lab Chip* **2012**, *12* (21), 4544. https://doi.org/10.1039/c2lc40634a.

(47) Klibanov, A. L.; Shevchenko, T. I.; Raju, B. I.; Seip, R.; Chin, C. T. Ultrasound-Triggered Release of Materials Entrapped in Microbubble-Liposome Constructs: A Tool for Targeted Drug Delivery. *J. Control. Release* **2010**, *148* (1), 13–17. https://doi.org/10.1016/j.jconrel.2010.07.115.

(48) Bourn, M. D.; Batchelor, D. V. B.; Ingram, N.; McLaughlan, J. R.; Coletta, P. L.; Evans, S. D.; Peyman, S. A. High-Throughput Microfluidics for Evaluating Microbubble Enhanced Delivery of Cancer Therapeutics in Spheroid Cultures. *J. Control. Release* **2020**. https://doi.org/10.1016/j.jconrel.2020.06.011.

(49) Bourn, M.; Batchelor, D. V.; Ingram, N.; McLaughlan, J. R.; Coletta, L.; Evans, S. D.; Peyman, S. Organ on Chip Models for the Evaluation of Microbubble Based Therapeutic Delivery. In *Progress in Biomedical Optics and Imaging - Proceedings of SPIE*; 2020; Vol. 11235, p 21. https://doi.org/10.1117/12.2551605.

(50) Ingram, N.; McVeigh, L. E.; Abou-Saleh, R. H.; Maynard, J.; Peyman, S. A.;

McLaughlan, J. R.; Fairclough, M.; Marston, G.; Valleley, E. M. A.; Jimenez-Macias, J. L.; Charalambous, A.; Townley, W.; Haddrick, M.; Wierzbicki, A.; Wright, A.; Volpato, M.; Simpson, P. B.; Treanor, D. E.; Thomson, N. H.; Loadman, P. M.; Bushby, R. J.; Johnson, B. R. G.; Jones, P. F.; Evans, J. A.; Freear, S.; Markham, A. F.; Evans, S. D.; Coletta, P. L. Ultrasound-Triggered Therapeutic Microbubbles Enhance the Efficacy of Cytotoxic Drugs by Increasing Circulation and Tumor Drug Accumulation and Limiting Bioavailability and Toxicity in Normal Tissues. *Theranostics* **2020**, *10* (24), 10973–10992. https://doi.org/10.7150/thno.49670.

(51) Hashizume, H.; Baluk, P.; Morikawa, S.; McLean, J. W.; Thurston, G.; Roberge, S.; Jain, R. K.; McDonald, D. M. Openings between Defective Endothelial Cells Explain Tumor Vessel Leakiness. *Am. J. Pathol.* **2000**, *156* (4), 1363–1380. https://doi.org/10.1016/S0002-9440(10)65006-7.

(52) Heldin, C. H.; Rubin, K.; Pietras, K.; Östman, A. High Interstitial Fluid Pressure - An Obstacle in Cancer Therapy. *Nat. Rev. Cancer* **2004**, *4* (10), 806–813. https://doi.org/10.1038/nrc1456.

(53) Greish, K. Enhanced Permeability and Retention (EPR) Effect for Anticancer Nanomedicine Drug Targeting. In *Cancer Nanotechnology: Methods and Protocols*; Grobmyer, S. R., Moudgil, B. M., Eds.; Humana Press: Totowa, NJ, 2010; pp 25–37. https://doi.org/10.1007/978-1-60761-609-2_3.

(54) Perera, R. H.; Wu, H.; Peiris, P.; Hernandez, C.; Burke, A.; Zhang, H.; Exner, A. A. Improving Performance of Nanoscale Ultrasound Contrast Agents Using N,N-Diethylacrylamide Stabilization. *Nanomedicine Nanotechnology, Biol. Med.* **2017**, *13* (1), 59–67. https://doi.org/10.1016/j.nano.2016.08.020.

(55) Wu, H.; Abenojar, E. C.; Perera, R.; De Leon, A. C.; An, T.; Exner, A. A. Time-Intensity-Curve Analysis and Tumor Extravasation of Nanobubble Ultrasound Contrast Agents. *Ultrasound Med. Biol.* **2019**, *45* (9), 2502–2514. https://doi.org/10.1016/j.ultrasmedbio.2019.05.025.

(56) Peyman, S. A.; McLaughlan, J. R.; Abou-Saleh, R. H.; Marston, G.; Johnson, B. R. G.; Freear, S.; Coletta, P. L.; Markham, A. F.; Evans, S. D. On-Chip Preparation of Nanoscale Contrast Agents towards High-Resolution Ultrasound Imaging. *Lab Chip* **2016**, *16* (4), 679–687. https://doi.org/10.1039/C5LC01394A.

(57) Epstein, P. S.; Plesset, M. S. On the Stability of Gas Bubbles in Liquid-Gas Solutions. *J. Chem. Phys.* **1950**, *18* (11), 1505–1509. https://doi.org/10.1063/1.1747520.

(58) Ebina, K.; Shi, K.; Hirao, M.; Hashimoto, J.; Kawato, Y.; Kaneshiro, S.; Morimoto, T.; Koizumi, K.; Yoshikawa, H. Oxygen and Air Nanobubble Water Solution Promote the Growth of Plants, Fishes, and Mice. *PLoS One* **2013**, *8* (6), 2–8. https://doi.org/10.1371/journal.pone.0065339.

(59) Hernandez, C.; Abenojar, E. C.; Hadley, J.; De Leon, A. C.; Coyne, R.; Perera, R.; Gopalakrishnan, R.; Basilion, J. P.; Kolios, M. C.; Exner, A. A. Sink or Float? Characterization of Shell-Stabilized Bulk Nanobubbles Using a Resonant Mass Measurement Technique. *Nanoscale* **2019**, *11* (3), 851–855. https://doi.org/10.1039/c8nr08763f.

(60) Bunkin, N. F.; Shkirin, A. V. Nanobubble Clusters of Dissolved Gas in Aqueous Solutions of Electrolyte. II. Theoretical Interpretation. *J. Chem. Phys.* **2012**, *137* (5). https://doi.org/10.1063/1.4739530.

(61) Fine Bubble Technology — General Principles for Usage and Measurement of Fine Bubbles — Part 1: Terminology. ISO 20480-1:2017., 2017.

(62) Nittayacharn, P.; Yuan, H.-X.; Hernandez, C.; Bielecki, P.; Zhou, H.; Exner, A. A. Enhancing Tumor Drug Distribution with Ultrasound-Triggered Nanobubbles. *J. Pharm. Sci.* **2019**, 1–8. https://doi.org/10.1016/j.xphs.2019.05.004.

(63) Cavalli, R.; Bisazza, A.; Trotta, M.; Argenziano, M.; Civra, A.; Donalisio, M.; Lembo, D. New Chitosan Nanobubbles for Ultrasound-Mediated Gene Delivery: Preparation and in Vitro Characterization. *Int. J. Nanomedicine* **2012**, *7*, 3309–3318. https://doi.org/10.2147/IJN.S30912.

(64) Shen, S.; Li, Y.; Xiao, Y.; Zhao, Z.; Zhang, C.; Wang, J.; Li, H.; Liu, F.; He, N.; Yuan, Y.; Lu, Y.; Guo, S.; Wang, Y.; Liao, W.; Liao, Y.; Chen, Y.; Bin, J. Folate-Conjugated Nanobubbles Selectively Target and Kill Cancer Cells via Ultrasound-Triggered Intracellular Explosion. *Biomaterials* **2018**, *181*, 293–306. https://doi.org/10.1016/j.biomaterials.2018.07.030.

(65) Hernandez, C.; Nieves, L.; De Leon, A. C.; Advincula, R.; Exner, A. A. Role of Surface Tension in Gas Nanobubble Stability under Ultrasound. *ACS Appl. Mater. Interfaces* **2018**, *10* (12), 9949–9956. https://doi.org/10.1021/acsami.7b19755.

(66) Tan, B. H.; An, H.; Ohl, C.-D. How Bulk Nanobubbles Might Survive. *Phys. Rev. Lett.* **2020**, *124* (13), 134503. https://doi.org/10.1103/physrevlett.124.134503.

(67) Zhu, J.; An, H.; Alheshibri, M.; Liu, L.; Terpstra, P. M. J.; Liu, G.; Craig, V. S. J. Cleaning with Bulk Nanobubbles. *Langmuir* **2016**, *32* (43), 11203–11211. https://doi.org/10.1021/acs.langmuir.6b01004.

(68) Sang, H. H.; Jiao, X. Y.; Wang, S. F.; Guo, W. H.; Salahou, M. K.; Liu, K. H. Effects of Micro-Nano Bubble Aerated Irrigation and Nitrogen Fertilizer Level on Tillering, Nitrogen Uptake and Utilization of Early Rice. *Plant, Soil Environ.* **2018**, *64* (7), 297–302. https://doi.org/10.17221/240/2018-PSE.

(69) Cheng, B.; Bing, C.; Xi, Y.; Shah, B.; Exner, A. A.; Chopra, R. Influence of Nanobubble Concentration on Blood–Brain Barrier Opening Using Focused Ultrasound Under Real-Time Acoustic Feedback Control. *Ultrasound Med. Biol.* **2019**,

45 (8), 2174–2187. https://doi.org/10.1016/j.ultrasmedbio.2019.03.016.

(70) Rak, D.; Sedlák, M. Comment on "Bulk Nanobubbles or Not Nanobubbles: That Is the Question." *Langmuir* **2020**, *36* (51), 15618–15621. https://doi.org/10.1021/acs.langmuir.0c01614.

(71) Daeichin, V.; Rooij, T. Van; Skachkov, I.; Ergin, B.; Specht, P. A. C.; Lima, A.; Ince, C.; Bosch, J. G.; Steen, A. F. W. Van Der; Jong, N. De. Microbubble Composition and Preparation for Imaging : In Vitro and In Vivo Evaluation. *IEEE Trans. Ultrason. Ferroelectr. Freq. Control* **2017**, *64* (3), 555–567.

(72) Khan, M. S.; Hwang, J.; Seo, Y.; Shin, K.; Lee, K.; Park, C.; Choi, Y.; Hong, J. W.; Choi, J. Engineering Oxygen Nanobubbles for the Effective Reversal of Hypoxia. *Artif. Cells, Nanomedicine Biotechnol.* **2018**, *46* (sup3), S318–S327. https://doi.org/10.1080/21691401.2018.1492420.

(73) Song, R.; Peng, S.; Lin, Q.; Luo, M.; Chung, H. Y.; Zhang, Y.; Yao, S. PH-Responsive Oxygen Nanobubbles for Spontaneous Oxygen Delivery in Hypoxic Tumors. *Langmuir* **2019**, *35*, 10166–10172. https://doi.org/10.1021/acs.langmuir.8b03650.

(74) Batchelor, D. V. B.; Abou-Saleh, R. H.; Coletta, P. L.; McLaughlan, J. R.; Peyman, S. A.; Evans, S. D. Nested Nanobubbles for Ultrasound-Triggered Drug Release. *ACS Appl. Mater. Interfaces* **2020**, *12* (26), 29085–29093. https://doi.org/10.1021/acsami.0c07022.

(75) Zhang, X.; Zheng, Y.; Wang, Z.; Huang, S.; Chen, Y.; Jiang, W.; Zhang, H.; Ding, M.; Li, Q.; Xiao, X.; Luo, X.; Wang, Z.; Qi, H. Methotrexate-Loaded PLGA Nanobubbles for Ultrasound Imaging and Synergistic Targeted Therapy of Residual Tumor during HIFU Ablation. *Biomaterials* **2014**, *35* (19), 5148–5161. https://doi.org/10.1016/j.biomaterials.2014.02.036.

(76) Lin, C. Y.; Pitt, W. G. Acoustic Droplet Vaporization in Biology and Medicine. *Biomed Res. Int.* **2013**, *2013*. https://doi.org/10.1155/2013/404361.

(77) Cavalli, R.; Bisazza, A.; Giustetto, P.; Civra, A.; Lembo, D.; Trotta, G.; Guiot, C.; Trotta, M. Preparation and Characterization of Dextran Nanobubbles for Oxygen Delivery. *Int. J. Pharm.* **2009**, *381* (2), 160–165. https://doi.org/10.1016/j.ijpharm.2009.07.010.

(78) Cavalli, R.; Bisazza, A.; Rolfo, A.; Balbis, S.; Madonnaripa, D.; Caniggia, I.; Guiot, C. Ultrasound-Mediated Oxygen Delivery from Chitosan Nanobubbles. *Int. J. Pharm.* **2009**, *378* (1–2), 215–217. https://doi.org/10.1016/j.ijpharm.2009.05.058.

(79) Cavalli, R.; Bisazza, A.; Trotta, M.; Argenziano, M.; Civra, A.; Donalisio, M.; Lembo, D. New Chitosan Nanobubbles for Ultrasound-Mediated Gene Delivery: Preparation and in Vitro Characterization. *Int. J. Nanomedicine* **2012**, *7*, 3309–3318. https://doi.org/10.2147/IJN.S30912.

(80) Wu, M.; Zhao, H.; Guo, L.; Wang, Y.; Song, J.; Zhao, X.; Li, C.; Hao, L.; Wang, D.; Tang, J. Ultrasound-Mediated Nanobubble Destruction (UMND) Facilitates the Delivery of A10-3.2 Aptamer Targeted and SiRNA-Loaded Cationic Nanobubbles for Therapy of Prostate Cancer. *Drug Deliv.* **2018**, *25* (1), 226–240. https://doi.org/10.1080/10717544.2017.1422300.

(81) Perera, R. H.; Wu, H.; Peiris, P.; Hernandez, C.; Burke, A.; Zhang, H.; Exner, A. A. Improving Performance of Nanoscale Ultrasound Contrast Agents Using N,N-Diethylacrylamide Stabilization. *Nanomedicine Nanotechnology, Biol. Med.* **2017**, *13* (1), 59–67. https://doi.org/10.1016/j.nano.2016.08.020.

(82) Abdalkader, R.; Kawakami, S.; Unga, J.; Higuchi, Y.; Suzuki, R.; Maruyama, K.; Yamashita, F.; Hashida, M. The Development of Mechanically Formed Stable Nanobubbles Intended for Sonoporation-Mediated Gene Transfection. *Drug Deliv.* **2017**, *24* (1), 320–327. https://doi.org/10.1080/10717544.2016.1250139.

(83) Borden, M. A.; Longo, M. L. Dissolution Behavior of Lipid Monolayer-Coated, Air-Filled Microbubbles: Effect of Lipid Hydrophobic Chain Length. *Langmuir* **2002**, *18* (24), 9225–9233. https://doi.org/10.1021/la026082h.

(84) Krupka, T. M.; Solorio, L.; Wilson, R. E.; Wu, H.; Azar, N.; Exner, A. A. Formulation and Characterization of Echogenic Lipid-Pluronic Nanobubbles. *Mol. Pharm.* **2010**, *7* (1), 49–59. https://doi.org/10.1021/mp9001816.

(85) Wang, C. H.; Huang, Y. F.; Yeh, C. K. Aptamer-Conjugated Nanobubbles for Targeted Ultrasound Molecular Imaging. *Langmuir* **2011**, *27* (11), 6971–6976. https://doi.org/10.1021/la2011259.

(86) Van Rooij, T.; Luan, Y.; Renaud, G.; Van Der Steen, A. F. W.; De Jong, N.; Kooiman, K. Acoustical Response of DSPC versus DPPC Lipid-Coated Microbubbles. In *IEEE International Ultrasonics Symposium, IUS*; 2013; pp 310–313. https://doi.org/10.1109/ULTSYM.2013.0080.

(87) Abou-Saleh, R. H.; Swain, M.; Evans, S. D.; Thomson, N. H. Poly(Ethylene Glycol) Lipid-Shelled Microbubbles: Abundance, Stability, and Mechanical Properties. *Langmuir* **2014**, *30* (19), 5557–5563. https://doi.org/10.1021/la404804u.

(88) Yu, Z.; Wang, Y.; Xu, D.; Zhu, L.; Hu, M.; Liu, Q.; Lan, W.; Jiang, J.; Wang, L. G250 Antigen-Targeting Drug-Loaded Nanobubbles Combined with Ultrasound Targeted Nanobubble Destruction: A Potential Novel Treatment for Renal Cell Carcinoma. *Int. J. Nanomedicine* **2020**, *15*, 81–95. https://doi.org/10.2147/IJN.S230879.

(89) Chen, C. C.; Borden, M. A. Ligand Conjugation to Bimodal PEG Brush Layers on Microbubbles. *Langmuir* **2010**, *26* (16), 13183–13194. https://doi.org/10.1021/la101796p.Ligand.

(90) Wang, L.; Zhang, M.; Tan, K.; Guo, Y.; Tong, H.; Fan, X.; Fang, K.; Li, R. Preparation

of Nanobubbles Carrying Androgen Receptor SiRNA and Their Inhibitory Effects on Androgen-Independent Prostate Cancer When Combined with Ultrasonic Irradiation. *PLoS One* **2014**, *9* (5). https://doi.org/10.1371/journal.pone.0096586.

(91) Inglut, C. T.; Sorrin, A. J.; Kuruppu, T.; Vig, S.; Cicalo, J.; Ahmad, H.; Huang, H. C. Immunological and Toxicological Considerations for the Design of Liposomes. *Nanomaterials* **2020**, *10* (2). https://doi.org/10.3390/nano10020190.

(92) Wydro, P.; Krajewska, B.; Ha, K.; Wydro, P. Chitosan as a Lipid Binder : A Langmuir Monolayer Study of Chitosan − Lipid Interactions. *Am. Chem. Soc.* **2007**, 2611–2617. https://doi.org/10.1021/bm700453x.

(93) Cavalli, R.; Argenziano, M.; Vigna, E.; Giustetto, P.; Torres, E.; Aime, S.; Terreno, E. Preparation and in Vitro Characterization of Chitosan Nanobubbles as Theranostic Agents. *Colloids Surfaces B Biointerfaces* **2015**, *129*, 39–46. https://doi.org/10.1016/j.colsurfb.2015.03.023.

(94) Yasui, K.; Tuziuti, T.; Kanematsu, W. Mysteries of Bulk Nanobubbles (Ultrafine Bubbles); Stability and Radical Formation. *Ultrason. Sonochem.* **2018**, *48* (March), 259–266. https://doi.org/10.1016/j.ultsonch.2018.05.038.

(95) Millare, J. C.; Basilia, B. A. Nanobubbles from Ethanol-Water Mixtures: Generation and Solute Effects via Solvent Replacement Method. *ChemistrySelect* **2018**, *3* (32), 9268–9275. https://doi.org/10.1002/slct.201801504.

(96) Alheshibri, M.; Qian, J.; Jehannin, M.; Craig, V. S. J. A History of Nanobubbles. *Langmuir* **2016**, *32* (43), 11086–11100. https://doi.org/10.1021/acs.langmuir.6b02489.

(97) Yin, T.; Wang, P.; Li, J.; Wang, Y.; Zheng, B.; Zheng, R.; Cheng, D.; Shuai, X. Tumor-Penetrating Codelivery of SiRNA and Paclitaxel with Ultrasound-Responsive Nanobubbles Hetero-Assembled from Polymeric Micelles and Liposomes. *Biomaterials* **2014**, *35* (22), 5932–5943. https://doi.org/10.1016/j.biomaterials.2014.03.072.

(98) Xing, Z.; Wang, J.; Ke, H.; Zhao, B.; Yue, X.; Dai, Z.; Liu, J. The Fabrication of Novel Nanobubble Ultrasound Contrast Agent for Potential Tumor Imaging. *Nanotechnology* **2010**, *21* (14). https://doi.org/10.1088/0957-4484/21/14/145607.

(99) Khan, M. S.; Hwang, J.; Lee, K.; Choi, Y.; Seo, Y.; Jeon, H.; Hong, J. W.; Choi, J. Anti-Tumor Drug-Loaded Oxygen Nanobubbles for the Degradation of HIF-1α and the Upregulation of Reactive Oxygen Species in Tumor Cells. *Cancers (Basel).* **2019**, *11* (10), 19–23. https://doi.org/10.3390/cancers11101464.

(100) Henry, W. III. Experiments on the Quantity of Gases Absorbed by Water, at Different Temperatures, and under Different Pressures. *Philos. Trans.* **1803**, *93*.

(101) Bosca, F.; Bielecki, P. A.; Exner, A. A.; Barge, A. Porphyrin-Loaded Pluronic

Nanobubbles: A New US-Activated Agent for Future Theranostic Applications. *Bioconjug. Chem.* **2018**, *29* (2), 234–240. https://doi.org/10.1021/acs.bioconjchem.7b00732.

(102) Khan, M. S.; Hwang, J.; Lee, K.; Choi, Y.; Jang, J.; Kwon, Y.; Hong, J. W.; Choi, J. Surface Composition and Preparation Method for Oxygen Nanobubbles for Drug Delivery and Ultrasound Imaging Applications. *Nanomaterials* **2019**, *9* (1), 4–9. https://doi.org/10.3390/nano9010048.

(103) Yang, H.; Deng, L.; Li, T.; Shen, X.; Yan, J.; Zuo, L.; Wu, C.; Liu, Y. Multifunctional PLGA Nanobubbles as Theranostic Agents: Combining Doxorubicin and P-Gp SiRNA Co-Delivery into Human Breast Cancer Cells and Ultrasound Cellular Imaging. *J. Biomed. Nanotechnol.* **2015**, *11* (12), 2124–2136. https://doi.org/10.1166/jbn.2015.2168.

(104) Yang, H.; Shen, X.; Yan, J.; Xie, X.; Chen, Z.; Li, T.; Li, S.; Qin, X.; Wu, C.; Liu, Y. Charge-Reversal-Functionalized PLGA Nanobubbles as Theranostic Agents for Ultrasonic-Imaging-Guided Combination Therapy. *Biomater. Sci.* **2018**, *6* (9), 2426–2439. https://doi.org/10.1039/c8bm00419f.

(105) Hernandez, C.; Gulati, S.; Fioravanti, G.; Stewart, P. L.; Exner, A. A. Cryo-EM Visualization of Lipid and Polymer-Stabilized Perfluorocarbon Gas Nanobubbles - A Step Towards Nanobubble Mediated Drug Delivery. *Sci. Rep.* **2017**, *7* (1), 1–8. https://doi.org/10.1038/s41598-017-13741-1.

(106) Zhu, L.; Wang, L.; Liu, Y.; Xu, D.; Fang, K.; Guo, Y. CAIX Aptamer-Functionalized Targeted Nanobubbles for Ultrasound Molecular Imaging of Various Tumors. *Int. J. Nanomedicine* **2018**, *13*, 6481–6495. https://doi.org/10.2147/IJN.S176287.

(107) Tian, Y.; Liu, Z.; Zhang, L.; Zhang, J.; Han, X.; Wang, Q.; Cheng, W. Apatinib-Loaded Lipid Nanobubbles Combined with Ultrasound-Targeted Nanobubble Destruction for Synergistic Treatment of HepG2 Cells in Vitro. *Onco. Targets. Ther.* **2018**, *11*, 4785–4795. https://doi.org/10.2147/OTT.S170786.

(108) Peng, Y.; Zhu, L.; Wang, L.; Liu, Y.; Fang, K.; Lan, M.; Shen, D.; Liu, D.; Yu, Z.; Guo, Y. Preparation of Nanobubbles Modified with a Small-Molecule CXCR4 Antagonist for Targeted Drug Delivery to Tumors and Enhanced Ultrasound Molecular Imaging. *Int. J. Nanomedicine* **2019**, *14*, 9139–9157. https://doi.org/10.2147/IJN.S210478.

(109) Yu, Z.; Hu, M.; Li, Z.; Dan Xu; Zhu, L.; Guo, Y.; Liu, Q.; Lan, W.; Jiang, J.; Wang, L. Anti-G250 Nanobody-Functionalized Nanobubbles Targeting Renal Cell Carcinoma Cells for Ultrasound Molecular Imaging. *Nanotechnology* **2020**, *31* (20). https://doi.org/10.1088/1361-6528/ab7040.

(110) Fan, X.; Wang, L.; Guo, Y.; Xiong, X.; Zhu, L.; Fang, K. Inhibition of Prostate Cancer

Growth Using Doxorubicin Assisted by Ultrasound-Targeted Nanobubble Destruction. *Int. J. Nanomedicine* **2016**, *11*, 3585–3596. https://doi.org/10.2147/IJN.S111808.

(111) Abenojar, E. C.; Nittayacharn, P.; De Leon, A. C.; Perera, R.; Wang, Y.; Bederman, I.; Exner, A. A. Effect of Bubble Concentration on the in Vitro and in Vivo Performance of Highly Stable Lipid Shell-Stabilized Micro- and Nanoscale Ultrasound Contrast Agents. *Langmuir* **2019**. https://doi.org/10.1021/acs.langmuir.9b00462.

(112) Fan, X.; Wang, L.; Guo, Y.; Tu, Z.; Li, L.; Tong, H.; Xu, Y.; Li, R.; Fang, K. Ultrasonic Nanobubbles Carrying Anti-PSMA Nanobody: Construction and Application in Prostate Cancer-Targeted Imaging. *PLoS One* **2015**, *10* (6), 1–13. https://doi.org/10.1371/journal.pone.0127419.

(113) Yin, T.; Wang, P.; Zheng, R.; Zheng, B.; Cheng, D.; Zhang, X.; Shuai, X. Nanobubbles for Enhanced Ultrasound Imaging of Tumors. *Int. J. Nanomedicine* **2012**, *7*, 895–904. https://doi.org/10.2147/IJN.S28830.

(114) Eklund, F.; Alheshibri, M.; Swenson, J. Differentiating Bulk Nanobubbles from Nanodroplets and Nanoparticles. *Curr. Opin. Colloid Interface Sci.* **2021**, 101427. https://doi.org/10.1016/j.cocis.2021.101427.

(115) Stetefeld, J.; Mckenna, S. A.; Patel, T. R. Dynamic Light Scattering : A Practical Guide and Applications in Biomedical Sciences. *Biophys. Rev.* **2016**, 409–427. https://doi.org/10.1007/s12551-016-0218-6.

(116) Nirmalkar, N.; Pacek, A. W.; Barigou, M. On the Existence and Stability of Bulk Nanobubbles. *Langmuir* **2018**, *34*, 10964–10973. https://doi.org/10.1021/acs.langmuir.8b01163.

(117) Midtvedt, D.; Eklund, F.; Olsén, E.; Midtvedt, B.; Swenson, J.; Höök, F. Size and Refractive Index Determination of Subwavelength Particles and Air Bubbles by Holographic Nanoparticle Tracking Analysis. *Anal. Chem.* **2020**, *92* (2), 1908–1915. https://doi.org/10.1021/acs.analchem.9b04101.

(118) Abenojar, E. C.; Bederman, I.; de Leon, A. C.; Zhu, J.; Hadley, J.; Kolios, M. C.; Exner, A. A. Theoretical and Experimental Gas Volume Quantification of Micro-and Nanobubble Ultrasound Contrast Agents. *Pharmaceutics* **2020**, *12* (3). https://doi.org/10.3390/pharmaceutics12030208.

(119) Yin, T.; Wang, P.; Li, J.; Zheng, R.; Zheng, B.; Cheng, D.; Li, R.; Lai, J.; Shuai, X. Ultrasound-Sensitive SiRNA-Loaded Nanobubbles Formed by Hetero-Assembly of Polymeric Micelles and Liposomes and Their Therapeutic Effect in Gliomas. *Biomaterials* **2013**, *34* (18), 4532–4543. https://doi.org/10.1016/j.biomaterials.2013.02.067.

(120) Moore, M. J.; Bodera, F.; Hernandez, C.; Shirazi, N.; Abenojar, E.; Exner, A. A.; Kolios, M. C. The Dance of the Nanobubbles: Detecting Acoustic Backscatter from

Sub-Micron Bubbles Using Ultra-High Frequency Acoustic Microscopy. *Nanoscale* **2020**, *12* (41), 21420–21428. https://doi.org/10.1039/d0nr05390b.

(121) Kanematsu, W.; Tuziuti, T.; Yasui, K. The Influence of Storage Conditions and Container Materials on the Long Term Stability of Bulk Nanobubbles — Consideration from a Perspective of Interactions between Bubbles and Surroundings. *Chem. Eng. Sci.* **2020**, *219*, 115594. https://doi.org/10.1016/j.ces.2020.115594.

(122) Kwan, J. J.; Borden, M. A. Lipid Monolayer Collapse and Microbubble Stability. *Adv. Colloid Interface Sci.* **2012**, *183–184*, 82–99. https://doi.org/10.1016/j.cis.2012.08.005.

(123) Liu, H.; Cao, G. Effectiveness of the Young-Laplace Equation at Nanoscale. *Sci. Rep.* **2016**, *6*, 1–10. https://doi.org/10.1038/srep23936.

(124) Jin, J.; Wang, R.; Tang, J.; Yang, L.; Feng, Z.; Xu, C.; Yang, F.; Gu, N. Dynamic Tracking of Bulk Nanobubbles from Microbubbles Shrinkage to Collapse. *Colloids Surfaces A Physicochem. Eng. Asp.* **2020**, *589* (January), 124430. https://doi.org/10.1016/j.colsurfa.2020.124430.

(125) Yin, T.; Wang, P.; Zheng, R.; Zheng, B.; Cheng, D.; Zhang, X.; Shuai, X. Nanobubbles for Enhanced Ultrasound Imaging of Tumors. *Int. J. Nanomedicine* **2012**, *7*, 895–904. https://doi.org/10.2147/IJN.S28830.

(126) Nirmalkar, N.; Pacek, A. W.; Barigou, M. Interpreting the Interfacial and Colloidal Stability of Bulk Nanobubbles. *Soft Matter* **2018**, *14* (47), 9643–9656. https://doi.org/10.1039/c8sm01949e.

(127) Michailidi, E. D.; Bomis, G.; Varoutoglou, A.; Kyzas, G. Z.; Mitrikas, G.; Mitropoulos, A. C.; Efthimiadou, E. K.; Favvas, E. P. Bulk Nanobubbles: Production and Investigation of Their Formation/Stability Mechanism. *J. Colloid Interface Sci.* **2020**, *564*, 371–380. https://doi.org/10.1016/j.jcis.2019.12.093.

(128) Weijs, J. H.; Seddon, J. R. T.; Lohse, D. Diffusive Shielding Stabilizes Bulk Nanobubble Clusters. *ChemPhysChem* **2012**, *13* (8), 2197–2204. https://doi.org/10.1002/cphc.201100807.

(129) Ohgaki, K.; Khanh, N. Q.; Joden, Y.; Tsuji, A.; Nakagawa, T. Physicochemical Approach to Nanobubble Solutions. *Chem. Eng. Sci.* **2010**, *65* (3), 1296–1300. https://doi.org/10.1016/j.ces.2009.10.003.

(130) Alzaraa, A.; Gravante, G.; Chung, W. Y.; Al-Leswas, D.; Bruno, M.; Dennison, A. R.; Lloyd, D. M. Targeted Microbubbles in the Experimental and Clinical Setting. *AJS* **2012**, *204*, 355–366. https://doi.org/10.1016/j.amjsurg.2011.10.024.

(131) Averkiou, M. A.; Bruce, M. F.; Powers, J. E.; Sheeran, P. S.; Burns, P. N. Imaging Methods for Ultrasound Contrast Agents. *Ultrasound Med. Biol.* **2020**, *46* (3), 498–517. https://doi.org/10.1016/j.ultrasmedbio.2019.11.004.

(132) McLaughlan, J. R.; Harput, S.; Abou-Saleh, R. H.; Peyman, S. A.; Evans, S.; Freear, S. Characterisation of Liposome-Loaded Microbubble Populations for Subharmonic Imaging. *Ultrasound Med. Biol.* **2017**, *43* (1), 346–356. https://doi.org/10.1016/j.ultrasmedbio.2016.09.011.

(133) Wilson, S. R.; Burns, P. N.; Kono, Y. Contrast-Enhanced Ultrasound of Focal Liver Masses: A Success Story. *Ultrasound Med. Biol.* **2020**, *46* (5), 1059–1070. https://doi.org/10.1016/j.ultrasmedbio.2019.12.021.

(134) Watanabe, A.; Sheng, H.; Endo, H.; Feril, L. B.; Irie, Y.; Ogawa, K.; Moosavi-Nejad, S.; Tachibana, K. Echographic and Physical Characterization of Albumin-Stabilized Nanobubbles. *Heliyon* **2019**, *5* (6), e01907. https://doi.org/10.1016/j.heliyon.2019.e01907.

(135) Sun, C.; Sboros, V.; Butler, M. B.; Moran, C. M. In Vitro Acoustic Characterization of Three Phospholipid Ultrasound Contrast Agents from 12 to 43 MHz. *Ultrasound Med. Biol.* **2014**, *40* (3), 541–550. https://doi.org/10.1016/j.ultrasmedbio.2013.10.010.

(136) de Leon, A.; Perera, R.; Hernandez, C.; Cooley, M.; Jung, O.; Jeganathan, S.; Abenojar, E.; Fishbein, G.; Sojahrood, A. J.; Emerson, C. C.; Stewart, P. L.; Kolios, M. C.; Exner, A. A. Contrast Enhanced Ultrasound Imaging by Nature-Inspired Ultrastable Echogenic Nanobubbles. *Nanoscale* **2019**, *11* (33), 15647–15658. https://doi.org/10.1039/c9nr04828f.

(137) Pellow, C.; Acconcia, C.; Zheng, G.; Goertz, D. E. Threshold-Dependent Nonlinear Scattering from Porphyrin Nanobubbles for Vascular and Extravascular Applications. *Phys. Med. Biol.* **2018**, *63* (21). https://doi.org/10.1088/1361-6560/aae571.

(138) JafariSojahrood, A.; Nieves, L.; Hernandez, C.; Exner, A.; Kolios, M. C. Theoretical and Experimental Investigation of the Nonlinear Dynamics of Nanobubbles Excited at Clinically Relevant Ultrasound Frequencies and Pressures: The Role Oflipid Shell Buckling. In *IEEE International Ultrasonics Symposium (IUS)*; 2017; pp 6–9.

(139) Marmottant, P.; van der Meer, S.; Emmer, M.; Versluis, M.; de Jong, N.; Hilgenfeldt, S.; Lohse, D. A Model for Large Amplitude Oscillations of Coated Bubbles Accounting for Buckling and Rupture. *J. Acoust. Soc. Am.* **2005**, *118* (6), 3499–3505. https://doi.org/10.1121/1.2109427.

(140) Zhang, J.; Chen, Y.; Deng, C.; Zhang, L.; Sun, Z.; Wang, J.; Yang, Y.; Lv, Q.; Han, W.; Xie, M. The Optimized Fabrication of a Novel Nanobubble for Tumor Imaging. *Front. Pharmacol.* **2019**, *10* (May), 1–15. https://doi.org/10.3389/fphar.2019.00610.

(141) Smeenge, M.; Tranquart, F.; Mannaerts, C. K.; De Reijke, T. M.; Van De Vijver, M. J.; Laguna, M. P.; Pochon, S.; De La Rosette, J. J. M. C. H.; Wijkstra, H. First-in-Human Ultrasound Molecular Imaging with a VEGFR2-Specific Ultrasound Molecular Contrast Agent (BR55) in Prostate Cancer a Safety and Feasibility Pilot

Study. *Invest. Radiol.* **2017**, *52* (7), 419–427. https://doi.org/10.1097/RLI.0000000000000362.

(142) Rojas, J. D.; Lin, F.; Chiang, Y. C.; Chytil, A.; Chong, D. C.; Bautch, V. L.; Kimryn Rathmell, W.; Dayton, P. A. Ultrasound Molecular Imaging of VEGFR-2 in Clear-Cell Renal Cell Carcinoma Tracks Disease Response to Antiangiogenic and Notch-Inhibition Therapy. *Theranostics* **2018**, *8* (1), 141–155. https://doi.org/10.7150/thno.19658.

(143) Wilson, K. E.; Wang, T. Y.; Willmann, J. K. Acoustic and Photoacoustic Molecular Imaging of Cancer. *J. Nucl. Med.* **2013**, *54* (11), 1851–1854. https://doi.org/10.2967/jnumed.112.115568.

(144) Zhu, L.; Guo, Y.; Wang, L.; Fan, X.; Xiong, X.; Fang, K.; Xu, D. Construction of Ultrasonic Nanobubbles Carrying CAIX Polypeptides to Target Carcinoma Cells Derived from Various Organs. *J. Nanobiotechnology* **2017**, *15* (1), 1–16. https://doi.org/10.1186/s12951-017-0307-0.

(145) Collis, J.; Manasseh, R.; Liovic, P.; Tho, P.; Ooi, A.; Petkovic-Duran, K.; Zhu, Y. Cavitation Microstreaming and Stress Fields Created by Microbubbles. *Ultrasonics* **2010**, *50* (2), 273–279. https://doi.org/10.1016/j.ultras.2009.10.002.

(146) Prentice, P.; Cuschieri, A.; Dholakia, K.; Prausnitz, M.; Campbell, P. Membrane Disruption by Optically Controlled Microbubble Cavitation. *Nat. Phys.* **2005**, *1* (2), 107–110. https://doi.org/10.1038/nphys148.

(147) Tan, Y.; Tajik, A.; Chen, J.; Jia, Q.; Chowdhury, F.; Wang, L.; Chen, J.; Zhang, S.; Hong, Y.; Yi, H.; Wu, D. C.; Zhang, Y.; Wei, F.; Poh, Y.-C.; Seong, J.; Singh, R.; Lin, L.-J.; Doğanay, S.; Li, Y.; Jia, H.; Ha, T.; Wang, Y.; Huang, B.; Wang, N. Matrix Softness Regulates Plasticity of Tumour-Repopulating Cells via H3K9 Demethylation and Sox2 Expression. *Nat. Commun.* **2014**, *5*, 1–12. https://doi.org/10.1038/ncomms5619.

(148) Marano, F.; Argenziano, M.; Frairia, R.; Adamini, A.; Bosco, O.; Rinella, L.; Fortunati, N.; Cavalli, R.; Catalano, M. G. Doxorubicin-Loaded Nanobubbles Combined with Extracorporeal Shock Waves: Basis for a New Drug Delivery Tool in Anaplastic Thyroid Cancer. *Thyroid* **2016**, *26* (5), 705–716. https://doi.org/10.1089/thy.2015.0342.

(149) Tayier, B.; Deng, Z.; Wang, Y.; Wang, W.; Mu, Y.; Yan, F. Biosynthetic Nanobubbles for Targeted Gene Delivery by Focused Ultrasound. *Nanoscale* **2019**, *11* (31), 14757–14768. https://doi.org/10.1039/c9nr03402a.

(150) Xie, X.; Lin, W.; Liu, H.; Deng, J.; Chen, Y.; Liu, H.; Fu, X.; Yang, Y. Ultrasound-Responsive Nanobubbles Contained with Peptide–Camptothecin Conjugates for Targeted Drug Delivery. *Drug Deliv.* **2016**, *23* (8), 2756–2764.

https://doi.org/10.3109/10717544.2015.1077289.

(151) Nittayacharn, P.; Abenojar, E.; De Leon, A.; Wegierak, D.; Exner, A. A. Increasing Doxorubicin Loading in Lipid-Shelled Perfluoropropane Nanobubbles via a Simple Deprotonation Strategy. *Front. Pharmacol.* **2020**, *11* (May), 1–10. https://doi.org/10.3389/fphar.2020.00644.

(152) Gallois, L.; Fiallo, M.; Garnier-Suillerot, A. Comparison of the Interaction of Doxorubicin, Daunorubicin, Idarubicin and Idarubicinol with Large Unilamellar Vesicles Circular Dichroism Study. *Biochim. Biophys. Acta - Biomembr.* **1998**, *1370* (1), 31–40. https://doi.org/10.1016/S0005-2736(97)00241-1.

(153) Lin, W.; Xie, X.; Yang, Y.; Fu, X.; Liu, H.; Yang, Y.; Deng, J. Thermosensitive Magnetic Liposomes with Doxorubicin Cell-Penetrating Peptides Conjugate for Enhanced and Targeted Cancer Therapy. *Drug Deliv.* **2016**, *23* (9), 3436–3443. https://doi.org/10.1080/10717544.2016.1189983.

(154) Lin, W.; Xie, X.; Deng, J.; Liu, H.; Chen, Y.; Fu, X.; Liu, H.; Yang, Y. Cell-Penetrating Peptide-Doxorubicin Conjugate Loaded NGR-Modified Nanobubbles for Ultrasound Triggered Drug Delivery. *J. Drug Target.* **2016**, *24* (2), 134–146. https://doi.org/10.3109/1061186X.2015.1058802.

(155) Chandan, R.; Banerjee, R. Pro-Apoptotic Liposomes-Nanobubble Conjugate Synergistic with Paclitaxel: A Platform for Ultrasound Responsive Image-Guided Drug Delivery. *Sci. Rep.* **2018**, *8* (1), 1–15. https://doi.org/10.1038/s41598-018-21084-8.

(156) Prabhakar, A.; Banerjee, R. Nanobubble Liposome Complexes for Diagnostic Imaging and Ultrasound-Triggered Drug Delivery in Cancers: A Theranostic Approach. *ACS Omega* **2019**, *4* (13), 15567–15580. https://doi.org/10.1021/acsomega.9b01924.

(157) Paasonen, L.; Sipilä, T.; Subrizi, A.; Laurinmäki, P.; Butcher, S. J.; Rappolt, M.; Yaghmur, A.; Urtti, A.; Yliperttula, M. Gold-Embedded Photosensitive Liposomes for Drug Delivery: Triggering Mechanism and Intracellular Release. *J. Control. Release* **2010**, *147* (1), 136–143. https://doi.org/10.1016/j.jconrel.2010.07.095.

(158) Srivastava, R. K.; Sasaki, C. Y.; Hardwick, J. M.; Longo, D. L. Bcl-2-Mediated Drug Resistance: Inhibition of Apoptosis by Blocking Nuclear Factor of Activated T Lymphocytes (NFAT)-Induced Fas Ligand Transcription. *J. Exp. Med.* **1999**, *190* (2), 253–265. https://doi.org/10.1084/jem.190.2.253.

(159) Xie, X.; Yang, Y.; Lin, W.; Liu, H.; Liu, H.; Yang, Y.; Chen, Y.; Fu, X.; Deng, J. Cell-Penetrating Peptide-SiRNA Conjugate Loaded YSA-Modified Nanobubbles for Ultrasound Triggered SiRNA Delivery. *Colloids Surfaces B Biointerfaces* **2015**, *136*, 641–650. https://doi.org/10.1016/j.colsurfb.2015.10.004.

(160) Pellow, C.; Abenojar, E. C.; Exner, A. A.; Zheng, G.; Goertz, D. E. Concurrent Visual

and Acoustic Tracking of Passive and Active Delivery of Nanobubbles to Tumors. *Theranostics* **2020**, *10* (25), 11690–11706. https://doi.org/10.7150/thno.51316.

(161) Pellow, C.; O'Reilly, M. A.; Hynynen, K.; Zheng, G.; Goertz, D. E. Simultaneous Intravital Optical and Acoustic Monitoring of Ultrasound-Triggered Nanobubble Generation and Extravasation. *Nano Lett.* **2020**, *20* (6), 4512–4519. https://doi.org/10.1021/acs.nanolett.0c01310.

(162) Maeda, H.; Wu, J.; Sawa, T.; Matsumura, Y.; Hori, K. Tumor Vascular Permeability and the EPR Effect in Macromolecular Therapeutics: A Review. *J. Control. Release* **2000**, *65* (1–2), 271–284. https://doi.org/10.1016/S0168-3659(99)00248-5.

(163) Matsumura, Y.; Maeda, H. A New Concept for Macromolecular Therapeutics in Cancer Chemotherapy: Mechanism of Tumoritropic Accumulation of Proteins and the Antitumor Agent Smancs. *Cancer Res.* **1986**, *46* (8), 6387–6392.

(164) Sindhwani, S.; Syed, A. M.; Ngai, J.; Kingston, B. R.; Maiorino, L.; Rothschild, J.; MacMillan, P.; Zhang, Y.; Rajesh, N. U.; Hoang, T.; Wu, J. L. Y.; Wilhelm, S.; Zilman, A.; Gadde, S.; Sulaiman, A.; Ouyang, B.; Lin, Z.; Wang, L.; Egeblad, M.; Chan, W. C. W. The Entry of Nanoparticles into Solid Tumours. *Nat. Mater.* **2020**, *19* (5), 566–575. https://doi.org/10.1038/s41563-019-0566-2.

(165) Dai, Q.; Wilhelm, S.; Ding, D.; Syed, A. M.; Sindhwani, S.; Zhang, Y.; Chen, Y. Y.; Macmillan, P.; Chan, W. C. W. Quantifying the Ligand-Coated Nanoparticle Delivery to Cancer Cells in Solid Tumors. *ACS Nano* **2018**, *12* (8), 8423–8435. https://doi.org/10.1021/acsnano.8b03900.

(166) Everett, D. H. *Basic Principles of Colloid Science*; Royal Society of Chemistry, 1988.

(167) Israelachvili, J. N.; Mitchell, D. J.; Ninham, B. W. Theory of Self-Assembly of Lipid Bilayers and Vesicles. *BBA - Biomembr.* **1977**, *470* (2), 185–201. https://doi.org/10.1016/0005-2736(77)90099-2.

(168) Derjaguin, B. A Theory of Interaction of Particles in Presence of Electric Double Layers and the Stability of Lyophobe Colloids and Disperse Systems. *Prog. Surf. Sci.* **1993**, *43* (1–4), 1–14. https://doi.org/10.1016/0079-6816(93)90010-S.

(169) Derjaguin, B.; Landau, L. Theory of the Stability of Strongly Sharged Yophocis Sols and the Adhesion of Strongly Charged Particles in Solution of Electrolytes. *Acta Physiochim.* **1941**, *14* (633).

(170) Verwey, E. J. W.; Overbeek, J. T. G. Theory of the Stability of Lyophobic Colloids. *Journal of Physical and Colloid Chemistry*. 1947, pp 631–636. https://doi.org/10.1021/j150453a001.

(171) Nirmalkar, N.; Pacek, A. W.; Barigou, M. Interpreting the Interfacial and Colloidal Stability of Bulk Nanobubbles. *Soft Matter* **2018**, *14* (47), 9643–9656. https://doi.org/10.1039/c8sm01949e.

(172) Torchilin, V. P.; Omelyanenko, V. G.; Papisov, M. I.; Bogdanov, A. A.; Trubetskoy, V. S.; Herron, J. N.; Gentry, C. A. Poly(Ethylene Glycol) on the Liposome Surface: On the Mechanism of Polymer-Coated Liposome Longevity. *BBA - Biomembr.* **1994**, *1195* (1), 11–20. https://doi.org/10.1016/0005-2736(94)90003-5.

(173) Woodle, M. C.; Lasic, D. D. Sterically Stabilized Liposomes Therapeutics. *Biochim. Biophys. Acta - Gen. Subj.* **1992**, *1113* (1113), 171–199.

(174) Senior, R.; Becher, H.; Monaghan, M.; Agati, L.; Zamorano, J.; Vanoverschelde, J. L.; Nihoyannopoulos, P.; Edvardsen, T.; Lancellotti, P.; Delgado, V.; Gimelli, A.; Cosyns, B.; Gerber, B.; Donal, E.; Flachskampf, F.; Haugaa, K.; Cardim, N.; Masci, P. G. Clinical Practice of Contrast Echocardiography: Recommendation by the European Association of Cardiovascular Imaging (EACVI) 2017. *Eur. Heart J. Cardiovasc. Imaging* **2017**, *18* (11), 1205. https://doi.org/10.1093/ehjci/jex182.

(175) Apfel, R. E.; Holland, C. K. Gauging the Likelihood of Cavitation from Short-Pulse, Low-Duty Cycle Diagnostic Ultrasound. *Ultrasound Med. Biol.* **1990**, *17* (2), 179–185. https://doi.org/https://doi.org/10.1016/0301-5629(91)90125-G.

(176) Nelson, T. R.; Fowlkes, J. B.; Abramowicz, J. S.; Church, C. C. Ultrasound Biosafety Considerations for the Practicing Sonographer and Sonologist. *J. Ultrasound Med.* **2009**, *28* (2), 139–150. https://doi.org/10.7863/jum.2009.28.2.139.

(177) Murthi, S.; Ferguson, M.; Sisely, A. Diagnostic Ultrasound - Physics and Equipment. In *Diagnostic Ultrasound - physics and equipment*; 2010; pp 4–22.

(178) Medwin, H. Counting Bubbles Acoustically: A Review. *Ultrasonics* **1977**, *15* (1), 7–13. https://doi.org/10.1016/0041-624X(77)90005-1.

(179) Ainslie, M. A.; Leighton, T. G. Review of Scattering and Extinction Cross-Sections, Damping Factors, and Resonance Frequencies of a Spherical Gas Bubble. *J. Acoust. Soc. Am.* **2011**, *130* (5), 3184–3208. https://doi.org/10.1121/1.3628321.

(180) Plesset, M. S.; Prosperetti, A. Bubble Dynamics and Cavitation. *Annu. Rev. Fluid Mech.* **1977**, *9*, 145–185.

(181) Kooiman, K.; Van Rooij, T.; Qin, B.; Mastik, F.; Vos, H. J.; Versluis, M.; Klibanov, A. L.; De Jong, N.; Villanueva, F. S.; Chen, X. Focal Areas of Increased Lipid Concentration on the Coating of Microbubbles during Short Tone-Burst Ultrasound Insonification. *PLoS One* **2017**, *12* (7). https://doi.org/10.1371/journal.pone.0180747.

(182) Sijl, J.; Overvelde, M.; Dollet, B.; Garbin, V.; de Jong, N.; Lohse, D.; Versluis, M. "Compression-Only" Behavior: A Second-Order Nonlinear Response of Ultrasound Contrast Agent Microbubbles. *J. Acoust. Soc. Am.* **2011**, *129* (4), 1729–1739. https://doi.org/10.1121/1.3505116.

(183) Duck, F. A. Nonlinear Acoustics in Diagnostic Ultrasound. *Ultrasound Med. Biol.* **2002**, *28* (1), 1–18. https://doi.org/10.1016/S0301-5629(01)00463-X.

(184) van Rooij, T.; Luan, Y.; Renaud, G.; van der Steen, A. F. W.; Versluis, M.; de Jong, N.; Kooiman, K. Non-Linear Response and Viscoelastic Properties of Lipid-Coated Microbubbles: DSPC versus DPPC. *Ultrasound Med. Biol.* **2015**, *41* (5), 1432–1445. https://doi.org/10.1016/j.ultrasmedbio.2015.01.004.

(185) Sojahrood, A. J.; Earl, R.; Li, Q.; Porter, T. M.; Kolios, M. C.; Karshafian, R. Nonlinear Dynamics of Acoustic Bubbles Excited by Their Pressure Dependent Subharmonic Resonance Frequency: Oversaturation and Enhancement of the Subharmonic Signal. **2019**, 1–18.

(186) Leighton, T. G. *The Acoustic Bubble*; Academic Press, 1997.

(187) Chen, W. S.; Brayman, A. A.; Matula, T. J.; Crum, L. A. Inertial Cavitation Dose and Hemolysis Produced in Vitro with or without Optison®. *Ultrasound Med. Biol.* **2003**, *29* (5), 725–737. https://doi.org/10.1016/S0301-5629(03)00013-9.

(188) McLaughlan, J. R.; Cowell, D. M. J.; Freear, S. Gold Nanoparticle Nucleated Cavitation for Enhanced High Intensity Focused Ultrasound Therapy. *Phys. Med. Biol.* **2018**, *63* (1). https://doi.org/10.1088/1361-6560/aa97e9.

(189) Baldan, A. Progress in Ostwald Ripening Theories and Their Applications in Nickel-Base Super Alloys. *J. Mater. Sci.* **2002**, *37*, 2379–2405.

(190) Lifshitz, I. M.; Slyozov, V. V. The Kinetics of Precipitation from Supersaturated Solid Solutions. *J. Phys. Chem. Solids* **1961**, *19* (1), 35–50. https://doi.org/https://doi.org/10.1016/0022-3697(61)90054-3.

(191) Wagner, V. C. Theorie Der Alterung von Niederschlagen Durch Umlosen (Ostwald-Reifung). *Zeitschrift für Elektrochemie, Berichte der Bunsengesellschaft für Phys. Chemie* **1961**, *65* (7–8), 581–591.

(192) Howell, J. R.; Mengüc, M. P.; Daun, K.; Siegel, R. *Thermal Radiation Heat Transfer*, 7th ed.; CRCm Taylor & Francis, 2020. https://doi.org/https://doi.org/10.1201/9780429327308.

(193) Roach, L.; Coletta, P. L.; Critchley, K.; Evans, S. D. Controlling the Optical Properties of Gold Nanorods in One-Pot Syntheses. *J. Phys. Chem. C* **2022**, *126* (6), 3235–3243. https://doi.org/10.1021/acs.jpcc.1c10447.

(194) Knights, O.; Freear, S.; McLaughlan, J. R. Improving Plasmonic Photothermal Therapy of Lung Cancer Cells with Anti-EGFR Targeted Gold Nanorods. *Nanomaterials* **2020**, *10* (7), 1–13. https://doi.org/10.3390/nano10071307.

(195) Bohren, C. F.; Huffmand, D. R. *Absorption and Scattering of Light by Small Particles*; Wiley-VCH, 1998. https://doi.org/10.1002/9783527618156.

(196) Roach, L. Biomedical Application of Phospholipid – Functionalised Gold Nanorods for Cancer Therapy. **2019**, No. September.

(197) Acheson, D. J. *Elementary Fluid Dynamics*; Oxford University Press, 1990.

(198) Beebe, D. J.; Mensing, G. A.; Walker, G. M. Physics and Applications of Microfluidics in Biology. *Annu. Rev. Biomed. Eng.* **2002**, *4*, 261–286. https://doi.org/10.1146/annurev.bioeng.4.112601.125916.

(199) Avila, K.; Moxey, D.; De Lozar, A.; Avila, M.; Barkley, D.; Hof, B. The Onset of Turbulence in Pipe Flow. *Science (80-.).* **2011**, *333* (6039), 192–196. https://doi.org/10.1126/science.1203223.

(200) Abraham, J. P.; Sparrow, E. M.; Minkowycz, W. J. Internal-Flow Nusselt Numbers for the Low-Reynolds-Number End of the Laminar-to-Turbulent Transition Regime. *Int. J. Heat Mass Transf.* **2011**, *54* (1–3), 584–588. https://doi.org/10.1016/j.ijheatmasstransfer.2010.09.012.

(201) Sompayrac, L. *How Cancer Works*; Jones and Bartlett, 2004.

(202) Armistead, F. J. Mechanical Phenotyping of Single Cells Using Shear and Inertial Microfluidics, University of Leeds, 2019.

(203) Bortolini, C.; Dong, M. Preparation and Characterization of Peptide Aggregations and Their Au- Labeled Complex by Transmission Electron Microscopy. **2014**, 868–874.

(204) Peyman, S. A.; McLaughlan, J. R.; Abou-Saleh, R. H.; Marston, G.; Johnson, B. R. G.; Freear, S.; Coletta, P. L.; Markham, A. F.; Evans, S. D. On-Chip Preparation of Nanoscale Contrast Agents towards High-Resolution Ultrasound Imaging. *Lab Chip* **2016**, *16* (4), 679–687. https://doi.org/10.1039/c5lc01394a.

(205) Abou-Saleh, R. H.; Armistead, F. J.; Batchelor, D. V. B.; Johnson, B. R. G.; Peyman, S. A.; Evans, S. D. Horizon: Microfluidic Platform for the Production of Therapeutic Microbubbles and Nanobubbles. *Rev. Sci. Instrum.* **2021**, *92* (7), 074105. https://doi.org/10.1063/5.0040213.

(206) Nie, L.; McLaughlan, J. R.; Cowell, D. M. J.; Carpenter, T. M.; Freear, S. Subharmonic Plane Wave Imaging of Liposome-Loaded Microbubbles. *IEEE Int. Ultrason. Symp. IUS* **2018**, *2018-Janua*. https://doi.org/10.1109/ULTSYM.2018.8580201.

(207) Batchelor, D. V. B.; Armistead, F. J.; Ingram, N.; Peyman, S. A.; Mclaughlan, J. R.; Coletta, P. L.; Evans, S. D. Nanobubbles for Therapeutic Delivery: Production, Stability and Current Prospects. *Curr. Opin. Colloid Interface Sci.* **2021**, *54*, 101456. https://doi.org/10.1016/j.cocis.2021.101456.

(208) Churchman, A. H.; Mico, V.; de Pablo, J. G.; Peyman, S. A.; Freear, S.; Evans, S. D. Combined Flow-Focus and Self-Assembly Routes for the Formation of Lipid Stabilized Oil-Shelled Microbubbles. *Microsystems Nanoeng.* **2018**, *4* (June 2017), 17087. https://doi.org/10.1038/micronano.2017.87.

(209) Garstecki, P.; Gitlin, I.; Diluzio, W.; Whitesides, G. M.; Kumacheva, E.; Stone, H. A. Formation of Monodisperse Bubbles in a Microfluidic Flow-Focusing Device. *Appl. Phys. Lett.* **2004**, *85* (13), 2649–2651. https://doi.org/10.1063/1.1796526.

(210) Garstecki, P.; Fuerstman, M. J.; Stone, H. A.; Whitesides, G. M. Formation of Droplets and Bubbles in a Microfluidic T-Junction - Scaling and Mechanism of Break-Up. *Lab Chip* **2006**, *6* (3), 437–446. https://doi.org/10.1039/b510841a.

(211) Sine, J.; Urban, C.; Thayer, D.; Charron, H.; Valim, N.; Tata, D. B.; Schiff, R.; Blumenthal, R.; Joshi, A.; Puri, A. Photo Activation of HPPH Encapsulated in "Pocket" Liposomes Triggers Multiple Drug Release and Tumor Cell Killing in Mouse Breast Cancer Xenografts. *Int. J. Nanomedicine* **2014**, *10*, 125–145. https://doi.org/10.2147/IJN.S72143.

(212) Subbarao, N. K.; MacDonald, R. C. Experimental Method to Correct Fluorescence Intensities for the Inner Filter Effect. *Analyst* **1993**, *118* (7), 913–916. https://doi.org/10.1039/AN9931800913.

(213) Kopechek, J. A.; Haworth, K. J.; Radhakrishnan, K.; Huang, S. L.; Klegerman, M. E.; McPherson, D. D.; Holland, C. K. The Impact of Bubbles on Measurement of Drug Release from Echogenic Liposomes. *Ultrason. Sonochem.* **2013**, *20* (4), 1121–1130. https://doi.org/10.1016/j.ultsonch.2012.12.005.

(214) Yan, F.; Li, L.; Deng, Z.; Jin, Q.; Chen, J.; Yang, W.; Yeh, C. K.; Wu, J.; Shandas, R.; Liu, X.; Zheng, H. Paclitaxel-Liposome-Microbubble Complexes as Ultrasound-Triggered Therapeutic Drug Delivery Carriers. *J. Control. Release* **2013**, *166* (3), 246–255. https://doi.org/10.1016/j.jconrel.2012.12.025.

(215) Abou-Saleh, R. H.; Peyman, S. A.; Johnson, B. R. G.; Marston, G.; Ingram, N.; Bushby, R.; Coletta, P. L.; Markham, A. F.; Evans, S. D. The Influence of Intercalating Perfluorohexane into Lipid Shells on Nano and Microbubble Stability. *Soft Matter* **2016**, *12* (34), 7223–7230. https://doi.org/10.1039/C6SM00956E.

(216) U.S. Food and Drug Admins. Doxil Label. **1995**, 1–34.

(217) Raffy, S.; Teissié, J. Control of Lipid Membrane Stability by Cholesterol Content. *Biophys. J.* **1999**, *76* (4), 2072–2080. https://doi.org/10.1016/S0006-3495(99)77363-7.

(218) Zhou, Y.; Yang, K.; Cui, J.; Ye, J. Y.; Deng, C. X. Controlled Permeation of Cell Membrane by Single Bubble Acoustic Cavitation. *J. Control. Release* **2012**, *157* (1), 103–111. https://doi.org/10.1016/j.jconrel.2011.09.068.

(219) Qin, P.; Lin, Y.; Jin, L.; Du, L.; Yu, A. C. H. Impact of Microbubble-to-Cell Parameters on Heterogeneous Sonoporation at the Single-Cell Level. *2015 IEEE Int. Ultrason. Symp. IUS 2015* **2015**, 9–12. https://doi.org/10.1109/ULTSYM.2015.0292.

(220) Wrenn, S. P.; Dicker, S. M.; Small, E. F.; Dan, N. R.; Mleczko, M.; Schmitz, G.; Lewin, P. A. Bursting Bubbles and Bilayers. *Theranostics* **2012**, *2* (12), 1140–1159. https://doi.org/10.7150/thno.4305.

(221) King, D. A.; O'Brien, W. D. Comparison between Maximum Radial Expansion of

Ultrasound Contrast Agents and Experimental Postexcitation Signal Results. *J. Acoust. Soc. Am.* **2011**, *129* (1), 114–121. https://doi.org/10.1121/1.3523339.

(222) Wallace, N.; Dicker, S.; Lewin, P.; Wrenn, S. P. Inertial Cavitation Threshold of Nested Microbubbles. *Ultrasonics* **2015**, *58*, 67–74. https://doi.org/10.1016/j.ultras.2014.12.004.

(223) Ueno, M.; Yoshida, S.; Horikoshi, I. Characteristics of the Membrane Permeability of Temperature-Sensitive Liposome. *Bulletin of the Chemical Society of Japan*. 1991, pp 1588–1593. https://doi.org/10.1246/bcsj.64.1588.

(224) Wu, Q.; Mannaris, C.; May, J. P.; Bau, L.; Polydorou, A.; Ferri, S.; Carugo, D.; Evans, N. D.; Stride, E. Investigation of the Acoustic Vaporization Threshold of Lipid-Coated Perfluorobutane Nanodroplets Using Both High-Speed Optical Imaging and Acoustic Methods. *Ultrasound Med. Biol.* **2021**, *47* (7), 1826–1843. https://doi.org/10.1016/j.ultrasmedbio.2021.02.019.

(225) Evans, D. R.; Parsons, D. F.; Craig, V. S. J. Physical Properties of Phase-Change Emulsions. *Langmuir* **2006**, *22* (23), 9538–9545. https://doi.org/10.1021/la062097u.

(226) Zheng, L.; Yapa, P. D. Buoyant Velocity of Spherical and Nonspherical Bubbles/Droplets. *J. Hydraul. Eng.* **2002**, *126* (11), 852–854. https://doi.org/10.1061/(asce)0733-9429(2000)126:11(852).

(227) TWI Global. The Beam Spread of an Ultrasonic Probe in the Far Zone https://www.twi-global.com/technical-knowledge/faqs/faq-what-factors-influence-the-beam-spread-of-an-ultrasonic-probe-in-the-far-zone.

(228) Koch, M.; Suhr, C.; Roth, B.; Meinhardt-Wollweber, M. Iterative Morphological and Mollifier-Based Baseline Correction for Raman Spectra. *J. Raman Spectrosc.* **2017**, *48* (2), 336–342. https://doi.org/10.1002/jrs.5010.

(229) Ruckenstein, E. Nanodispersions of Bubbles and Oil Drops in Water. *Colloids Surfaces A Physicochem. Eng. Asp.* **2013**, *423*, 112–114. https://doi.org/10.1016/j.colsurfa.2013.01.056.

(230) Doinikov, A. A.; Bouakaz, A. Theoretical Investigation of Shear Stress Generated by a Contrast Microbubble on the Cell Membrane as a Mechanism for Sonoporation. *J. Acoust. Soc. Am.* **2010**, *128* (1), 11–19. https://doi.org/10.1121/1.3419775.

(231) Yang, H.; Cai, W.; Xu, L.; Lv, X.; Qiao, Y.; Li, P.; Wu, H.; Yang, Y.; Zhang, L.; Duan, Y. Nanobubble-Affibody: Novel Ultrasound Contrast Agents for Targeted Molecular Ultrasound Imaging of Tumor. *Biomaterials* **2015**, *37*, 279–288. https://doi.org/10.1016/j.biomaterials.2014.10.013.

(232) Rupert, D. L. M.; Mapar, M.; Shelke, G. V.; Norling, K.; Elmeskog, M.; Lötvall, J. O.; Block, S.; Bally, M.; Agnarsson, B.; Höök, F. Effective Refractive Index and Lipid Content of Extracellular Vesicles Revealed Using Optical Waveguide Scattering and

Fluorescence Microscopy. *Langmuir* **2018**, *34* (29), 8522–8531. https://doi.org/10.1021/acs.langmuir.7b04214.

(233) Charalambous, A.; Mico, V.; McVeigh, L. E.; Marston, G.; Ingram, N.; Volpato, M.; Peyman, S. A.; McLaughlan, J. R.; Wierzbicki, A.; Loadman, P. M.; Bushby, R. J.; Markham, A. F.; Evans, S. D.; Coletta, P. L. Targeted Microbubbles Carrying Lipid-Oil-Nanodroplets for Ultrasound-Triggered Delivery of the Hydrophobic Drug, Combretastatin A4. *Nanomedicine Nanotechnology, Biol. Med.* **2021**. https://doi.org/https://doi.org/10.1016/j.nano.2021.102401.

(234) Armistead, F. J.; Gala De Pablo, J.; Gadêlha, H.; Peyman, S. A.; Evans, S. D. Cells Under Stress: An Inertial-Shear Microfluidic Determination of Cell Behavior. *Biophys. J.* **2019**, *116* (6), 1127–1135. https://doi.org/10.1016/j.bpj.2019.01.034.

(235) van Rooij, T.; Skachkov, I.; Beekers, I.; Lattwein, K. R.; Voorneveld, J. D.; Kokhuis, T. J. A.; Bera, D.; Luan, Y.; van der Steen, A. F. W.; de Jong, N.; Kooiman, K. Viability of Endothelial Cells after Ultrasound-Mediated Sonoporation: Influence of Targeting, Oscillation, and Displacement of Microbubbles. *J. Control. Release* **2016**, *238*, 197–211. https://doi.org/10.1016/j.jconrel.2016.07.037.

(236) Dentamaro, M.; Lux, F.; Vander Elst, L.; Dauguet, N.; Montante, S.; Moussaron, A.; Burtea, C.; Muller, R. N.; Tillement, O.; Laurent, S. Chemical and in Vitro Characterizations of a Promising Bimodal AGuIX Probe Able to Target Apoptotic Cells for Applications in MRI and Optical Imaging. *Contrast Media Mol. Imaging* **2016**, *11* (5), 381–395. https://doi.org/10.1002/cmmi.1702.

(237) Tapani, E.; Taavitsainen, M.; Lindros, K.; Vehmas, T.; Lehtonen, E. Toxicity of Ethanol in Low Concentrations: Experimental Evaluation in Cell Culture. *Acta radiol.* **1996**, *37* (6), 923–926. https://doi.org/10.3109/02841859609175470.

(238) Frinking, P. J. A.; Tardy, I.; Théraulaz, M.; Arditi, M.; Powers, J.; Pochon, S.; Tranquart, F. Effects of Acoustic Radiation Force on the Binding Efficiency of BR55, a VEGFR2-Specific Ultrasound Contrast Agent. *Ultrasound Med. Biol.* **2012**, *38* (8), 1460–1469. https://doi.org/10.1016/j.ultrasmedbio.2012.03.018.

(239) Beekers, I.; Van Rooij, T.; Verweij, M. D.; Versluis, M.; De Jong, N.; Trietsch, S. J.; Kooiman, K. Acoustic Characterization of a Vessel-on-a-Chip Microfluidic System for Ultrasound-Mediated Drug Delivery. *IEEE Trans. Ultrason. Ferroelectr. Freq. Control* **2018**, *65* (4), 570–581. https://doi.org/10.1109/TUFFC.2018.2803137.

(240) Kooiman, K.; Foppen-Harteveld, M.; De Jong, N. Ultrasound-Mediated Targeted Microbubble Sonoporation of Endothelial Cells. *J. Control. Release* **2010**, *148* (1), e62–e63. https://doi.org/S0168-3659(10)00506-7 [pii]\r10.1016/j.jconrel.2010.07.025.

(241) Wang, M.; Zhang, Y.; Cai, C.; Tu, J.; Guo, X.; Zhang, D. Sonoporation-Induced Cell

Membrane Permeabilization and Cytoskeleton Disassembly at Varied Acoustic and Microbubble-Cell Parameters. *Sci. Rep.* **2018**, *8* (1), 1–12. https://doi.org/10.1038/s41598-018-22056-8.

(242) Kooiman, K.; Foppen-Harteveld, M.; Der Steen, A. F. W. Van; De Jong, N. Sonoporation of Endothelial Cells by Vibrating Targeted Microbubbles. *J. Control. Release* **2011**, *154* (1), 35–41. https://doi.org/10.1016/j.jconrel.2011.04.008.

(243) Karshafian, R.; Bevan, P. D.; Williams, R.; Samac, S.; Burns, P. N. Sonoporation by Ultrasound-Activated Microbubble Contrast Agents: Effect of Acoustic Exposure Parameters on Cell Membrane Permeability and Cell Viability. *Ultrasound Med. Biol.* **2009**, *35* (5), 847–860. https://doi.org/10.1016/j.ultrasmedbio.2008.10.013.

(244) Chen, C. C.; Sheeran, P. S.; Wu, S.-Y.; Olumolade, O. O.; Dayton, P. A.; Konofagou, E. E. Targeted Drug Delivery with Focused Ultrasound-Induced Blood-Brain Barrier Opening Using Acoustically-Activated Nanodroplets. *J. Control. Release* **2013**, *172*, 795–804. https://doi.org/10.1016/j.jconrel.2013.09.025.

(245) Bhutto, D. F.; Murphy, E. M.; Priddy, M. C.; Centner, C. C.; Moore IV, J. B.; Bolli, R.; Kopechek, J. A. Effect of Molecular Weight on Sonoporation-Mediated Uptake in Human Cells. *Ultrasound Med. Biol.* **2018**, *44* (12), 2662–2672. https://doi.org/10.1016/j.ultrasmedbio.2018.08.008.

(246) Segers, T.; Lohse, D.; Versluis, M.; Frinking, P. Universal Equations for the Coalescence Probability and Long-Term Size Stability of Phospholipid-Coated Monodisperse Microbubbles Formed by Flow Focusing. *Langmuir* **2017**, *33* (39), 10329–10339. https://doi.org/10.1021/acs.langmuir.7b02547.

(247) Segers, T.; De Rond, L.; De Jong, N.; Borden, M.; Versluis, M. Stability of Monodisperse Phospholipid-Coated Microbubbles Formed by Flow-Focusing at High Production Rates. *Langmuir* **2016**, *32* (16), 3937–3944. https://doi.org/10.1021/acs.langmuir.6b00616.

(248) Batchelor, D. V. B.; Abou-saleh, R. H.; Coletta, L.; Mclaughlan, J. R.; Peyman, S. A.; Evans, S. D. Nested-Nanobubbles for Ultrasound Triggered Drug Release. **2020**.

(249) Silke, R.; Guillaume, L.; Ine, D. C.; Brans, T.; Heleen, D.; Braeckmans, K.; Michel, V.; Stefaan C, D. S.; Ine, L. Sonoprinting of Nanoparticle-Loaded Microbubbles: Unraveling the Multi-Timescale Mechanism. *Biomaterials* **2019**, *217* (June), 119250. https://doi.org/10.1016/j.biomaterials.2019.119250.

(250) Segers, T.; Versluis, M. Acoustic Bubble Sorting for Ultrasound Contrast Agent Enrichment. *Lab Chip* **2014**, *14* (10), 1705–1714. https://doi.org/10.1039/C3LC51296G.

(251) Midtvedt, B.; Olsén, E.; Eklund, F.; Höök, F.; Adiels, C. B.; Volpe, G.; Midtvedt, D. Fast and Accurate Nanoparticle Characterization Using Deep-Learning-Enhanced Off-

Axis Holography. *ACS Nano* **2021**, *15* (2), 2240–2250. https://doi.org/10.1021/acsnano.0c06902.

(252) Abou-Saleh, R. H.; Delaney, A.; Ingram, N.; Batchelor, D. V. B.; Johnson, B. R. G.; Charalambous, A.; Bushby, R. J.; Peyman, S. A.; Coletta, P. L.; Markham, A. F.; Evans, S. D. Freeze-Dried Therapeutic Microbubbles: Stability and Gas Exchange. *ACS Appl. Bio Mater.* **2020**. https://doi.org/10.1021/acsabm.0c00982.

(253) Trefalt, G.; Borkovec, M. Overview of DLVO Theory. *Lab. Colloid Surf. Chem. Univ. Geneva* **2014**, 1–10.

(254) Zetasizer Nano Series User Manual. 2013.

(255) Harvie, A. J. Quantum Dot Redox Sensors : Understanding Excited State Dynamics, 2018.

(256) Micó Egea, V. Developing Microbubble-Nanodroplet Composites for Enhanced Hydrophobic Drug Delivery, 2017.